



AVERTISSEMENT

Ce document est le fruit d'un long travail approuvé par le jury de soutenance et mis à disposition de l'ensemble de la communauté universitaire élargie.

Il est soumis à la propriété intellectuelle de l'auteur. Ceci implique une obligation de citation et de référencement lors de l'utilisation de ce document.

D'autre part, toute contrefaçon, plagiat, reproduction illicite encourt une poursuite pénale.

Contact : ddoc-theses-contact@univ-lorraine.fr

LIENS

Code de la Propriété Intellectuelle. articles L 122. 4

Code de la Propriété Intellectuelle. articles L 335.2- L 335.10

http://www.cfcopies.com/V2/leg/leg_droi.php

<http://www.culture.gouv.fr/culture/infos-pratiques/droits/protection.htm>



UNIVERSITÉ
DE LORRAINE



LABORATOIRE
RÉACTIONS
ET GÉNIE
DES PROCÉDÉS



Title: Synthesis and catalytic activity of ZIF-8 and doped-ZIF-8 crystals. Stability and cytotoxicity evaluation.

Aleksandra Schejn

PhD thesis

Supervisors: **Professor Raphaël Schneider, Professor Véronique Falk**

Doctoral School: **Sciences and Engineering of Resources, Processes, Products, Environment.**

Specialization: **Engineering of the Products, Processes and Industrial Systems.**

COMPOSITION DU JURY

Rapporteurs:

- **Gerhard Pirngruber**, Ingénieur de recherches IFP Energies nouvelles, Solaize
- **Emmanuel Guillon**, Professeur, Université de Reims Champagne-Ardenne, Reims

Examineurs:

- **Christian Serre**, Directeur de Recherches CNRS, Université de Versailles-St-Quentin, Institut Lavoisier, Versailles
- **Lavinia Balan**, Chargée de recherche CNRS, Institut de Science des Matériaux de Mulhouse, Mulhouse

Directeurs de thèse:

- **Véronique Falk**, Professeur, Université de Lorraine, Nancy
- **Raphaël Schneider**, Professeur, Université de Lorraine, Nancy

Acknowledgments

First of all, I would like to express my sincere thanks to prof. Raphael Schneider for giving me this great opportunity to work in his research group, for his supervisions, brilliant guidance and - the most important - for huge support and encouragement throughout last three years. I also want to extend my gratitude to prof. Véronique Falk for her co-supervision, patience in responding on all my questions and numerous discussions. Both of you opened my mind and offered me almost endless possibilities for my research ideas. MERCI BEAUCOUP!

Also I want to acknowledge all the people that help me and contribute with their hard work to my PhD: Jean-François Remy, Kévin Mozet, Lavinia Balan, Abdelhay Aboulaich, Ghouti Medjahdi, Thomas Mazet, Lionel Aranda, Jean-Pascal Piret, Elise Dumotier, and Jorge Mendoza.

Furthermore, I would like to thank the members of my team for being my friends, their humour, unending jokes, open ears and support, especially Oleksii Kolmykov, Florian Donat, Clement Dezanet, Hatem Moussa, Bilel Chouchene, Afef Yakoubi, Fedia Joudi, Faouzi Achouri, Jordan Rollot, Caroline Charbonnel, Anissa Ahres, Syama Santhakumar, all Erasmus students from Poland passed through our lab: Monika Buczek, Pawel Kunstmann, Anna Jankowiak, Natalia Nowaczyk, Marcin Kapela, Wojciech Bialowas, people from Faculty of Pharmacy in Nancy: Anne Sapin-Minet, Ming Luo and Wen Wu. I love you guys☺ It was a pleasure to spend time with you (not only in the lab).

I feel so happy and thankful to have the support of my best friends: Justyna Przybyl, Nina Owiesna, Pranay Mojakar. Even from the distance, I feel you are always close. You kept the things light and me smiling.

Last, but certainly not least, I would like to thank my parents and brother for their endless love and the motivation they gave me during all the time. Thank you with all my heart and soul!

List of content

Acknowledgments	2
List of content.....	3
Abbreviations	6
Introduction	8
Chapter 1: Bibliographic studies	10
1.1 Metal Organic Frameworks.....	11
1.1.1 History in brief	11
1.1.2 Structure	11
1.1.3 Properties.....	23
1.1.4 Possible application of metal-organic frameworks	27
1.2 Zeolitic imidazolate frameworks.....	33
1.2.1 ZIFs structure	33
1.2.2 Zeolitic Imidazolate Framework-8	36
1.2.3 ZIF-8 synthesis	37
1.2.4 ZIF-8 growth mechanism	41
1.2.5 ZIF-8 applications	42
1.3 General information on carbon dioxide conversion	45
1.3.1 Cyclic carbonates	46
1.4 Catalyst shaping	48
1.4.1 Generalities on the mechanical properties of porous materials.....	48
1.4.2 ZIF-8 shaping	49
1.5 General information on cytotoxicity of nanoparticles.....	51
1.6 Characterization methods for metal-organic frameworks	53
1.6.1 Scanning electron microscopy.....	53
1.6.2 Transmission Electron Microscopy.....	55
1.6.3 X-ray diffractometry.....	56
1.6.4 BET surface area	59
1.6.5 Thermogravimetric analysis	62
1.6.6 Other techniques.....	63
1.7 Techniques for cytotoxicity evaluation	67
1.8 References	69
Chapter 2: Experimental part	75
2.1 Materials.....	75
2.2 General information on the characterization techniques	75
2.3 Procedures	76

2.3.1 Synthesis of the materials.....	76
2.3.2 Catalytic experiments.....	77
2.3.3 Shaping of the ZIF-8 catalyst.....	79
2.3.4 Cytotoxicity studies.....	80
Chapter 3: ZIF-8 design, synthesis and functionalization.....	83
3.1 Controlling ZIF-8 nano- and microcrystal formation and reactivity through zinc salts variations.....	84
3.1.1 Abstract.....	84
3.1.2 Introduction.....	85
3.1.3 Results and discussion.....	86
3.1.4 Conclusions.....	92
3.1.5 References.....	92
3.2 Cu ²⁺ -doped Zeolitic Imidazolate Frameworks (ZIF-8): Efficient and Stable Catalysts for Cycloadditions and Condensation Reactions.....	94
3.2.1 Abstract.....	94
3.2.2 Introduction.....	95
3.2.3 Results.....	96
3.2.4 Conclusions.....	107
3.2.6 References.....	108
3.3 Fe ₃ O ₄ @ZIF-8: Magnetically recoverable catalysts by loading Fe ₃ O ₄ nanoparticles inside a zinc imidazolate framework.....	111
3.3.1 Abstract.....	111
3.3.2 Introduction.....	112
3.3.3 Results.....	113
3.3.4 Conclusions.....	121
3.3.5 References.....	122
Chapter 4: ZIF-8 material for carbon dioxide conversion into cyclic carbonates.....	124
4.1 Synthesis of ZIF-8 crystals and application to carbon dioxide conversion.....	125
4.1.2 Introduction.....	126
4.1.3 Results and discussion.....	126
4.3.4 Conclusions.....	133
4.3.5 References.....	134
Chapter 5: Cytotoxicity of ZIF-8 doped and undoped samples.....	135
5.1 Impact of ZIF-8 samples on viability and reactive oxygen species production in A549 alveolar lung cells and IHK keratinocytes cell cultures.....	136
5.1.1 Abstract.....	136
5.1.2 Introduction.....	136
5.1.3 Results.....	137
5.1.4 Conclusions.....	149
5.1.5 References.....	150

5.2 In vitro digestion model of ZIF-8 particles	151
5.2.1 Abstract	151
5.2.2 Introduction	151
5.2.3 Results	152
5.2.4 Conclusions	160
5.2.5 References	162
Chapter 6: Conclusions and perspectives	163
List of figures	168
List of tables	172
Résumé	173
Résumé	179
Abstract	180

Abbreviations

ANA	Analcine topology
BASF	Badische Anilin- und Soda- Fabrik (eng. Baden Aniline and Soda Factory)
BBR	Building Block Replacement
BC	Benzalkonium chloride
CAU	Christian Albrechts University
CMC-Na	Carboxymethylcellulose sodium salt
CTAB	Cetyltrimethylammonium bromide
DEF	Diethylformamide
DFTT	Zeolite-dft topology
DMF	Dimethylformamide
DRS	Diffuse Reflectance Spectroscopy
DXP	N,N-bis(2,6-dimethylphenyl)-3,4:9,10-perylene tetracarboxylic diimide
EDTA	Ethylenediamine tetraacetic acid
FACS	Fluorescence activated cell sorting
FIrpic	(2-carboxypyridyl)bis(3,5-difluoro-2-(2-pyridyl)phenyl)iridium(III)
GIS	Gismondine topology
GMET	Gmelinite topology
HBSS	Hank's buffered salt solution; Hank's balanced salt solution
HKUST	Hong Kong University of Science and Technology
Hmim	2-Methylimidazole
ICEEL	Institut Carnot Energie et Environnement en Lorraine
IHK	Immortalized human keratinocytes
IM	Imidazole
IRMOF	Isorecticular Metal Organic Framework
IUPAC	International Union of Pure and Applied Chemistry
LMCT	Ligand-to-metal charge transfer
LTAT	Linde Type A topology
MICA	Materials Institute Carnot Alsace
MIL	Materials of Institute Lavoisier
MERT	Merlinoite topology
MLCT	Metal-to-ligand charge transfer
MNPs	Magnetic Nanoparticles
MOF	Metal Organic Frameworks
MOP	Metal Organic Polyhedra
MOZ	Zeolite Framework Type ZSM-10 (One Zero) topology
MTS	3-(4,5-dimethylthiazol-2-yl)-5-(3-carboxymethoxyphenyl)-2-(4-sulfophenyl)-2H-tetrazolium)
NOTT	Nottingham University metal organic framework
NU	Northwestern University
PSE	Post-Synthetic Exchange
PSM	Post-Synthetic Modification
POZT	Specific topology of ZIF-95 comprises four cages A, B, C and D
RCSR	Reticular Chemistry Structural Resource

RHOT	Zeolite-rho topology
SALE	Solvent-assisted linker exchange
SBU	Secondary Building Units
SEM	Scanning Electron Microscopy
SIN-1	3-(4-morpholinyl)sydnimine hydrochloride
SNU	Seoul National University
SODT	Sodalite topology
TCPB	1,3,5-tri(4-carboxyphenoxy)benzene
TEM	Transmission Electron Microscopy
TGA	Thermogravimetric analysis
UiO	University of Oslo
XRD	X-ray diffractometry
ZIF	Zeolitic Imidazolate Framework

Introduction

This work was carried out with the ICEEL and MICA Carnot Institutes financial support and scientific resources available at the LRGP (Laboratoire Réactions et Génie des Procédés) laboratory in Nancy, France. In particular, the aim of the project was bounded up with the area of structure design and engineering of new materials directed into catalytic applications. In our research, we chose metal-organic frameworks (MOFs) as interesting and promising candidates of self-ordered, highly porous, and easily tunable systems. Moreover, the composition as well as the properties of these materials can be tailored by selecting appropriate building blocks, functionalities and the crystal growth conditions.

We would like to show evaluation of the possibilities for the rational structure design using as an example zeolitic imidazolate framework-8 (ZIF-8). The advantage of the ZIF-8 is that its structure is composed of zinc metal centers tetrahedrally coordinated with methylimidazole linkers in 3D arrangement. This kind of network gives an abundance of open, catalytically active sites and upstanding surface area. Furthermore, the framework can act as a template for further modification and functionalization.

The main objectives of this study were, firstly, the preparation of ZIF-8 materials and ZIF-8 heterostructures with properties adapted to the desired application, and then shaping of the catalyst to obtain the best form of material for industrial scale-up utilization.

The first chapter is dedicated to bibliographic study of the present subject. We put the background informations on the metal-organic frameworks and ZIF-8 material. We also described the experimental techniques for the materials characterization.

The very first task of the project was connected with the synthesis of ZIF-8 crystals. We developed protocols combining different experimental conditions, like starting precursors, solvent, functionalities, temperature, and reaction time. We monitored the effect of these procedures on the obtained products. Especially, we traced their physical and chemical properties (like crystal size, morphology, and porosity) and finally the influence of these changes on the material catalytic activity. These experiments led the publication of three scientific articles:

Schejn A., Balan L., Falk V., Aranda L., Medjahdi G., Schneider R., Controlling ZIF-8 nano- and microcrystal formation and reactivity through zinc salt variations. *CrystEngComm*, 2014, 16, 4493-4500 doi: [10.1039/C3CE42485E](https://doi.org/10.1039/C3CE42485E)

Schejn A., Aboulaich A., Balan L., Falk V., Lalevée J., Medjahdi G., Aranda L., Mozet K., Schneider R., Cu²⁺-doped zeolitic imidazolate frameworks (ZIF-8): Efficient and stable catalysts for cycloadditions and condensation reactions. *Catal. Sci. Technol.*, 2015, 5, 1829-1839 doi: [10.1039/C4CY01505C](https://doi.org/10.1039/C4CY01505C)

Schejn A., Mazet T., Falk V., Balan L., Aranda L., Medjahdi G., Schneider R., Fe₃O₄@ZIF-8: magnetically recoverable catalysts by loading Fe₃O₄ nanoparticles inside a zinc imidazolate framework. *Dalton Trans.*, 2015, 44, 10136-10140 doi: [10.1039/C5DT01191D](https://doi.org/10.1039/C5DT01191D)

The rational design of ZIF-8 material, obtained results and arising advantages are discussed in details in the chapter 2.

The use of ZIF-8 material as heterogeneous catalyst presents also capabilities for many reactions of greatly important, environmental problem, like carbon dioxide reduction or conversion. Motivated by this objective, we used ZIF-8 crystals in the cyclic carbonates production using CO₂ as C1-synthon. As the reaction could be scale-up at the industrial level, we tried to shape the powder in the form of pellets and use it under the same conditions. The outcomes from this research are summarized in the chapter 3.

Being aware of the nanomaterials influence on the human's life and health, we extended our investigations through ZIF-8 cytotoxicity experiments. We conducted the screening of ZIF-8, Cu- and Fe-doped ZIF-8 crystals using as models skin keratinocytes IHK and pulmonary A549 cells. We selected these human cell cultures as possible first contacted and suffered from exposition on airborne ZIF-8. We also tested the fate of the particles when ingested using *in vitro* digestion model under fed conditions. We supplemented all these informations with particles stability tests in various media. This part was performed in the collaboration with Namur Nanosafety Centre, Namur University, Belgium. The results are highlighted in the chapter 4.

Finally, in the chapter 5, general conclusions and perspectives to this work are given. We also described our preliminary work on the incorporation of quantum dots inside ZIF-8 cavities, presenting two different approaches and giving very first remarks on this study.

Chapter 1: Bibliographic studies

“ideal synthesis” is one which: “...creates a complex molecule... in a sequence of only construction reactions involving no intermediary refunctionalizations, and leading directly to the target, not only its skeleton but also its correctly placed functionality”

(Hendrickson, J.B. J. Am. Chem. Soc. 1975, 97, 5784)

The design and synthesis of metal organic frameworks (MOFs) materials has been an area of intense research over the past decade. Specifically, the porous nature of many of these materials makes them attractive for various applications. This chapter will serve to provide the background information into the areas concerning:

- (1) General description of metal organic frameworks: the history, properties, applications.
- (2) Zeolite types of MOFs with the detailed study of ZIF-8 material, which is the object of this PhD thesis.
- (3) Characterization techniques used during the study of ZIF-8 for the determination of its beneficial properties.

1.1 Metal Organic Frameworks

1.1.1 History in brief

Porous coordination polymers, also known as metal organic frameworks represent a relatively new class of compounds that have attracted vast attention due to their tunable chemical and physical properties. The term ‘metal organic framework’ firstly appeared in the publication of Yaghi and Li in 1995 and was related to $\text{Cu}(4,4'\text{-bpy})_{1.5}\cdot\text{NO}_3(\text{H}_2\text{O})_{1.25}$ network.¹ In fact, the story of these materials began earlier in the 1960s with the first announcement on coordination polymers chemistry.² Over the years, many new structures have been discovered. In 1999, Williams and coworkers reported on HKUST-1 metal organic framework.³ The same year, Yaghi group enlightened the structure and properties of MOF-5.⁴ Then, starting from 2002, Materials of Institute Lavoisier (MILs) were discovered by Férey and coworkers: MIL-53(Cr)⁵, MIL-53(Al)⁶. Férey’s studies on MIL-101⁷ showed that the crystal structure can be predicted by combination of both targeted chemistry and global optimization simulations. In 2006, a challenge to obtain MOFs with exceptional chemical stability was taken by Yaghi, who presented a set of different zinc imidazolate-based networks: ZIF-1,4,6,8,10,11 with zinc, ZIF-9,12 with cobalt and ZIF-5 with mixture of zinc and indium.⁸ According to this report, the structure of ZIF-8 wasn’t altered after boiling in methanol, water, benzene for 7 days and in sodium hydroxide concentrated solution for 24 h. Two years after, in 2008, a novel framework: UiO-66 joined to the list of MOFs after being described by Lillerud group at University of Oslo.⁹ The other important metal organic framework – NOTT, series 100-103, with tetracarboxylate ligands, was synthesized and analyzed in parallel at Nottingham University by Schröder and collaborators.¹⁰ Then, in 2010 Rosi and coworkers solvothermally synthesized Bio-MOF-11 ($\text{Co}_2(\text{ad})_2(\text{CO}_2\text{CH}_3)_2$) for the improved selective carbon dioxide capture.¹¹ In 2011, the first MOF, CAU-5, with photoswitchable linkers, capable upon UV irradiation to change from *trans* to *cis* isomer was developed by Stock’s group from Christian Albrechts University in Kiel.¹²

Previous studies in the area of MOFs mainly concern on transition metal based materials. The main group metal based networks have been less explored. Very recently, porous coordination polymers composed of Li or Mg are upon wide attention, because of their prominent properties that may bring improved gas adsorption. Mg-substituted MOF-74 reported in 2008 by Caskey and Matzger¹³ showed promising results in this field that was later confirmed in the work of Yaghi and co-workers.¹⁴ But still the proper synthesis of these materials is problematic.

During the past decade, hundreds of metal-organic compounds have been developed and studies on these structures establish the background of a new discipline of metal organic frameworks chemistry. At current rates of the synthesis progress, approximately 40 000 networks by 2025 will have been engineered according to the newest calculations.¹⁵ This big explosion of the knowledge followed by the industrial large-scale production developments should open the doors for real-world applications of these materials.

1.1.2 Structure

Coordination polymers and metal organic frameworks belong to an interdisciplinary field that combines inorganic and coordination chemistry. Metal organic frameworks (MOFs) are in fact porous

coordination polymers, usually with crystalline structure that consists of metal ions or clusters and organic linkers (e.g. derivatives of imidazole, terephthalate, or carboxylate). IUPAC recommendations from 2013 gave a description of these complex materials as coordination networks with organic ligands containing potential voids.¹⁶ The definition includes the fact that many systems are flexible and could change in structure depending on the environmental conditions.

The inorganic part of the network is formed by the metal:

- transition elements (copper, iron, zinc)
- rare-earth (scandium, yttrium)
- p-block (aluminium, gallium)

or clusters, that consist of metal center and anions (O^{2-} , F^- , Cl^- , OH^- ,...) that give the polyhedra conformation. For example, ZnO_4 tetrahedra structure is found in MOF-5 (see figure 1.1) or ZnN_4 conformation in ZIF-8. These inorganic parts are then extended and linked together with an organic part, which is usually simple bi-, tri- or tetradentate anions. Then, upon the connectivity between single M-L-M building units, specific arrays in 2-D or 3-D dimensionality are prepared. Moreover, the coordination preference, geometry, kinetic stability of the metal ions, together with ligand geometry, flexibility, chirality play an important role in the topology formation.¹⁷ The right choice of inorganic and organic variants, in well define synthesis conditions, gives opportunity to create the network with desired properties.

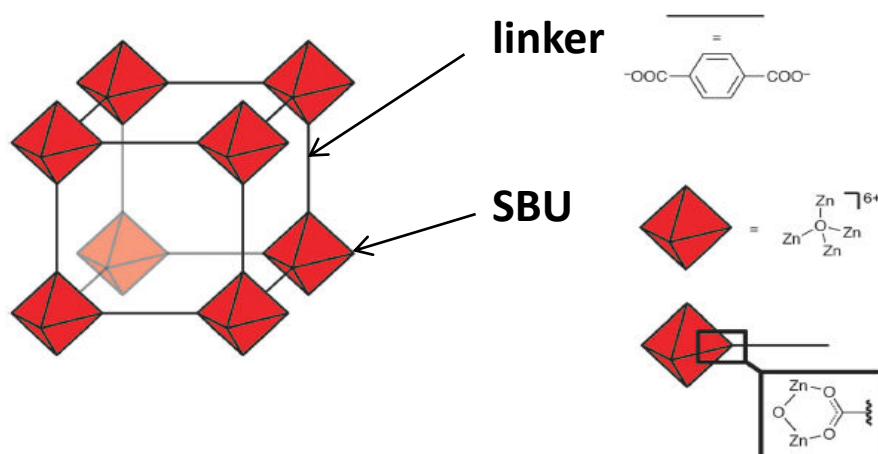
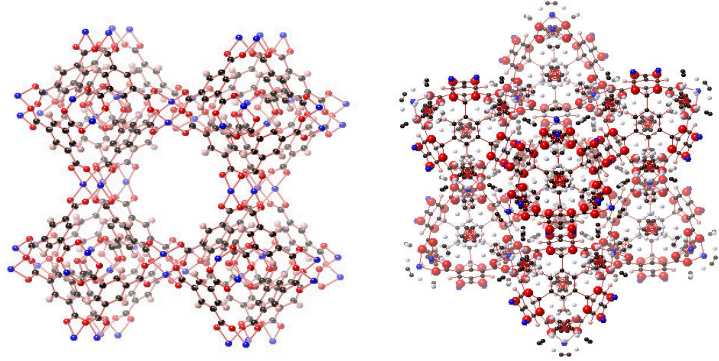
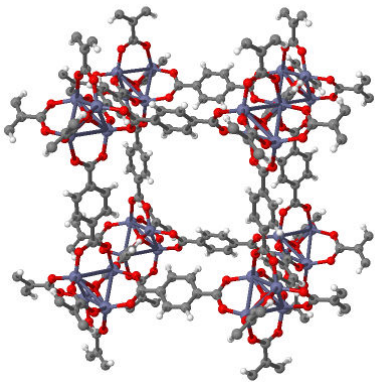
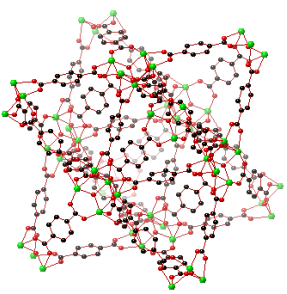
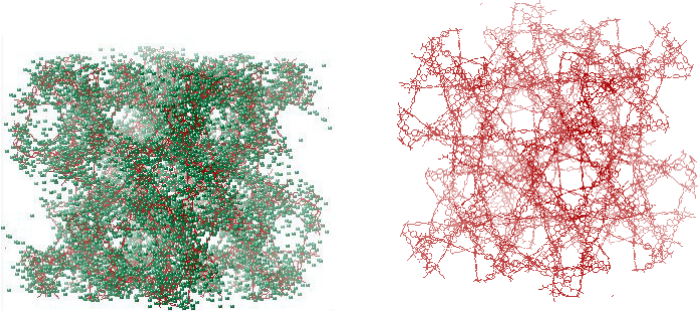
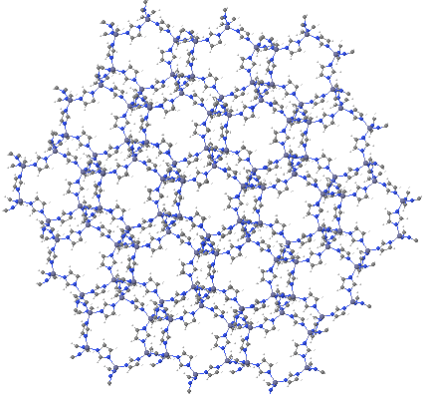
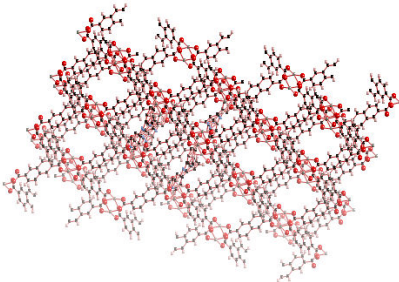


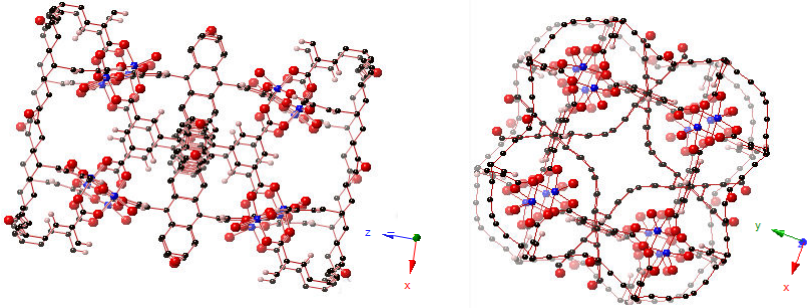
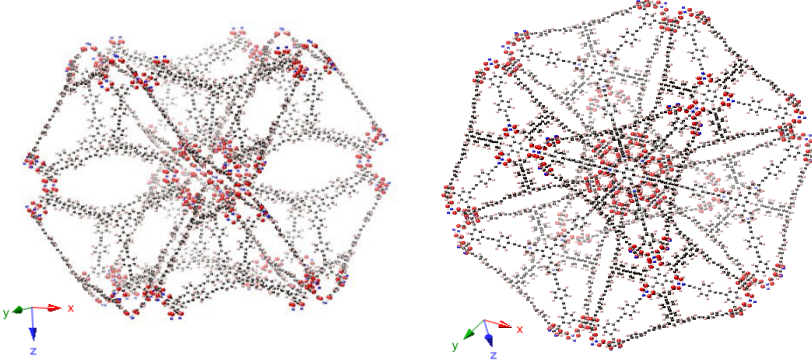
Fig. 1.1 Scheme of metal-organic framework's assembly: MOF-5 from Ranocchiari M., van Bokhoven J. A., *Phys. Chem. Chem. Phys.*, 2011, 13, 6388–6396

Table 1.1 presents the most famous examples from the metal organic frameworks family.

Table 1.1 Typical metal organic frameworks and their composition.

Name	Metal	Ligand
	Structure	
HKUST-1 Basolite C300 $C_{18}H_6Cu_3O_{12}$	Cu	1,3,5-benzenetricarboxylic acid
	 <p>black - C, red - O, blue - copper, pale pink - hydrogen</p>	
MOF-5 $C_{24}H_{12}Zn_4O_{13}$	Zn	1,4-benzenedicarboxylic acid
	 <p>grey - C, red - O, blue - Zn, white - hydrogen</p>	
UiO-66 $C_8H_8Zr_6O_{14}$	Zr	1,4-benzenedicarboxylic acid
	 <p>black - C, red - O, green - Zr</p>	

Name	Metal	Ligand
	Structure	
MIL-101 $C_{24}H_{17}CrO_{16}$	Cr	1,4-benzenedicarboxylic acid
	 <p>black - C, green - O, pink - Cr, H - not shown</p>	
ZIF-8 Basolite Z1200 $C_8H_{12}N_4Zn$	Zn	2-methylimidazole
	 <p>grey - C, blue - N, violet/grey - Zn</p>	
CAU-5 $C_{20}H_{12}N_2ZnO_4$	Zn	2,6-naphthalenedicarboxylic acid 3-azo-phenyl-4,4'-bipyridine
	 <p>black - C, red - O, pale blue - N, pale pink - H, grey - Zn</p>	

Name	Metal	Ligand
	Structure	
NOTT-109 $C_{35}H_{43}N_3Cu_2O_{16}$	Cu	2,2'-dimethoxy-4,4'-biphenyldicarboxylic acid
	 <p>black - C, red - O, blue - copper, pale pink - hydrogen</p>	
NU-110 $C_{26}H_{11}CuO_4$	Cu	hexacarboxylated linkers
	 <p>black - C, red - O, blue - copper, pale pink - hydrogen</p>	

The complexity in the MOFs networks is often compared to the structure of proteins, where the macromolecule is defined by four different levels: primary, secondary, tertiary and quaternary structures.¹⁸ This accurate comparison visualizes how the single units of the network integrate together and how this relation influences on the MOF's properties. The primary structure of MOF can be characterized as a connection of metal to the linker. Metal ions are then surrounded by oxygen or nitrogen into M-O-C or M-N-C, clusters that are named as secondary building units (SBUs).¹⁹ The secondary structure is formed by the assembled into 3D the primary nets. Then the tertiary arrangement is formed by supermolecular building blocks. Finally, the quaternary composition consists of supermolecular motifs of tertiary levels. The flexible structure of MOF can properly be designed to produce the material with desirable functionality and crystal morphology that fits in the idea of structure-activity relationship that will be described in following paragraphs.

1.1.2.1 Structure modification within metal-organic frameworks

Metal-organic frameworks are well-defined, supramolecular 3D structures whose architecture consists of metal-containing part, connected by the organic linkers, forming networks with inert voids, empty spaces and cavities.²⁰ Concerning variety of possible linkers and derivatives as well as different metal centres coordinating with these organic units, the library of MOFs structures is infinite. On the other hand, this abundance gives a challenge to target the synthesis of desired MOFs with customized functionalities and proper porosity. Recently, rational design has gained tremendous interest. The properties of constructional subunits should be considered before the synthesis to address the desired material for a specific use.

According to the MOF structure, the material can be modified by:

- changing the linkers within the framework,
- exchange or doping in metal ions/secondary building units,
- introducing of some species within pores and cavities (figure 1.2).

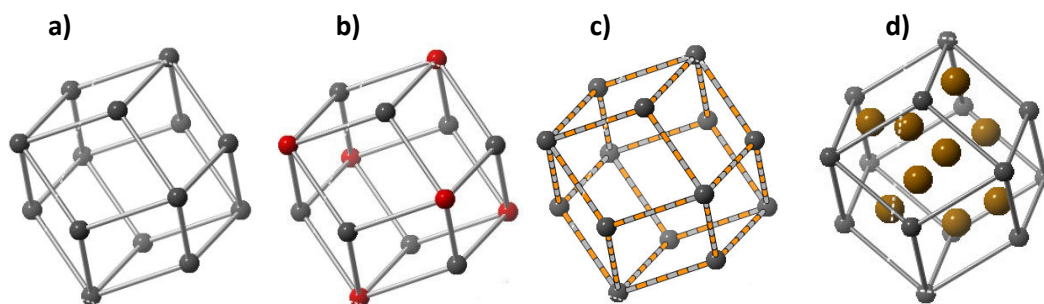


Fig. 1.2 Different strategies for MOF's functionalization: (a) non-modified, (b) metal-exchanged, (c) ligand-exchanged, (d) active species-encapsulated networks.

All of these actions create more complex structures and pore/cavities environment. It was previously described by Yaghi et al. in 2015²¹ as “heterogeneity”. The definition of this term is explaining the presence of various kinds of building blocks or covalently linked functionalities onto the backbone structure of single MOF. This results in the creation of vacancies, multiple pore sizes and all deviations from normal, perfect order of the framework (figure 1.3). On the other hand, the controlled disorders of the framework can be profitable. MOFs gain unique, additional chemical and physical properties, thus influencing on the activity.

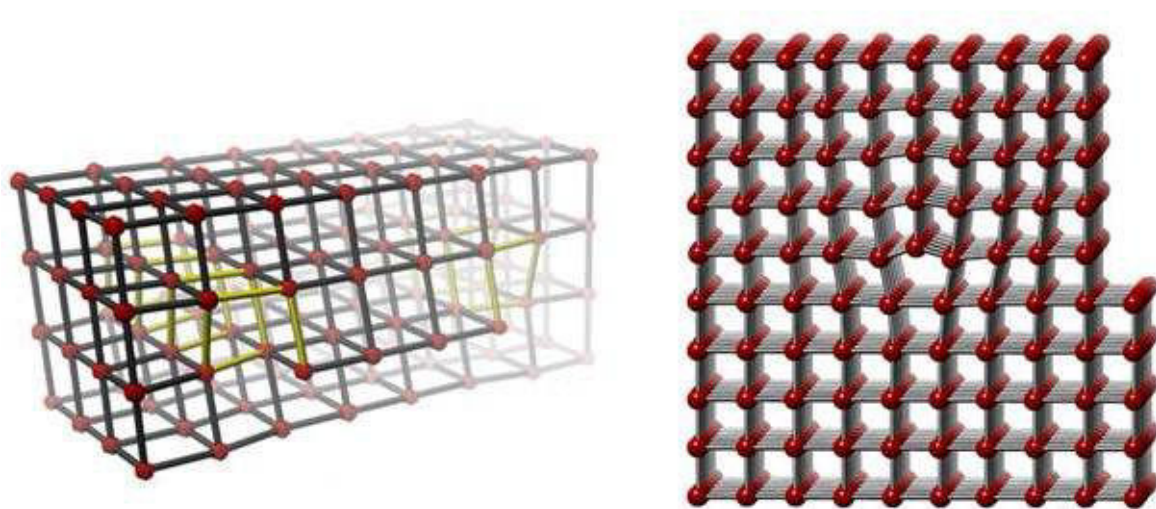


Fig. 1.3 Example of structural dislocations within the framework (simplified picture).

The ability to design and engineer the MOF's structure and the properties has led to rapid development in chemical engineering. Recent advances can be categorized in structural and functional approaches. The structural approach is connected with rational design of the framework in terms of desired structure, morphology, size, and porosity. Utilization of functional approaches result in the materials with proper functionalities for a particular applications.²⁰

Many interesting principles have been investigated in pre-synthetic design. The structural transformations can be predicted by computational simulations, modelling and theoretical studies, thereafter evaluated during the synthesis of desired MOF. When building blocks for the MOF's construction are selected, important factors, like possibility of different conformations of the organic ligands, complexity of the linker enabling to interpenetrate the framework or various clusters formation by metal ions should be considered. One of the examples is given by Bosch *et al.* 2014 who demonstrated the influence of selected precursors on the resulting product. The trial was based on indium-benzenedicarboxylate framework and the modification by introducing in the precursors mixture lithium hydroxide.²² The new network $\{\text{Li}[\text{In}(1,3\text{-BDC})_2]\}_n$ presented 1600 % higher surface area and 275 % hydrogen uptake compared to the parent framework.

Moreover, all the experimental conditions for the synthesis (temperature, reaction time, pressure, mixing speed,...) should be carefully chosen and monitored, because these parameters can hardly affected the final product. The material with many disorders and coordinatively unsaturated metal sites is in fact not stable and will transform into more thermodynamically favourable form. This situation has been reported by Lin *et al.* in 2012²³ for the transformation of polymorphs $[\text{Zn}_3(\text{TCPB})_2 \times 2\text{DEF}] \times 3\text{DEF}$ into $[\text{Zn}_3(\text{TCPB})_2 \times 2\text{H}_2\text{O}] \times 2\text{H}_2\text{O} \times 4\text{DMF}$ during the temperature-induced dynamic processes.

Postsynthetic modification

The other strategy to functionalize the material is the post-synthesis modification (PSM).²⁴ This means the existed framework is functionalized via chemical ways by using building blocks present in the structure. Moreover, PSM is conducted without damaging the integrity of changing the infrastructure of the selected framework. PSM was briefly described by Cohen in 2010²⁵, who specified that the post-synthetic transformations can be achieved by respecting the following rules:

1. The pores of MOFs should be in appropriate size to allow all the reagents for the modification enter inside the lattice. Unless, only the exterior part will be modified.
2. Available functional groups that can undergo chemical modification should be present in the MOFs structure.
3. MOFs should resist in the applied reaction conditions necessary to make the transformations.
4. MOFs should be stable against by-products or wastes found in the reaction mixture (like radicals).

PSM is mainly connected with building block replacement (BBR) and could be conducted using three pathways: solvent-assisted linker exchange (SALE), not-bridging ligand replacement and transmetalation.²⁶ The groups exposed by MOFs linkers could be required for the functionalization. The organic ligands can act in some reactions and transform into other functional species (see figure 1.4).

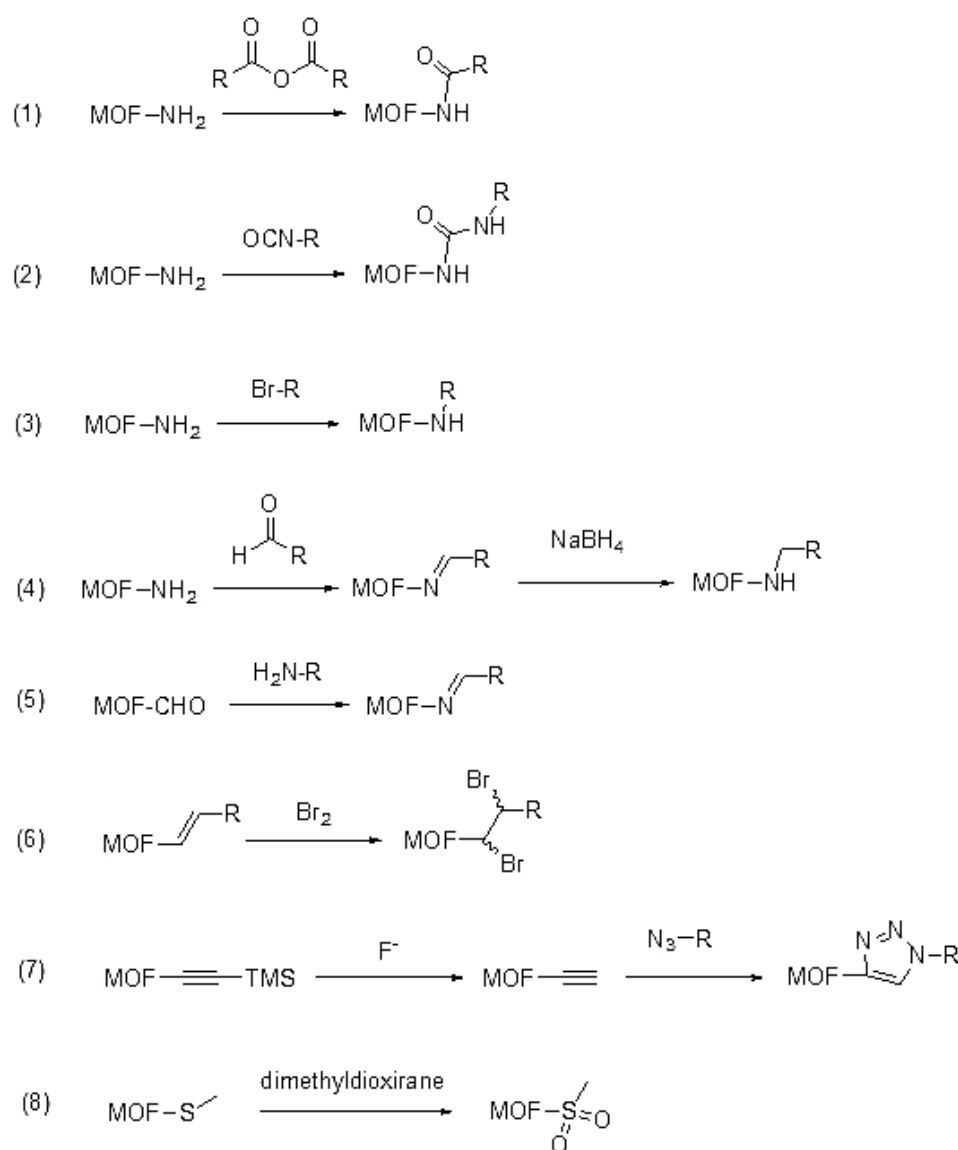


Fig. 1.4 Different post-synthetic strategies for MOF's functionalization. [from Cohen, 2010]

It is also possible to make post-synthetic exchange (PSE) either on inorganic or on organic building blocks. It was presented by Kim *et al.* in 2012 for the partial exchange of Zr for Ti in the UiO-66

material.²⁷ In this work, the authors also explored linkers exchange between MIL-53(Al)-NH₂ and MIL-53(Al)-Br when these two materials were mixed together in water and the substitution 2-amino- for 2-bromo- group in MIL-68(In). The process of replacing the linkers in a parent MOF with linkers of choice via a heterogeneous reaction in carefully selected solvent is commonly known as “SALE” (solvent-assisted linker exchange). This method was evaluated in the work of Karagiari *et al.* in 2015²⁸, where they replaced isophthalate with a conjugate base of trimesic acid in NU-125 framework. With the ZIF-8 material, they also replaced the Hmim linker for the IM linker, thus modifying the apertures dynamics and accessibility of the network.²⁹

Another possibility is metal-doping processes that led to partial or total exchange of the inorganic part within the framework by new ions. The transmetalation phenomenon was shown by Song *et al.* in 2012 for Zn-PMOF-2.³⁰ The material was soaked in 0.1 M copper nitrate solution and the results of gradual substitution of Zn-ions by Cu-ions and monitored overtime (figure 1.5).

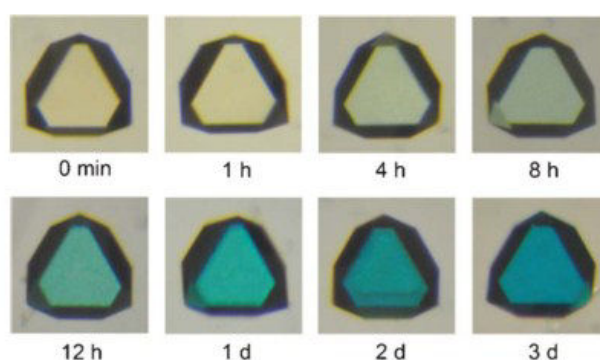


Fig. 1.5 Optical microscopic images of the Zn-PMOF-2 single crystal after exchange with Cu.³⁰

The new isostructural Cu-MOF material was thermodynamically more stable compared to the original one. According to these observations, we can generally say that the transmetalation processes can be achieved using the metals that are strong enough to replace the existing metallic position in the metal-linker moieties and produce more energetically suitable connections in the network. Other example was given by Song *et al.* in 2012³¹ where the transmetalation was used for the improvement of the framework stability of the parental network. The results are summarized on the figure 1.6.

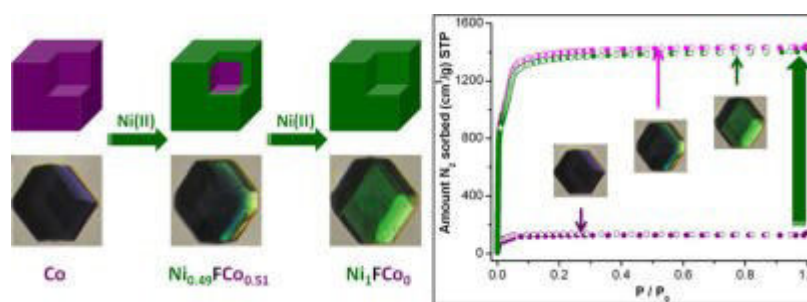


Fig. 1.6 Transmetalation of Co-containing SBU for Ni-ions conducted on M₆(1,3,5-benzenetribenzoate)₄(4,4'-dipyridyl)₃ framework.³¹

Functionalization by incorporation of diverse components inside metal-organic frameworks

Methods for encapsulation

Encapsulation of some active species inside MOFs pores is one of the functionalization techniques for these materials. The hybrid system formation is dictated by the chemistry of both – the support and the species to be incorporated. The entrapped molecules should be appropriate with the size to fit the cavities of the porous matrix. The following two main approaches are here possible:³²

1. “ship in the bottle” – assembling the active species within the pores of the matrix; techniques used:

- impregnation (ex. impregnation of metal ions Li^+ , Mg^{2+} , Ca^{2+} , Co^{2+} , Ni^{2+} in the pore of anionic SNU-100' framework to enhance isosteric heat, selectivity, uptake capacity of CO_2 adsorption in the MOF),³³

- solvent-free gas phase loading (ex. loading of MOF-5, MOF-177, UCM-1 with perylene derivative DXP or octa-coordinated iridium complex Firpic),³⁴

2. “bottle around the ship” – assembling the support around the active species, like polyoxometalates (ex. POM@UiO-67 prepared by this way, because the impregnation methods failed).³⁵

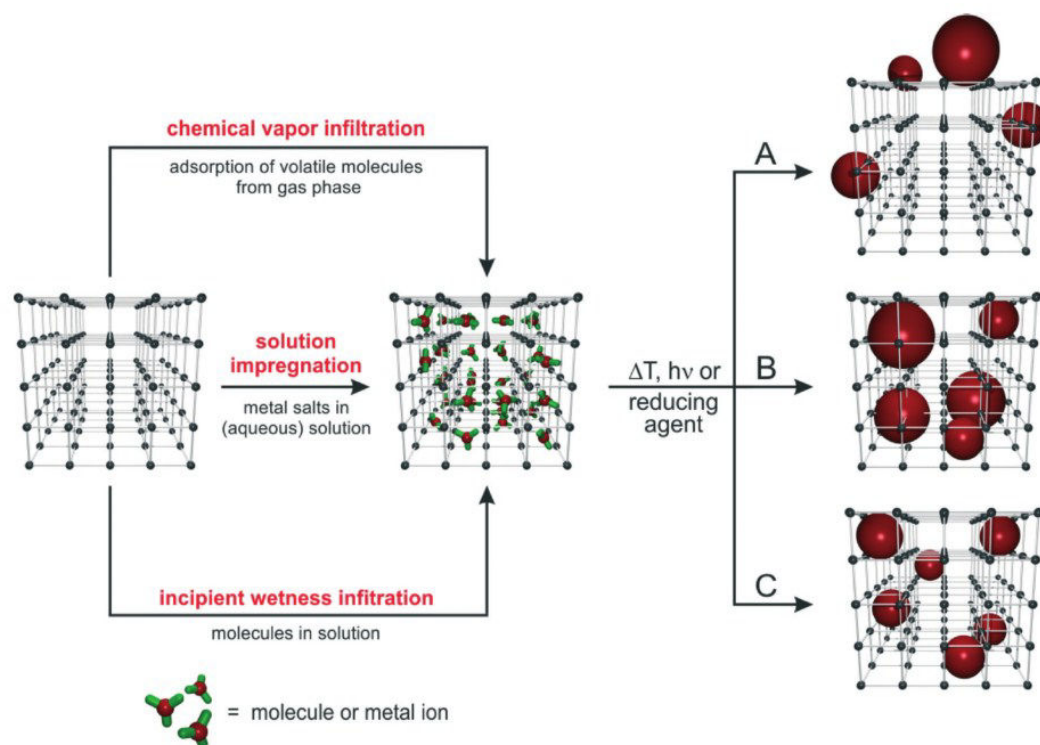


Fig. 1.7 Scheme of the techniques for the formation of nanoparticles supported on MOFs. The MOF framework can be decorated outside with NPs (A), interpenetrated with NPs (B), enclose the NPs within pores (C). [from Rösler *et al.* 2015]³⁶

Examples of hybrid structures

The abundance of MOFs topologies offers many advantages towards the encapsulation of different kind of functional species (figure 1.8). A plenty of MOF-based composites can be synthesized, depending on the final application of the material. Metal-embedded systems are mainly designed for catalytic purposes where MOFs act as supports which stabilize the inorganic nanoparticles and

improve recovery of the catalyst. For some reactions, the framework also enhances adsorption capacity of gaseous phase and then the reaction conducted with the catalyst particles is more efficient. MOFs with embedded biomolecules, like drugs or enzymes can be used in biological or pharmaceutical technologies.³⁷ Luminescent particles incorporated within these materials can be applied for sensing or optical use. Sometimes, the incorporated functionalities are used as templates to generate special order within the framework. It was explained by Zhang *et al.* in 2015³⁸ for two MOFs, ZIF-8 and UiO-66 in which gold nanoparticles were embedded and then the etching process was applied to generate the mesopores.

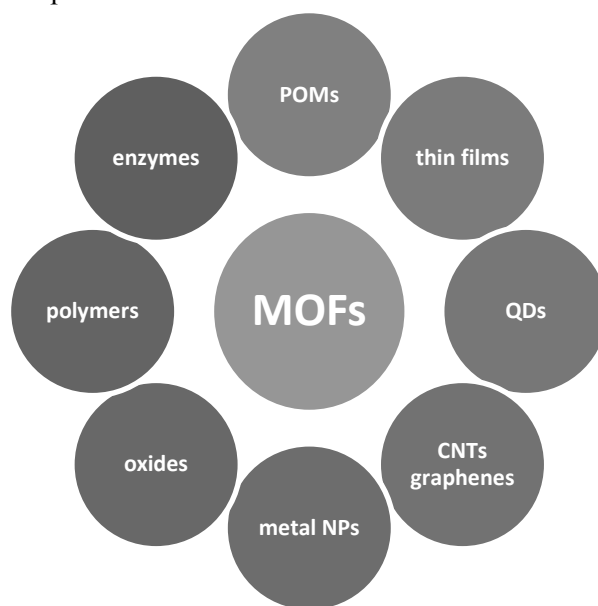


Fig. 1.8 MOFs functional composites.³⁹

The organic struts of MOFs can incorporate many types of macrocyclic structures, like crown ethers, cyclodextrines, calixarenes, cucurbit[n]uriles, pillararenes, cyclams, cyclens, or N₃-nonanes. As an example, we can mention the UWDM-1 framework composed of [2]pseudorotaxane-based linkers bonded with copper ions.⁴⁰ Another complex hybrid material is MIL-101(Cr) functionalized with pyridine. The material can be used as stationary phase for HPLC separation of tocopherols. The benefits originated from this connection are high efficiency and good precision in the separation of α -, β -, γ -, and δ -tocopherols.⁴¹ Many other examples of various host-guest structures are presented in table 2.1.1.

Table 1.2 Examples of hybrid guest-MOF systems.

MOF	Guest	hybrid	Benefits	References
ZIF-8	PVP-modified cytochrome C	cytc/ZIF-8	higher peroxidase activity, detection of explosive peroxides in solution	Lyu F., Zhang Y., Zare R. N., Ge J., Liu Z., <i>Nano Lett.</i> , 2014 , 14, 5761-5765
ZIF-8	NaYF ₄	NaYF ₄ /ZIF-8	luminescent protection against quenchers bigger than the pore size of MOF	Wang F., Han Y., Lim C. S., Lu Y., Wang J., Xu J., Chen H., Zhang C., Hong M., Liu X., <i>Nature</i> , 2010 , 463, 1061-1065
ZIF-8	CdTe quantum dots	CdTe/ZIF-8	luminescence protection, protection	Zhang H., Cui Z., Wang Y., Zhang K., Ji X., Lü C., Yang B., Gao M.,

MOF	Guest	hybrid	Benefits	References
			against quenchers bigger than pore size of MOF	<i>Adv. Mater.</i> , 2003 , 15, 777-780
ZIF-8	1-ethyl-3-methyl imidazolium bis (trifluoromethyl sulfonyl)amide)	EMI-TSFA@ZIF-8	Stabilizing liquid phase of ionic liquids to lower temperature, the dynamics control of the ions	Fujie K., Yamada T., Ikeda R., Kitagawa H., <i>Angew. Chem. Int. Ed.</i> , 2014 , 53, 11302-11305
MOF-1	A1/A2-difunctionalized Pillar[5]arene	P5A-MOF-1	racemic separation of analytes mixtures	Stout N. L., Fairen-Jimenez D., Iehl J., lalonde M. B., Snurr R. Q., Farha O. K., Hupp J. T., Stoddart J. F., <i>J. Am. Chem Soc.</i> , 2012 , 134, 17436-17439
SNU-90' NH₂-MOF-177	Mg nanocrystals	Mg@SNU-90'	hydrogen storage and transport improvement (increase isosteric heat of the H ₂ physisorption and decrease the temp. for chemisorption/desorption	Lim D.-W., Yoon J. W., Ryu K. Y., Suh M. P., <i>Angew. Chem. Int. Ed.</i> , 2012 , 51, 9814-9817
HKUST-1	Au	Au-HKUST-1	oxidation of alcohols	Ishida T., Nagaoka M., Akita T., Haruta M., <i>Chem. Eur J</i> , 2008 , 14, 8456-8460.
MIL-53 NH₂-MIL-53	Pd	Pd@MIL-53	Heck coupling, Suzuki-Miyaura	Huang Y., Gao S., Liu T., Lü J., Lin X., Li H., Cao R., <i>ChemPlusChem</i> , 2012 , 77, 106-112 Huang Y., Zheng Z., Liu T., Lü J., Lin Z., Li H., Cao R., <i>Catal. Commun.</i> , 2011 , 14, 27-31
IRMOF-3	rhodamine (RB)	B RB@IRMOF-3	luminescent sensor for typical volatile compounds: orthodichlorobenzene, chlorobenzene, benzene, toluene, p-xylene, methanol, ethanediol	Yue Y., Binder A. J., Song R., Cui Y., Chen J., Hensley D. K., Dai S., <i>Dalton Trans.</i> , 2014 , 43, 17893-17898
MIL-96	bimetallic Ni-Pt nanoparticles	Ni-Pt/MIL-96	synergistic effect in hydrogen generation from the aqueous solution of hydrazine	Wen L., Du X., Su J., Luo W., Cai P., Cheng G., <i>Dalton Trans.</i> , 2015 , 44, 6212-6218
MIL-101	Fe ₃ O ₄ -COOH	Fe ₃ O ₄ @MIL-101	Efficient peptides/proteins enrichment, magnetic responsiveness, enrichment of the protein biomarkers from bacterial cell lysates and discrimination of <i>E. coli</i> at the strain level	Wei J.-P., Qiao B., Song W.-J., Chen T., Ii F., Li B.-Z., Wang J., Han Y., Huang Y.-F., Zhou Z.-J., <i>Analytica Chimica Acta</i> , 2015 , 868, 36-44
HKUST-1	Poly L-lactic acid (PLLA)	PLLA-HKUST-1	larger affinity to water	Elangovan D., Nidoni U., Yuzay I. E., Selke S. E. M., Auras R., <i>Ind.</i>

MOF	Guest	hybrid	Benefits	References
				<i>Eng. Chem. Res.</i> , 2011 , 50, 11136-11142
[Cu(OOC-C ₆ H ₄ -C ₆ H ₄ -COO) ₂] _n MOF	microperoxidase-11 (MP-11)	MP-11-MOF	oxidation of methylene blue and α -methylstyrene	Balkus K. J., Pisklak T. J., Huang R., <i>ACS Symposium Series</i> , 2008 , 986, <i>Biomolecular Catalysis</i> , Chapter 4, 76-98
CAU-1-NH ₂	Polydopamine	CAU-1-NH ₂ @polydopamine	incorporated into polymethyl methacrylate matrix, high O ₂ permeability, capability of CO ₂ capture, hydrophobic behavior	Cao L., Lv F., Liu Y., Wang W., Huo Y., Fu X., Sun R., Lu Z., <i>Chem. Commun.</i> , 2015 , 51, 4364-4367
uranium(VI) polycarboxylates (UOFs)	methyl viologen iodide MV·2I	MV·2I-UOF	degradation of rhodamine B upon visible light irradiation	Li H.-H., Zeng X.-H., Wu H.-Y., Jie X., Zheng S.-T., Chen Z.-R., <i>Cryst. Growth Des.</i> , 2015 , 15, 10-13

1.1.3 Properties

Crystal engineering faces a big challenge to produce structures with desired properties that will be useful in certain field of application. Proper design of metal organic frameworks gives the possibility to control properties of the material. MOFs are well known from their various topologies and well-defined porous structure. The framework structure is composed of linked cages, cavities or channels, which allow small molecules to enter depending on the pore diameter. This specific system of voids explains the relatively low density of these compounds. The empty spaces created within the network by metal-ligand interactions play crucial role in the functional application such as catalysis, separation or gas storage because of the increase in surface area.⁴² Table 1.3 summarizes the BET surface area and pore volumes of the most common networks.

Table 1.3 Comparison of surface area and pore volumes of zeolites vs. different MOFs.^{43 44 45 46 47}

MOF	BET surface area [m ² /g]	Pore volume [cm ³ /g]	Ref.
(Al)SBA-15	436	0.94	45
RHO-ZMOF	563	0.22	44
H-BEA	674	0.22	45
β SiO ₂	687	0.26	44
NaY	842	0.31	44
[La(BTB)(H ₂ O)×3DMF] _n	1014	0.48	47
CAU-1	1268	0.61	46
CPO-27-Ni	1423	0.54	44
Basolite C300	1499	0.64	45
ZIF-76	1561	0.6	44

ZIF-8	1813	0.65	44
HKUST-1	1842	0.74	44
MFU-4 L	2750	1.26	43
NOTT-102	2940	1.14	43
PCN-61	3000	1.36	43
MOF-5	3800	1.55	43
PCN-66	4000	1.36	43
MIL-101c	4230	2.15	43
NOTT-116	4660	2.17	43
NU-109E	7010	3.75	43
NU-110E	7140	4.40	43

Metal-organic frameworks are also considered to be flexible materials, where rigid elements (metal clusters and linkers) are connected by flexible joints or hinges.⁴⁸ These as called “weak points” determine the mechanical characterization of the network. The hinges in some of MOFs enable the linkers to rotate and hence modulate the entrance through the cavities. It’s important in case of MOFs loadings with guest molecules, like drugs or nanoparticles.

Metal organic frameworks pores are uniform in size with diameter of 3-20 Å and 55-90% of voids volumes.⁴⁹ The materials with more than 40% in the pore fraction should be tested in terms of mechanical stability, especially during the pressurizations.⁵⁰ To facilitate the applications of MOFs, it is needed to assemble the powder in more compact form, like tablet or pellet. The processing requires the use of high pressures that could have an impact on the materials crystallinity and porosity. The deformation could lead to reversible or not reversible changes in the structure. A stable material should keep its integrity without pore collapse or amorphization. It was shown for zirconium MOF, UiO-66 with porosity of about 52.6% to be more resistant on the pressurization than zinc-based MOF-5 with porosity 76.5%, ZIF-8 with porosity 45.8% or Cu-based HKUST-1 with porosity 68.7%. The results were associated with higher shear modulus for these frameworks. These structures having “breathing” facilities expand or contract when the guest molecules (an air, gases or particles) are evacuated or uptaken without dramatic structural changes. Increase in mechanical robustness can be achieved by introduction of some specific structure’s modulators, ex. trifluoroacetic acid into UiO-66.⁵¹ Chemical and thermal stability of MOFs is the other key advantage. Considerable efforts have been undertaken to understand the behavior of these structures when treated with water steam. Hydrothermal stability of the catalyst is important in context of the industrial application where small amounts of water could be present at elevated temperatures of some processes. The water molecules could partially destroy the connection between SBUs and linkers in the network and then cause problems with catalytic activity or material’s regeneration after the reaction.⁵² Willis *et al.* 2009 presented an explanation in the bond strength between the metal cluster and the linker. It was shown in comparative study of different frameworks that the oxidation state of the metal, type of coordination, chemical functionality of organic linker can influence on the stability. It was clearly visible that the ZIF-8 framework was the most resistant material when exposed to 50% steam. The results are briefly summarized at the figure 1.9.

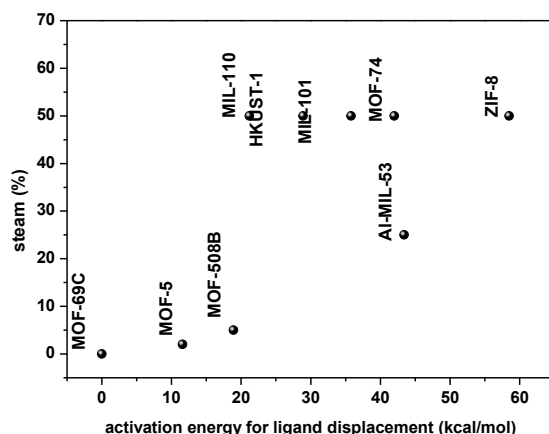


Fig. 1.9 Steam stability map for the MOFs discussed by Willis *et al.*³⁰

Table 1.4 Comparison between MOFs and zeolites.(adapted and supplemented from⁵³)

Properties	Zeolites	MOFs
framework type	inorganic	inorganic-organic
SBU	[SiO ₄] or [AlO ₄]	various
crystallinity	very good	very good
surface area [m ² /g]	200-700	500-10,000
pore volume [cm ³ /g]	0.1-0.5	0.3-3.0
pore diameter [nm]	< 2	< 10
thermal stability	mostly stable > 400°C	usually unstable above 400°C
chemical stability	depending on the Si/Al ratio	sensitive in moisture and chemicals
metal site density	few %	dozens of %
type of active site	Limited	not limited
Lewis acidity	metal sites in network	coordinatively unsaturated metal sites
Functionalization	generally difficult	rich chemical possibilities available

Zeolites are very well known from its thermal and chemical stability. But despite having big resistance to the environmental conditions and changes, they are not so flexible compared to MOFs. MOFs can be easily functionalized, thus leading to materials more stable against hydrolysis as was shown for phenylurea modified Al-MIL-101-URPh.⁵⁴ Table 1.3 briefly gives advantages and disadvantages of both materials zeolites and MOFs.

The emissive phenomenon for some kind of porous coordination polymers has also gained considerable attention over last years. The hybrid-nature of some structures allows observation of the fluorescence, phosphorescence or scintillation.⁵⁵ According to the MOFs composition, a wide range of interactions resulting in emission of the light could be possible (see figure 1.10 and one of the examples at the figure 1.11):

a) luminescence based on the linker: originating from the ligand, ex. 4,5,9,10-tetrahydropyrene 2,7-carboxylic acid, derivatives of dipyridoquinoxalines or stilbenes,

b) metal-based emission: ex. Gd-BTC doped with Tb prepared for 2,4-dinitrotoluene detection emits in green region 544 nm, when excited at 300 nm,⁵⁶

c) ligand-to-metal charge transfer (LMCT): ex. MOF-5, where the 1,4-benzenetricarboxylate linkers upon excitation 350 nm transfer the energy to ZnO_4 clusters, resulting in an emission located at 525 nm,⁵⁷

d) metal-to-ligand charge transfer (MLCT): ex. $Zn_2(IM)_4DMF$ network when excited at 380 nm emits at 445 nm,⁵⁸

e) host-guest composite's luminescence: ex. the composite of branched poly(ethyleneimine)-capped carbon quantum dots encapsulated in ZIF-8 framework exhibits strong blue fluorescence at 440 nm upon excitation at 365 nm.⁵⁹

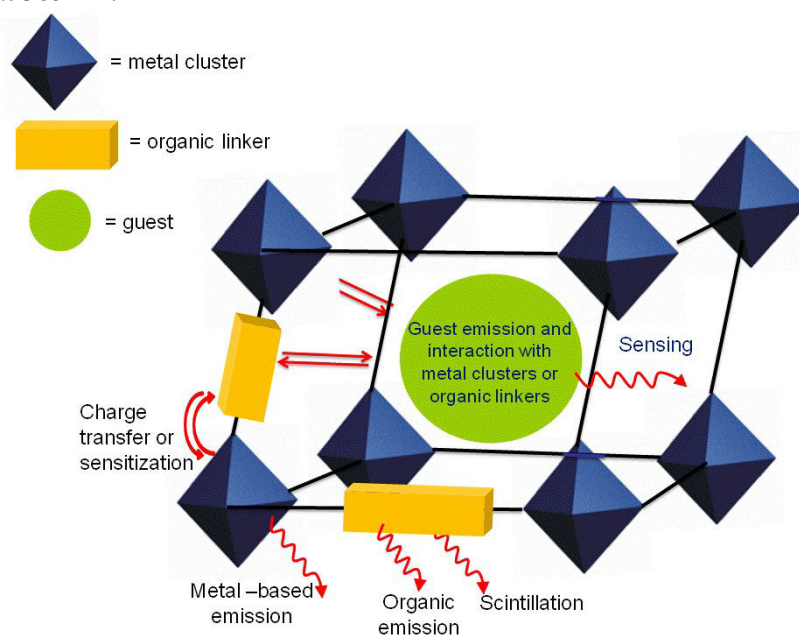


Fig. 1.10 Scheme presenting possible emission phenomena in MOFs. (ref. Chem. Soc. Rev., 2009, 38, 1330-1352 – from the website of C. A. Bauer)

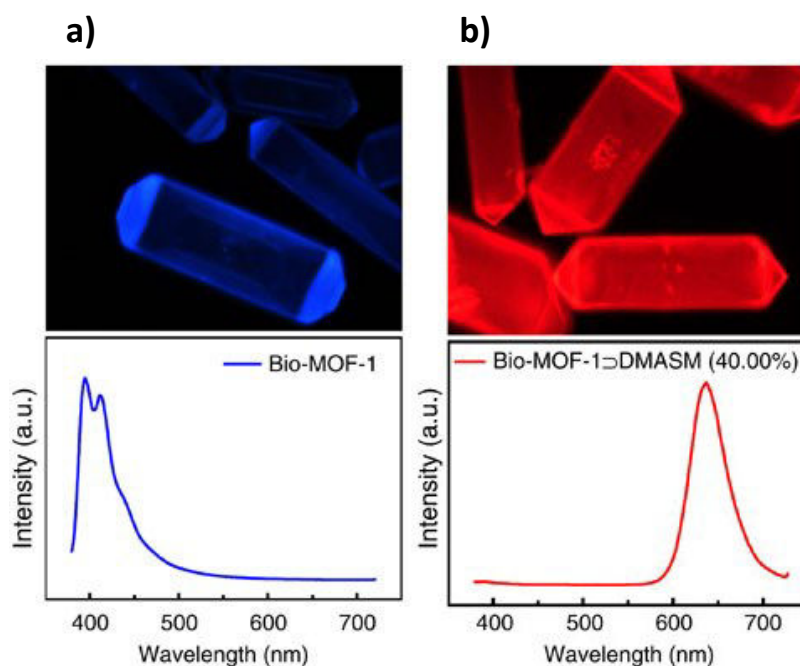


Fig. 1.11 Example of a fluorescent metal-organic framework: evolution of luminescence in Bio-MOF-1 upon excitation 340 nm. (ref. Yu J., Cui Y., Xu H., Yang Y., Wang Z., Chen B., Qian G., *Nature Communication*, 2013, 4:2719, 1-7)

Another important attribute of metal organic frameworks is magnetism. It can be achieved by the presence of paramagnetic centers inside the network, briefly metals which possess of spin quantum number and magnetic anisotropy – V, Cr, Mn, Fe, Co, Ni, Cu.⁶⁰ The other possibility is to introduce within the network magnetic components, like most significant nanoparticles Fe₃O₄, CoFe₂O₄, NiFe₂O₄ or C-coated Co.⁶¹ The subject of magnetic metal-organic frameworks will be described in details in the chapter 2.3.

1.1.4 Possible application of metal-organic frameworks

Taking an advantage from the specific properties of MOFs, these materials can be applied in numerous and various domains. The presence of open metal sites, the high uniform porosity and surface area, the absence of non-accessible volumes can be beneficial for adsorption, separation, purification or catalysis. Thanks to their very regular, organized composition, MOFs are being considered for the encapsulation of various species, like small molecules or oligomers.⁶² In this chapter, we briefly describe the potential of MOFs over the most significant application fields.

1.1.4.1 Gas adsorption

Many researches have been devoted to adsorption of large quantity of strategic gases such as H₂, CH₄, CO₂, O₂, NO_x, C₂H₂, ... that are produced on a very big scale by the human activity. However, interest in the gas sorption properties of MOFs is generally focused on increasing the uptake of fuel gases such as H₂, and CH₄ – the low carbon content and large chemical energies of these molecules make them highly attractive as replacements for fossil fuels. The highest reported value (2347 mg/g) for an excess carbon dioxide uptake was achieved with MOF-200 at 298 K, 50 bar.⁶³ NU-100 was found to have the

best properties for hydrogen uptake (9.0 wt% at 77 K, 56 bar).⁶⁴ The best results in the methane adsorption were reported for PCN-14 frameworks (212 mg/g).⁶⁵

As practical example of MOFs big capacity for gas storage is a trial undertaken by the BASF firm. In their project, Basolite C300 was placed in thirteen containers and filled with natural gas at 200 bars. Then, these tanks were used for Volkswagen Caddy Eco Fuel to drive successfully from Berlin to Bangkok, 32,000 km. During the test, the car had the consumption of ~ 7 kg of gas per 100 km. Moreover, the car produced 1.3 tons less of carbon dioxide when compared to standard car with 1.6 L engine.⁶⁶ The Texas A&M University in the project of prof. Zhou in collaboration with General Motors (GM), Lawrence Berkeley National Laboratory (LBNL) and Research Triangle Institute (RTI) are working together on methane-based tanks and adaptation of porous material to store much larger amount of the gas and then deliver low-pressure gas when needed.

1.1.4.2 Catalysis

MOFs have been widely considered as heterogeneous catalysts due to their high crystallinity, well dispersed active sites over the framework and their ability to be chemically and physically adapted for specific chemical transformations.⁶⁷ An ideal catalyst should be easy to synthesize, have high activity, high selectivity and, after the catalytic process, should be easy to separate from the reaction mixture. MOFs are expected to have good potential in many catalytic reactions based on their readily accessible cavities, variety of transition metals possibility and the ease of incorporation of functional groups in the framework structures. Moreover, because of their solid feature, they act as heterogeneous catalysts that can be easily recoverable from the reaction mixture. In the catalytic process, MOFs can play a role either as a support for other particles responsible for the catalytic property or as a “real” catalyst depending on the active sites forming the structure. Table 1.5 presents some applications of various MOFs in the catalysis.

Table 1.5 Selected examples of metal-organic frameworks in the catalysis.

1. MOFs as a support for the catalyst		
Structure	Reaction	reference
Ru/MIL-96	hydrolytic dehydrogenation of ammonia borane	68
Pd/ZIF-8	selective hydrogenation of cinnamaldehyde	69
Pd/MIL-101	oxidation of benzyl alcohol to benzaldehyde	70
Rh/MOF-5	hydroformylation reaction of olefins	71
Ni@MOF-5	carbon dioxide methanation	72
IrNPs@ZIF-8	hydrogenation of cyclohexene and phenylacetylene	73
2. Metal active site (Lewis acid site)		
Structure	Reaction	reference
[Cu₃(BTC)₂]	olefin epoxidation, alcohol oxidation	74
[Cu₃(BTC)₂]	Pechmann condensation – coumarins synthesis	75
MIL-100(Fe)	Friedel-Crafts acylation	
	Beckmann rearrangement of oximes	
	Knoevenagel condensation	

	Prins reaction of β -pinen with formaldehyde annulation reaction	
MIL-100(Sc, M) M=Al, Cr, Fe	alcohol oxidation, production of ketones from (hetero)aromatics and hemiacetal	76
MIL-100(Fe) MIL-101(Fe)	oxidation of anthracene to anthraquinone with tert-butyl hydroperoxide	77
heteropolyacid@MIL-101(Cr)	ethyl acetate hydrolysis and acetic acid esterification	78
Zn-DPPG	aldol condensation	79
3. Linker-based active site (Lewis base site)		
Structure	Reaction	reference
MOF-74 (2,5-dioxidoterephthalate, Mg²⁺, Co²⁺, Ni²⁺, Cu²⁺, Zn²⁺)	Knoevenagel condensation Michael additions	80
IRMOF-3_{DEF} IRMOF-3_{DMF} MIL-53(Al)NH₂	Knoevenagel condensation	81
Zn(II)IRMOF-Proline	Aldol reactions between acetone or cyclopentanone with 4-nitrobenzaldehyde	82
TIF-1 (tripodal imidazolate framework-1 with Co(II) nodes)	conjugate addition of alcohols to α,β -unsaturated ketones	83
NU-601 (with hydrogen bonding urea strut)	Friedel-Crafts bonding between N-methylpyrrole and (E)-1-nitroprop-1-ene	84

1.1.4.3 Separation

MOFs with an adequate network structure and well-defined pore size can also be good candidates for separation of gaseous mixtures (figure 1.12). Certain functionalities and coordinatively unsaturated metal sites may enhance specific interactions between the network and catch selectively inside the pores the molecules of interest.⁸⁵ There is a plenty of different reports on the natural gas purification using MOFs that has widely been considered with numerous adsorbants. Polysulfone mixed matrix membranes based on MIL-125(Ti)-NH₂ were used for the selective capture of carbon dioxide from the mixture of CO₂/CH₄.⁸⁶ Another example is the UTSA-15 framework that showed good selectivity in CO₂/CH₄ and C₂H₂/CH₄ separation.⁸⁷ Effectiveness in the SF₆/N₂ separation was tested with MIL-100(Fe) granules, that showed better performance when compared with standard Zeolite 13X.⁸⁸ Hybrid ZIF-8 and ZIF-90 Matrimid MMMs were successfully explored for H₂/CO₂ mixtures. In the context of the contaminants removal, the porous character of MOFs has shown a big advantage in the field of nanofiltration. For example, polyphenyl sulfone membranes with copper-1,3,5-benzenetricarboxylate nanoparticles were used for solvent resistant separation of dye from methanol.⁸⁹ Harmful and toxic gases, like H₂S or NH₃, can easily be sensed and captured by MOFs. Volatile organic compounds, xylene and ethylbenzene were efficiently stocked inside MIL-53(Al)

framework.⁹⁰ In addition, the structure and catalytic properties of MOFs give the possibility to not only capture but as well decompose the toxic substances as demonstrated for Au@ZIF-8 catalysed oxidation of CO to CO₂.⁹¹

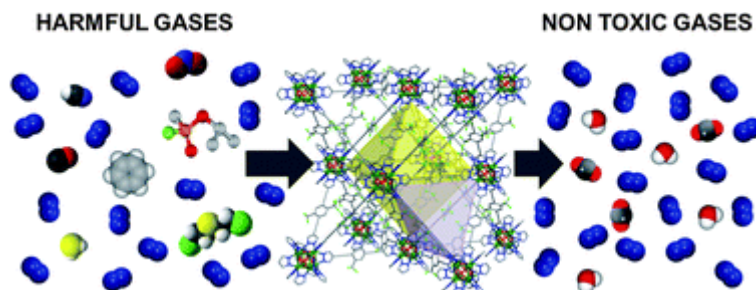


Fig. 1.12 Scheme of metal-organic frameworks activity in gas separation (Chem.Soc.Rev., 2014, 43, 5419).

1.1.4.4 Biomedical application

Recently, many MOFs have been investigated in the biomedical field as potential drug carriers, drug storage systems, imaging and sensing.⁹² MOFs structure can propose an intrinsic biodegradability and versatile functionality that helps to graft drug molecules inside the framework. In the MOFs studies for drug delivery, biocompatibility of the metal and linker has the first priority. The inorganic part of the framework with metals that naturally occur in the body (such as iron, copper, manganese, nickel, and zinc) and non-toxic organic ligands are the best choices.

Bio-MOF-100 has been presented as an ideal example of biocompatible material for the drug encapsulation.^{93 94} This framework with the high surface area 4300 m²/g, low density 0.302 g/cm³ and the highest reported pore volume 4.3 cm³/g has shown the highest ibuprofen uptake within wide range of different MOFs in a comparative simulated study (MIL-53: 231 mg/g; CD-MOF-1: 274 mg/g; MOF-74: 425 mg/g; MIL-100: 645 mg/g; MIL-101: 1291 mg/g; Bio-MOF-100: 1975 mg/g). The other advantage of bio-MOF-100 is its structure that is composed of non-harmful ingredients: zinc-adeninate building blocks.

Another example is BioMIL-5, in which the framework consists of zinc atoms connected with azelaic acid, both known from their antibacterial and anti-inflammatory properties. The expected properties were tested against *Staphylococcus aureus* and *S. epidermidis*. During the incubation with bacteria, the BioMIL-5 framework was gradually disintegrated and the released molecules interacted with the cells. These results showed that the framework could be successfully applied in antibacterial treatment.⁹⁵

MOFs built with appropriate blocks can be considered as agents for magnetic resonance imaging (MRI). Significant effort has been devoted to the development of alternative contrast agents based on gadolinium, such as gadolinium-nicotinate framework⁹⁶, Gd(BDC)_{1.5}(H₂O)₂ or [Gd(1,2,4-BTC)-(H₂O)₃]H₂O.⁹⁷ Clusters of this type have shown very high relaxivities and could be considered as an excellent opportunity for biomedical or biological imaging.

According to a big demand of proper “vehicle” systems in the encapsulation science, MOFs can propose numerous possibilities. Some of the examples for biologically active species entrapment inside MOFs are listed in the table 1.6.

Table 1.6 Functionalization of different MOFs and benefits arising form the hybrid structure.

MOF	Guest	hybrid	Benefits	References
MIL-100(Fe)	caffeine (CAF)	CAF@MIL-100(Fe)	controlled release	Cunha D., Yahia M. B., Hall S., Miller S. R., Chevreau H., Elkaïm E., Maurin G., Horcajada P., Serre C., <i>Chem. Mater.</i> , 2013 , 25, 2767-2776
MIL-127(Fe)		CAF@MIL-127(Fe)		
MIL-53(Fe)		CAF@MIL-53(Fe)		
UiO-66(Zr)		CAF@UiO-66(Zr)		
MIL-100(Fe)	doxorubicin (DOX)	DOX-MOF-100(Fe)	DOX fluorescence quenching and remarkable thermal and photochemical stability	Arnad R., Borghi F., Manoli F., Manet I., Agostoni V., Reschiglian P., Gref R., Monti S., <i>J. Phys. Chem.B</i> , 2014 , 118, 8532-8539
Cu-BTC Basolite C300	Polyurethane	polyurethane/Cu-BTC	facilitate NO generation from bioavailable S-nitrosothiols	Harding J. L., Reynolds M. M., <i>J. Mater. Chem. B</i> , 2014 , 2, 2530-2536
UiO	fluorescein isothiocyanate (FITC)	FITC-UiO	for real time measurement of intracellular pH in live cells	He C., Lu K., Lin W., <i>J. Am. Chem. Soc.</i> , 2014 , 136, 12253-12256
UiO	silencing multidrug resistance siRNA (Bcl-2, P-glycoprotein, survivin), cisplatin (Cis)	siRNA/UiO-Cis	enhancement of therapeutic efficacy <i>in vitro</i> in ovarian cancer cells	He C., Lu K., Liu D., Lin W., <i>J. Am. Chem. Soc.</i> , 2014 , 136, 5181-5184
ZIF-8	fluorescein (FITC) camptothecin (CPT)	FITC@ZIF-8 CPT@ZIF-8	drug delivery (cell line MCF-7 breast cancer)	Zhuang J., Kuo C.-H., Chou L.-Y., Lin D.-Y., Weerapana E., Tsung C.-K., <i>ACS Nano</i> , 2014 , 8, 2812-2819

There are a number of strategies for incorporation of these active ingredients inside MOFs cavities. As presented at the figure 1.13(1), one of the possibilities is based simply on the synthesis using building blocks with relevant specific characteristics. The other way is to attach the molecules of interest by covalent or non-covalent interactions within the framework (figure 1.13(2a) and 1.13(2b)). Here the

MOF structure acts as a host matrix for guest compound.

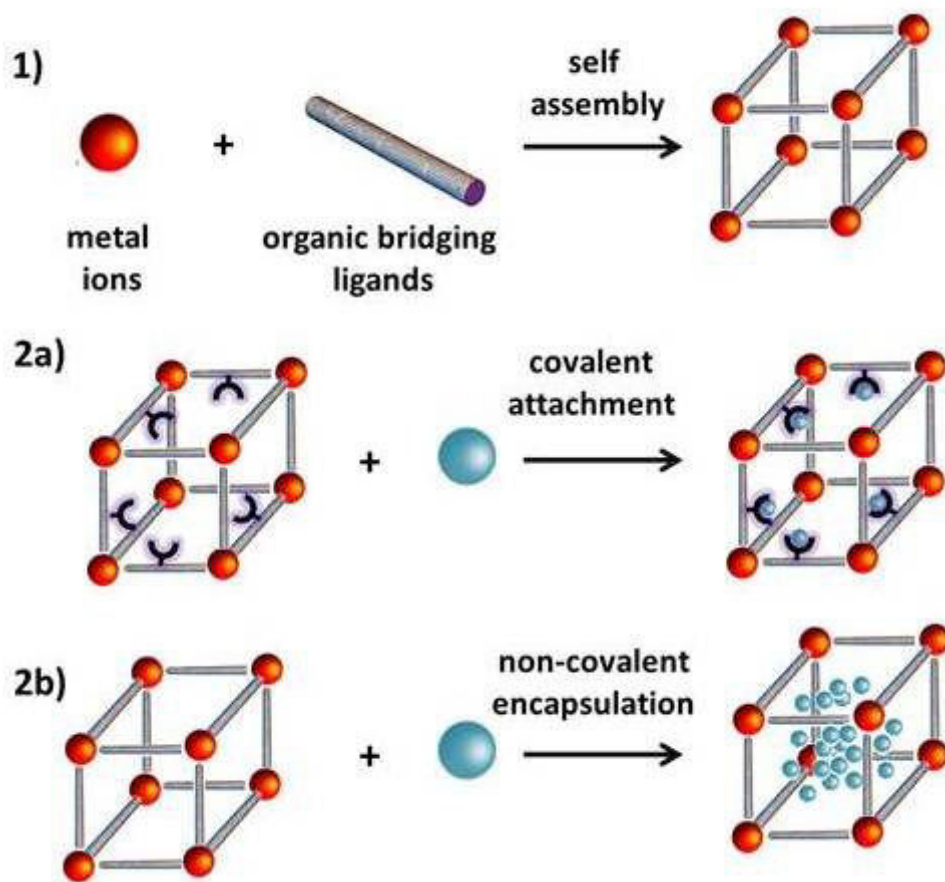


Fig. 1.13 Different strategies to entrap the therapeutic agents inside the framework: (2a) covalent and (2b) by non-covalent attachment. (reprinted from Della Rocca J., Liu D., Lin W., *Accounts of Chemical Research*, 2011, 44, 957-968)

The encapsulation within MOFs is discussed with details in the chapter 1.2.

1.2 Zeolitic imidazolate frameworks

1.2.1 ZIFs structure

Zeolitic imidazolate frameworks (ZIFs) form a subfamily of MOFs with the structure composed of metals tetrahedrally coordinated with imidazolates, the conformation similar to the one found in zeolites. Zeolite network consists of SiO_4^{4-} and AlO_4^{4-} tetrahedra, where Al or Si atoms are placed in the centers and oxygens flank the corners (figure 1.14).⁹⁸ Zeolites structures represent long-range ordering materials with well-defined crystals rigidity. The lack of organic functionalities limited the possible application area. The first mineral zeolite - stilbit was discovered in 1756 by Cronsted, but the highest attention on zeolites has gained within last 50 years. Zeolites are used in big quantities in petroleum industry, in detergents as water softeners, in building materials, and in agriculture.⁹⁹ To open an access to new fields, a lot of effort has been devoted to the synthesis of structures with organic units as an integral part of the framework. ZIFs were successful answer on that need. In the few last years, a lot of different networks with various functionalities and topologies appeared (figure 1.15).

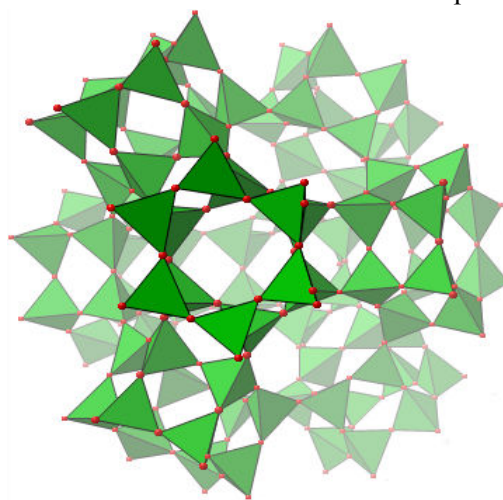


Fig. 1.14 Zeolite ZK5 (Si tetrahedra – green, O – red).

Regarding nomenclature of zeolitic imidazolate frameworks, in ZIF-n the number “n” is arbitrarily given by the authors who first reported the structure. In the ZIFs structure, the inorganic part is usually either Zn or Co ions, and the linker is an imidazole-based derivative (table 1.7). Although all these materials are chemically similar, they are quite different in the morphology, crystal size, pore diameters, and surface areas, thus leading to multiple applications.

The topology construction closely depends on the solvent, metal source, time of the reaction and imidazolate ligand functionalities.¹⁰⁰ Imidazole is composed of two non-equivalent amine groups in five-membered ring. Once the NH group deprotonated, a bidentate ligand is obtained, which is necessary to create supramolecular frameworks. The imidazole without any functional group forms unstable and dense frameworks. The situation changes when substituted in the position 2, 4 or 5. The sodalite SOD topology appears when the imidazole linkers have the additional group in the 2, the zeolite RHO with functionalities in the 4 and 5 positions. When benzimidazole linkers are substituted

in either 5 or 7, the LTA topology is allowed. More complex topologies (MOZ or POZ) are possible with 5-chlorobenzimidazole linkers or by mixing different imidazolate derivatives.

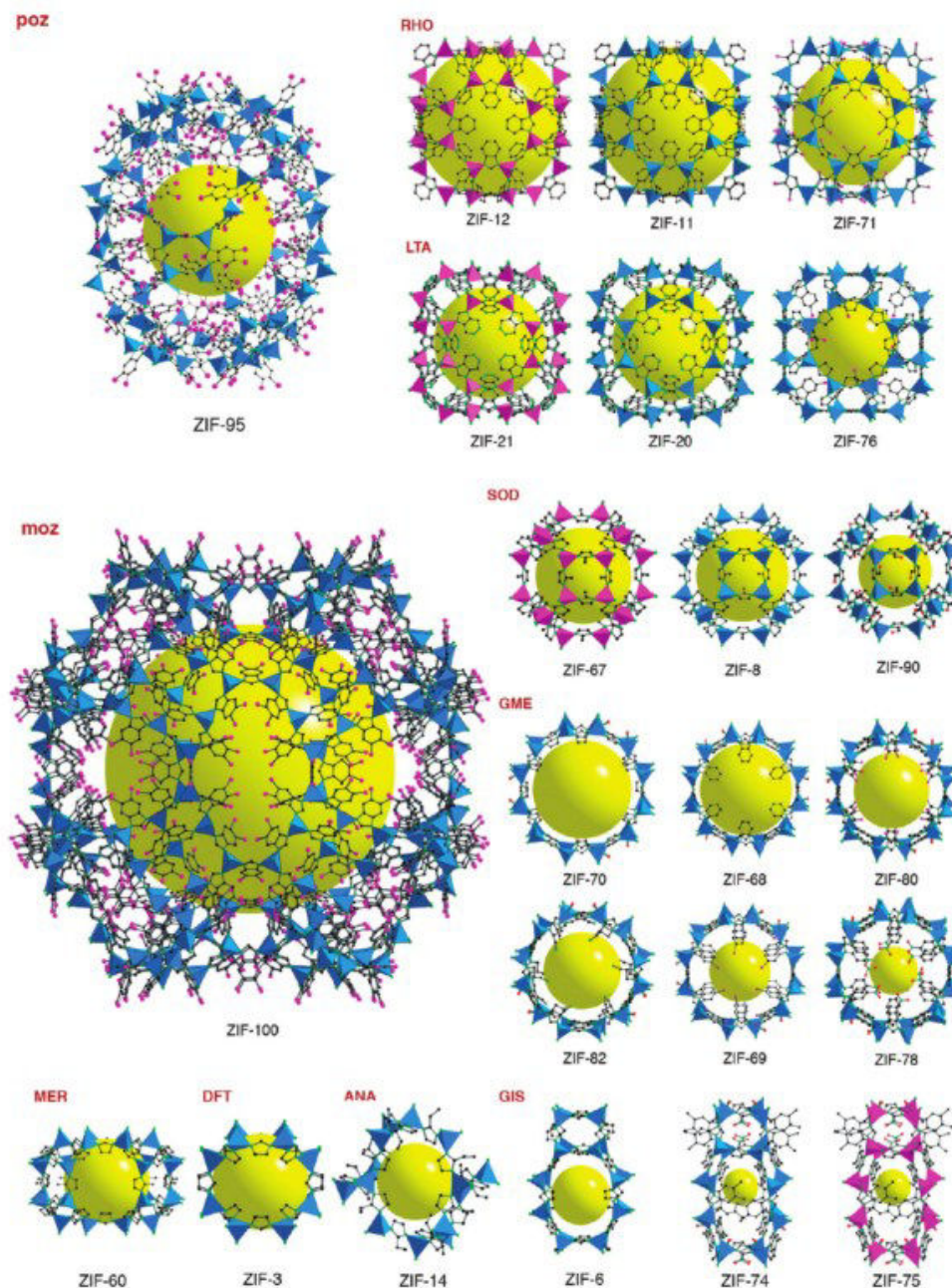


Fig. 1.15 Examples of ZIFs classified from the topology. Indications: ZnN_4 polyhedra in blue, CoN_4 polyhedra in pink, C in black, N in green, O in red, Cl in pink, yellow ball – empty void within the single unit cage (copied from Phan A., Doonan C. J., Uribe-Romo F. J., Knobler C. B., O’Keeffe M., Yaghi O. M., *Acc. Chem., Res.*, 2010, 43, 58-67)

Table 1.7 Summary of ZIF-8 topologies and building units.

ZIF framework	Topology	metal	linker
ZIF-12	Rho	Co	benzimidazole
ZIF-11	Rho	Zn	benzimidazole
ZIF-71	Rho	Zn	4,5-dichloroimidazole
ZIF-20	Lta	Zn	purine
ZIF-21	Lta	Co	purine
ZIF-76	Lta	Zn	imidazole 5-chlorobenzimidazole
ZIF-95	Poz	Zn	5-chlorobenzimidazole
ZIF-100	Moz	Zn	5-chlorobenzimidazole
ZIF-8	Sod	Zn	2-methylimidazole
ZIF-67	Sod	Co	2-methylimidazole
ZIF-90	Sod	Zn	imidazolate-2- carboxylaldehyde
ZIF-68	Gme	Zn	benzimidazole 2-nitroimidazole
ZIF-70	Gme	Zn	imidazole
ZIF-80	Gme	Zn	4,5- dichlorobenzimidazole 2-nitroimidazole
ZIF-69	Gme	Zn	2-nitroimidazole 5-chloroimidazole
ZIF-78	Gme	Zn	2-nitroimidazole 6-nitrobenzimidazole
ZIF-82	Gme	Zn	chloronitroimidazole nitroimidazole
ZIF-60	Mer	Zn	imidazole 1-methylimidazole
ZIF-3	Dft	Zn	imidazole
ZIF-14	Ana	Zn	ethylimidazole
ZIF-6	Gis	Zn	imidazole
ZIF-74	Gis	Zn	methylbenzimidazole nitroimidazole
ZIF-75	Gis	Co	methylbenzimidazole nitroimidazole

ZIFs as multifunctional materials are considered either in a pure or in hybrid films/membranes forms to meet with industrial applications. These structures can offer controllable and adaptable compositions, very high porosity, reproducibility and cost-effectiveness in the production on a bigger scale.

1.2.2 Zeolitic Imidazolate Framework-8

ZIF-8 combines the properties of two materials, zeolites and MOFs, including high porosity, high surface area (BET $\sim 1300\text{-}1800\text{ m}^2/\text{g}$), thermal (up to 550°C) and chemical resistance to boiling alkaline water and organic solvents. ZIF-8 is described with sodalite topology and formed via bridging between 2-methylimidazolate anions and zinc cations (corner sharing $\text{Zn}(\text{MeIM})_4$ tetrahedral units in which the Zn^{2+} ions are bridged with the Hmim- ligands). The ZIF-8 networks contain large pores of 11.6 \AA , with small apertures 3.4 \AA , cubic symmetry and cell dimension of 16.32 \AA .⁷ The framework of ZIF compounds closely resembles to the framework of zeolites, the bond angle in both structures is of 145° (figure 1.16).

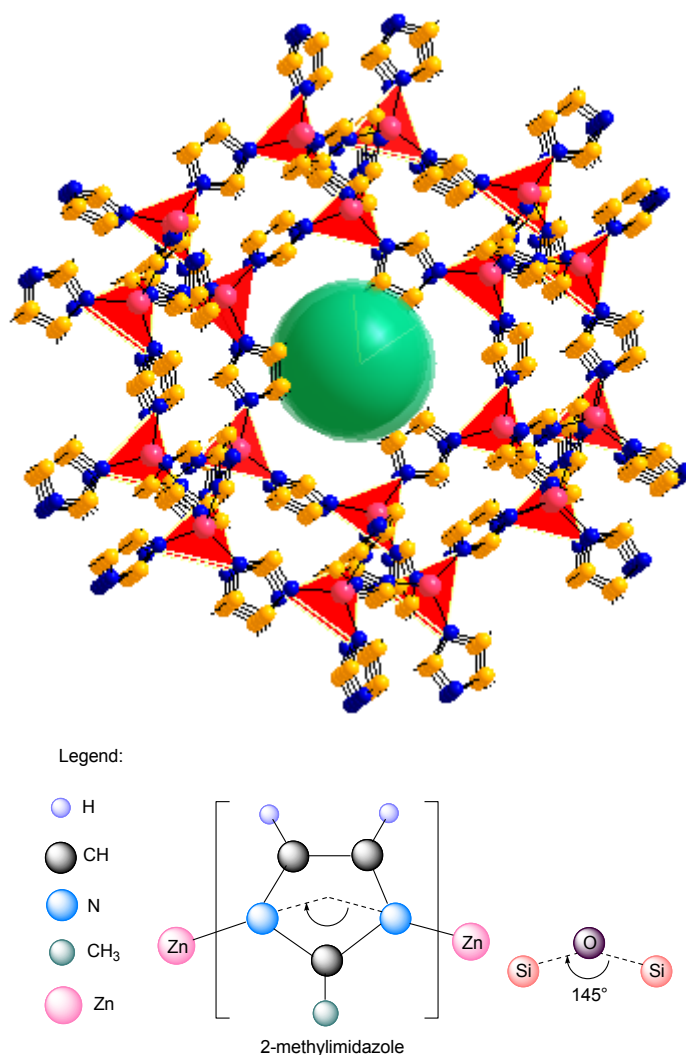


Fig. 1.16 Scheme of the ZIF-8 structure and Zn-(2-methylim)-Zn and Si-O-Si linkages in tetrahedral ZIF-8 and zeolite network respectively (green ball in the ZIF-8 presents an empty void).

The position of the zinc ions is rigid, but the 2-methylimidazole linkers are flexible and can rotate in the Zn-Zn axis changing the size of the pore aperture. Moreover, Zn^{2+} ions are acting as strong Lewis acids and N- with OH- groups as basic ones. These properties increased the interest in ZIF-8 materials, especially in the area of catalysis.

1.2.3 ZIF-8 synthesis

The ZIF-8 framework can be prepared via standard solvothermal/hydrothermal synthesis or by alternative ways, such as microwave, mechanochemical, electrochemical, sonochemical, microfluidic way. Table 1.8 presents an overview on the reported synthetic methods with the properties of the final product.

The kinetic parameters must be appropriate to allow nucleation and growth in the desired directions. The formation of ZIF-8 crystals depends on the solvation of the zinc ions in the solvent. For example, the zinc ions from zinc nitrate in methanol create complexes which are relatively weak and zinc ions can easily coordinate with Hmim. The speed of the nucleation provides small crystals. When zinc acetate is used as a precursor (the acetate group strongly interacts with zinc ion), the speed drastically slows leading to larger crystals.¹⁰¹ Until now, numerous strategies have been described for the synthesis of ZIF-8. Generally, synthesis is conducted at room temperature or under hydrothermal treatment, with molar ratio of the ZIF-8 precursors: zinc nitrate hexahydrate and 2-methylimidazole depending on the solvent (water - 1:70, methanol - 1:8, DMF - 1:1).

Basic protocols can be described as follows:

- for the synthesis in methanol: 0.001 mol $\text{Zn}(\text{NO}_3)_2$ and 0.008 mmol Hmim were dissolved in methanol to generate clear solutions, respectively; then, both were mixed together and aged at room temp. [CrystEngComm, 2013, 15, 1794-1801]
- for the synthesis in water: $\text{Zn}(\text{NO}_3)_2 \times 6 \text{H}_2\text{O}$ (1.17 g) is dissolved in 8 g DI water and Hmim (22.7 g) in 80 g DI water; then, mix under stirring at 22°C for 5 min.¹⁰²
- for the synthesis in DMF: Mix $\text{Zn}(\text{NO}_3)_2 \times 6 \text{H}_2\text{O}$ (1.672 g; 5.621 mmol) and Hmim (0.420 g; 5.117 mmol) in 125 mL DMF and heat in a sealed vial 5°C/min to 140°C for 24 h; then, cool down (0.4°C/min) to room temp and wash with DMF.¹⁰³

Considering the solvent, it was observed that methanol can be removed from the pores of ZIF-8 much easier than DMF, because of its smaller diameter. On the other hand, organic solvents are generally expensive and could cause toxicity and environmental problems. This is the reason why water is widely used for ZIF-8 preparation (molecules are smaller than the SOD cage and have no impact on the environment).¹⁰⁴

In relation to the crystal size, over the last years, many options have been proposed with using structure directing agents, like 1% poly(diallyldimethylammonium chloride) or cetyltrimethylammonium bromide.^{105 106}

The size of ZIF-8 crystals can be controlled not only by surfactants but also by varying the reaction time. It was shown that the structural evolution of ZIF-8 is correlated with time and the process can be divided into three stages:

- $t < 10$ min – the nucleation stage - incubation time to nucleate ZIF-8; $\text{size}_{(10\text{min})} \sim 50$ nm, spherical in shape,
- $10 < t < 60$ min – the growth stage – for the increase of crystallinity; $\text{size}_{(30\text{min})} \sim 230 \pm 40$ nm, facets observed in some crystals,
- $t > 60$ min – the stationary phase – crystallization rate is constant, metastable phase is consumed; $\text{size}_{(12\text{h})} \sim 500 \pm 40$ nm.¹⁰⁷

Large-sized ZIF-8 crystals exhibit the highest surface area, which is connected with the evolution of micropores in the structure, for example 50 nm-sized ZIF-8 has 1530 m²/g while 2000 nm-sized-ZIF-8 – 1960 m²/g, which is interesting in the catalysis and adsorption field [Chem. Commun., 2013, 49, 2521-523].

Table 1.8 Summary of different synthetic protocols and properties of resulting ZIF-8 material.

Synthesis method	Solvent	Conditions	Properties of the material	Reference
Microwave-assisted ionothermal	ionic liquid 1-butyl-3-methyl-imidazolium tetrafluoroborate	140°C, ambient pressure, 10-60 min	300-500 nm in diameter, pore volume: 0.337 cm ³ /g, BET 471 m ² /g	Yang L., Lu H., <i>Chin. J. Chem.</i> , 2012 , 30, 1040-1044
Microwave-assisted solvothermal	DMF	140°C-180°C; 2-24 h	Comparison of conventional electric heating and microwave 10-120 µm in size BET 646-409 m ² /g	Park J. H., Park S. H., Jhung S. H., <i>Journal of the Korean Chemical Society</i> , 2009 , 53, 553-559
Eutectic mixture	urea-choline	100°C	Crystals well-dispersed in ethanol and formed stable suspension without settlement 50-300 nm size	Liu C., Sun F., Zhou S., Tian Y., Zhu G., <i>CrystEngComm</i> , 2012 , 14, 8365-8367
Solvothermal/Hydrothermal	methanol or isopropanol	in 250 mL stainless steel high pressure Parr reactor 100 psia/H ₂ ; stirring 150°C/ 5h	Size 0.5 – 3 µm in 2-propanol 0.5 – 1.5 µm in CH ₃ OH	Zhu M., Jasinski J. B., Carreon M. A., <i>J. Mater. Chem.</i> , 2012 , 22, 7684-7686
	methanol	1h at room temperature	28 ± 15 nm (Z-average) polydispersity index 0.083 nm 1696 ± 16 m ² /g BET 1904 ± 3 m ² /g Langmuir Z potential +31 mV	Demessence A., Boissière C., Grosso D., Horcajada P., Serre C., Férey G., <i>J. Mater. Chem.</i> , 2010 , 20, 7676-7681
	DMF	140°C ; 24 h	sensitive to Cu ²⁺ Cd ²⁺ and acetone stable up to 500°C 1501 m ² /g	Liu S., Xiang Z., Hu Z., Zheng X., Cao D., <i>J. Mater. Chem.</i> , 2011 , 21, 6649-6653
	DMF	140°C; 24 h	colorless polyhedral crystals	Pan Y., Ma D., Liu H., Wu H., He D., Li Y., <i>J. Mater. Chem.</i> , 2012 , 22, 10834-10839
	water	22°C; 5 min	85 nm, excellent thermal, hydrothermal, solvothermal stability, SOD structure; microporous volume 0.31 cm ³ /g; BET 1079 m ² /g; Langmuir 1173 m ² /g	Pan Y., Lin Y., Zeng G., Zhao L., Lai Z., <i>Chem. Commun.</i> , 2011 , 47, 2071-2073
	aqueous ammonia/methanol	RT; 48h	1368 m ² /g BET	Zhou X., Zhang H. P., Wang G. Y., Yao Z. G., Tang Y. R., Zheng S. S.,

Synthesis method	Solvent	Conditions	Properties of the material	Reference
				<i>Journal of Molecular Catalysis A: Chemical</i> , 2013 , 366, 43-47
	water	RT; 10 min	30-70 nm Z potential + 29.9 mV The material absorbed ssDNA which is negatively charged	Liu S., Wang L., Tian J., Luo Y., Chang G., Asiri A. M., Al-Youbi A. O., Sun X., <i>ChemPlusChem</i> , 2012 , 77, 23-26
	water	T-type micromixer 1h	25mL/min – 188 ± 33 nm 30mL/min – 150 nm batch reactor system (control) 344 ± 341 nm	Yamamoto D., Maki T., Watanabe S., Tanaka H., Miyahara M. T., Mae K., <i>Chemical Engineering Journal</i> , 2013 , 227, 145-150
	aqueous ammonia/methanol	RT; 48h	Cubic symmetry $a=17.050(8) \text{ \AA}$ BET=1460 m ² /g	Chizallet C., Lazare S., Bazer-Bachi D., Bonnier F., Lacocq V., Soyer E., Quoineaud A. A., Bats N., <i>J. Am. Chem. Soc.</i> , 2010 , 132, 12365-12377
	methanol	RT; 10 min – 12h	10 min – spherical, 50nm, metastable phase 30 min - 230±40nm, some crystals show facets, larger crystals+metastable phase 60 min – 230±20nm, homogeneous pure crystals 12 h – 500±40nm, became less homogeneous	Venna S. R., Jasinski J. B., Carreon M. A., <i>J. Am. Chem. Soc.</i> , 2010 , 132, 18030-18033
	DMF	140°C; 24h	1810 m ² /g Langmuir 1630 m ² /g BET Pore volume 0.636 cm ³ /g Stable in boiling benzene(7days), methanol(7days), water(7days) and 0.1 and 8 M aqueous sodium hydroxide (24h)	Park K. S., Ni Z., Côté A. P., Choi J. Y., Huang R., Uribe-Romo F. J., Chae H. K., O’Keeffe M., Yaghi O. M., <i>PNAS</i> , 2006 , 103, 10186-10191
	DMF	140°C ; 24h	Yield 25% (based on 2-MIM) Stable up to 400°C Specific surface area 1810 m ² /g SOD Size: 159 µm	Nguyen L. T. L., Le K. K. A., Phan N. T. S., <i>Chin. J. Catal.</i> , 2012 , 33, 688-696
	methanol with 1% poly(diallyldimethyl ammonium chloride)	RT; 24h	57±7 nm BET 1264 m ² /g micropore volume 0.51cm ³ /g	Nune S. K., Thallapally P. K., Dohnalkova A., Wang C., Liu J., Exarhos G. J., <i>Chem. Commun.</i> , 2010 , 46, 4878-4880

Synthesis method	Solvent	Conditions	Properties of the material	Reference
	DMF	130°C; 24h	Broad near-UV excitation range 350-430nm, broad photoluminescence emission at 445nm	Shen C.-C., Chen W.-T., Lin R.-S., <i>Dalton Trans.</i> , 2012 , 41, 11885-11888
	methanol	RT; 1h	46 nm from XRD DLS diameter 49 nm Polydispersity index 0.09 Nano ZIF-8 less stable thermally than micro ZIF-8 BET 962 m ² /g; pore volume 0.36 cm ³ /g (for micro ZIF-8: 1630; 0.64) ZIF-8 ζ +55 mV	Cravillon J., Münzer S., Lohmeier S.-J., Feldhoff A., Huber K., Wiebcke M., <i>Chem. Mater.</i> , 2009 , 21, 1410-1412
Dry-gel conversion	water	120°C; 24h	BET 1470 m ² /g Pore volume 0.69 cm ³ /g	Shi Q., Chen Z., Song Z., Li J., Dong J., <i>Angew. Chem. Int. Ed.</i> , 2011 , 50, 672
Mechanochemical	no solvent	RT; 100 rpm; 3-240 h	BET 390-1480 m ² /g Pore volume 0.47-1.05 cm ³ /g	Tanaka S., Kida K., Nagaoka T., Ota T., Miyake Y., <i>Chem. Commun.</i> , 2013 , 49, 7884-7886
Electrochemical	DMF, methanol, ethanol, water	RT; 10 min	BET 1262-1695 m ² /g Pore volume 0.56-0.66 cm ³ /g	Joaristi A. M., Juan-Alcañiz J., Serra-Crespo P., Kapteijn F., Gascon J., <i>Cryst. Growth Des.</i> , 2012 , 12, 3489-3498

1.2.4 ZIF-8 growth mechanism

The shape and symmetry control over nanocrystals have been widely investigated in recent years, because this could influence the optical, optoelectronic, magnetic, and catalytic properties of the material.¹⁰⁸ In the ZIF-8 structure, the most energetically favorable is rhombic dodecahedron morphology whose formation depends on the synthetic conditions and the reaction time. A detailed growth mechanism has been already explained by Carreon M. A. *et al.* 2010⁸⁴ and Wiebecke M. *et al.*¹⁰⁹ and is shown in the scheme presented by Kida *et al.* 2013 on the figure 1.27¹¹⁰.

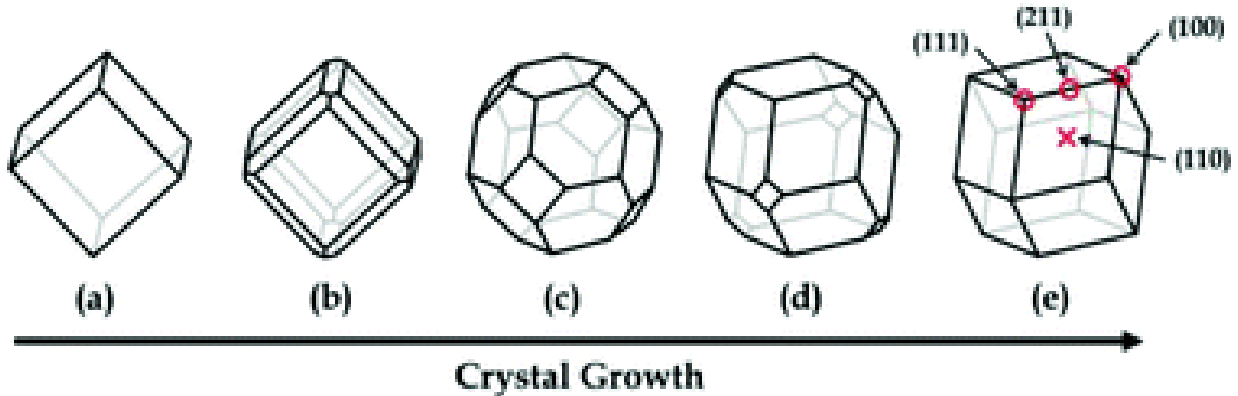


Fig. 1.17 Evolution of the geometrical particle shapes over time determined for ZIF-8.

The process of the crystals evolution could be well described using Wulff construction. The cubes appear only with $\{100\}$ planes, while rhombic dodecahedrons are totally covered with $\{110\}$ planes. The particles grow either in $\{100\}$ or $\{110\}$ direction and the final shape of the crystal is determined with the speed growth in the direction of one from these faces. During the crystal development, intermediate forms – truncated rhombic dodecahedrons expose twelve $\{110\}$, six $\{100\}$, showing an increased fraction of the energetically less favorable faces. The facet $\{100\}$ with the highest growth rate is reduced overtime. The resulting crystals, with a slower-growing $\{110\}$ facets, are created. The degree of truncation is given by the following equation:

$$R_{TR} = 2 - \frac{2}{\sqrt{2}} \cdot \left[\frac{\gamma_{100}}{\gamma_{110}} \right]^{12}$$

When $R_{TR} = 1$ the crystal has fully truncated shape, while $R_{TR} = 0$ no truncation is observed for rhombic dodecahedron. This explanation meets with the fact that $\{110\}$ faces have the lowest surface energy ($\frac{\gamma_{100}}{\gamma_{110}} \geq \sqrt{2}$).¹¹¹

The other factor “R” describing this process is denoted as the growth speed along the $\{100\}$ to that along $\{110\}$ directions.¹¹² According to the calculations based on this theorem, the values for different structures are as follows:

- cube $R = 0.7$,
- truncated cube $R = 0.8$,
- truncated rhombic dodecahedron $R = 1.24$,
- rhombic dodecahedron $R = 1.41$.

The crystallization process for ZIF-8 requires the activation energy for the nucleation and crystal growth of 115.1 kJ/mol and 87.7 kJ/mol, respectively.¹¹³ Lim *et al.* 2015¹¹⁴ indicated the complex of

($[\text{Zn}_4(\text{C}_4\text{N}_2\text{H}_5)_4(\text{C}_4\text{N}_2\text{H}_6)_2(\text{NO}_3)_3]^+$) in the nucleation process, essentially in the formation of the four-membered ring unit in the sodalite framework.

Different surface topographies and sizes of the ZIF-8 crystals can be possible, depending on the conditions chosen for the synthesis. Thus playing with the procedures, it's relatively easy to obtain the material with interesting morphology and properties that have an impact on the application field.

1.2.5 ZIF-8 applications

Both Zn^{2+} and 2-methylimidazole are known as catalysts. BASF described the utilization of 2-methylimidazole in the production of pharmaceuticals, pesticides, dyes, textile auxiliaries, photographic chemicals, corrosion inhibition, in polyurethanes and as curing agent for epoxy resins. Zinc can be applied in reactions, such as oxidative esterification of aldehydes or oxidation of benzyl alcohols to aldehydes and sulfides to sulfoxides.¹¹⁵ Zinc salts are cheap and can replace many toxic elements commonly used in some reactions. As an example, Enthaler *et al.* has developed a new Pd-free method for the transformation of amides into nitriles.¹¹⁶ In this context, the connection of Zn^{2+} with 2-methylimidazole which is found in ZIF-8, seems to be attractive in the catalytic area. Indeed, ZIF-8 has been explored in the transesterification of rapeseed oil¹¹⁷ or in the conversion of CO_2 to chloropropene carbonate¹¹⁸. Other examples are the Friedel-Crafts acylation of anisole with benzoyl chloride¹¹⁹ and the Knoevenagel reaction between benzaldehyde and malononitrile.¹²⁰ ZIF-8 crystals are interesting candidates as heterogeneous catalysts because of their long lifetime, easy recycling and separation from the products, high activity and selectivity for most of the reaction.

Moreover, ZIF-8 can be considered as a support for metals or metal oxide particles. These functional "host-guest" systems are giving new opportunities and extend the area of possible application, especially in the catalysis domain. Examples of these hybrid structures and their application are presented in the Table 1.9.

Table 1.9 Examples of host-guest systems based on ZIF-8 material.

Structure	Guest	Application	Reference
Ni@ZIF-8	nickel nanoparticles	hydrogen generation from hydrolysis of aqueous ammonia borane NH_3BH_3	Li P.-Z., Aranishi K., Xu Q., <i>Chem. Commun.</i> , 2012 , 48, 3173-3175
PVP-Pd@ZIF-8	PVP-Pd	hydrogenation of 1,4-butanediol with selectivity to 1,4-butanediol	Zhang M., Yang Y., Li C., Lin Q., Williams C. T., Liang C., <i>Catal. Sci. Technol.</i> , 2014 , 4, 329-332
Au@ZIF-8	gold nanoparticles	aerobic oxidation of benzyl alcohol CO oxidation	Esken D., Turner S., Lebedev O. I., Van Tendeloo G., Fischer R. A., <i>Chem. Mater.</i> , 2010 , 22, 6393-6401 Jiang H.-L., Liu B., Akita T., Haruta M., Sakurai H., Xu Q., <i>J. Am. Chem. Soc.</i> , 2009 , 131, 11302-11303
$\alpha\text{-Al}_2\text{O}_3$ @ZIF-8	$\alpha\text{-Al}_2\text{O}_3$	H_2 separation membrane	Xie Z., Yang J., Wang J., Bai J., Yin H., Yuan B., Lu J., Zhang Y., Zhou L., Duan C., <i>Chem. Commun.</i> , 2012 , 48, 5977-5979
Fe_3O_4 @ZIF-8	Fe_3O_4 nanoparticles	Knoevenagel reaction, magnetic separation	Zhang T., Zhang X., Yan X., Kong L., Zhang G., Liu H., Qiu J., Yeung K. L., <i>Chemical Engineering Journal</i> , 2013 , 228, 398-404
GQDs@ZIF-8	graphene quantum dots	photoluminescence performance and preservation	Biswal B. P., Shinde D. B., Pillai V. K., Banerjee R., <i>Nanoscale</i> , 2013 , 5, 10556-

Structure	Guest	Application	Reference
ZnO@ZIF-8	ZnO	CO ₂ activation – formation of carbonates and chemisorbed CO ₂ ^{δ-} species	10561 Esken D., Noei H., Wang Y., Wiktor C., Turner S., Van Tendeloo G., Fischer R. A., <i>J. Mater. Chem.</i> , 2011 , 21, 5907-5915
GaN@ZIF-8	gallium nitride	suggested for photocatalysis, hydrogen generation, water splitting using visible light	Esken D., Turner S., Wiktor C., Kalidindi S. B., Van Tendeloo G., Fischer R. A., <i>J. Am. Chem. Soc.</i> , 2011 , 133, 16370-16373
Pt/ZIF-8 loaded TiO₂	Pt	phenol degradation	Isimjan T. T., Kazemian H., Rohani S. Ray A. K., <i>J. Mater. Chem.</i> , 2010 , 20, 10241-10245
Pd/ZIF-8	Pd	Selectivity in hydrogenation of cinnamaldehyde to hydro-cinnamaldehyde Suzuki-Miyaura cross-coupling reaction	Zhao Y., Liu M., Fan B., Chen Y., Lv W., Lu N., Li R., <i>Catalysis Communications</i> , 2014 , 57, 119-123 Dang T. T., Zhu Y., Ngiam J. S. Y., Ghosh S. C., Chen A., Seayad A. M., <i>ACS Catal.</i> , 2013 , 3, 1406-1410
Ru/ZIF-8	Ru (0) nanoparticles	Dehydrogenation of dimethylamine-borane	Yurderi M., Bulut A., Zahmakiran M., Gülcan M., Özkar S., <i>Applied Catalysis B: Environmental</i> , 2014 , 160-161, 534-541
CAF@ZIF-8	caffeine	erug encapsulation, controlled release	Liédana N., Galve A., Rubio C., Téllez C., Coronas J., <i>ACS Appl. Mater. Interfaces</i> , 2012 , 4, 5016-5021
DOXO-ZIF-8	doxorubicin	cancer cells delivery (NCI-H292, HT-29, HL-60)	Vasconcelos I. B., da Silva T. G., Militão G. C. G., Soares T. A., Rodrigues N. M., Rodrigues M. O., da Costa N. B., Freire R. O., Junior S. A., <i>RSC Adv.</i> , 2012 , 2, 9437-9442

As mentioned, ZIF-8 can be used for storage or entrapping different molecules. The effective embedding of guest molecules requires the proper pore size, shape and flexible but controllable gate-opening properties of ZIF-8. On the other hand, only molecules with the size fitting to the ZIF-8 pores can be embedded without dramatic architectural changes of the framework. It is as well very important in the size-selective gas sorption and separation. A membrane composed of Ultem®/ZIF-8 was successfully used for CO₂/N₂ mixture selective separation.¹²¹ ZIF-8 deposited on porous α -alumina support showed good sharp separation towards C2/C3.¹²² In another work, it was proven that ZIF-8 has high flexibility of the aperture and superhydrophobic pore surface that could help to selectively sieve iso-C₄H₈ from iso-C₄H₁₀ or n-C₄H₁₀ from iso-C₄H₁₀ with selectivity 180 and 2.5×10⁶ respectively.¹²³ This material can also be used as a novel adsorbent in aqueous solutions of benzotriazoles from environmental water¹²⁴ or separation of theophylline from mixture with caffeine and diprophylline.¹²⁵ In the context of water pollution and purification, ZIF-8 can be useful for removal of many dangerous compounds. The best example is humic acid, a water contaminant that during chlorination process can transform into harmful trihalomethane and haloacetic acid. It was shown for this compound that ZIF-8 has much higher capacity of adsorption when compared with activated carbon, fly ash, zeolites or graphite.¹²⁶ This adsorption is enhanced via π - π stacking interactions that appear between imidazole of ZIF-8 and benzene rings present in humic acid. We can easily observe leading results for ZIF-8 among other commonly used materials (table 1.10).

Table 1.10 Humic acid adsorption for various adsorbents (Lin K.-Y. A., Chang H.-A., *Water Air Soil Pollut.*, 2015, 226, 1-17).

Adsorbent	T (°C)	Adsorption capacity (mg/g)	Reference
ZIF-8	20	70.2	Lin K.-Y. A., Chang H.-A., <i>Water Air Soil Pollut.</i> , 2015 , 226, 1-17
	40	95.1	
	60	111.7	
Chitin	27	27.3	Ngah W. S. W., Musa A., <i>Science</i> , 1998 , 69, 2305-2310
Chitosan	27	28.88	
Activated bentonite	25	10.75	Douliou D., Leodopoulos C., Gimouhopoulos K., Rigas F., <i>Journal of Colloid and Interface Science</i> , 2009 , 340, 131-141
Amine functional rice husk ash	25	8.2	Imyim A., Prapalimrunsi E., <i>Journal of Hazardous Materials</i> , 2010 , 184, 775-781
Graphite	30	50.1	Hartono T., Wang S., Ma Q., Zhu Z., <i>Journal of Colloid and Interface Science</i> , 2009 , 333, 114-119
Activated carbon	25	45.4	Daifullah A. A. M., Girgis B. S., Gad H. M. H., <i>Colloids and Surfaces A: Physicochemical and Engineering Aspects</i> , 2004 , 235, 1-10
Carbon nanotube	25	60.5	Tsai Y. P., Doong R. A., Yang J. C., Chuang P. C., Chou C. C., Lin J. W., <i>Advanced Materials Research</i> , 2013 , 747, 221-224

Hierarchical ZIF-8 crystals produced with CTAB and l-histidine as co-templates present much higher activity than activated carbon in removal of toxic arsenates^{127 128} or phthalic acid and diethyl phthalate.¹²⁹ The material was used also in the adsorption kinetics tests with I₃⁻ anions and rhodamine B.¹³⁰ With these two compounds, it was clearly observed that the particle aperture of ZIF-8 affected the adsorption kinetics. I₃⁻ anions are small enough to enter the pores, while rhodamine with its larger molecule was only adsorbed on the surface.

Taking into account the advantages of ZIF-8 as a very selective sieve and adsorbent, this material was applied as pseudostationary phase for capillary electrokinetic chromatography.¹³¹ In this case, the material showed good separation of phenolic isomers: p-benzenediol, m-benzenediol, o-benzenediol, m-nitrophenol, p-nitrophenol, o-nitrophenol, because the negatively charged surface of the framework interacted with phenolic groups of the molecules.

The capabilities and high potential of ZIF-8 have been widely discussed in numerous applications. Both pure ZIF-8 and ZIF-8-based hybrid structures have been developed over last few years. The incorporation of other nanocomponent into the material may extend and facilitate the utilization of the complex structure. A large number of supported materials were synthesized and the science of ZIF-8 is expected to grow in the future on the industrial scale up. As far, only the BASF firm produces ZIF-8 for commercial purposes (ZIF-8 is commercially available from Sigma Aldrich as Basolite Z1200).

Nevertheless, more information and research are still required for this material, especially in the area of engineering of the final product as well as ecotoxicity and environmental influence to be a precious candidate for wide-spread use towards the industry.

1.3 General information on carbon dioxide conversion

Carbon dioxide is the most abundant among the greenhouse gases and the overproduction by human's activity causes a big environmental problem. A heavy consumption of fossil fuels and high development of industrial activities are the main contributors to the resulting global warming effect. It is estimated that CO₂ involves in more than 60% to the global warming effect.¹³² For many years, the technologies for CO₂ reduction has attracted enormous attention. The systems for carbon dioxide storage and sequestration (CCS) have developed rapidly to limit the concentration of this gas in the atmosphere. CCS could reduce up to 14% of the CO₂ levels required in 2050 to ensure the global temperature increase stays below 2°C.¹³³ One of the most popular solutions is CO₂ capture from the large point sources (like power plants) and injection into geologic formations. These natural containers (depleted oil and gas fields, saline formations, unmineable coal seals) could store the carbon dioxide for at least 200 years.¹³⁴ The other possibility to handle the CO₂ problem is to use it as a source for the chemical transformations. Figure 1.18 shows variety of different pathways where carbon dioxide molecule can act as C1 building block.

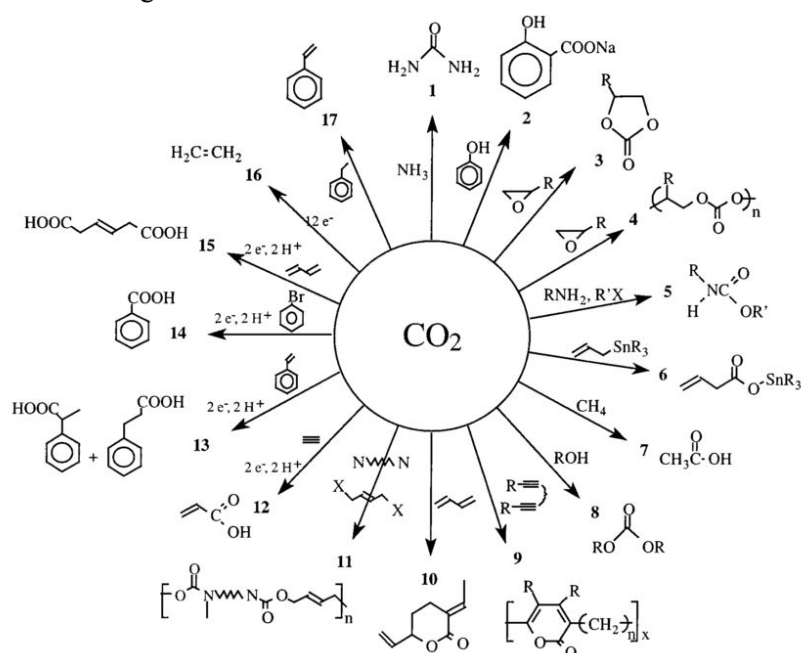


Fig. 1.18 Carbon dioxide conversion into useful chemicals. (reprinted from [135])

The CO₂ reuse is on the other hand a big challenge because of its high stability. The C=O bond energy is 750 kJ/mol which is much higher than C-C 336 kJ/mol, C-O 327 kJ/mol or C-H 411 kJ/mol.¹³⁶ Thus, to be able to consider the carbon dioxide transformation it is necessary to activate the molecule. The coordination with transition metals is one of the possibilities in this context. An interaction between the metal and the LUMO orbital of carbon dioxide results in a net transfer of electron density. That effects in a weakened C-O bond and opening of the molecule for binding with other compounds.

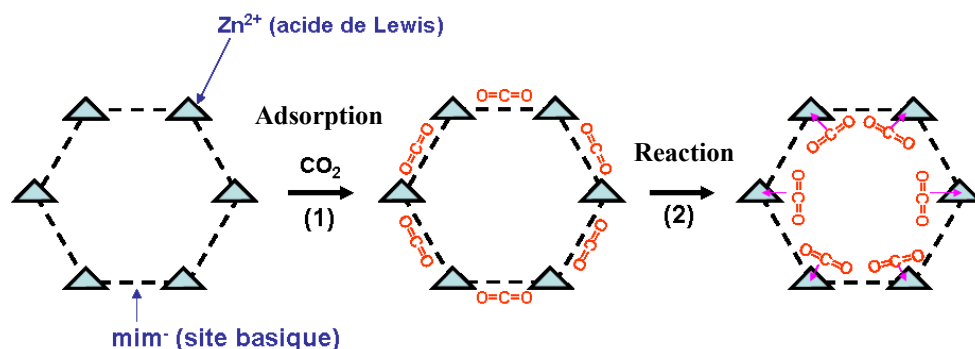
Many benefits arise from the utilization of carbon dioxide in chemical transformations. The naturally abundant CO₂ is cheap, nontoxic, nonflammable, and renewable as feedstock. Moreover, it can replace toxic chemicals such as phosgene and isocyanates. By using CO₂, we can produce materials like polymers via alternative ways and create new, more efficient and economical routes compared to the current methods. Finally, carbon dioxide reuse could have a positive impact on the global carbon balance.

Carbon dioxide can be useful as a solvent or as a raw material. Examples of the reaction where CO₂ plays as a solvent are the synthesis of α -tocopherol or conversion of pulegon for the synthesis of menthone, carvone or thymol.^{137,138} The advantage of these reactions is the elimination of organic solvents. The most important products, originating from the use of CO₂ as a raw component, are the products of hydrogenation, hydroformylation, oxidation, polymerization reactions, like polyurethanes, polyesters, polyamides and polycarbonates.¹³⁹

1.3.1 Cyclic carbonates

Cyclic carbonates can be widely used as reactive intermediates, solvents or precursors for polymers.¹⁴⁰ One of the most prominent examples is glycerol carbonate which found applications as a precursor for lubricants, solvents, coatings, detergents and cosmetics industry.¹⁴¹ The synthesis of cyclic carbonates has a wide history background. These compounds have been synthesized using dialkylcarbonate, diphenylcarbonate, or phosgene derivatives. According to the most ecofriendly preparation, utilization of carbon dioxide is giving a big promise. As we have already said, the conversion requires a catalyst that will activate both CO₂ and the compound in which CO₂ will be inserted. ZIF-8 is an ideal candidate for this kind of reactions because contains sites that are able to adsorb carbon dioxide and then participate as heterogeneous catalyst in the reaction chain (scheme 1.1).

Scheme 1.1 ZIF-8 role in the conversion of carbon dioxide.



The conversion is highly energetic and could lead to many by-products, so an appropriate catalyst is one of the requirements necessary to provide the highest selectivity of the desired product. The reaction depends strongly on the experimental conditions: temperature, carbon dioxide pressure, solvents and the reaction time. These parameters hardly influence on the reaction kinetics.

In this work, we used cyclic oxides as precursors for the cyclic carbonates production. The reaction consists of the following steps: opening of the cyclic ring, activation of carbon dioxide, insertion of the CO₂ and enclosure of the carbonate ring. We conducted the conversion with ZIF-8 which was acting as heterogeneous catalyst. The porous properties and an abundance of the catalytic active sites were the most important advantages of the material that facilitate the progress of the reaction.

In the final word, we would like to show some relations between the type of the commonly used catalysts, conditions and the final conversion. We chose the most prominent examples of the catalysts (including ZIF-8 material) and their efficiency in the carbon dioxide conversion with epichlorohydrin, styrene oxide and propylene oxide. The results are presented in the table 1.11.

Table 1.11 Examples of carbon dioxide conversions by using cyclic epoxides and various heterogeneous catalysts.

Catalyst	Epoxide	Pressure [bar]	Temperature [K]	Time [h]	Conversion [%]	Reference
Binary and bifunctional (salen)cobalt(III)-based catalyst system	epichlorohydrin	20	273	24	Selectivity for polymer	J. Am. Chem. Soc. 2011, 133, 15191-15199
Ti(Al)-SBA-15 modified with alkyl amines (adenine, imidazole, guanine) (Al-SBA-15-<i>pr</i>-Ade)	Epichlorohydrin	6.9	398	4	98,1	Microporous and Mesoporous Materials 2006, 90, 314-326
	Styrene oxide	6.9	398	8	98,4	
SAPO-56 ZIF-8 Cu-MOF	Epichlorohydrin	10	373	4	~43 ~33 ~33	Dalton Trans., 2013, 42, 6732-6735
Cu₃(BTC)₂	Epichlorohydrin	7	343-373	4	at 373 K: 63.8	Dalton Trans., 2014, 43, 3285-3296
Co based catalysts Co/LCl₂/Cl₂	Epichlorohydrin	50	RT	20	96	Catal. Sci. Technol. 2012, 2, 1021-1026
	Styrene oxide				60	
	Cyclohexene oxide				76	
[TBA]₂ZnBr₂Br₂	Styrene oxide	50	353	0,5	94	Catal Lett 2010, 135, 263-268
UiO-66 UiO-66-NH₂ Mg-MOF-74 CuBTC MIL-101 ZIF-8 IRMOF-3 MOF-5	Styrene oxide (solvent: chlorobenzene)	20	373	4	94 95 94 48 63 11 33 1	Applied Catalysis A: General 2013, 453, 175-180
Hydroxyl-functionalized Imidazolium bromides	Propylene oxide	4	343	16	95	ChemCatChem 2015, 7, 94-98
Mg-MOF-74	Styrene oxide (solvent: chlorobenzene)	5-20	373	0,5-4	95	Energy Environ. Sci., 2012, 5, 6465-6473

Hf-NU-1000 (Zr based 1,3,6,8-tetrakis(p-benzoic acid)pyrene with benzoic acid as modulator)	Styrene oxide	1.013	293	56	100	J. Am. Chem. Soc. 2014, 136, 15861-15864
Cu₂(OAc)₂/SiO₂ with DMAP as cocatalyst	Epichlorohydrin	20	353	14	90	Asian Journal of Chemistry 2011, 23, 3344-3346
ZIF-8	Epichlorohydrin	7	343-373	4	100 (at high temp diols and dimers)	ACS Catal. 2012, 2, 180-183
ZIF-8	Styrene oxide	7	373	10	54	Catalysis Communications 2013, 32, 36-40
ZIF-8	epichlorohydrin	7	343 353 373	4	65,5 84,1 98,2	Indian Journal of Chemistry 2012, 51A, 1306-1314

1.4 Catalysis shaping

1.4.1 Generalities on the mechanical properties of porous materials

In order to understand the flexibility, elastic behavior and structural stability of metal organic frameworks, it is necessary to conduct full tensorial analysis. The fundamental mechanical description of soft porous crystals is given by Hooke's law, which is connecting the stress σ and framework deformation ϵ :¹⁴²

$$\sigma = C \times \epsilon$$

σ – stress – force applied to the surface
 ϵ – deformation
 C – elasticity tensor or stiffness tensor

The mechanical behavior of the crystal could be described by the factors such as Young's modulus (E), linear compressibility (β), shear modulus (G) and Poisson's ratio (ν) (figure 1.19).

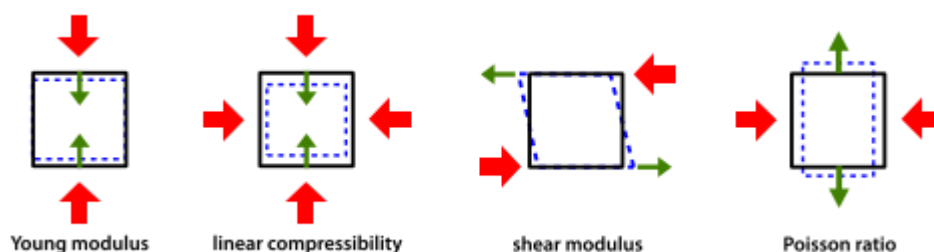


Fig. 1.19 Elastic characteristics of the material. [reprinted from Ortiz *et al.* 2012]

The Young's modulus describes elastic properties of the object which is either stretched or compressed and shows the relation between the forces applied to the surface and changes in some spatial dimension (like length, angle or volume).

The compressibility is the reciprocal of bulk modulus, which explains how much the material will be compressed under a given amount of external pressure. In fact bulk modulus is a ratio between changes in pressure to the fractional volume compression.

The shear modulus, also called rigidity modulus, shows deformations appearing when the force is applied tangentially, transversely or laterally to the face of an object.

Poisson's ratio is a negative relation between transverse and axial strain of the material subjected to the force from one direction. The material in these conditions tends to expand in the perpendicular direction. This phenomenon is called a Poisson effect. The Poisson's ratio is given by the following equation:

$$\nu = -\frac{\epsilon_t}{\epsilon_a}$$

ν – Poisson's ratio

ϵ – strain, deformation, is change in length, angle, volume to the initial length, angle, volume (strains are unitless)

ϵ_t – transverse strain

ϵ_a – axial strain

Metal organic frameworks are very famous for their ordered network. In the structure we can find the nodes connecting linkers with metal centers or secondary building units. These nodes are either flexible or rigid depending on the linker's architecture. When the pressure is applied, the framework deforms without collapse of the structure till the specific limit value of the pressure. Then, the increased forces resulted in the amorphization and complete degradation of the assembly. In this context, it's highly important to understand and describe key mechanical properties of the materials to take an advantage and open new opportunities from their flexibility. A detailed description of the elastic properties for MOFs opens possibilities for tuning and shaping the material for a specific purpose.

1.4.2 ZIF-8 shaping

Metal organic frameworks are materials which properties gained tremendous attention in the area of catalysis in the last few years. The solid form of the ZIF-8 and stability of the framework are key advantages in terms of use in heterogeneous catalytic processes. However, the utilization of the catalyst on an industrial scale requires postmodification of the powder. The nanoparticle in a form of powder is relatively hard to work with and handle out safety or recovery needs. The post-processing of the material, like compression, is then necessary to facilitate application at the industrial domain. While the synthesis of the ZIF-8 material is widely studied and documented, the shaping and formulation is rather niche knowledge.¹⁴³

The most explored shaping process for powders is compression. According to the structure of ZIF-8 and metal organic frameworks in general, the process of tableting is a big challenge. These porous materials when treated by pressure show changes in the internal porosity. In this context, the three mechanical processes can be involved:

- compaction – when the void spaces between the crystals are squeezed out through mild deformations,
- compression – when the free pore volume of the particle is reduced through the crystal collapse,
- cataclysmic ductile collapse – when the compacted crystals are fractured and amorphized due to the too high compression forces.

A single unit of ZIF-8 contains one nanosized pore, localized in the center (volume of 2456 \AA^3). The pores are connected through eight channels.¹⁴⁴ The applied pressure is responsible for some transitions in the structure. While increasing the compression force, the imidazolate linkers rotate thus changing the symmetry of the channels. These result in the modifications of the voids accessibility. Figure 1.20 presents the compression effect on the crystals of ZIF-8.

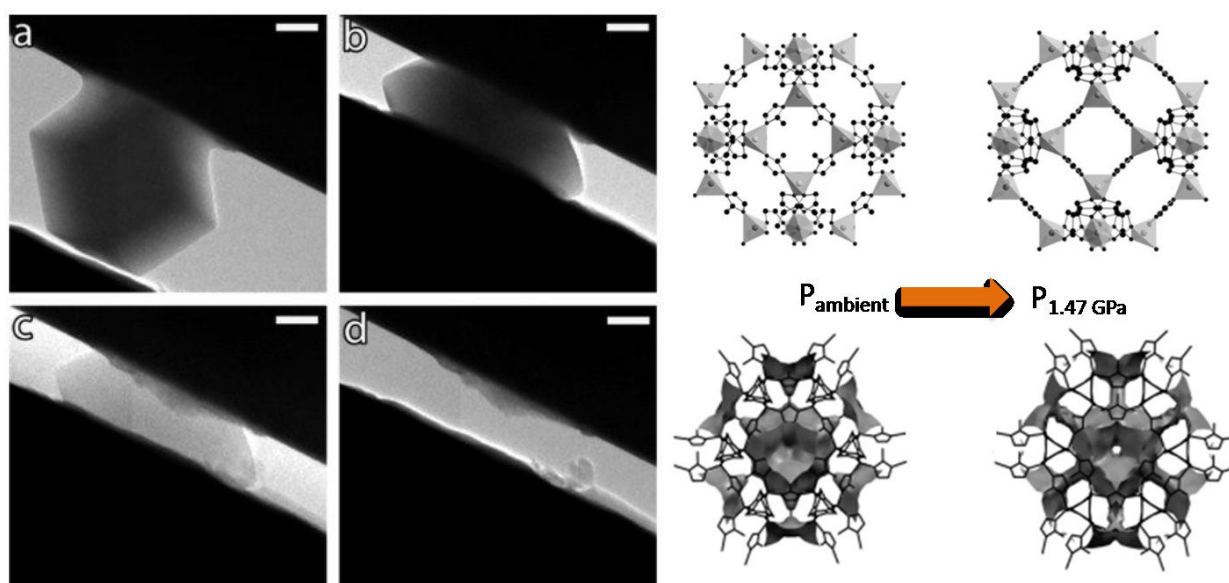


Fig. 1.20 *In situ* compression experiment on ZIF-8 crystal. Images present: the ZIF-8 single crystal before the test (a), during the increased compression force (b), (c), (d) [reprinted from¹⁴⁵] and simulation of the linkers arrangement with voids analysis of ZIF-8 material upon pressure. [reprinted from Moggach *et al.* 2009].

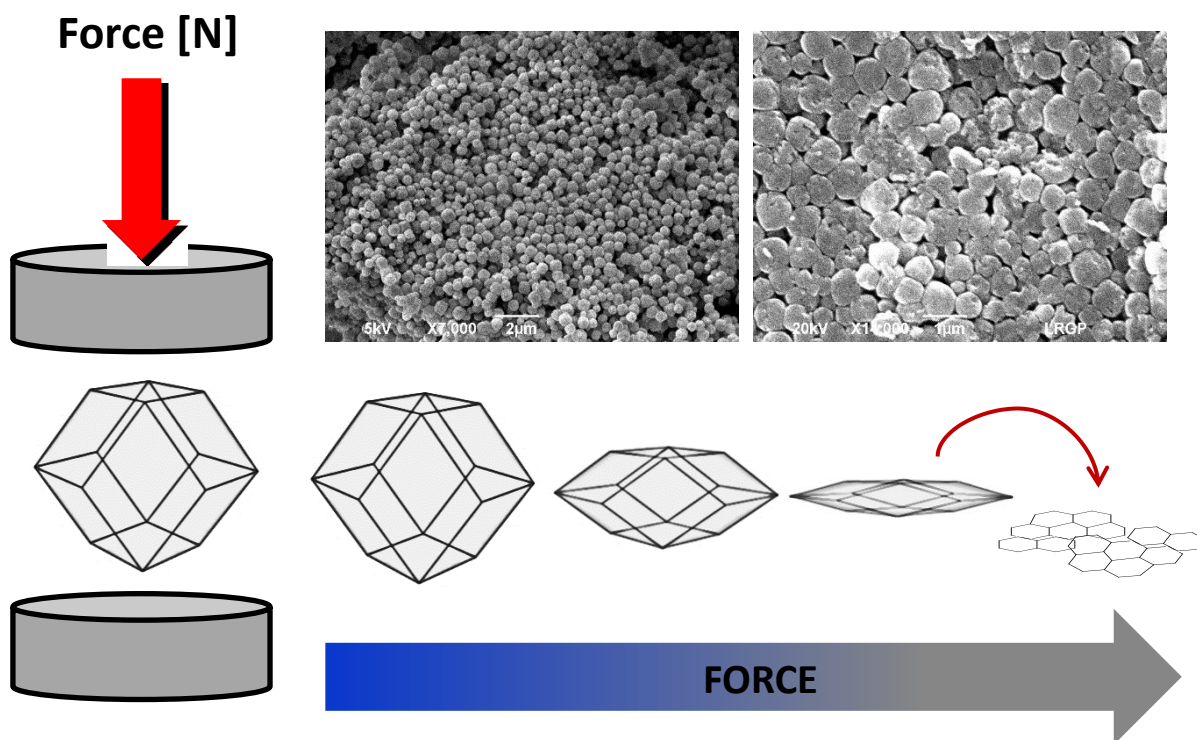
At the beginning of the test ZIF-8 crystals are rhombic dodecahedrons. One of these crystals was placed between the punches and slowly deformed when an increasing force was applied. The sample was markedly reduced in crystallinity and structural order. In the end of the test the material had amorphous feature. The similar trends were observed by Chapman *et al.*¹⁴⁶ where they tested changes in the specific surface area of ZIF-8. They demonstrated that ZIF-8 is highly compressible and only extremely high pressures caused irreversible amorphization. It was also shown by Ortiz *et al.* that ZIF-8 resisted up to 0.4 GPa and the crystals were more flexible when the guests molecules were present inside the pores.¹⁴⁷

To shape the material and still maintain the properties required for selected application, it's necessary to choose proper conditions of the compression. In this work we would like to answer on the requirements for the utilization of ZIF-8 heterogeneous catalyst on an industrial range. One of the solutions could be compaction of the ZIF-8 powder, thus resulting in easier recovery and safe handling during operations. We used INSTRON 5549 testing instrumentation to make the ZIF-8 tablets. The

INSTRON machine is commonly used for examination of the materials by tensile, compression, fatigue, impact and rheology. For our experiments the instrument was equipped with a punch and 4 mm round-shaped die to produce tablets from the ZIF-8 material. Each time the die was loaded with the same mass of the material (20 mg). The experiments were controlled with the displacement to force correlation. The speed of punch displacement was fixed at 10 mm/min during the compression and 15 mm/min during the ascending.

The obtained tablets of ZIF-8 material were further investigated in the CO₂ conversion with epichlorohydrin as a model reaction of this study. The obtained results were compared with these for ZIF-8 in powder and ZIF-8 functionalized with magnetic Fe₃O₄ particles (scheme 1.2).

Scheme 1.2 The particle deformation during the compaction process.



1.5 General information on cytotoxicity of nanoparticles

Highly growing interest in nanomaterials research gives the necessity to investigate the toxicity of these structures. Commercialization and daily exposure could induce some harmful implications. These aspects have not been studied enough, especially for emerging materials like MOFs. Some initial studies are required to reflect possible sources of exposure, potential risks and effects. Then, it is necessary to put the background of the safe use of all forms of nanoparticles.

Still it is challenging to choose the appropriate models and protocols for the cytotoxicity investigations.¹⁴⁸ The cell type must be selected according to the realistic consideration about the exposure and introduction way of the nanomaterials within the human body. We could assume that the first, direct contacts are by the skin, inhalation or ingestion, next by ocular or intravenous administration (figure 1.21). It is also highly important to define the dose of the nanoparticles for the cytotoxicity studies. The nanoparticles, like metal-organic frameworks (that are not dispersible in the culture media) have the tendency to diffuse, settle, agglomerate and adsorb on the surface some

components of the media (proteins, ions). Moreover metal-organic frameworks properties (composition, size, hydrophobicity, low density, charges) can markedly influence on the final effect of the deposited doses. The toxicity can also originate from the dissolution of the nanoparticles in the media, reactions occur with the degradation products and buffer components (figure 1.22). This phenomenon was illustrated by Shen *et al.* for ZnO nanoparticles. ZnO gradually decomposed in Zn^{2+} ions and reacted with carbonates and phosphates forming nanocomplexes that had no influence on the cells.¹⁴⁹ In practice, all this makes the tests more complicated to conduct and the results to understand.¹⁵⁰

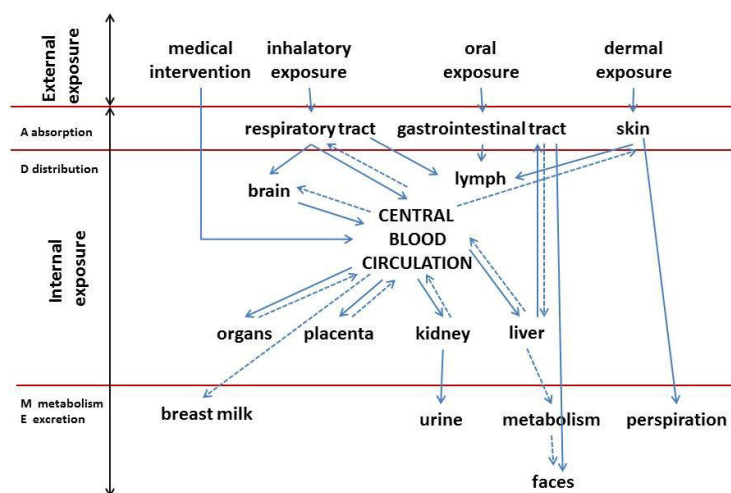


Fig. 1.21 Kinetic properties of nanoparticle in the body (ADME model). [reprinted from Hagens *et al.* 2007]

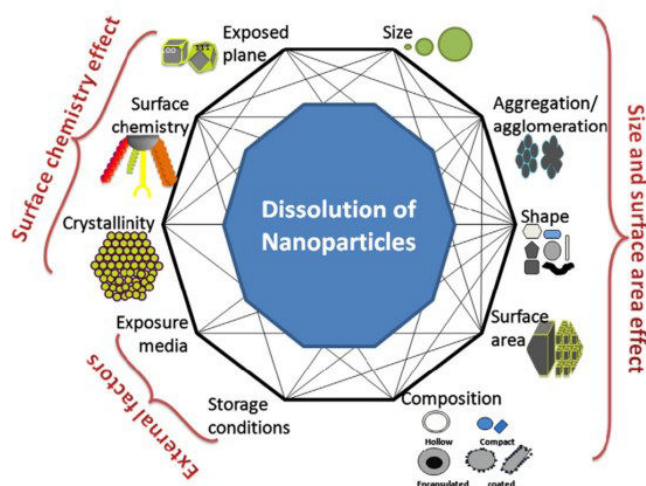


Fig. 1.22 The factors that can affect particles dissolution and the particles fate when exposed to the cell culture environment.¹⁵¹

1.6 Characterization methods for metal-organic frameworks

In this part we will describe the characterization methods which were used in the present study in order to determine physical and chemical properties of our products.

1.6.1 Scanning electron microscopy

Scanning electron microscopy (SEM) is a method which helps to take an insight into topography, morphology, chemistry, crystallography, orientation of grains in the material. With SEM, the maximum magnification can be up to 1,000,000. Using SEM, it is also possible to conduct *in situ* experiments, like reactions under the atmosphere of different gases, influence of the temperature on the sample or to image challenging samples (biological or wet structures).¹⁵²

The SEM technique is based on the signals produced when an electron beam interacts with a sample. These interactions can be divided into elastic and inelastic. The elastic interactions result from the deflection of electrons by specimen atomic nucleus or electrons from outer shell of similar energy. When the incident electrons are scattered of more than 90°, they are called backscattered electrons. These electrons escape from the surface of the sample with energy higher than 50 kV. The inelastic interactions appeared when the substantial energy of the electron beam is transferred into the specimen atoms. During the ionization of the sample, the electrons of the specimen are excited and that occurs in secondary electrons formation. The energy of these is lower than 50 kV.

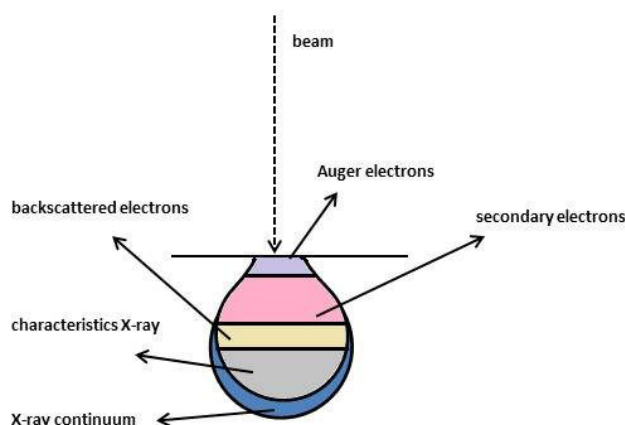


Fig. 1.23 Illustration of the signals produced by electron beam-specimen interactions.¹⁵³

The other events can cause the emission of Auger electrons, cathodoluminescence or X-ray. Briefly, the signals produced by the sample are then recognized by the detectors of the instrument and the specimen is visualized at the image (figure 1.23 and 1.24). The specimen can be observed using low vacuum, high vacuum, environmental, cryogenic or thermogenic techniques.

The preparation of the image consists of several steps: sample coating (commonly by sputtering or evaporation), microscope setup: microscope optimization and sample positioning, and final photographing. The coating procedure is really important to prevent the charge-up of the specimen surface and/or to increase the secondary electron emission. Depending on the purpose and magnification, the metals with high yield of secondary electrons used for this case are carbon, gold, gold-paladium, platinum.¹⁵⁴ The image resolution is mainly achieved by combining the magnification of the selected region of the specimen with focus and astigmatism adjustments.

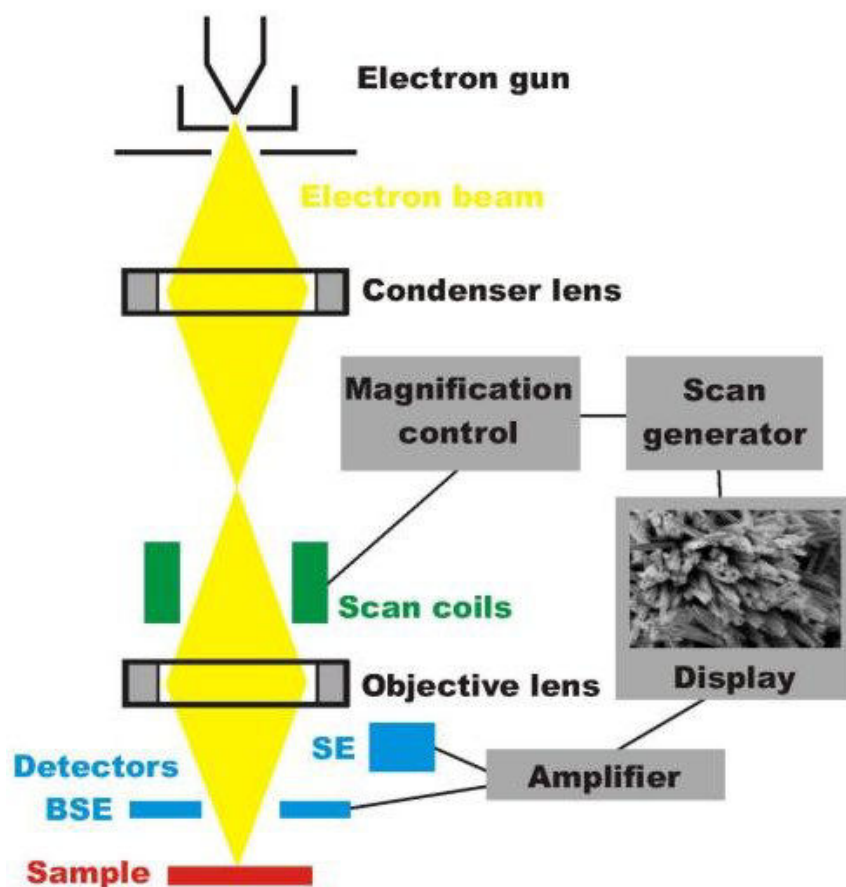


Fig. 1.24 Scheme of scanning electron microscope [from Skilbred A. W. B., Fjeld H., University of Oslo, Mena3100 presentation]

The other advantage of SEM is the possibility to generate high-energy electrons. This phenomenon gives an opportunity to test the sample by energy dispersive X-ray spectroscopy (EDX) that is also called “microanalysis”. X-ray signals are usually produced when the primary electrons of the beam cause the ejection of the electrons from the inner shell of the sample. In this state of an atom, the electrons from the outer shell are going to fill the vacancy. The K orbital is composed of only one suborbital, but in the case of L, M and N orbitals, it is more complicated because they consist of three, five and seven suborbitals, respectively. Then, an electron can move towards the suborbitals also. X-ray produced during the transition is characteristic for the element and can be detected qualitatively and quantitatively. The microanalysis can give us the percentage composition of the sample.

The instrument used for the samples characterization in this work is JEOL Scanning Electron Microscope Model JSM-6490LV. Preparation of each specimen was based on the fixation on the platinum plot and covered with Au-Pd thin layer using JEOL Fine Coat Ion Sputter JFC-1100. Observations of the samples were conducted using 10 kV of accelerating voltage, spotsize 30 μm and secondary electron (SE) detector. The instrument is accompanied with SamX NumeriX DXP-X10P digital X-ray processor for the microanalysis experiments. The EDX was conducted with 20kV accelerating voltage and spotsize 60 μm .

1.6.2 Transmission Electron Microscopy

The transmission electron microscopy technique is suitable for the thin specimens to visualize them with the magnification of 10^3 - 10^6 and it is possible to see the array of the atoms in the crystal structure. In TEM, the source of illumination is a beam of electrons of very short wavelength, emitted from a tungsten filament. The beam of electron that strikes the sample is partially transmitted through the very thin specimen. Then, it carries information about the structure of the specimen. According to the wavelike character of the electrons and the equation proposed by Louis de Broglie [1] to describe this phenomenon, we can briefly explain the principal of TEM imaging.

$$\lambda = \frac{h}{p} = \frac{h}{m \times v} \quad [1]$$

$h = 6.626 \times 10^{-34}$ Js (the Planck constant)
 p – momentum [N·s = kg·m/s]
 m – mass [kg]
 v – speed of the electron [m/s]

When the electron is emitted into vacuum from a heated filament and accelerated through a potential difference of 50 V, the speed of the electron is $\sim 4.2 \times 10^6$ m/s and $\lambda \approx 0.17$ nm. This value is similar to the atomic dimensions. The resolution of transmission electron microscope is limited by aberrations inherent in electromagnetic lenses, to about 1-2 Å.

Transmission electron microscopy analysis offers the possibility to characterize the size, morphology, and crystal phase of the framework. It was proven to be crucial for MOFs in imaging of pores¹⁵⁵ or embedded nanoparticles (figure 1.25).¹⁵⁶ This is not possible by using scanning electron microscope where we characterize mainly the surface of the materials.

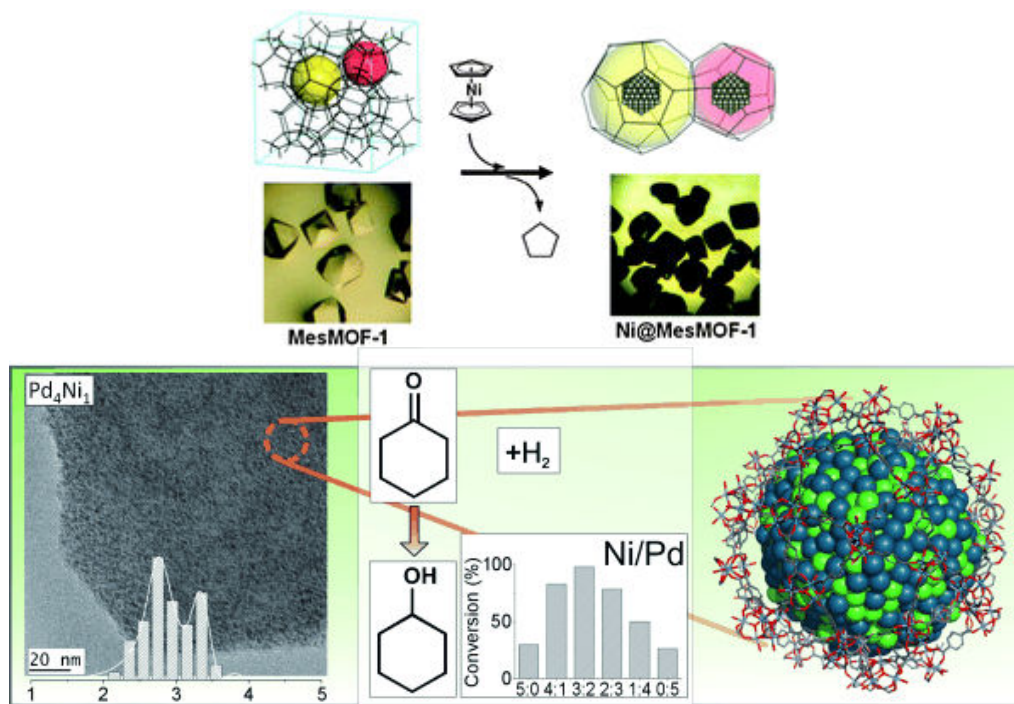


Fig. 1.25 Examples of Ni-embedded MesMOF-1 [ref. Park *et al.*, 2010] (a) and Pd/Ni@MIL-101 [ref. Hermannsdörfer *et al.*, 2012](b).

For MOFs structures, to maximally avoid damaging the framework pores, the microscopy experiments have to be conducted under liquid nitrogen environment and using an acceleration voltage of 80 kV. The applied conditions reduce the influence of electron beam that induces damage to sensitive samples. Manipulating at 80 kV improves the stability of the material and saves the frameworks pores. TEM is moreover an analytical tool when combined with X-ray microanalysis, extending from simple imaging of internal defects to a correlation of chemical composition, crystallographic and defects analysis of the materials.

In this study, we characterized the samples by using a Philips CM20 instrument and before each experiment the particles of ZIF-8 were dispersed in methanol onto a carbon film supported copper grid.

1.6.3 X-ray diffractometry

X-ray diffractometry offers the most complete tool for the visualization of the arrangement of atoms into crystalline structures. This knowledge is the base on which we build our understanding of the synthesis process, structure and properties of the analyzed sample. By using diffraction, it is possible to see the special arrangement of atoms in materials. For this purpose, an incident wave with the wavelength comparable to the spacings between atoms is concentrated on a material and a detector is moved about to register the directions and intensities of the outgoing diffracted waves.¹⁵⁷ The diffraction pattern of the material composed of the orderly fashion with defined symmetry, regular, repeating, is showing the specific peaks depending on the crystals lattice. When the material shows amorphous or disordered face, there is no peak characteristic for the lattice.

Crystals with symmetrical lattice are composed of single units cells repeated in three dimensions, showing specific array. Unit cells in the crystal are identical and then the morphology of the crystal is

determined by single cell size and shape and symmetry of the motif. The single cell is described by lengths a, b, c and angles α, β, γ . Based on the shape of the single unit cell, 14 different lattices can be constructed (figure 1.26). These lattices are called *Bravais lattices* and combined together with 32 symmetry types are giving 230 different space groups.

We can determine seven crystals systems that are later subdivided into 32 crystallographic point groups (table 1.12).

Table 1.12 Definition of crystal systems.

Crystal system	Relations	Point group
Triclinic	$a \neq b \neq c, \alpha \neq \beta \neq \gamma \neq 90^\circ$	1, $\bar{1}$
Monoclinic	$a \neq b \neq c, \alpha = \gamma, \beta \neq 90^\circ$	2, $\bar{2}$ or m, 2/m
Orthorhombic	$a \neq b \neq c, \alpha = \beta = \gamma = 90^\circ$	222, mm2, Mmm
Tetragonal	$a = b \neq c, \alpha = \beta = \gamma = 90^\circ$	4, $\bar{4}$, 4/m, 422, 4mm, $\bar{4} 2m$, 4/mmm
Rhombohedral Trigonal	$a = b = c, \alpha = \beta = \gamma \neq 90^\circ$	3, $\bar{3}$, 312, 3m, $\bar{3} m$
Hexagonal	$a = b \neq c, \alpha = \beta, \gamma = 120^\circ$	6, $\bar{6}$, 6/m, 622, 6mm, $\bar{6} m2$, 6/m mm
Cubic	$a = b = c, \alpha = \beta = \gamma = 90^\circ$	23, m $\bar{3}$, 432, $\bar{4} 3m$, m $\bar{3} m$

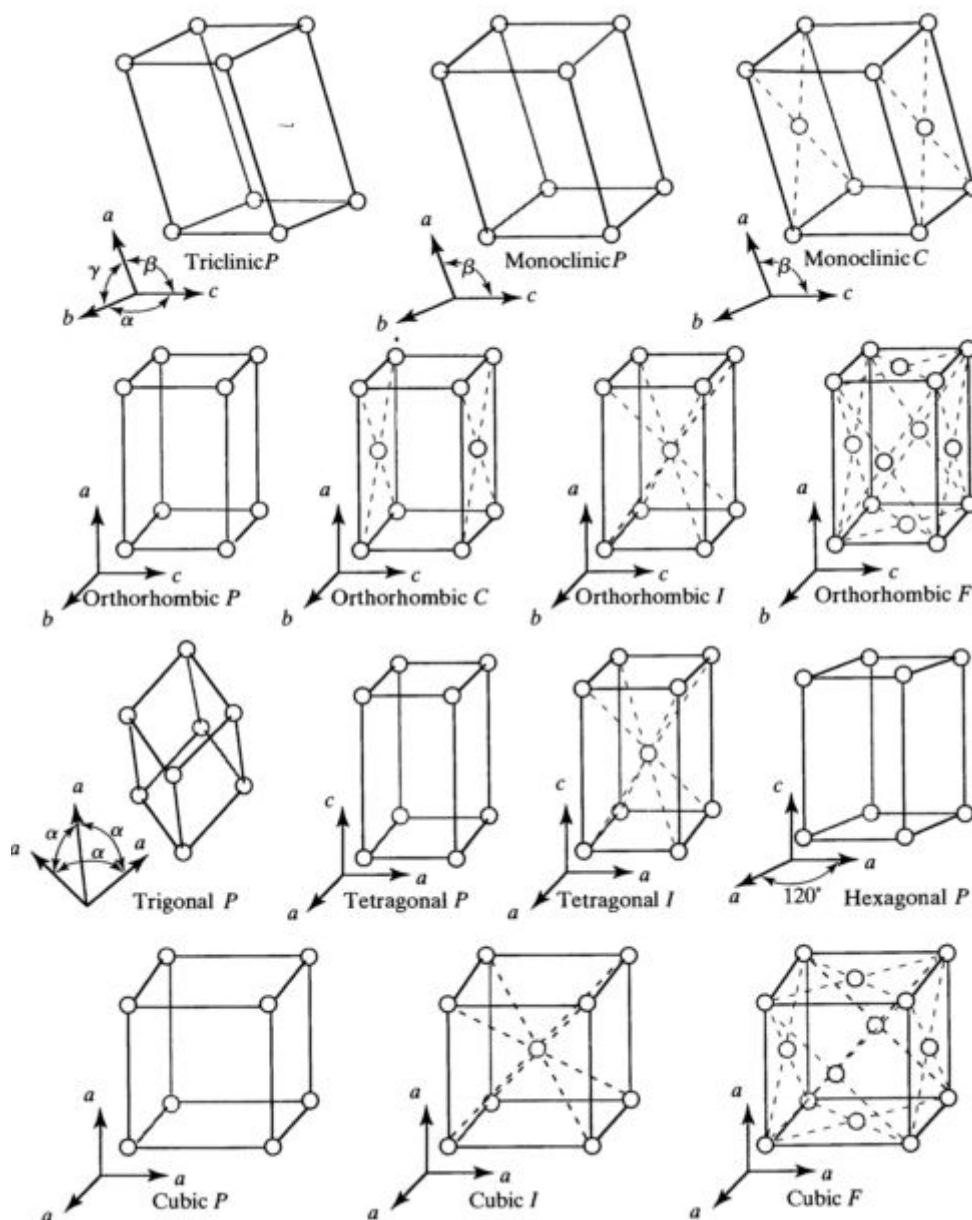


Fig. 1.26 Illustration of Bravais lattices (*P* – primitive, *I* – body-centered, *F* – face-centered, *C* – base-centered). [Ref. van Holde K. E., Johnson W. C., Ho P. S., X-Ray Diffraction (chapter 6) from Principles of Physical Biochemistry, Prentice-Hall, 1998, 242-311]

XRD diffraction pattern recorded for a material is giving informations about crystallinity and also about its purity. From XRD peaks, we can get the insight into crystals defects, such as impurities, dislocations, planar faults, internal strains, and small precipitates.

In this work, the XRD diagrams were measured using Panalytical X'Pert Pro MPD diffractometer with CuK α radiation ($\lambda = 0.15418$ nm). The X-ray powder diffraction data were collected from Panalytical AXS with a goniometer radius 240 mm, fixed divergence slit module (1/2 $^\circ$ divergence slit, 0.04 rd Soller slits) and an X'Celerator as a detector.

1.6.4 BET surface area

Metal organic frameworks are porous materials which structures consisting of voids, that are crucial for separations, gas storage, catalysis and chemical sensing. Specific surface area is described by the ratio A/m_s , [m^2/g] between absolute surface area A of the solid material and its mass m_s . For most of the materials, its usually reported as BET area determined by using adsorption isotherms of nitrogen at 77 K commonly known as the theory of Brunauer, Emmett and Teller.¹⁵⁸ The BET theory and the values obtained by combining the gas adsorption/desorption isotherms are used as the most convenient to compare different types of microporous solids. In the Brunauer-Emmett-Teller method, the gas adsorption is assumed as a multilayer formation.

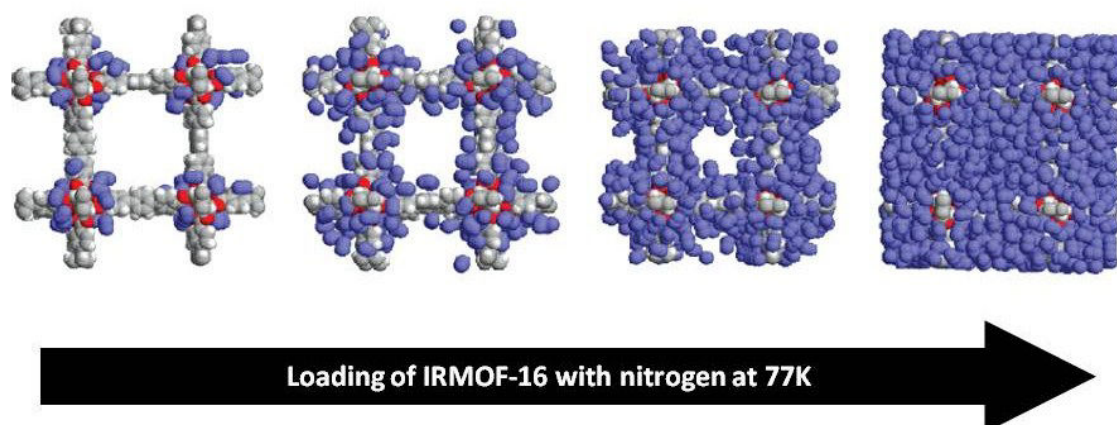


Fig. 1.27 Simulation of nitrogen loading in IRMOF-16. [ref. Walton *et al.*, 2007]

As shown on figure 1.27, the adsorption of the gas firstly occurs at the corners of the cavities. Then, the process continues among the pores freely till the framework is completely loaded with the gas. The gas is bonded with the surface by weak van der Waals forces. To apply the BET method, the gas chosen for the adsorption experiments must be adsorbed by physically, shouldn't cause structural changes of the framework, disrupt chemical bonds or interact with active sites of the material. The most common gases used for BET analysis are nitrogen, argon and krypton.

For the adsorption isotherm determination by volumetric way, known amounts of the gas are introduced stepwise into the sample cell containing the powder material previously dried and outgassed by heating under vacuum. The amount of gas adsorbed is the difference of gas admitted to the gas filling the dead volume. The dead volume is a free space in the sample cell including connections. The obtained adsorption isotherm is the function of the amount gas adsorbed (in mmol/g) and the relative pressure p/p_0 (figure 1.28).

The BET plot is given by the following equation:

$$\frac{1}{V_a(P_0/P-1)} = \frac{1}{V_m C} + \frac{C-1}{V_m C} \frac{P}{P_0} \quad [2]$$

V_a – volume of gas adsorbed at standard temperature and pressure (STP; 273.15 K and $1.013 \cdot 10^5$ Pa)
[mL]

P/P_0 – relative pressure [dimensionless]

V_m – volume of adsorbate as monolayer [mL]
 C – BET constant [dimensionless]

The BET experiments are usually performed within the range 0.05 to 0.3 in the relative pressure which corresponds to the formation of monolayer.

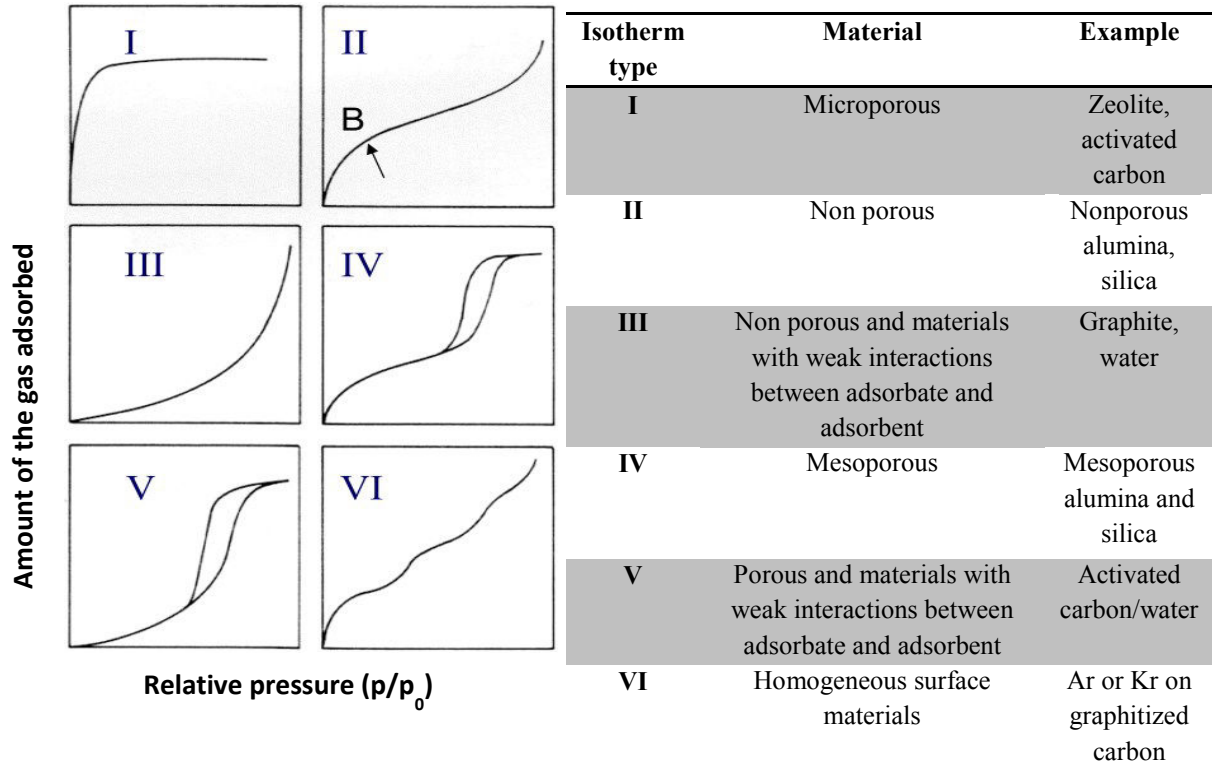


Fig. 1.28 Illustration of the adsorption isotherms and description for the different types.¹⁵⁹

The adsorption isotherm can be successfully applied for the pore volume calculations.

Pore volume

$$V_{liq} = \frac{P_a V_{ads} V_m}{RT} [3]$$

V_{liq} – volume of liquid N_2 in pore
 P_a – ambient pressure
 V_{ads} – volume of gas adsorbed
 V_m – molar volume of liquid adsorbate

The average pore size can be estimated from the pore volume taking into account the assumption of cylindrical pore geometry. Other pore geometries require some additional information from the hysteresis to choose and apply the appropriate model. In our study, we used the Horvath-Kawazoe method adapted for cylindrical pores with Saito & Foley model for determination of the size.¹⁶⁰ The Horvath-Kawazoe method is applicable for slitlike geometry and the potential energy ϵ of the

interaction for one adsorbed molecule at the distance z from an atom in the surface layer is described as:

$$\epsilon(z) = K\epsilon^*[-(\frac{\sigma}{z})^4 + (\frac{\sigma}{z})^{10}] \quad [4]$$

ϵ - potential energy of interaction [N·m/molecules]

ϵ^* - potential energy minimum [N·m/molecules]

K - coefficient

σ - distance from an atom in the surface layer at zero interaction energy [nm/molecules]

z - distance from an atom in the surface layer [nm]

This equation was modified by Everett and Powl for the cylindrical potential and expressed as:

$$\epsilon(r) = \frac{5}{2}\pi\epsilon^*[\frac{21}{32}(\frac{d_0}{r_p})^{10} \sum_{k=0}^{\infty} \alpha_k (\frac{r}{r_p})^{2k} - (\frac{d_0}{r_p})^4 \sum_{k=0}^{\infty} \beta_k (\frac{r}{r_p})^{2k}] \quad [5]$$

d - diameter of an atom [nm]

d_0 - arithmetic mean of diameters of adsorbate and adsorbent atoms [nm]

r - diameter for central axis [nm]

r_p - radius of micropore cylinder [nm]

α_k - constant $\alpha_k^{0.5} = \frac{\Gamma(-4.5)}{\Gamma(-4.5-k)\Gamma(k+1)}$

β_k - constant $\beta_k^{0.5} = \frac{\Gamma(-1.5)}{\Gamma(-1.5-k)\Gamma(k+1)}$

Γ - gamma function

Thus in case of the averaged cylindrical potential the model equation gains the form of:

$$\epsilon_{LA} = \frac{\int_0^{r_p-d_0} \epsilon(r) 2\pi r dr}{\int_0^{r_p-d_0} 2\pi r dr}$$

$$\ln\left(\frac{P}{P_0}\right) = \frac{3}{4} \frac{\pi N_{AV}}{RT} \frac{(N_A A_A - A + N_E A_E - A)}{d_0^4} \times \sum_{k=0}^{\infty} \left[\frac{1}{k+1} \left(1 - \frac{d_0}{r_p}\right)^{2k} \left\{ \frac{21}{32} \alpha_k \left(\frac{d_0}{r_p}\right)^{10} - \beta_k \left(\frac{d_0}{r_p}\right)^4 \right\} \right] \quad [6]$$

N_{AV} - Avogadro's number [molecules/mole]

N - density per unit area [molecules/cm²]

A - adsorbate

E - adsorbent

$A-A$ - adsorbate-adsorbate-adsorbent interaction

$A-E$ - adsorbate-adsorbent interaction

For BET measurements and for the investigation of textural properties of the ZIF-8 samples, we used a Micrometrics ASAP 2420 instrument. The samples were out-gassed overnight in vacuum at 40°C to remove all adsorbed substances. The nitrogen adsorption isotherms were performed at 77K and the collected data analysed using the BET method.

1.6.5 Thermogravimetric analysis

Thermogravimetric analysis (TGA) is a technique which uses heating to start some reactions and physical changes in the material. By this method, we can easily determine the fractions of volatile components present in the structure of analysed sample. The TG is monitoring the specimen mass change in the range of time and temperature. The influence of the heat causes transitions and thermal decomposition of the material and by this weight loss over increasing temperature and with the time. This is measured quantitatively and shown as endotherms, exotherms, weight-loss plots on heating or cooling. The TGA instrument is usually accompanied with FTIR or mass spectrometer to examine the products of the thermal degradation.

The instrument for TGA analysis is composed of a micro-thermobalance that measures any changes in the sample mass caused by oxygen adsorption, thermal degradation, oxidation or other heterogeneous reactions when the temperature is applied. In the standard procedure, the heating rate is of 5 °C/min starting from room temperature up to 800°C (figure 1.29). The plot of the mass with the temperature gives us the information about the events happened with the sample during the experiment.

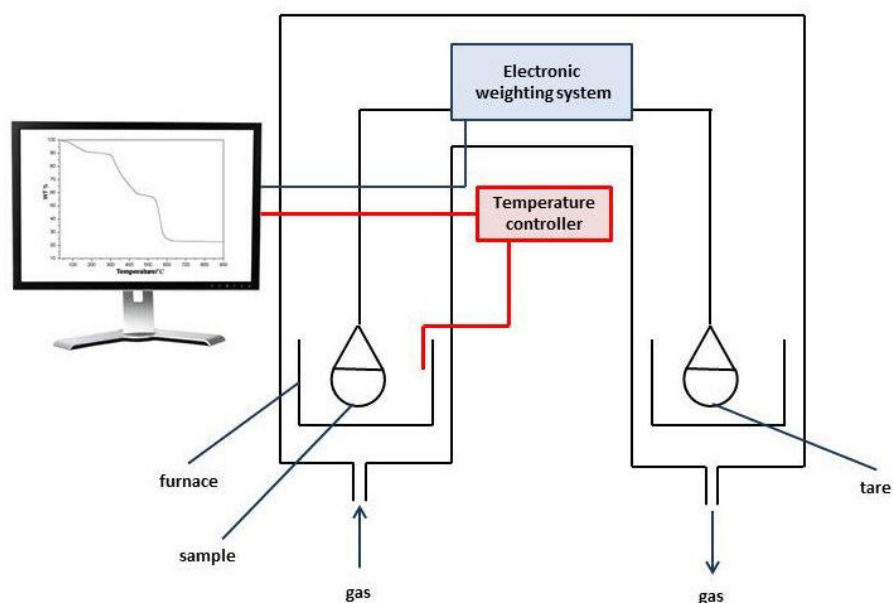


Fig. 1.29 Scheme of TGA instrument.

Usually the TGA is combined with a mass spectrometer (MS) or a Fourier transform-infrared spectrometer (FT-IR). That allows to determine the nature of the gaseous reaction products formed during the experiments.

Mass spectrometry detects substances by identifying and measuring the intensity of molecular fragment ions of different mass-to-charge ratio (m/z). Firstly, the gas molecules are ionized in the ion source. Then, the positively-charged fragments are separated according to their m/z value by a combination of magnetic and electrostatic fields. It gives the sensitive and qualitative-quantitative detection of the gaseous products.

The TGA technique allows identification of the chemical composition of mixture, because each part of the complex behaves differently in the temperature change. Moreover, TGA could be a useful tool for detection of the additives present in the matrix. Other application of the TGA method we can find in

the studies of oxidation, reduction or investigation of chemical reactions like catalysis, syntheses or polymerization.

In this study, we used TGA for ZIF-8 particles to detect the thermal stability of the framework. We used a SETARAM Setsys Evolution thermoanalyzer coupled with an Omnistar GSD301C-Pfeiffer Vacuum mass spectrometer. The samples were placed into platinum crucibles and heated in an air flow with a ramp of 5°C/min. The temperature for each sample was set from room temperature till 800°C.

1.6.6 Other techniques

1.6.6.1 Diffuse reflectance spectroscopy (DRS)

We have examined the surface structure of Cu-doped ZIF-8 samples by diffuse reflectance spectroscopy, which is highly sensitive technique for the analysis of solids and powders. This technique relies on the concentrated projection of the light from the spectrometer beam into the sample. The light is then reflected, scattered and transmitted through the material. The back reflected and diffusely scattered light is recognized by the detector. The relation of the diffuse reflectance of the sample, absorption and scattering coefficients is given by the Schuster-Kubelka-Munk remission equation:¹⁶¹

$$f(R) = \frac{(1-R_{\infty})^2}{2R_{\infty}} = \frac{K}{S} [7]$$

R_{∞} - absolute reflectance of the sample

K – molar absorption coefficient

S – scattering coefficient

This theory considers the following assumptions: the incident light diffuse, the distribution is isotropic, the particles are randomly distributed and much smaller than the layer's thickness.

We usually measure not the absolute reflectance but the reflectance relative to a standard. In a spectrum of diffuse reflectance, the ratio of the light scattered from the layer of powder sample and perfect non absorbing reference sample is plotted in a function of wavelength. For the DRS measurement, the secondary standards are mainly considered (according to the fact that perfectly reflecting diffuser doesn't exist in the nature which the reflectance is equal to 1).¹⁶² The standards commonly used in DRS studies are listed in the table 1.13.

Table 1.13 The secondary standards definition.¹⁶³

Standard	Absolute reflectance	The wavelength range
smoked MgO	close to 0.98	visible light
DIN5033 barium sulfate	0.973-0.988	380-750 nm
	>0.95	750-1500 nm
PTFE – polytetrafluoroethylene	>0.99	400-1500 nm
Spectralon	>0.95	250-2500 nm

The DRS optics are composed of integrating spheres (as called photometer spheres or Ulbricht spheres), fiber optics and mirror optics. The sphere is covered with secondary standard coating, like barium sulfate, MgO for UV-Vis measurements or PTFE for UV-Vis-NIR, Au for 800 nm to MIR analyses.

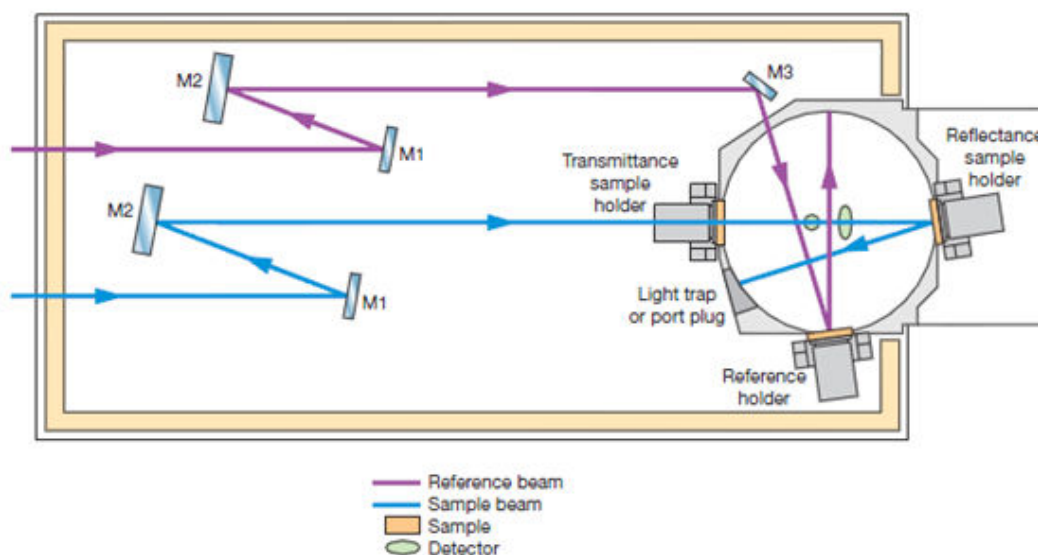


Fig. 1.30 Optical design of the integrating sphere (Perkin Elmer instrumentation).

The specimen is placed in front of the sample beam light window. The beam is directed at the sample and the light reflected from the sample is collected on the detector. When using a sphere with a reference holder, the second beam is striking the standard. The obtained value of the reflectance is the relative reflectance with respect to the reflectance of the reference standard powder (figure 1.30).

When light is directed at the sample at an angle of 0° , specular reflected light exits the integrating sphere and is not detected. As a result, only diffuse reflected light is measured.

The DRS technique is commonly used to determine the bandgaps of semiconducting materials.

1.6.6.2 Superconducting quantum interference device SQUID

Magnetism is a physical phenomenon mediated by a magnetic field. The principal of magnetism is found in the orbital and spin motions of electrons and how the electrons interact with one another. The description of the material magnetic properties is given by their response when exposed to the

magnetic fields. The magnetization (M), flux density (B) and applied magnetic field are presented by the following equation:

$$B = H + 4\pi M \text{ [8]}$$

B- flux density [G] or [T] ($1 \text{ G} = 10^{-4} \text{ T}$)

H – applied magnetic field [Oe] or [A/m]

M – magnetization, usually given in electromagnetic units (emu) per gram, cm^2 , mole or atom

The amount of current induced by the sample is related to the magnetic moment of the material. The relations between the magnetization (M) changes with the temperature (T) and applied magnetic field (H) are necessary to understand the magnetism presented by the material. The most important types of magnetism are paramagnetism, diamagnetism and ferromagnetism.¹⁶⁴

For the material with diamagnetic properties, this relation is also linear and reversible but the slope is negative (fig. 1.31 (a)). In paramagnets, the plot M(H) is linear, reversible and the line intersects zero (fig. 1.31 (b)). For ferromagnets, the plot is not linear and not reversible (magnetic hysteresis) and the magnetization saturation is observed (fig. 1.31 (c)).

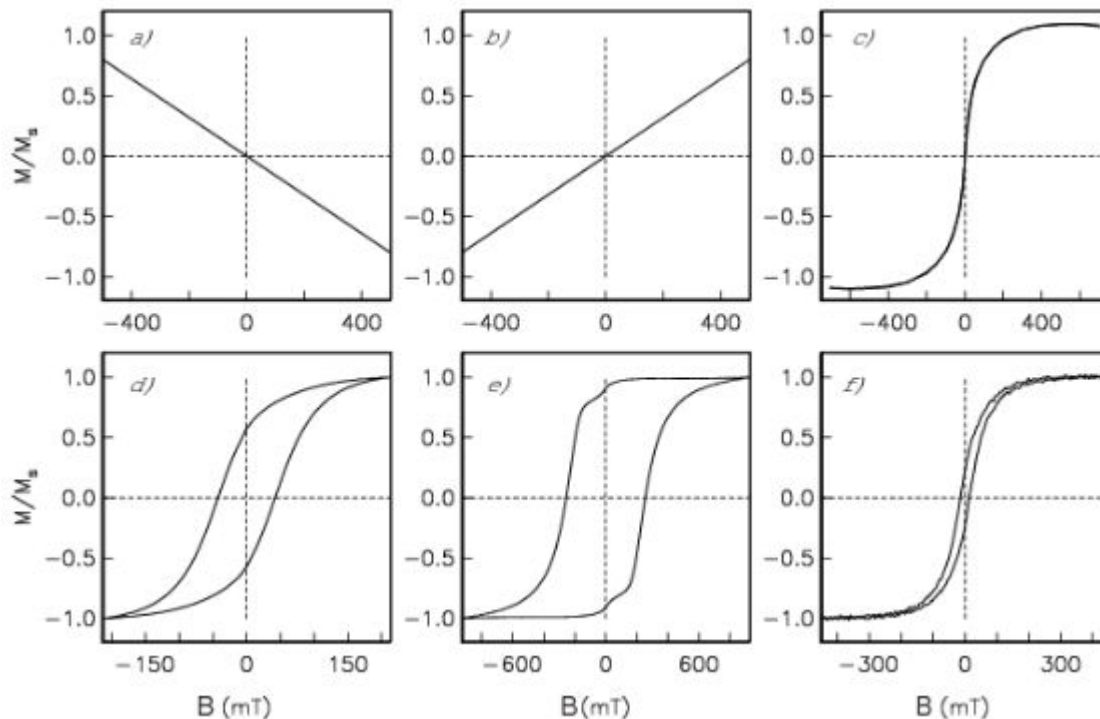


Fig. 1.31 Hysteresis loops for diamagnetic (a), paramagnetic (b), superparamagnetic (c), uniaxial, single domain (d), magnetocrystalline, single domain (e), “pseudo-single domain”(f) materials. [Tauxe L. et al., 2014]¹⁶⁵

In ferromagnetic kind of material, the existence of irreversibility is shown by zero-field-cooled/field-cooled (ZFC/FC) measurements.¹⁶⁶ For this experiment, the sample is first cooled to the lowest temperature in $H = 0$. Once stabilized, the magnetic field is applied and the magnetic moment of the material is measured in relation to increased temperature. This is ZFC part. Then, the sample is cooled in the same field to the lowest temperature and once again presented as a function of temperature (FC part) (figure 1.32). Characteristic separation of the two curves is the evidence of the irreversibility.

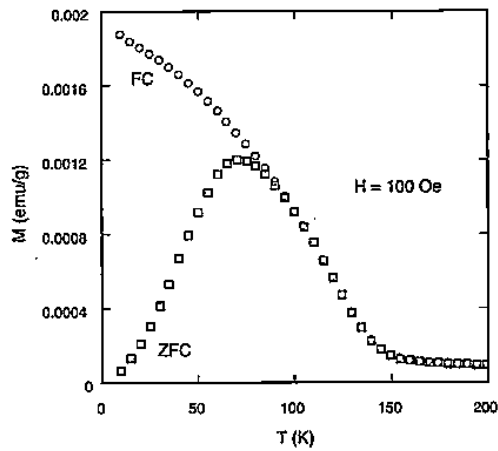


Fig. 1.32 Magnetization as a function of temperature for ferromagnetic material. (ref. McElfresh M., 1994)

In this study, to test magnetic properties of the $\text{Fe}_3\text{O}_4@\text{ZIF-8}$ composite, we used vibrating sample magnetometer.

SQUID measurement is presenting the strength of the magnetic moment produced by a magnetized sample. Briefly, the sample moves through superconducting, balanced detection coils (gradiometers), at a specific temperature and in homogenous magnetic field. The magnetic moment of the sample induces an electric current in the detection coils. This current produced by the sample is not suppressed, because the coils, the connecting wires and the SQUID input coil compose a closed superconducting loop (figure 1.33).¹⁶⁷ A small change in magnetic flux in the detection coils induces a comparative change in the persistent current in the detection circuit. The flux integration is prepared when the sample is moved from one side of the gradiometer to the other. Then the signal is transmitted to the SQUID by a flux transformer. The detected current is converted into voltage and the signal from the sample is proportional to the magnetic moment.

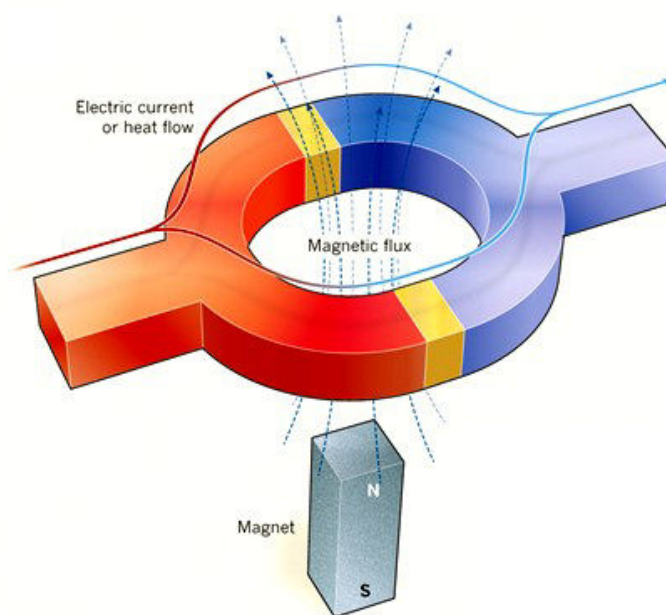


Fig. 1.33 SQUID superconducting loop (two Josephson junctions/insulating barriers responsible for the loop is no longer quantized) – two yellow blocks — sandwiched between the two superconductors (red and blue).

The results from this experimental setup are shown in the chapter 2.

1.7 Techniques for cytotoxicity evaluation

1.7.1 MTS assay

The most common methods used for the evaluation of cells viability are colorimetric assays: MTT, MTS, resazurin (Alamar Blue), 5-bromo-2-deoxyuridine, protease-based or luminogenic ATP-assays.^{168,169} We used MTS method to determine the amount of viable cells of A549 and IHK cultures after being exposed to the ZIF-8 samples. The mechanism of this assay is based on the reduction of MTS compound 3-(4,5-dimethylthiazol-2-yl)-5-(3-carboxymethoxyphenyl)-2-(4-sulfophenyl)-2H-tetrazolium into MTS formazan (figure 1.34) by living cells. The quantity of the formazan product is proportional to the number of metabolically active cells.¹⁷⁰ The formazan can be detected by using UV-visible spectroscopy monitoring the peak at 490 nm.

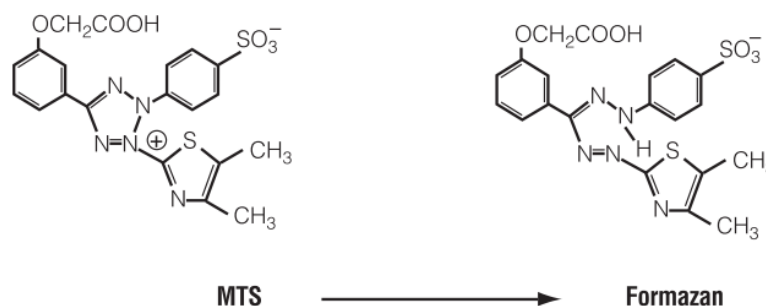


Fig. 1.34 Reduction of MTS reagent into colorful formazan product.

1.7.2 Fluorescence-activated cell sorting

Flow cytometry is a technique that is able to analyze multiple physical characteristics of specimen, like cells, when they flow in a fluid stream through a beam of light. These cells properties that can be considered are size, granularity, complexity, and fluorescence intensity. A flow cytometer is composed of the following elements (figure 1.35):

1. fluidic system that provides the particles in a stream for the interrogation of laser beam,
2. optics system which is made of lasers to illuminate the particles and filters to direct the signal to the detectors,
3. electronic system that collects the detected light signals (events) and transform in an electronic information, then reported by the computer.

The flow cytometer can be programmed with sort gate system which is applied for capturing only the cells with preselected characteristics, like intensity of the fluorescence. The signals can be quantitatively measured according to the response from specific cells.

In our study, we used fluorescence-activated cell sorting by flow cytometry for the determination of reactive oxygen species produced when the IHK and A549 cells were in contact with ZIF-8 samples. The method used for this evaluation was based on a fluorometric assay - the oxidation of 2',7'-dichlorodihydrofluorescein diacetate (H_2 -DCF-DA) in the cells affected with ROS produced by the ZIF-8 particles. Briefly, the oxidation of intracellular entrapped H_2 -DCF-DA requires removal of the diacetate group by esterases. In the second step, the activated H_2 -DCF is converted by H_2O_2 and peroxides to the fluorescent derivative 2',7'-dichlorofluorescein (DCF). The cells become fluorescent and can be analysed by fluorescence-activated cell sorting (FACS). However, for the experiments appropriate controls have to be designed. In order to measure the response from specific cells, we related the results to the chosen references.

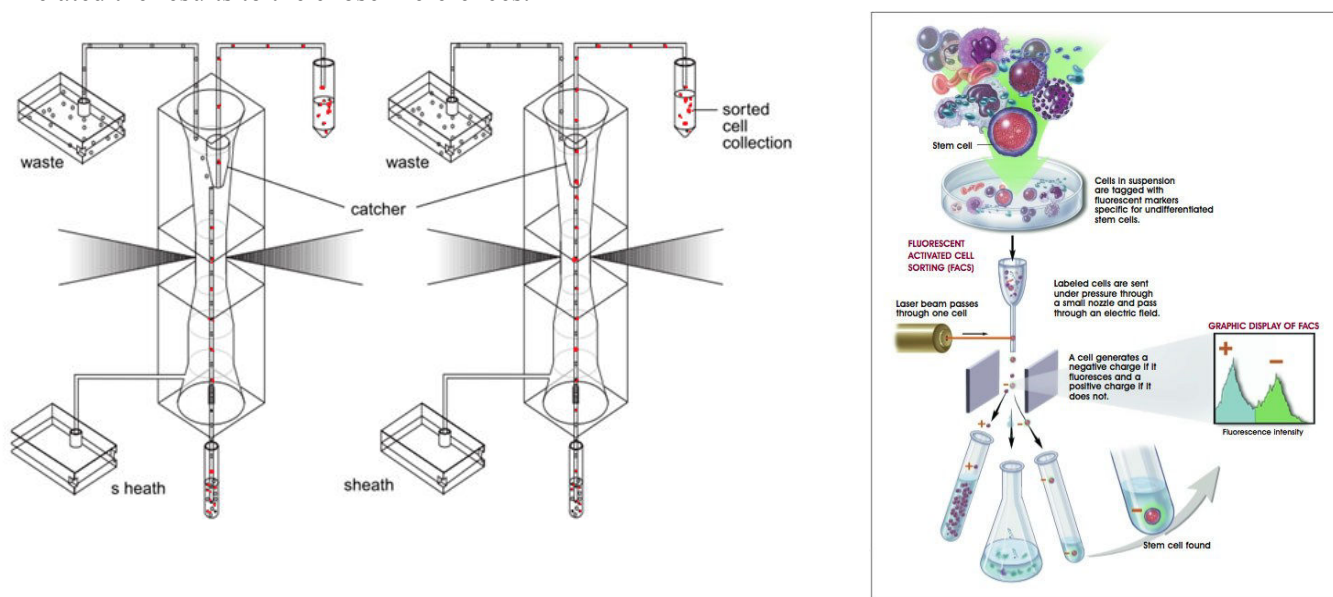


Fig. 1.35 Principal of the fluorescence-activated cell sorting and an example on STEM cell sorting.^{171,172}

1.8 References

- (1) (a)Yaghi O. M., Li H., *J. Am. Chem. Soc.* **1995**, 117, 10401-10402; (b)Yaghi O. M., Li G., Li H., *Nature*, **1995**, 378, 703-706
- (2) Bailar, J. C. Jr., *Prep. Inorg. React.* **1964**, 1, 1-27
- (3) Chui S. S.-Y., Lo S. M.-F., Charmant J. P. H., Orpen A. G., Williams I. D., *Science*, **1999**, 283, 1148-1150
- (4) Li H., Eddaoudi M., O’Keeffe M., Yaghi O. M., *Nature*, **1999**, 402, 276-279
- (5) Serre C., Millange F., Thouvenot C., Nogues M., Marsolier G., Louer D., Férey G., *J. Am. Chem. Soc.*, **2002**, 124, 13519-13526
- (6) Férey G., Latroche M., Serre C., Millange F., Loiseau T., Percheron-Guégan A., *Chem. Commun.*, **2003**, 2976-2977
- (7) Lebedeu O. I., Millange F., Serre C., Van Tendeloo G., Férey G., *Chem. Mater.*, **2005**, 17, 6525-6527
- (8) Park K. S., Ni Z., Cote A. P., Choi J. Y., Huang R., Uribe-Romo F. J., Chae H. K., O’Keeffe M., Yaghi O. M., *PNAS*, **2006**, 103, 10186-10191
- (9) Cavka J. H., Jakobsen S., Olsbye U., Guillou N., Lamberti C., Bordiga S., Lillerud K. P., *J. Am. Chem. Soc.*, **2008**, 130, 13850-13851
- (10) Lin X., Telepeni I., Blake A. J., Dailly A., Brown C. M., Simmons J. M., Zoppi M., Walker G. S., Thomas K. M., Mays T. J., Hubberstey P., Champness N. R., Schröder M., *J. Am. Chem. Soc.*, **2009**, 131, 2159-2171
- (11) Au J., Geib S. J., Rosi N. L., *J. Am. Chem. Soc.*, **2010**, 132, 38-39
- (12) Modrow A., Zargarani D., Herges R., Stock N., *Dalton Trans.*, **2011**, **40**, 4217-4222
- (13) Caskey S. R., Wong-Foy A. G., Matzger A. J., *J. Am. Chem. Soc.*, **2008**, 130, 10870-10871
- (14) Glover T., Peterson G., Shindler B., Britt D., Yaghi O. M., *Chem. Eng. Sci.*, **2011**, 66, 163-170
- (15) Allendorf M. D., Stavila V., *CrystEngComm.*, **2015**, 17, 229-246
- (16) Batten S. R., Champness N. R., Chen X.-M., Garcia-Martinez J., Kitagawa S., Öhrström L., O’Keeffe M., Suh M. P., Reedijk J., *Pure Appl. Chem.*, **2013**, 1715-1724
- (17) Cheetham A. K., Rao C. N. R., Feller R. K., *Chem. Commun.*, 2006,4780-4795
- (18) Allendorf M. D., Stavila V., *CrystEngComm.*, **2015**, 17, 229-246
- (19) Eddaoudi M., Moler D. B., Li H., Chen B., Reineke T. M., O’Keeffe M., Yaghi O. M., *Acc. Chem. Res.*, **2001**, 34, 319-330
- (20) Zhang M. Z., Bosch M., Gentle III T., Zhou H.-C., *CrystEngComm.*, **2014**, 16, 4069-4083
- (21) Furukawa H., Müller U., Yaghi O. M., *Angew. Chem., Int. Ed.*, **2015**, 54, 3417-3430
- (22) Bosch M., Zhang M., Feng D., Yuan S., Wang X., Chen Y.-P., Zhou H.-C., *APL Materials*, **2014**, 2, 124103, 1-5
- (23) Lin X.-M., Li T.-T., Wang Y.-W., Zhang L., Su C.-Y., *Chemistry – An Asian Journal*, **2012**n 7, 2796-2804
- (24) Lei J., Qian R., Ling P., Cui L., Ju H., *Trend. Anal. Chem.*, **2014**, 58, 71-78
- (25) Cohen S. M., *Chem. Sci.*, **2010**, 1, 32-36
- (26) Deria P., Mondloch J. E., Karagiari O., Bury W., Hupp J. T., Farha O. K., *Chem. Soc. Rev.*, **2014**, 43, 5896-5912
- (27) Kim M., Cahill J. F., Fei H., Prather K. A., Cohen S. M., *J. Am. Chem. Soc.*, **2012**, 134, 18082-18088
- (28) Karagiari O., Vermeulen N. A., Klet R. C., Wang T. C., Moghadam P. Z., Al-Juaid S. S., Stoddart J. F., Hupp J. T., Farha O. K., *Inorg. Chem.*, **2015**, 54, 1785-1790

-
- (29) Karagiari O., Lalonde M. B., Buy W., Sarjeant A. A., Farha O. K., Hupp J. T., *J. Am. Chem. Soc.*, **2012**, 134, 18790-18796
- (30) Song X., Jeong S., Kim D., Lah M. S., *CrystEngComm*, **2012**, 14, 5453-5756
- (31) Song X., Kim T. K., Kim H., Kim D., Jeong S., Moon H. R., Lah M. S., *Chem. Mater.*, **2012**, 24, 3065-3073
- (32) Juan-Alcañiz J., Gascon J., Kapteijn F., *J. Mater. Chem.*, **2012**, 22, 10102-10118
- (33) Park H. J., Suh M. P., *Chem. Sci.*, **2013**, 4, 685-690
- (34) Müller M., Devaux A., Yang C.-H., De Cola L., Fischer R. A., *Photochem. Photobiol. Sci.*, **2010**, 9, 846-853
- (35) Salomon W., Roch-Marchal C., Mialane P., Rouschmeyer P., Serre C., Haouas M., Taulelle F., Yang S., Ruhlmann L., Dolbecq A., *Chem. Commun.*, **2015**, 51, 2972-2975
- (36) Rösler C., Fischer R. A., *CrystEngComm*, **2015**, 17, 199-217
- (37) Domingos S., André V., Queresma S., Martins I. C. B., Minas da Piedade M. F., Duart M. T., *J. Pharm Pharmacol.*, **2015**, 67, 830-846
- (38) Zhang W., Liu Y., Lu G., Wang Y., Li S., Cui C., Wu J., Xu Z., Tian D., Huang W., DuCheneu J. S., Wei W. D., Chen H., Yang Y., Huo F., *Adv. Mater.*, **2015**, 27, 2923-2929
- (39) Zhu Q.-L., Xu Q., *Chem. Soc. Rev.*, **2014**, 43, 5468-5512
- (40) Zhang H., Zou R., Zhao Y., *Coordin. Chem. Rev.*, **2015**, 292, 74-90
- (41) Yang F., Yang C.-X., Yan X.-P., *Talanta*, **2015**, 137, 136-142
- (42) Fletcher A. J., Thomas K. M., Rosseinsky M. J., *J. Solid State Chem.*, **2005**, 178, 2491-2510
- (43) Farha O. K., Eryazici I., Jeong N. C., Hauser B. G., Wilmer C. E., Sarjeant A. A., Snurr R. Q., Nguyen S. T., Yazaydin A. Ö., Hupp J. T., *J. Am. Chem. Soc.*, **2012**, 134, 15016-15021
- (44) Peralta D., Chaplais G., Simon-Masseron A., Barthlet K., Chizallet C., Quineaud A.-A., Pirngruber G. D., *J. Am. Chem. Soc.*, 2012, 134, 8115-8126
- (45) Pérez-Mayoral E., Čejka J., *ChemCatChem*, **2011**, 3, 157-159
- (46) Si X., Jiao C., Li F., Zhang J., Wang S., Lin S., Li Z., Sun L., Xu F., Gabelica Z., Schick C., *Energy Environ. Sci.*, 2011, 4, 4522-4527
- (47) Mu B., Li F., Huang Y., Walton K. S., *J. Mater. Chem.*, **2012**, 22, 10172-10178
- (48) Sarkisov L., Martin R. L., Haranczyk M., Smit B., *J. Am. Chem. Soc.*, **2014**, 136, 2228-2231
- (49) Kuppler R. J., Timmons D. J., Fang Q.-R., Li J.-R., Makal T. A., Young M. D., Yuan D., Zhao D., Zhuang W., Zhou H.-C., *Coord. Chem. Rev.*, **2009**, 253, 3042-3066
- (50) Wu H., Yildirim T., Zhou W., *J. Phys. Chem. Lett.*, **2013**, 4, 925-930
- (51) Van de Voorde B., Stassen I., Bueken B., Vermoortele F., De Vos D., Ameloot R., Tan J.-C., Bennett T. D., *J. Mater. Chem. A*, **2015**, 3, 1737-1742
- (52) Low J. J., Benin A. I., Jakubczak P., Abrahamian J. F., Faheem S. A., Willis R. R., *J. Am. Chem. Soc.*, **2009**, 131, 15834-15842
- (53) Chen B., Yang Z., Zhu Y., Xia Y., *J. Mater. Chem. A*, **2014**, 2, 16811-16831
- (54) Wittmann T., Siegel R., Reimer N., Milius W., Stock N., Senker J., *Chem. Eur. J.*, **2015**, 21, 314-323
- (55) Allendorf M. D., Bauer C. A., Bhakta R. K., Houk R. J. T., *Chem. Soc. Rev.*, **2009**, 38, 1330-1352
- (56) Campagnol N., Rezende Souza E., De Vos D. E., Binnemans K., Fransaer J., *Chem. Commun.*, **2014**, 50, 12545-12547
- (57) Feng P. L., Perry IV J. J., Nikodemski S., Jacobs B. W., Meek S. T., Allendorf M. D., *J. Am. Chem. Soc.*, **2010**, 132, 15487-15489
- (58) Shen C.-C., Chen W.-T., Liu R. S., *Dalton Trans.*, **2012**, 41, 11885-11888
- (59) Lin X., Gao G., Zheng L., Chi Y., Chen G., *Anal. Chem.*, **2014**, 86, 1223-1228

-
- (60) Kurmoo M., *Chem. Soc. Rev.*, **2009**, 38, 1353-1379
- (61) Ricco R., Malfatti L., Takahashi M., Hill A. J., Falcaro P., *J. Mater. Chem. A*, **2013**, 1, 13033-13045
- (62) Czaja A. U., Trukhan N., Müller U., *Chem. Soc. Rev.*, **2009**, 38, 1284-1293
- (63) Furukawa H., Ko N., Go Y. B., Aratani N., Choi S. B., Choi E., Yazaydin A. Ö., Snurr R. Q., O’Keffe M., Kim J., Yaghi O. M., *Science*, **2010**, 329, 424-428
- (64) Farha O. K., Yazaydin A. Ö., Eryazici I., Malliakas C. D., Hauser B. G., Kanatzidis M. G., Nguyen S. T., Snurr R. Q., Hupp J. T., *Nat. Chem.*, **2010**, 2, 944-948
- (65) Ma S., Sun D., Simmons J. M., Collier C. D., Yuan D., Zhou H.-C., *J. Am. Chem. Soc.*, **2008**, 130, 1012-1016
- (66) Yilmaz B., Trukhan N., Müller U., *Chin. J. Catal.*, **2012**, 33, 3-10
- (67) Tanabe K. K., Cohen S. M., *Inorg. Chem.*, **2010**, 49, 6766-6774
- (68) Wen L., Su J., Wu X., Cai P., Luo W., Cheng G., *International Journal of Hydrogen Energy*, **2014**, 39, 17129-17135
- (69) Zhao Y., Liu M., Fan B., Chen Y., Lv W., Lu N., Li R., *Catalysis Communication*, **2014**, 57, 119-123
- (70) Bhattacharjee S., Kim J., Ahn W.-S., *J. Nanosci. Nanotechnol.*, **2014**, 14, 2546-2552
- (71) Van Vu T., Kosslich H., Schulz A., Harloff J., Paetzold E., Lund H., Kragl U., Schneider M., Fulda G., *Micropor. Mesopor. Mat.*, **2012**, 154, 100-106
- (72) Zhen W., Li B., Lu G., Ma J., *Chem. Commun.*, **2015**, 51, 1728-1731
- (73) Zahmakiran M., *Dalton Trans.*, **2012**, 41, 12690-12696
- (74) Qi Y., Luan Y., Yu J., Peng X., Wang G., *Chem. Eur. J.*, **2015**, 21, 1589-1597
- (75) Opanasenko M., *Catalysis Today*, **2015**, 243, 2-9
- (76) Mitchell L., Williamson P., Ehrlichová B., Anderson A. E., Seymour V. R., Ashbrook S. E., Acerbi N., Daniels L. M., Walton R. I., Clarke M. L., Wright P. A., *Chem. Eur. J.*, **2014**, 20, 17185-17197
- (77) Kholdeeva O. A., Skobelev I. Y., Ivanchikova I. D., Kovalenko K. A., Fedin V. P., Sorolein A. B., *Catal. Today*, **2014**, 238, 54-61
- (78) Zang Y., Shi J., Zhao X., Kong L., Zhang F., Zhong Y., *React. Kinet. Mech. Catal.*, **2013**, 109, 77-89
- (79) Zhu W., He C., Wu X., Duan C., *Inorg. Chem. Commun.*, **2014**, 39, 83-85
- (80) Valvekens P., Vandichel M., Waroquier M., Van Speybroeck V., De Vos D., *J. Catal.*, **2014**, 317, 1-10
- (81) Gascon J., Aktay U., Hernandez-Alonso M. D., van Klink G. P. M., Kapteijn F., *J. Catal.*, **2009**, 261, 75-87
- (82) Lun D. J., Waterhouse G. I. N., Telfer S. G., *J. Am. Chem. Soc.*, **2011**, 133, 5806-5809
- (83) Lalonde M. B., Farha O. K., Scheidt K. A., Hupp J. T., *ACS Catal.*, **2012**, 2, 1550-1554
- (84) Roberts J. M., Fini B. M., Sarjeant A. A., Farha O. K., Hupp J. T., Scheidt K. A., *J. Am. Chem. Soc.*, **2012**, 134, 3334-3337
- (85) Barea E., Montoro C., Navarro J. A. R., *Chem. Soc. Rev.*, **2014**, 43, 5419-5430
- (86) Guo X., Huang H., Ban Y., Yang Q., Xiao Y., Li Y., Yang W., Zhong C., *J. Membrane Sci.*, **2015**, 478, 130-139
- (87) Chen Z., Xiang S., Arman H. D., Mondal J. U., Li P., Zhao D., Chen B., *Inorg. Chem.*, **2011**, 50, 3442-3446
- (88) Kim P.-J., You Y.-W., Park H., Chang J. S., Bae Y.-S., Lee C.-H., Suh J. K., *Chem. Eng. J.*, **2015**, 262, 683-690

-
- (89) Sani N. A. A., Lau W. J., Ismail A. F., *RSC Adv.*, **2015**, 5, 13000-13010
- (90) Finsy V., Kirschhock C. E. A., Vedts G., Maes M., Alaerts L., De Vos D. E., Baron G. V., Denayer J. F. M., *Chem. Eur. J.*, **2009**, 15, 7724-7731
- (91) Jiang H.-L., Liu B., Akita T., Haruta M., Sakurai H., Xu Q., *J. Am. Chem. Soc.*, **2009**, 131, 11302-11303
- (92) Keskin S., Kizilel S., *Ind. Eng. Chem. Res.*, **2011**, 50, 1799-1812
- (93) An J., Fraha O. K., Hupp J. T., Pohl E., Yeh J. I., Rosi N. L., *Nat. Commun.*, **2012**, 3:604, 1-6
- (94) Bernini M. C., Fairen-Jimenez D., Pasinetti M., Ramirez-Pastor A. J., Snurr R. Q., *J. Mater. Chem. B*, **2014**, 2, 766-774
- (95) Tamames-Tabar C., Imbuluzqueta E., Guillon N., Serre C., Miller S. R., Elkaïm E., Horcajada P., Blanco-Prieto M. J., *CrystEngComm.*, **2015**, 17, 456-462
- (96) Lin X., Zhang Q., Chen J., Kong X., Long L.-S., Wang C., Lin W., *RSC Adv.*, **2015**, 5, 2914-2919
- (97) Liu D., Lu K., Poon C., Lin W., *Inorg. Chem.*, **2014**, 53, 1916-1924
- (98) Chen B., Yang Z., Zhu Y., Xia Y., *J. Mater. Chem. A*, **2014**, 2, 16811-16831
- (99) Mravec D., Hudec J., Janotka I., *Chem. Pap.*, **2005**, 59, 62-69
- (100) Pimentel B. R., Parulkar A., Zhou E., Brunelli N. A., Lively R. P., *ChemSusChem.*, **2014**, 7, 3202-3240
- (101) Torad N. L., Hu M., Kamachi Y., Takai K., Imura M., Naito M., Yamauchi Y., *Chem. Commun.*, **2013**, 49, 2521-2523
- (102) Pan Y., Liu Y., Zeng G., Zhao L., Lai Z., *Chem. Commun.*, **2011**, 47, 2071-2073
- (103) Liu S., Xiang Z., Hu Z., Zheng X., Cao D., *J. Mater. Chem.*, **2011**, 21, 6649-6653
- (104) Kida K., Okita M., Fujita K., Tanaka S., Miyake Y., *CrystEngComm*, **2013**, 15, 1794-1801
- (105) Nune S. K., Thallapally P. K., Dohnalkova A., Wang C., Liu J., Exarhos G. J., *Chem. Commun.*, **2010**, 46, 4878-4880
- (106) Pan Y., Heryadi D., Zhou F., Zhao L., Lestari G., Su H., Lai Z., *CrystEngComm.*, **2011**, 13, 6937-6940
- (107) Venna S. R., Jasinski J. B., Carreon M. A., *J. Am. Chem. Soc.*, **2010**, 132, 18030-18033
- (108) Zhang X., Dong C., Zapfen J. A., Ismathullakhan S., Kang Z., Jie J., Zhang X., Chang J. C., Lee C.-S., Lee S.-T., *Angew. Chem. Int. Ed.*, **2009**, 48, 9121-9123
- (109) a) Cravillon J., Nayuk R., Springer S., Feldhoff A., Huber K., Wiebcke M., *Chem. Mater.*, **2011**, 23, 2130-2141; b) Cravillon J., Schroeder A., Bux H., Rothkirch A., Caro J., Wiebcke M., *CrystEngComm*, **2012**, 14, 492-498; c) Cravillon J., Münzer S., Lohmeier S.-J., Feldhoff A., Huber K., Wiebcke M., *Chem. Mater.*, **2009**, 21, 1410-1412
- (110) Kida K., Fujita K., Shimada T., Tanaka S., Miyake Y., *Dalton Trans.*, **2013**, 42, 11128-11135
- (111) Vystavel T., Palasantzas G., Koch S. A., De Hosson J. T. M., *Appl. Phys. Lett.*, **2003**, 83, 3909-3911
- (112) Wang C. M., Baer D. R., Amonette J. E., Engelhard M. H., Qiang Y., Antony J., *Nanotechnology*, **2007**, 18, 255603, 1-7
- (113) Moh P. Y., Brenda M., Anderson M. W., Attfield M. P., *CrystEngComm.*, **2013**, 15, 9672-9678
- (114) Lim I. H., Schrader W., Schüth F., *Chem. Mater.*, **2015**, 27, 3088-3095
- (115) Wu X.-F., *Tetrahedron Lett.*, **2012**, 53, 6123-6126
- (116) Wu X.-F., *Tetrahedron Lett.*, **2012**, 53, 3397-3399
- (117) Chizallet C., Lazare S., Bazer-Bachi D., Bonnier F., Lecocq V., Soyer E., Quoineaud A.-A., Bats N., *J. Am. Chem. Soc.*, **2010**, 132, 12365-12377
- (118) Miralda C. M., Macias E. E., Zhu M., Ratnasamy P., Carreon M. A., *ACS Catal.*, **2012**, 2, 180-183

-
- (119) Nguyen L. T. L., Le K. K. A., Phan N. T. S., *Chin. J. Catal.*, **2012**, 33, 688-696
- (120) Nguyen L. T. L., Le K. K. A., Phan N. T. S., *ACS Catal.*, **2011**, 1, 120-127; Jin R., Bian Z., Li J., Ding M., Gao L., *Dalton Trans.*, **2013**, 42, 3936-3940
- (121) Dai Y., Johnson J. R., Karvan O., Sholl D. S., Koros W. J., *J. Membrane Sci.*, **2012**, 401-402, 76-82
- (122) Pan Y., Lai Z., *Chem. Commun.* **2011**, 47, 10275-10277
- (123) Zhang C., Lively R. P., Zhang K., Johnson J. R., Karvan O., Koros W. J., *J. Phys. Chem. Lett.*, **2012**, 3, 2130-2134
- (124) Jiang J.-Q., Yang C.-X., Yan X.-P., *ACS Appl. Mater. Interfaces*, **2013**, 5, 9837-9842
- (125) Yan F., Liu Z. Y., Chen J.-L., Sun X.-Y., Li X.-J., Su M.-X., Li B., Di B., *RSC Adv.*, **2014**, 4, 33047-33054
- (126) Lin K.-Y. A., Chang H.-A., *Water Air Soil Pollut.*, **2015**, 226, 1-17
- (127) Wu Y.-n., Zhou M., Zhang B., Wu B., Li J., Qiao J., Guan X., Li F., *Nanoscale*, **2014**, 6, 1105-1112
- (128) Jian M., Lin B., Zhang G., Lin R., Zhang X., *Colloid Surface A*, **2015**, 465, 67-76
- (129) Khan N. A., Jung B. K., Hasan Z., Jhung S. H., *J. Hazard. Mater.*, **2015**, 282, 194-200
- (130) Fan X., Wang W., Li W., Zhou J., Wang B., Zheng J., Li X., *ACS Appl. Mater. Interfaces*, **2014**, 6, 14994-14999
- (131) Li L.-M., Wang H.-Y., Yan X.-P., *Electrophoresis*, **2012**, 33, 2896-2902
- (132) Wang C.-C., Zhang Y.-Q., Wang P., *Journal of Molecular Structure*, **2015**, 1083, 127-136
- (133) Carneiro J., Martinez R., Suárez I., Zarhloule Y., Rimi A., *Environ., Earth Sci.*, **2015**, 73, 2951-2962
- (134) Figueroa J. D., Fout T., Plasynski S., McIlvried H., Srivastava R. D., *International Journal of Greenhouse Gas Control*, **2008**, 2, 9-20
- (135) Arakawa H., Aresta M., Armor J. N., Barteau M. A., Beckman E. J., Bell A. T., Bercaw J. E., Creutz C., Dinjus E., Dixon D. A., Domen K., DuBois D. L., Eckert J., Fujita E., Gibson D. H., Goddard W. A., Goodman D. W., Keller J., Kubas G. J., Kung H. H., Lyons J. E., Manzer L. E., Marks T. J., Morokuma K., Nicholas K. M., Periana R., Que L., Rostrup-Nielson J., Sachtler W. M. H., Schmidt L. D., Sen A., Somorjai G. A., Stair P. C., Stults B. R., Tumas W., *Chem. Rev.*, **2001**, 101, 953-996
- (136) Liu Y., Yang Y., Sun Q., Wang Z., Huang B., Dai Y., Qin X., Zhang X., *ACS Appl. Mater. Interfaces*, **2013**, 5, 7654-7658
- (137) Kokubo Y., Hasegawa A., Kuwata S., Ishihara K., Yamamoto H., Ikariya T., *Adv. Synth. Catal.*, **2005**, 347, 220-224
- (138) Bogel-Lukasik E., *J. of Supercritical Fluids*, **2015**, 99, 121-128
- (139) Beckman E. J., *J. of Supercritical Fluids*, **2004**, 28, 121-191
- (140) Behr A., Eilting J., Irawadi K., Leschinski J., Lindner F., *Green Chem.*, **2008**, 10, 13-30
- (141) Pyo S.-H., Persson P., Mollaahmad M. A., Sørensen K., Lundmark S., Hatti-Kaul R., *Pure Appl. Chem.*, **2012**, 84, 637-661
- (142) Ortiz A. U., Boutn A., Fuchs A. H., Coudert F.-X., *Phys.Rev. Lett.*, **2012**, 109, 195502
- (143) Bazer-Bachi D., Assié L., Lecocq V., Harbuzaru B., Falk V., *Powder Technology*, **2014**, 255, 52-59
- (144) Moggach S. A., Bennett T. D., Cheetham A. K., *Angew. Chem. Int. Ed.*, **2009**, 48, 7087-7089
- (145) Su Z., Miao Y.-R., Mao S.-M., Zhang G.-H., Dillon S., Miller J. T., Suslick K. S., *J. Am. Chem. Soc.*, **2015**, 137, 1750-1753
- (146) Chapman K. W., Halder G. J., Chupas P. J., *J. Am. Chem. Soc.*, **2009**, 131, 17546-17547

-
- (147) Ortiz A. U., Boutin A., Fuchst A. H., Coudert F.-X., *J. Phys. Chem. Lett.*, 2013, 4, 1861-1865
- (148) Kong B., Seog J. H., Graham L. M., Lee S. B., *Nanomedicine*, **2011**, 6, 929-941
- (149) Shen C., James S. J., de Jonge M. D., Turney T. W., Wright P. F. A., Feltis B. N., *Toxicological Sciences*, **2013**, 136, 120-130
- (150) Lozano O., Mejia J., Piret J.-P., Saout C., Dogné J.-M., Toussaint O., Lucas S., *Journal of Physics : Conference Series*, 2013, 429, 012013, 1-10
- (151) Misra S. K., Dybowska A., Berhann D., Luoma S. N., Valsami-Jones E., *Science of the Total Environment*, **2012**, 438, 225-232
- (152) Joy D. C., *Curr. Opin. Solid St. M.*, **1997**, 2, 465-468
- (153) Zhou W., Wang Z. L., *Scanning Electron Microscopy for Nanotechnology : Techniques and Applications*, Springer, 2007 (ISBN: 978-0-387-33325-0)
- (154) *A guide to Scanning Electron Microscope Observation* by JEOL
- (155) Wiktor C., Turner S., Zacher D., Fischer R. A., Van Tendeloo G., *Micropor. Mesopor. Mat.*, **2012**, 162, 131-135
- (156) (a) Park Y. K., Choi S. B., Nam H. J., Jung D.-Y., Ahn H. C., Choi K., Furukawa H., Kim J., *Chem. Commun.*, **2010**, 46, 3086-3088 ; (b) Hu P., Zhuang J., Chou L.-Y., Lee H. K., Ling X. Y., Chuang Y.-C., Tsung C. K., *J. Am. Chem. Soc.*, **2014**, 136, 10561-10564 ; (c) Hermannsdörfer J., Friedrich M., Miyajima N., Albuquerque R. Q., Kümmel S., Kempe R., *Angew. Chem. Int. Ed.*, **2012**, 51, 11473-11477
- (157) Fultz B., Howe J., *Transmission Electron Microscopy and Diffractometry of Materials Graduate Texts in Physics*, Springer Berlin Heidelberg, **2013**, 1-57
- (158) Walton K. S., Snurr R. Q., *J. Am. Chem. Soc.*, **2007**, 129, 8552-8556
- (159) (a) Rouquerol F., Rouquerol J., Sing K., *Academic Press*, London, **1999**; (b) Sing K. S. W., Everett D. H., Haul R. A. W., Moscou L., Pierotti R. A., Rouquerol J., Siemieniowska T., *Pure Appl. Chem.*, **1985**, 57, 603-619
- (160) (a) Saito A., Foley H. C., *Am. Inst. Chem. Eng. J.*, **1991**, 37, 429-436; (b) Saito A., Foley H. C., *Microporous Mater.*, **1995**, 3, 531-542; (c) Horvath G., Kawazoe K., *J. Chem. Eng. J.*, **1983**, 16, 470-475
- (161) Ranga Rao G., Ranjan Sahu H., *Proc. Indian Acad. Sci. (Chem. Sci.)*, **2001**, 113, 651-658
- (162) Wyszecski G., Stiles W.S., **1982**, *Color Science: Concepts and methods, quantitative data and formule*, 2nd ed. John Wiley & Sons, New York
- (163) Torrent J., Barrón V., **2008**, Chapter 13 from *Methods of Soil Analysis: Mineralogical methods. Part 5*, Ulery A. L. & Dress L. R. Editors, Madison
- (164) McElfresh M., **1994**, *Fundamentals of Magnetism and Magnetic Measurements Featuring Quantum Design's Magnetic Property Measurement System*, Quantum Design
- (165) Tauxe, L., Banerjee, S.K., Butler, R.F. and van der Voo R, *Essentials of Paleomagnetism*, 2nd Web Edition, **2014**
- (166) Hansen M. F., Morup S., *J. Magn. Magn. Mater.*, **1999**, 203, 214-216
- (167) Simmonds R. W., *Nature*, **2012**, 492, 358-359
- (168) Riss T. L., Moravec R. A., Niles A. L., Benink H. A., Worzella T. J., Minor L., *Cell viability assays. Assay Guidance Manual*, Eli Lilly & Company and the National Center for Advancing Translational Sciences, **2004**
- (169) Vega-Avila E., Pugsley M. K., *Proc. West., Pharmacol. Soc.*, **2011**, 54, 10-14
- (170) Huang K. T., Chen Y. H., Walker A. M., *BioTechniques*, **2004**, 37, 406-412
- (171) *Introduction to Flow Cytometry: A learning Guide*, **2000**, BD Bioscience
- (172) <http://stemcells.nih.gov/StaticResources/info/scireport/images/figure2.jpg>

Chapter 2: Experimental part

2.1 Materials

The chemicals used in the experiments were zinc acetate dihydrate (98+%, Aldrich), anhydrous zinc acetate (99,99%, Aldrich), zinc bromide (98%, Riedel de Haën), zinc chloride (98%, Aldrich), zinc nitrate hexahydrate (98%, Aldrich), zinc perchlorate hexahydrate (Aldrich), zinc sulphate heptahydrate (99%, Merck), copper nitrate trihydrate (99.5%, Merck), sodium chloride (99-100.5%, Carlo Erba), sodium sulphate ($\geq 99\%$, Carlo Erba), Iron (+3) chloride hexahydrate (Lancaster; 98%), iron (+2) sulfate heptahydrate (Aldrich; $\geq 99\%$), sodium citrate tribasic dihydrate (99%, Aldrich), 2-methylimidazole Hmim (99%, Aldrich), 4-bromobenzaldehyde (99%, Aldrich), malononitrile (99%, Aldrich), acetylacetone (99%, Aldrich), 2-aminobenzophenone (98%, Aldrich), aniline (99.5%, Aldrich), benzyl bromide ($\geq 98\%$, Fluka), sodium azide ($\geq 99.5\%$, Aldrich), phenyl acetylene ($> 98\%$, Alfa Aesar), ethynyltrimethylsilane (98%, Aldrich), 1-octyl bromide (99%, Aldrich), methyl 5-bromovalerate (97%, Aldrich), Benzyl azide, 1-octyl azide and methyl 5-azidovalerate were prepared according to the synthetic protocol described in the following reference: O'Neil E. J., DiVittorio K. M., Smith B. D., *Org. Lett.* **2007**, *9*, 199-202; (\pm)-glycidol (96%, Aldrich), (\pm)-styrene oxide ($>98\%$, Alfa Aesar), (\pm)-epichlorohydrin (99%, Alfa Aesar), cyclohexene oxide ($>98\%$, Aldrich), ammonium hydroxide solution ca. 25% (Aldrich), ethanol ($\geq 99.8\%$, Aldrich), and methanol ($\geq 99.9\%$, Aldrich) DMSO ($\geq 99.7\%$, Fisher), diethyl ether ($\geq 99.5\%$, Aldrich) chlorobenzene (98.5%, SDS), dichloromethane ($\geq 99.9\%$, Aldrich), dimethylformamide ($>99.8\%$, Riedel de Haën), dioxane ($>99\%$, Acros Organics), anisole (99%, Aldrich), and toluene ($\geq 99\%$, Prolabo) were used as received without further purification. All aqueous solutions were prepared using Milli-Q water (18.2 M Ω .cm, Millipore) as the solvent.

2.2 General information on the characterization techniques

Transmission electron microscopy (TEM) images were taken by placing a drop of the ZIF-8 particles in methanol onto a carbon film-supported copper grid. Samples were studied using a Philips CM20 instrument operating at 200 kV. Scanning electron microscopy (SEM) pictures were prepared using JEOL Scanning Electron Microscope JSM-6490 LV. The ZIF-8 material prepared from zinc acetylacetonate was viewed on a ISOPORETM membrane (Merck Milipore) with 0.2 μm pores size. The X-ray powder diffraction (XRD) diagrams of all samples were measured using Panalytical X'Pert Pro MPD diffractometer using Cu K α radiation. The X-ray powder diffraction data were collected from an X'Pert MPD diffractometer (Panalytical AXS) with a goniometer radius 240 mm, fixed divergence slit module (1/2 $^\circ$ divergence slit, 0.04 rd Sollers slits) and an X'Celerator as a detector. The powder samples were placed on a silicon zero-background sample holder and the XRD patterns were recorded at room temperature using Cu K α radiation ($\lambda = 0.15418$ nm). The textural properties of the materials were investigated with a Micromeritics ASAP 2420 instrument using liquid nitrogen (-196 $^\circ\text{C}$). Prior to the analyses, the samples were out-gassed overnight in vacuum at 40 $^\circ\text{C}$ on the degassing port followed by 4h out-gassing on the analyse port. The resulting isotherms were analysed using the BET (Brunauer-Emmett-Teller) method while the micropore volume (V_{micro}) was determined using the Horvath-Kawazoe (HK) equation with Saito-Foley adaptation for cylindrical pores. Thermogravimetric measurements were performed on a SETARAM Setsys Evolution thermoanalyzer coupled with an Omnistar GSD301C-Pfeiffer Vacuum mass spectrometer. Samples were filled into

platinum crucibles and heated in a flow air with a ramp of $5^{\circ}\text{C}\cdot\text{min}^{-1}$ from room temperature up to 800°C . ^1H NMR spectra were recorded in CDCl_3 using a 300 MHz spectrometer (Avance 300, Bruker, Bremen, Germany). Chemical shifts values are reported in ppm relative to the residual peak of the solvent. Diffuse reflectance UV-vis spectra of the samples were measured using a Shimadzu UV-2101 PC spectrophotometer. BaSO_4 is used as a standard for baseline measurements and spectra are recorded in a range of 200-1400 nm. A VARIAN 720-ES Inductively Coupled Plasma-Optical Emission Spectrometer (ICP-OES) was used for multi-elemental analyses. ESR experiments were carried out using a X-Band EMX-plus spectrometer (Bruker Biospin). The samples were investigated at room temperature. The double integration of the ESR spectrum is proportional to the concentration in paramagnetic centers.⁵⁴ A calibration was first done using 2,2,6,6-tetramethylpiperidine-1-oxyl (TEMPO) to ensure that this procedure was usable in solid state. TEMPO was also used as standard for calibration ($g = 2.0061$). The DC magnetization data were recorded using a PPMS (Quantum Design) in field up to 50000 Oe in the 5-300 K temperature range. No diamagnetism correction was applied. A VARIAN 720-ES Inductively Coupled Plasma-Optical Emission Spectrometer (ICP-OES) was used for multi-elemental analyses. Raman spectra of the samples were recorded on Horiba Scientific Jobin Yvon XploRA spectrometer coupled with optical microscope. Particle size distributions (PSD) (in number and weight) were measured with a disk centrifuge DC24000 system (CPS instruments Inc., USA). This measurement is based on the centrifugal liquid sedimentation (CLS) method according to Stokes' law using a 405 nm wavelength laser. This method is also known as Differential Centrifugal Sedimentation (DCS) or ultracentrifugation. The diameters measured are hydrodynamic diameters, which for spherical particles provide the real diameter (sphericity factor equal to 1). A certified calibration standard of PVC microparticles (226 nm), provided by CPS Instruments, was used to calibrate all the measurements. Each measurement was done by injecting 0.1 ml of the stock dispersion or 1 mL of the media dilution into the centrifugal disk. A standard dynamic light scattering was conducted on Malvern zeta sizer.

2.3 Procedures

2.3.1 Synthesis of the materials

Synthesis of ZIF-8.

A solution of the Zn^{2+} salt (1 mmol) and Hmim (660 mg, 8 mmol) in 11.3 mL of methanol were prepared separately. Then, in a three-neck-flask, the two solutions were mixed by dropwise addition of the Hmim solution to the Zn^{2+} salt solution. The synthesis was conducted under nitrogen flow at room temperature with stirring for 1 h. The ZIF-8 crystals were separated by centrifugation (4000 rpm, 15 min) and washed by methanol (3×30 mL). The nanocrystals were dried in air overnight before analysis.

Synthesis of doped ZIF-8.

A solution of the $\text{Zn}(\text{NO}_3)_2$ and $\text{Cu}(\text{NO}_3)_2$ (or $\text{Fe}(\text{OAc})_2$)(total 1 mmol) in 11.3 mL methanol and Hmim (660 mg, 8 mmol) in the same volume of methanol were prepared separately. Then, in a three-neck-flask, the two solutions were mixed by dropwise addition of the Hmim solution to the Zn^{2+} and Cu^{2+} (or Fe^{2+}) solution. The synthesis was conducted under nitrogen flow at room temperature with

stirring for 1 h. The Cu-doped (or Fe-doped) ZIF-8 crystals were separated by centrifugation (4000 rpm, 15 min) and washed with methanol (3×30 mL). The material was dried at room conditions overnight before analysis. To use the material in catalytic reactions, the Cu/ZIF-8 samples were activated by treatment of the powders at 200°C in a programmable oven for 6 h, and then cooled to room temperature naturally. The vials containing the Cu/ZIF-8 (or Fe/ZIF-8) powders were tightly capped and stored at room temperature before use.

Synthesis of citrate-capped Fe₃O₄ nanoparticles.

FeCl₃·6H₂O (6 mmol; 1.622 g) and FeSO₄·7H₂O (5 mmol; 1.39 g) were dissolved in 40 mL of water. 5 mL of a 28% ammonia solution were then added and the mixture heated at 90°C. Then 4.4 g (14.9 mmol) of sodium citrate were added to the flask and the mixture vigorously stirred for 30 min. Fe₃O₄ nanoparticles were recovered by magnetic separation, washed several times with ethanol and redispersed in water (100 mL).

Synthesis of Fe₃O₄@ZIF-8 nanoparticles.

15 mL of a freshly prepared citrate-capped Fe₃O₄ particles water solution were mixed under vigorous stirring with Hmim (4.31 g, 52.5 mmol) and the mixture stirred for 5 min. Then, 15 mL of a zinc nitrate aqueous solution (0.223 g; 0.75 mmol) were added, and the solution stirred for 10 min. Fe₃O₄@ZIF-8 particles were recovered by magnetic separation and purified by washing three times with water.

Synthesis of Fe₃O₄@Cu25%/ZIF-8 nanoparticles.

10 mL of a freshly prepared citrate-capped Fe₃O₄ particles water solution were mixed under vigorous stirring with Hmim (2.873 g, 35.03 mmol) and the mixture stirred for 5 min. Then, 10 mL of a zinc nitrate (0.111 g; 0.38 mmol) and copper nitrate (0.029 g; 0.12 mmol) aqueous solution were added, and the solution stirred for 10 min. Fe₃O₄@Cu_{25%}/ZIF-8 particles were recovered by magnetic separation and purified by washing three times with water.

2.3.2 Catalytic experiments

The ZIF-8 samples were activated by treatment of the powders at 200°C in a programmable oven for 6 h, and then cooled to room temperature naturally. The vials containing the ZIF-8 powders were tightly capped and stored at room temperature before use.

Knoevenagel condensation.

4-Bromobenzaldehyde (0.0925 g, 0.5 mmol) was dissolved in 5 mL of toluene, the ZIF-8 catalyst (9.2 g, 0.04 mmol) added and the mixture stirred for 5 min. Malononitrile was then injected (0.189 mL, 3 mmol) and the reaction was conducted with bubbling of Ar gas through the mixture for 5 h at room temperature. After centrifugation and concentration of the toluene phase, the crude reaction mixture was purified using silica gel column chromatography (petroleum ether – ethyl acetate (v/v), 95:5) and the product analyzed by ¹H NMR. ¹H NMR (CDCl₃, 300 MHz): δ 7.74 (d, $J = 8.7$ Hz, 2H), 7.73 (s, 1H), 7.67 (d, $J = 8.7$ Hz, 2H).

Friedländer reaction.

2-Aminobenzophenone (82.1 mg, 0.42 mmol) and ethyl acetoacetate (81.3 mg, 0.62 mmol, 1.48 equiv.) were added to Cu/ZIF-8 crystals (8 mol% of catalyst) dispersed in 2 mL of toluene. The mixture was stirred at 90°C and the progress of the reaction was monitored by TLC. After cooling, the reaction mixture was centrifuged and the toluene phase concentrated. The product was purified by flash chromatography and analyzed with ¹H and ¹³C NMR.

Combes reaction.

The catalysis was conducted in a solvent-free environment. Briefly, aniline (1 mmol) and acetylacetone (5 mmol) were mixed with 8 mol% of the Cu/ZIF-8 catalyst at 100°C for 3 h. Then, the catalyst was separated by centrifugation (4000 rpm, 15 min), washed three times with toluene and dried. The reaction mixture was centrifuged and the toluene phase concentrated. The product was purified by flash chromatography and analyzed with ¹H and ¹³C NMR.

Huisgen's dipolar cycloaddition.

Click reactions were conducted according to a slightly modified literature procedure.²⁷ The general protocol for 1,3-dipolar cycloaddition of the azides to the alkynes was as follows. The Cu/ZIF-8 catalyst (5 mol% of catalyst) in ethanol (6 ml) was placed inside a round bottom flask connected to a reflux condenser and the temperature was set to 70 °C under argon. Azide (1 mmol) and alkyne (1.2 mmol) were then added and the mixture was stirred during 3 h. Then the catalyst was isolated by centrifugation, washed with ethanol and dried. The product was purified by flash chromatography and analyzed with ¹H and ¹³C NMR.

CO₂ conversion.

Cycloaddition reactions of epichlorohydrin, glycidol, styrene oxide, cyclohexene oxide and CO₂ were carried out using Parr high pressure reactor. The constant temperature during the manipulation, as well as heating and cooling rate is provided by the heating jacket and thermocouple. The gas inlet valve at the top of reactor is connected to the CO₂ gas bottle (purity 99.999%) that allows introduction of the gas inside the reactor with desired pressure.

During the experiments without solvent, the reactor was charged with 18 mmol of cyclic epoxide and 2.5 mmol% catalyst. The reactor then was pressurized with CO₂ up to 7-12 bar. The temperature of the reactor was then increased with the rate 1.5 °C/min and maintain at 70-120°C for a given reaction time. When the reaction was completed, the reactor was cooled down with the rate 2°C/min. Once the reactor cooled, the pressure was released slowly. After the catalyst was separated and washed three times with methanol. The product of the reaction was concentrated by evaporation of the solvent and dried under vacuum for six hours. The product was analysed by NMR.

The reactions with solvents were conducted as following: the catalyst 2.5 mmol% was dispersed in 30 mL of solvent. Then 5 mmol of styrene oxide was injected into the dispersion and the mixture was mixed for 5 min at ambient temperature. The reactor was pressurized with CO₂ up to 10 bar and the temperature was set at 100°C. After 19-10h the reaction was completed by cooling down the reactor. The product was separated by washing the catalyst with methanol several times. After evaporation and drying the product was purified with flash chromatography (petroleum ether/ethyl acetate=90/10) and analysed with NMR.

Parr reactor instrumentation

In this study, the carbon dioxide conversion was conducted using a Parr reactor. Such reactors are used for screening catalysts in reactions that require high pressure operating. The system was successfully applied, as examples, for the hydrogenation of tetralin under mild conditions, the carbonylation of phenol to the corresponding methyl phenyl carbonate or for ethylene polymerization.

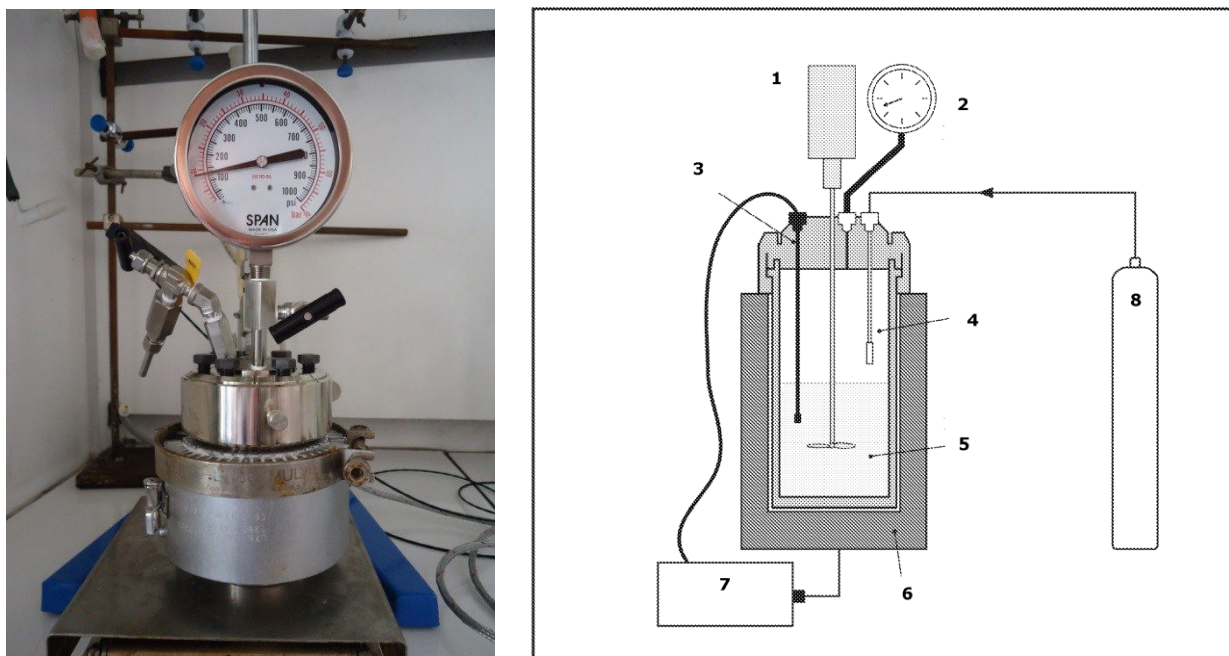


Fig. 2.1 Experimental setup of the Parr reactor: mixing system (1), pressure controller (2), temperature sonda (3), CO₂ inlet (4), reaction vessel (5), inox reactor (6), temperature controller (7), CO₂ bottle (8).

The reactor is composed of a closed stainless steel vessel with integrated temperature sonda and pressure controller. The system is supplemented with the gas and after the reaction, the gas is released by the outlet at the upper part of the reactor. The temperature inside the reactor is achieved with heating jacket which surrounds the vessel. The heating jacket and the sonda inside the reactor are connected together by the electronic device which dictates the proper temperature, heating/cooling rates and the reaction time.

2.3.3 Shaping of the ZIF-8 catalyst

INSTRON 5549 was used to compact the ZIF-8 powders. A cylindrical die of 4 mm in diameter and close fitting compression punch were used for this purpose. The compaction procedure was as follows: the die was filled with 20 mg of powder; and the speed of the punch is set at 10 mm/min during the compression until the selected pressure is reached. The punch finally rises at 15 mm/min during the ascent. The force applied in the compression is 1000, 2000, 3500 and 5000N (pressure of 79, 159, 278 and 398 MPa respectively).

2.3.4 Cytotoxicity studies

ZIF-8 nanoparticles suspensions.

A stock solution of each ZIF-8 doped and undoped sample was prepared at 1mg/mL (w/v) concentration in ultrapure water. The samples were sonicated using 42 kHz frequency ultrasound for 10 min followed with manual shaking and vortexed for 5 min. Then, an appropriate volume of the stock solution was diluted in the medium containing antibiotics.

Cytotoxicity assay.

The cytotoxicity tests were conducted on alveolar pulmonary cells A549 and human telomerase-immortalized keratinocytes IHK. A549 cells were cultured in Minimal Essential Medium (MEM, Gibco) + 10% fetal bovine serum (Gibco) and 1% penicillin-streptomycin (BioWhittaker). The other cell line, IHK was maintained in Epilife medium with human keratinocyte growth supplement (Cascade Biologics) and antibiotics (penicillin/streptomycin). The cells incubation was conducted in a 5% CO₂ incubator in humidified atmosphere at 37 °C.

MTS assay.

A549 or IHK cells were seeded into 96-well microtiter plate at the density of 5000 IHK cells and 10000 A549 cells per well. After 24 hours of pre-incubation, when the cells were allowed to attach, the old medium was removed and the cells were treated with 100 µL of ZIF-8 particles suspensions. A serial dilution resulted in five concentrations of the particles: 1 mg/mL, 10 mg/mL, 25 mg/mL, 50 mg/mL and 100 mg/mL. The negative and positive controls of the experiment were conducted in parallel. The two reference substances of the positive control were applied: 0.005 mg/mL benzalkonium chloride for IHK cells and 500 nM staurosporine for A549 cells. The negative control was conducted without NPs. Then the plates were incubated for 24 h at 37 °C. After the old medium was removed and the wells were filled with 120 µL of the mixture 10 mL Epilife medium + antibiotics + 2 mL of MTS probe. BIORAD xMARK Microplate Spectrophotometer (the absorbance at of formazan product at 490 nm) was used to read the 96 well microtiter plates after 1h (A549) or 2h - 3h (IHK). The quantity of formazan product is directly proportional to the number of metabolically active cells in the culture.

ROS evaluation.

A549 or IHK cells were seeded into 12-well microtiter plate at the density of 10000 of each cell line per well. After 24 h incubation the old medium was discarded. NPs dilutions with required concentrations (67.7 µg/mL for A549 and 15 µg/mL for IHK) were deposited inside the wells and incubated for another 24 h. Then the cells were washed with 1 mL HBSS and harvested for 3 min at 37 °C with 0.5 mL of trypsin-EDTA. The trypsin-EDTA action was stopped with 1 mL of the medium and the cells were collected by centrifugation. The cells were re-suspended in 100 µL 2.5 µM CM-H₂DCFDA in HBSS or in the mixture 100 µL CM-H₂DCFDA with positive control probe (SIN-1 = 3-(4-morpholinyl)sydnonimine hydrochloride). The samples were incubated at 37 °C for 20 min in darkness. After the cells were washed with 500 µL HBSS and spun down (5 min/1200 rpm/4°C) two times and finally re-suspended in 500 µL HBSS. The samples were stored in darkness as prepared and measured immediately using BD FACSCalibur (BD bioscience) flow cytometry system using excitation 488 nm, emission in green channel 530 ± 40 nm (band pass filter green channel, FL1 or equivalent).

Preparation of the gastric juices

The preparation of the digestion juices was undertaken using the stock solutions of organic compounds (provided by RIKILT) and the inorganic chemicals/reagents. Composition of digestive fluids are given in the table 2.1.

Table 2.1. Preparation of the juices for the fed *in vitro* digestion model.

Saliva		Gastric		Duodenal	
<u>Inorganic stock (RIKILT)</u>	<u>Total l</u>	<u>Inorganic stock (RIKILT)</u>	<u>Total l</u>	<u>Inorganic stock (RIKILT)</u>	<u>Total l</u>
KCl (89.6 g/l)	10 mL	NaCl (175.3 g/L)	15.7 mL	NaCl (175.3 g/L)	40 mL
KSCN (20 g/l)	10 mL	NaH ₂ PO ₄ ·H ₂ O (102.1 g/L)	3 mL	NaHCO ₃ (84.7 g/L)	40 mL
NaH ₂ PO ₄ ·H ₂ O (102.1 g/l)	10 mL	KCl (89.6 g/L)	9.2 mL	KH ₂ PO ₄ (8 g/L)	10 mL
Na ₂ SO ₄ (57 g/l)	10 mL	CaCl ₂ (30.2 g/L)	10 mL	KCl (89.6 g/L)	6.3 mL
NaCl (175.3 g/l)	1.7 mL	NH ₄ Cl (30.6 g/L)	10 mL	MgCl ₂ ·6H ₂ O (5 g/L)	10 mL
NaHCO ₃ (84.7 g/L)	20 mL	37% HCl	6.5 mL	HCl (37%)	180 µL
				CaCl ₂ (30.2 g/L)	5 mL
<u>Organic stock (RIKILT)</u>		<u>Organic stock (RIKILT)</u>		<u>Organic stock (RIKILT)</u>	
urea (25 g/l)	8 mL	glucose (65 g/L)	10 mL	urea (25 g/L)	4 mL
		glucuronic acid (2 g/L)	10 mL		
		urea (25 g/L)	3.4 mL		
		glucosaminehydrochloride (33 g/L)	10 mL		
<u>Add to mixture</u>		<u>Add to mixture</u>		<u>Add to mixture</u>	
Amylase	290 mg	BSA	1000 mg	BSA	1000 mg
uric acid	15 mg	pepsin	2500 mg	pancreatin	9000 mg
Mucin	25 mg	mucin	3000 mg	lipase	1500 mg
milli-Q water	fill to 1 L	milli-Q water	fill to 1 L	milli-Q water	fill to 1 L
Measured the pH = 6.8 ± 0.1.		Measured the pH = 1.3 ± 0.1		Measured the pH = 8.1 ± 0.1.	

The pH was measured and adjusted after total dissolution of all the components. The solutions were stored overnight at room temperature in the incubator. About 2 h prior to the experiments, the incubator was switched on and set at 37 ± 2°C.

In vitro digestion experiment

2.5 mg of ZIF-8, Fe_{10%}/ZIF-8 and Cu_{10%}/ZIF-8 samples were dispersed in 1 mL of the three fluids (saliva, gastric and duodenal) separately and incubated for certain time at 37°C to simulate the exposition of the particles to the juices during the digestion. The incubation times were 5 min in saliva, 5 min, 15 min, 2 h in gastric fluid and 2 h in intestinal fluid. After the samples were centrifuged (5 min, 10000 rpm) and washed three times with water to stop the action of digestive fluids. Then the samples were analyzed with CLS and SEM.

Stability test of the particles

2.5 mg of ZIF-8, Fe_{10%}/ZIF-8 and Cu_{10%}/ZIF-8 particles were dispersed 1 mL of methanol, water, phosphate buffer of pH 4.8 and 8.0. PBS buffers were prepared using two stock solutions of 0.0667 M Na₂HPO₄ (pH 8.8) and 0.0667 M NaH₂PO₄ (pH 4.6). For 10 mL PBS buffer of pH 4.8 we used 0.035 mL of Na₂HPO₄ solution and 9.965 mL of NaH₂PO₄. For 10 mL PBS buffer of pH 8.0, we mixed 9.69 mL of Na₂HPO₄ solution and 0.31 mL of NaH₂PO₄ solution. The ZIF-8 samples were incubated in methanol and water for 3 days and in PBS buffers for 2 h. Then all the samples were centrifuged (15000 rpm, 5 min) and washed three times with methanol or water. After drying, the materials were analyzed by scanning electron microscopy.

Additional test of ZIF-8 material in hydrochloric acid buffer pH 1.3

Dissolution media – buffer HCl pH 1.3 was prepared according to the protocol provided by International Pharmacopea. Briefly, 50 mL 0.2 M KCl was placed in a 200 mL volumetric flask. Then, 67.2 mL of 0.2 M HCl was introduced and water was added to the volume. pH of the prepared buffer was 1.3. The ZIF-8 particles were dispersed in the HCl-buffer with the concentration of 2.5 mg/mL and incubated for 0 – 90 min. The mass of the material was checked before and after the incubation. The remains of the material were analyzed before and after the test.

Chapter 3: ZIF-8 design, synthesis and functionalization

A key challenge to adapt a material for more specialized and sophisticated application is to properly design its structure or to integrate purposeful functionalities. Once the new structure is formed, the functionality can generate unique and novel properties directing the material for specific field.

In this chapter, we report on the improvements in the synthesis, structural modification and functionalization of ZIF-8. We present our investigations – the three publications using ZIF-8 as example.

In the first article, we would like to show a simple method for controlling the crystal size and the morphology of zeolitic imidazolate framework-8 nanocrystals in methanol solution. We also define the relations of the ZIF-8 crystal size on the reactivity in Knoevenagel and Friedländer reactions.

The second paper gives an example of the framework-doped with Cu to develop materials suitable for Cu-mediated reactions: Friedländer, Combes reactions and Huisgen's cycloaddition.

The last paper is connected with the ZIF-8 functionalization with Fe_3O_4 magnetic nanoparticles. The magnetic properties originating from this composite structure were successfully applied in the magnetic separation of the catalyst in model reactions catalyzed by ZIF-8 and copper-doped ZIF-8 particles.

These three strategies offer great potential and new opportunities to control the reactivity of ZIF-8 crystals in different applications. We want to show that the design and modifications on ZIF-8 materials can led to new, beneficial products with suitable form, adapted for special purposes.

3.1 Controlling ZIF-8 nano- and microcrystal formation and reactivity through zinc salts variations

Schejn A., Balan L., Falk V., Aranda L., Medjahdi G., Schneider R., CrystEngComm, 2014, 16, 4493-4500

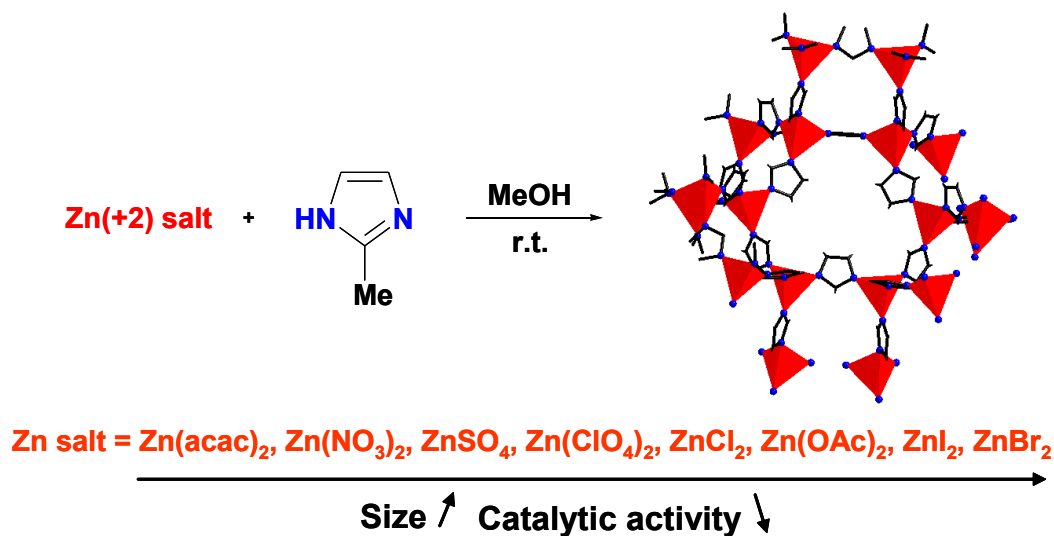


Fig. 3.1.1 Graphical abstract.

3.1.1 Abstract

We report here a simple method for controlling the crystal size and the morphology of zeolitic imidazolate framework-8 (ZIF-8) nanocrystals in methanol solution. ZIF-8 crystals were prepared by mixing 2-methylimidazole (Hmim) with various zinc salts for 1 h and using a Hmim/Zn(+2) salt molar ratio of 8/1. All products prepared were assigned to a sodalite-type structure and both particle size and morphology were found to be dependent on the reactivity of the Zn(+2) salt. Small ZIF-8 crystals with diameters varying between ca. 50 and 200 nm were obtained with reactive zinc salts like Zn(acac)₂, Zn(NO₃)₂, ZnSO₄ or Zn(ClO₄)₂ as demonstrated by SEM and TEM analyses. The use of ZnCl₂, Zn(OAc)₂ or ZnI₂ afforded crystals with sizes varying between ca. 350 and 650 nm. Finally, the low reactive ZnBr₂ salt was found to generate microsized crystals. Taking ZIF-8 crystals prepared from Zn(NO₃)₂, Zn(OAc)₂ and ZnBr₂ as representatives and through thermogravimetric analysis and BET measurements, we also demonstrated that changes in particles size induced changes in stability and in adsorption properties. The small sized ZIF-8 crystals produced from Zn(NO₃)₂ were found to exhibit the highest surface area (1700 m²/g) and the best catalytic activity in Knoevenagel condensation between 4-bromobenzaldehyde and malononitrile.

3.1.2 Introduction

Metal-organic frameworks (MOFs) are new microporous inorganic-organic hybrid materials that exhibit tunable structures, low density and ultrahigh surface areas. These materials may therefore have various potential applications in catalysis,¹⁻³ hydrogen storage,⁴⁻⁶ and CO₂ adsorption.^{7,8} Among MOFs, the so-called zeolitic imidazolate frameworks (ZIFs) have recently attracted considerable attention. In these materials, metal atoms such as Zn²⁺ are linked through N atoms by ditopic imidazolate (im⁻) ligand to form neutral frameworks.⁹⁻¹² Each Zn²⁺ atom connects four im⁻ and the {Zn²⁺(im⁻)₂} units are analogous to the {SiO₂} tetrahedra in zeolites and the Zn-im-Zn bond angle is similar to the Si-O-Si bond angle (145°). Guest-free ZIFs have the large surface area and pore volume of classical MOFs but also the high chemical and thermal stability of conventional zeolites.^{10,13} Due to these features, ZIFs show great potential for gas storage and separation.¹⁴⁻¹⁸

ZIF-8 (Zn(mim)₂, mim = 2-methylimidazole) is the most representative ZIF material with a sodalite zeolite-type topology, in which ZnN₄ tetrahedra are connected through imidazolate linkers forming cages 11.6 Å in diameter which are accessible through a narrow six-ring pore (3.4 Å).¹³ ZIF-8 has a high thermal stability (550°C in N₂), large surface area (BET: 1630-1700 m².g⁻¹),¹³ and a high chemical resistance to various solvents.^{19,20} All these properties are outstanding among MOFs, making ZIF-8 an ideal candidate for numerous industrial applications. Nevertheless, to open the way for applications such as sensors, catalysts or as material for gas separations, a real effort has to be made on shaping the ZIF-8 hybrid frameworks. Variations of morphology and size of ZIF-8 crystals is of great importance because these parameters can markedly affect the functional properties and the performances of these nanomaterials. Moreover, controlling the shape and size of ZIF nanoparticles may not only help the fundamental understanding of the crystallisation mechanisms but could also improve structural and morphological control in the synthesis of these novel porous materials. However, these important issues have only scarcely been addressed in the field of ZIF-8 nanomaterials.

In recent years, different strategies have been adopted to manipulate morphology and size of ZIF-8 crystals. Variation of synthetic parameters including solvent, concentration and molar ratio of reactants, temperature and duration can markedly affect the size of the crystals.^{21,22} An excess of the bridging ligand relative to the zinc salt is generally employed to increase the nucleation rate. Addition of sodium formate that acts as a base in the deprotonation equilibria of mim in the reaction medium was found to influence the crystal shape and size of ZIF-8 nanoparticles.^{23,24} Surfactants such as poly(diallyldimethylammonium chloride)²⁵ or cetyltrimethylammonium bromide²⁶ or the gelatin biopolymer²⁷ have also been used as growth inhibitors to limit ZIF-8 crystal size or to tune the crystal morphology. Finally, the use of auxiliary ligands such as amines or carboxylates acting as competitors to the mim bridging ligand can also modulate the crystallisation process and thus the particle size and morphology.²¹

Variation of zinc salts is largely unexplored for ZIF nanocrystals despite the advantages this offers in terms of simplicity and processability. For (Zn₄O[(OOC)₂C₆H₄]₃) (MOF-5), the influence of the zinc precursor on the morphology and size of nanocrystals produced was demonstrated by Biemmi *et al.*²⁸ Very recently, Torad *et al.* showed that replacing Zn(NO₃)₂ by Zn(OAc)₂ markedly slowed down the generation speed of ZIF-8 crystals, thus leading to large-sized nanoparticles.²⁹ The importance of the Zn(+2) precursor was also identified by Zhu *et al.* who discovered that ZnO nanoneedles could be produced during the synthesis of ZIF-8 crystals using zinc carbonate as zinc source.³⁰ However, these studies have not yielded more detailed information concerning the influence of the zinc precursor on the size and morphology of ZIF nanocrystals produced.

Here we report a systematic investigation of the influence of the zinc source on the morphology and size of ZIF-8 crystals. All reactions were conducted in methanol at room temperature. Our results

demonstrate that the reactivity of the zinc precursor is able to direct the assembly of metal-organic systems such as ZIF-8 nanocrystals and thus their catalytic activity. The surface areas and the thermal stabilities of the networks, determined using the Brunauer-Emmet-Teller (BET) method and thermogravimetric analysis (TGA) respectively, are also reported.

3.1.3 Results and discussion

Methanol is the most commonly used organic solvent for the production of ZIF-8 nanocrystals and was therefore used in experiments.^{21,31} Moreover, methanol only weakly interacts with the ZIF-8 framework and can thus much easier be removed than more polar solvents like DMF [32]. The procedure employs an excess of the bridging Hmim ligand with respect to the Zn(+2) source to increase the nucleation rate and works well at room temperature without the need of any activation. All syntheses were conducted with a molar ratio of Zn/Hmim/MeOH of 1/8/559 in analogy to previous report³³ and for a duration of 1 h. As recently described,³³ the structural evolution as a function of time for ZIF-8 nanoparticles can be divided in three stages: (i) fast nucleation ($t < 10$ min), (ii) growth stage ($10 < t < 60$ min) during which the crystallinity increases with time, and (iii) stationary phase ($t > 60$ min) during which the crystallisation remains constant but ZIF-8 nanoparticles transform into larger ones through Ostwald ripening (thermodynamically driven process in which small particles disappear at the expense of growing larger ones, which are energetically favored).³⁴ Therefore, one may assume that the ZIF-8 structure is fully developed after a reaction period of 1 h and the synthesis was then stopped. Products were then collected by centrifuging and washed with methanol several times. Syntheses were conducted with $\text{Zn}(\text{NO}_3)_2$, $\text{Zn}(\text{acac})_2$, $\text{Zn}(\text{ClO}_4)_2$, ZnSO_4 , $\text{Zn}(\text{OAc})_2$, ZnCl_2 , ZnBr_2 and ZnI_2 in order to gain insight into the reactivity and the role of the zinc counter-ion in changing the morphology and size of ZIF-8 crystals.

Using ZnSO_4 or $\text{Zn}(\text{acac})_2$, addition of a few droplets of Hmim caused the immediate precipitation of ZIF-8. With $\text{Zn}(\text{ClO}_4)_2$, the solution became turbid just after the addition of Hmim and precipitates appeared over time. With $\text{Zn}(\text{NO}_3)_2$ and ZnCl_2 , the solution became cloudy within 2 min but white precipitates were much dense with $\text{Zn}(\text{NO}_3)_2$. With these reactive salts, the large amount of deprotonated Hmim (mim^-) accelerates the formation of ZIF-8 via the coordination reaction of the Zn cations and mim^- . Using $\text{Zn}(\text{OAc})_2$ or ZnI_2 , a slower formation rate of ZIF-8 was observed and the colloidal solution formed within 2.5 min. Finally, with ZnBr_2 , the solution remained transparent at ambient temperature for at least 30 min and then precipitates appeared. These first observations clearly indicate that the Zn precursors may significantly accelerate or slow down the particle formation rate.

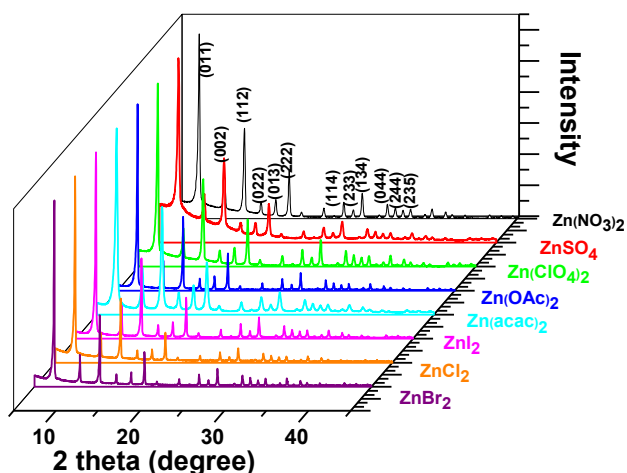


Fig. 3.1.2 XRD patterns of ZIF-8 nanocrystals prepared with different zinc precursors.

Each synthesis yielded pure-phase ZIF-8 crystals as demonstrated by X-ray diffraction (XRD) patterns (Fig. 3.1.2). Patterns generated by the ordered porous structure of the ZIF-8 particles between 2θ values of 5 and 40° can be observed and the peak broadening observed indicates the formation of nanosized crystals. The relative intensities and prominent peaks positions, including 011, 002, 112, 022, 013, and 222 are in good agreement with previous reports^{13,31} and confirm the sodalite structure, which is the typical structure of ZIF-8, and the well-defined peaks revealed the high crystallinity. The interplanar spacings calculated using Bragg's law from the reflection at different Bragg's angles correspond to a body centered cubic structure with a unit cell parameter of 17\AA and are in accordance with literature.

The correlation between the growth rate, the size and the morphology was next evaluated using Scanning Electron Microscopy (SEM) and Transmission Electron Microscopy (TEM) (Fig. 3.1.3 and 3.1.4). The growing of ZIF-8 crystals is known to evolve with time from cubes exposing 6 $\{100\}$ faces to intermediates shapes, and finally to rhombic dodecahedrons exposing 12 $\{110\}$ faces,²³ the latter being most likely the stable equilibrium morphology of ZIF-8 (Fig. 3.1.5). With $\text{Zn}(\text{acac})_2$, an average size of 45 nm was estimated from SEM and TEM images. Some isolated particles could be observed but the sample is mainly constituted of aggregates containing particles with poorly resolved shapes (Fig. 3.1.3a). With $\text{Zn}(\text{NO}_3)_2$, well-defined truncated rhombic dodecahedron crystals with an average size of $141 \pm 48\text{ nm}$, which is the typical ZIF-8 morphology, were obtained (Fig. 3.1.3b). Small sized ($211 \pm 60\text{ nm}$) truncated nanoparticles were obtained from ZnSO_4 . However, all the crystals exhibit holes indicating that they are in a stage of dissolution and that Ostwald ripening has likely taken place (Fig. 3.1.3c). Uniform in size nanoparticles with an average diameter of 224 nm were obtained using $\text{Zn}(\text{ClO}_4)_2$. The crystals were rather spherical, had bumpy surfaces but some angles could be observed on some of them (Fig. 3.1.3d). Using ZnCl_2 , larger crystals of ca. 300 nm together with many considerably smaller ones (ca. 150 nm) can be seen. Both the larger and the smaller crystals exhibit cubic and rhombic shapes (Fig. 3.1.3f).

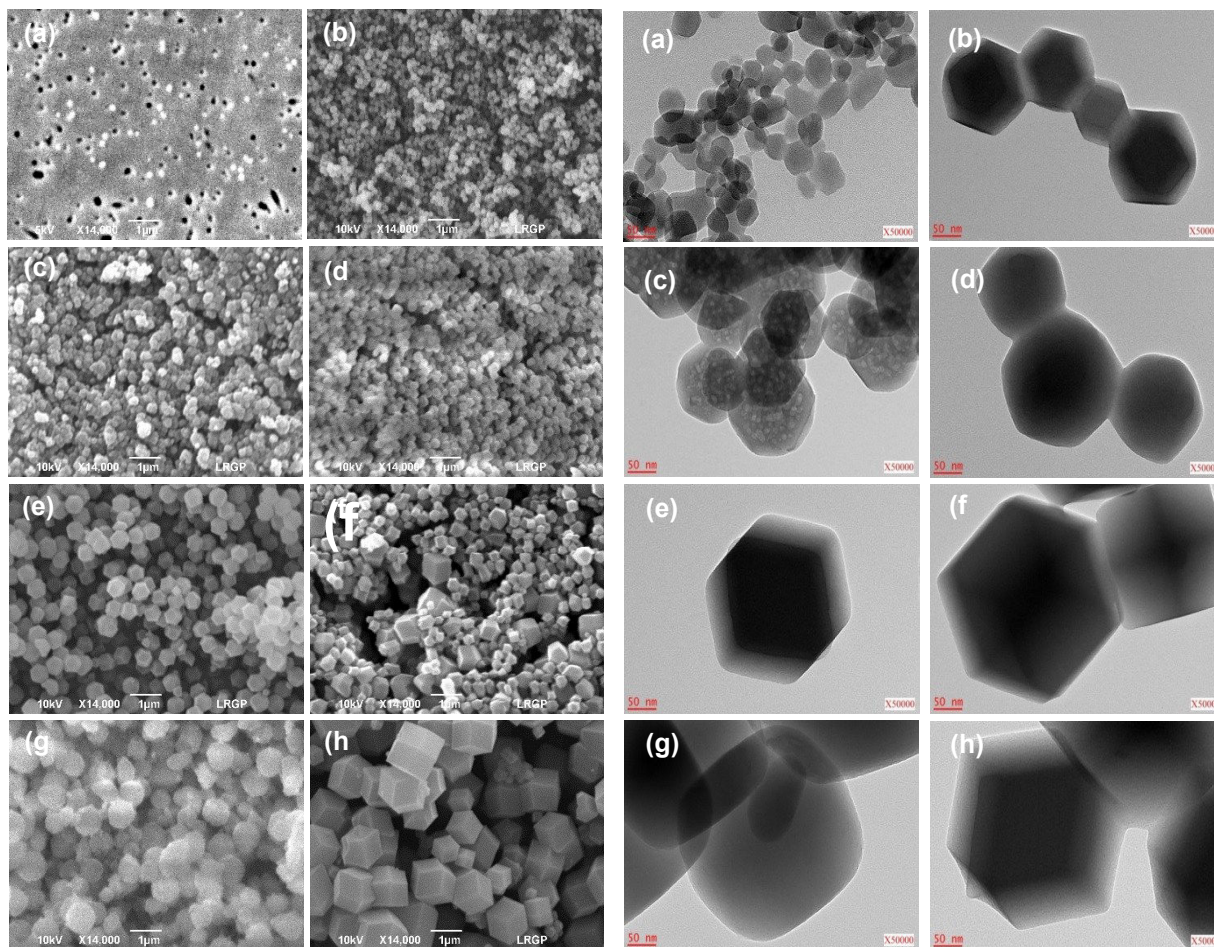


Fig. 3.1.3 SEM and TEM images of ZIF-8 crystals obtained after 1 h reaction using a Hmim/Zn ratio of 8/1 and starting from (a) $\text{Zn}(\text{Acac})_2$, (b) $\text{Zn}(\text{NO}_3)_2$, (c) ZnSO_4 , (d) $\text{Zn}(\text{ClO}_4)_2$, (e) $\text{Zn}(\text{OAc})_2$, (f) ZnCl_2 , (g) ZnI_2 , and (h) ZnBr_2 .

With these five reactive zinc precursors, a huge amount of Zn^{2+} ions are available to coordinate with Hmim and the number of nuclei generated by the complex formation is probably large resulting in a decrease of crystal size and crystal anisotropy. This is further supported by the maximum size of the crystals produced in these syntheses. The maximum size decreases because a larger number of nuclei can only grow to a smaller individual crystal size and the growth is stopped due to the rapid decrease of supersaturation.

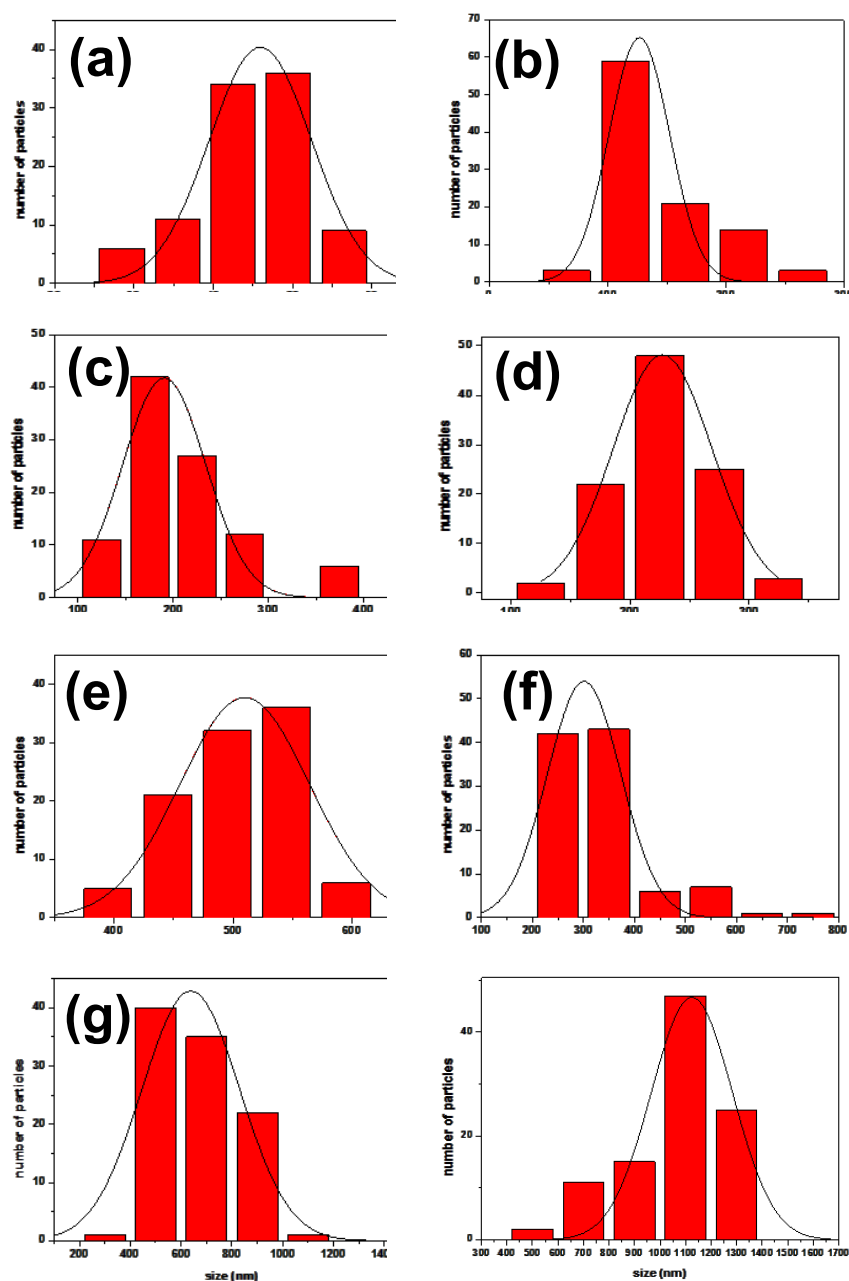


Fig. 3.1.4 Size distributions of ZIF-8 crystals obtained from SEM images described in Fig. 3.1.3.

With $\text{Zn}(\text{OAc})_2$ and ZnI_2 , the particles had the typical rhombic dodecahedron shape and their mean size is ca. 500 nm. The images show also that the particles have good uniformity, well-defined facets and sharp edges and corners (Fig. 3.1.3e and 3.1.3g). It is also worth to mention that the hydration degree of $\text{Zn}(\text{OAc})_2$ (anhydrous $\text{Zn}(\text{OAc})_2$ vs. $\text{Zn}(\text{OAc})_2 \cdot 2\text{H}_2\text{O}$) has no effect on the size and morphology of ZIF-8 crystals produced (data not shown). The largest nanocrystals, ca. 1050 nm in size, were observed with ZnBr_2 (Fig. 3.1.3h). Separated large grains with a rhombic dodecahedral shape were obtained together with cubes. All the particles have well-defined facets and sharp edges and corners. For this zinc precursor with lower reactivity, density of nuclei is reduced and nanoparticles grow through further direct addition of single monomeric mim^- and solvated Zn^{2+} ion species until the framework is formed.

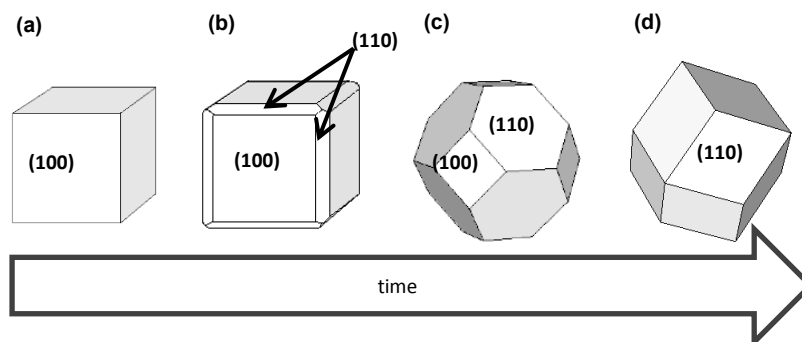


Fig. 3.1.5 Illustration of the crystal morphology evolution with time: (a) cube, (b) cube with truncated edges, (c) rhombic dodecahedron with truncated corners, and (d) rhombic dodecahedron.

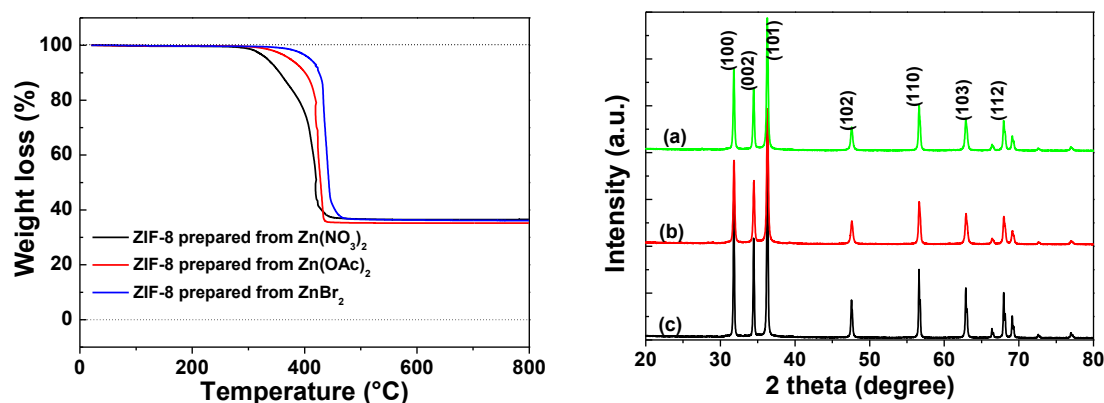


Fig. 3.1.6 TGA curves of ZIF-8 nanocrystals prepared from $\text{Zn}(\text{NO}_3)_2$ (black line), $\text{Zn}(\text{OAc})_2$ (red line), and ZnBr_2 (blue line) and XRD patterns of ZnO crystals obtained upon TGA experiments on ZIF-8 nanocrystals. (a) ZIF-8 prepared from zinc nitrate, (b) ZIF-8 prepared from zinc bromide, and (c) ZIF-8 prepared from zinc acetate.

Thermogravimetric analyses coupled to mass spectrometry (TGA/MS) were conducted on three representative samples prepared from $\text{Zn}(\text{NO}_3)_2$, $\text{Zn}(\text{OAc})_2$ and ZnBr_2 to gain information about the thermal stability of ZIF-8 nanocrystals (Fig. 3.1.6). From 20 to 250°C, the TGA curves exhibited only a very weak weight loss of less than 0.5%, corresponding to the removal of guest molecules (methanol or Hmim) and/or CO_2 from the cavities as indicated by MS analyses. A long plateau was then observed after the formation of the guest-free phase $\text{Zn}(\text{mim})_2$ until 350°C, indicating the good thermal stability of the three-dimensional network for all samples, which is comparable to that of the literature.¹³ Since nearly no weight loss is seen by TGA until 350°C before the onset of the exothermic decomposition of the mim bridging ligand, it is clear that the solvent or unreacted species have left the intracrystalline cavities during workup and that the synthetic protocol used affords highly pure nanocrystals that do not need solvent exchange and extensive drying for further use. The most significant feature observed in the TGA results is the size-dependent thermal stability up to 300°C in the case of the smaller 141-nm sized nanocrystals prepared from $\text{Zn}(\text{NO}_3)_2$, and up to 390°C in the case of the larger 1050 nm-sized crystals prepared from ZnBr_2 . A sharp weight loss step of ca. 63-64% was observed for all nanocrystals by further increasing the temperature from 400 to 500°C, indicating the thermal decomposition of ZIF-8 nanocrystals in that temperature range. This weight loss is in good agreement with the theoretical weight loss of 64% and indicates that zinc oxide [ZnO , $\text{Fw} = 81$] was

formed as the final calcination product of ZIF-8 nanocrystals [$\text{Zn}(\text{mim})_2$; Fw = 229] (see Fig. 3.1.6 for the XRD pattern of the product obtained which is in good accordance with ZnO reference pattern, JCPDS Card N° 79-2205).

The N_2 sorption properties of ZIF-8 samples prepared with $\text{Zn}(\text{NO}_3)_2$, $\text{Zn}(\text{OAc})_2$, and ZnBr_2 were next investigated (Fig. 3.1.7). It was found that they exhibited typical type-I adsorption isotherms with a high level of N_2 adsorption, indicating the microporous nature of the crystals. This was confirmed by the increase in the volume adsorbed at low relative pressures ($P/P_0 < 0.08$). The specific surface area and micropore volume of the ZIF-8 crystals prepared from $\text{Zn}(\text{NO}_3)_2$ were $1700 \pm 30 \text{ m}^2 \cdot \text{g}^{-1}$ and $0.66 \text{ cm}^3 \cdot \text{g}^{-1}$, values in perfect accordance with those of the literature ($S_{\text{BET}} = 1700 \text{ m}^2 \cdot \text{g}^{-1}$ and $V_{\text{micro}} = 0.64 \text{ cm}^3 \cdot \text{g}^{-1}$).¹³ Similar results were obtained with crystals prepared from ZnBr_2 ($S_{\text{BET}} = 1713 \pm 45 \text{ m}^2 \cdot \text{g}^{-1}$ and $V_{\text{micro}} = 0.63 \text{ cm}^3 \cdot \text{g}^{-1}$).

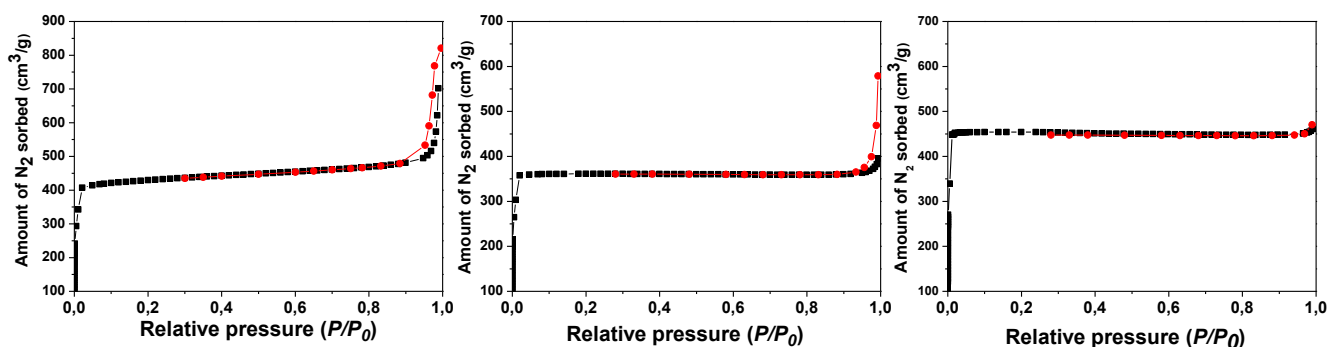


Fig. 3.1.7 Nitrogen sorption isotherms measured at 77 K on the powder ZIF-8 crystals obtained from (a) $\text{Zn}(\text{NO}_3)_2$, (b) $\text{Zn}(\text{OAc})_2$, and (c) ZnBr_2 . Black and red data correspond to the adsorption and desorption branches, respectively.

The BET surface areas of nanocrystals and pore volumes prepared from $\text{Zn}(\text{OAc})_2$ appear lower than those prepared from $\text{Zn}(\text{NO}_3)_2$ and ZnBr_2 ($S_{\text{BET}} = 1477 \pm 36 \text{ m}^2 \cdot \text{g}^{-1}$ and $V_{\text{micro}} = 0.55 \text{ cm}^3 \cdot \text{g}^{-1}$). The adsorption-desorption hysteresis loop of N_2 near $P/P_0 = 1$ originates from interparticles mesopores,³⁵ is consistent with the interparticles voids observed by SEM, and demonstrates the dual micro- and mesoporosity of ZIF-8 nanoparticles. It can further be observed that the adsorbed N_2 amount near $P/P_0 = 1$ increased for ZIF-8 crystals prepared with $\text{Zn}(\text{NO}_3)_2$ and $\text{Zn}(\text{OAc})_2$ compared to the sample prepared from ZnBr_2 . These results suggest that the interparticle porosity between ZIF-8 crystals produced from $\text{Zn}(\text{NO}_3)_2$ and $\text{Zn}(\text{OAc})_2$ increases due to the decrease in the particle size and confirms SEM and TEM results (*vide supra*).

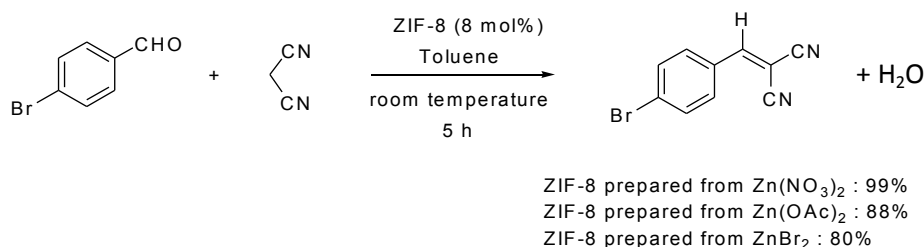


Fig. 3.1.8 Catalytic activities of ZIF-8 crystals prepared from different zinc sources in the Knoevenagel reaction.

In a last set of experiments, we evaluated the catalytic properties of ZIF-8 crystals produced from $\text{Zn}(\text{NO}_3)_2$, $\text{Zn}(\text{OAc})_2$, and ZnBr_2 in a Knoevenagel reaction involving malononitrile, which is well-established for ZIF-8 crystals.³⁶⁻³⁸ Condensations were conducted for 5 h at room temperature using 4-

bromobenzaldehyde as starting material and isolated yields in 2-(4-bromobenzylidene)malonitrile are reported in Fig. 3.1.8. As can be seen, the reaction worked effectively with the three catalysts but was only complete with ZIF-8 crystals produced from $\text{Zn}(\text{NO}_3)_2$. The reduced catalytic activity with the decrease of the external surface area of the ZIF-8 crystals is probably linked to the increase of adsorption rates of nanocrystals compared to microcrystals as recently observed with metal-organic framework nanofibers.³⁹

3.1.4 Conclusions

In conclusion, we demonstrated that phase pure ZIF-8 crystals can be produced from Hmim and various zinc sources in methanol at room temperature. The reactivity of the zinc salt in the growth solution was found to markedly affect the size and the morphology of ZIF-8 particles produced after 1 h reaction and at the same concentration in zinc salt. Small ZIF-8 nanocrystals with diameters varying between ca. 50 and 200 nm were obtained with reactive zinc salts like $\text{Zn}(\text{acac})_2$, $\text{Zn}(\text{NO}_3)_2$, ZnSO_4 or $\text{Zn}(\text{ClO}_4)_2$. The use of ZnCl_2 , $\text{Zn}(\text{OAc})_2$ or ZnI_2 afforded crystals with sizes varying between ca. 350 and 650 nm. Finally, the low reactive ZnBr_2 was found to generate microsized crystals. These significant changes in particle size induced distinctive changes in adsorption properties as demonstrated by BET measurements but also in the catalytic performances of ZIF-8 crystals in a Knoevenagel condensation used as model. The small sized crystals produced from $\text{Zn}(\text{NO}_3)_2$ exhibit the highest surface area and the best catalytic activity. Our results should open new opportunities to control the reactivity of ZIF-8 crystals in applications such as films and membranes.

3.1.5 References

- (1) Seo J.S., Whang D., Lee H., Jun S. I., Oh J., Jeon Y.J., Kim K., *Nature*, **2000**, 404, 982-986
- (2) Muller M., Hermes S., Kaehler K., van den Berg M. W. E., Mahler M., Fischer R. A., *Chem. Mater.*, **2008**, 20, 4576-4587
- (3) Gandora F., Puebla E. G., Iglesias M., Proserpio D. M., Shejko N., Monge M.A., *Chem. Mater.*, **2009**, 21, 655-661
- (4) Ma L. Q., Lee J. Y., Li J., Lin W. B., *Inorg. Chem.*, **2008**, 47, 3955-3957
- (5) Morris R.E., Wheatley P. S., *Angew. Chem. Int. Ed.*, **2008**, 47, 4966-4981
- (6) Hu Y. H., Zhang L., *Adv. Mater.*, **2010**, 22, E117-E130
- (7) Thallapally P. K., Tian J., Kishan M. R., Fernandez C. A., Dalgarno S. J., Mc Grail P. B., Warren J. E., Atwood J. L., *J. Am. Chem. Soc.*, **2008**, 130, 16842-16843
- (8) Yazaydin A. O., Snurr R. Q., Park T.-H., Koh K., Liu J., LeVan M. D., Benin A. I., Jakubczak P., Lanuza M., Galloway D. B., Low J. J., Willis R. R., *J. Am. Chem. Soc.*, **2009**, 131, 18198-18199
- (9) Wang B., Côté A. P., Furukawa H., O’Keeffe M., Yaghi O. M., *Nature*, **2008**, 453, 207-211
- (10) Banerjee R., Phan A., Wang B., Knobler C., Furukawa H., O’Keeffe M., Yaghi O. M., *Science*, **2008**, 319, 939-943
- (11) Hayashi H., Côté A. P., Furukawa H., O’Keeffe M., Yaghi O. M., *Nat. Mater.*, **2007**, 6, 501-506
- (12) Wu H., Zhou W., Yildirim T., *J. Am. Chem. Soc.*, **2007**, 129, 5314-5315
- (13) Park K. S., Ni Z., Côté A. P., Choi J. Y., Huang R. D., Uribe-Romo F. J., Chae H. K., O’Keeffe M., Yaghi O. M., *Proc. Natl. Acad. Sci. U.S.A.*, **2006**, 103, 10186-10191
- (14) Wu H., Zhou W., Yildirim T., *J. Am. Chem. Soc.*, **2009**, 131, 4995-5000
- (15) Pérez-Pellitero J., Amrouche H., Siperstein F. R., Pirngruber G., Nieto-Draghi C., Chaplais G., Simon-Masseron A., Bazer-Bachi D., Peralta D., Bats N., *Chem. Eur. J.*, **2010**, 16, 1560-1571
- (16) Venna S. R., Carreon M. A., *J. Am. Chem. Soc.*, **2010**, 132, 76-78
- (17) Krishna R., van Baten J. M., *J. Membr. Sci.*, **2010**, 360, 323-333
- (18) Huang A. S., Bux H., Steinbach F., Caro J., *Angew. Chem. Int. Ed.*, **2010**, 49, 4958-4961

- (19) Küsgens P., Rose M., Senkovska I., Fröde H., Henschel A., Siegle S., Kaskel S., *Microporous Mesoporous Mater.*, **2009**, 120, 325-330
- (20) Cychosz K. A., Matzger A. J., *Langmuir*, **2010**, 26, 17198-17202
- (21) Cravillon J., Nayuk R., Springer S., Feldhoff A., Huber K., Wiebcke M., *Chem. Mater.*, **2011**, 23, 2130-2141
- (22) Cravillon J., Schröder C. A., Nayuk R., Gummel J., Huber K., Wiebcke M., *Angew. Chem.*, **2011**, 123, 8217-8221
- (23) Cravillon J., Schröder C. A., Bux H., Rothkirch A., Caro J., Wiebcke M., *CrystEngCommun*, **2012**, 14, 492-498
- (24) Shah M., Kwon H. T., Tran V., Sachdeva S., Jeong H.-K., *Microporous Mesoporous Mater.*, **2013**, 165, 63-69
- (25) Nune S. K., Thallapally P. K., Dohnalkova A., Wang C., Liu J., Exarhos C. J., *Chem. Commun.*, **2010**, 46, 4878-4880
- (26) Pan Y., Heryadi D., Zhou F., Zhao L., Lestari G., Su H., Lai Z., *CrystEngCommun*, **2011**, 13, 6937-6940
- (27) Garai A., Shephard W., Huo J., Bradshaw D., *J. Mater. Chem. B*, **2013**, 1, 3678-3684
- (28) Biemmi E., Christian S., Stock N., Bain T., *Microporous Mesoporous Mater.*, **2009**, 117, 111-117
- (29) Torad N. L., Yu M., Kamachi Y., Takai K., Imura M., Naito N., Yamauchi Y., *Chem. Commun.*, **2013**, 49, 2521-2523
- (30) Zhu M., Venna S. R., Jasinski J. B., Carreon M. A., *Chem. Mater.*, **2011**, 23, 3590-3592
- (31) Cravillon J., Munzer S., Lohmeier S. J., Feldhoff A., Huber K., Wiebcke M., *Chem. Mater.*, **2009**, 21, 1410-1412
- (32) Bux H., Liang F., Li Y., Cravillon J., Wiebcke M., Caro J., *J. Am. Chem. Soc.*, **2009**, 131, 16000-16001
- (33) Venna S. R., Jasinski J. B., Carreon M. A., *J. Am. Chem. Soc.*, **2010**, 132, 18030-18033
- (34) Ratke L., Voorhes P. W. *Growth and Coarsening: Ripening in Material Processing; Springer: Berlin*, **2002**; p 117
- (35) Sing K. S. W., Everett D. H., Haul R. A. W., Moscou L., Pierotti L. A., Rouquérol J., Siemieniowska T., *Pure Appl. Chem.* 1985, **57**, 603-619
- (36) Tran V. P. N., Le K. K., Phan N. T. S., *ACS Catal.*, **2011**, 1, 120-127
- (37) Cho H.-Y., Kim J., Kim S.-N., Ahn W.-S., *Microporous Mesoporous Mater.*, **2013**, 169, 180-184
- (38) Jin R., Bian Z., Li J., Ding M., Gao L., *Dalton Trans*, **2013**, 42, 3936-3940
- (39) Ostermann R., Cravillon J., Weidmann C., Wiebcke M., Smarsly B. M., *Chem. Commun.*, **2011**, 47, 442-444

3.2 Cu²⁺-doped Zeolitic Imidazolate Frameworks (ZIF-8): Efficient and Stable Catalysts for Cycloadditions and Condensation Reactions

Schejn A., Aboulaich A., Balan L., Falk V., Lalevée J., Medjahdi G., Aranda L., Mozet K., Schneider R., *Catal. Sci. Technol.*, 2015, 5, 1829-1839

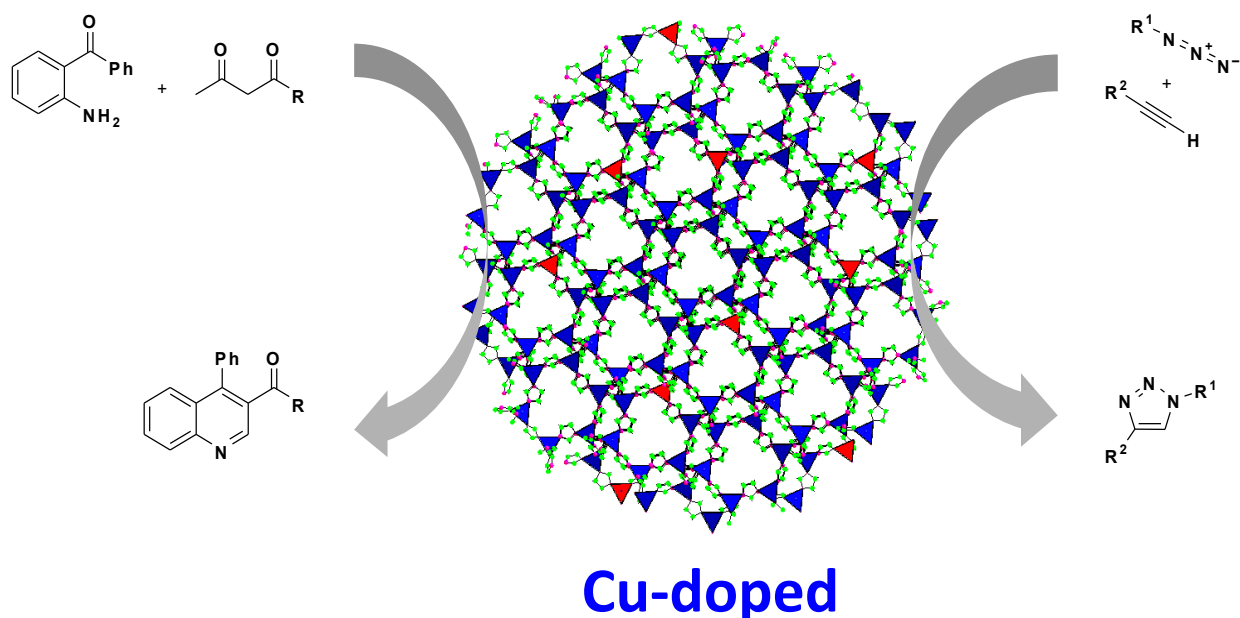


Fig. 3.2.1 Graphical abstract.

3.2.1 Abstract

Cu²⁺-doped zeolitic imidazolate frameworks (ZIFs) crystals were efficiently prepared by reaction of Cu(NO₃)₂, Zn(NO₃)₂, and 2-methylimidazole in methanol at room temperature. Scanning electron microscopy, transmission electron microscopy and X-ray diffraction showed that the Cu/ZIF-8 particles were nanosized (between ca. 120 and 170 nm) and that the body-centered cubic crystal lattice of the parent ZIF-8 framework is continuously maintained, regardless of the doping percentage. Moreover, thermogravimetric analyses and specific BET surface area measurements demonstrated that the doping doesn't alter the high stability of ZIF-8 crystals and that the porosity only decreases at a high doping percentage (8.7% in Cu²⁺). The Cu/ZIF-8 material showed excellent catalytic activity in the [3+2] cycloaddition of organic azides with alkynes and in Friedländer and Combes condensations due to the high catalyst surface area and the high dispersion of Cu/ZIF-8 particles. Notably, the Cu/ZIF-8 particles not only exhibit excellent performances but also had a great stability in the reaction, allowing their reuse up to ten times in condensation reactions. Our findings explored a simple and powerful way to incorporate metal ions into the backbones of open framework materials without losing their properties.

3.2.2 Introduction

Metal-organic frameworks (MOFs), which are porous crystalline materials consisting of metal ions or metal containing clusters coordinated to rigid organic molecules to form one-, two-, or three-dimensional networks, have attracted great attention due to their exceptional high surface area, high porosity, low density, and chemically tunable structures.¹⁻⁸ Among MOFs, the so-called zeolitic imidazolate frameworks (ZIFs) are extremely promising materials because they combine the pore size tunability of MOFs and the thermal stability of zeolites making them ideal candidates for applications such as gas storage,^{9,10} gas separation,^{6,11} catalysis¹² or drug delivery.¹³ ZIFs are constructed from tetrahedral units, in which each metal atom such as Zn^{2+} or Co^{2+} connects four imidazolate (im^-) ligands to form neutral frameworks.¹⁴⁻²⁰ ZIF-8 ($\text{Zn}(\text{mim})_2$, $\text{mim}^- = 2\text{-methylimidazolate}$), with the sodalite (SOD) topology, crystallizes in the cubic space group $I\bar{4}3m$ with a lattice constant of 16.992 Å and contains 276 atoms in the unit cell ($\text{Zn}_{12}\text{N}_{48}\text{C}_{96}\text{H}_{120}$). The sodalite cages possess a pore diameter of 11.6 Å and the aperture between two cages is 3.4 Å. ZIF-8 crystals are typical porous MOFs with unusual high thermal and chemical stability, as well as tunable zeotype topologies.^{2,14-19}

While the incorporation of metal or semiconductor nanoparticles into the ZIF framework is now well-documented,²⁰⁻²⁵ substitutional introduction of metal cations in the crystalline lattice has far less been studied. In the course of our studies related to the construction of ZIF-8 derived hybrid materials displaying sorptive, magnetic and/or catalytic properties, we sought to investigate the consequences of Cu^{2+} doping on the ZIF-8 framework. ZIF-8 is a wide bandgap material (bandgap energy $E_g = 4.9$ eV) and adsorbs only in the UV region.²⁶ Doping copper into ZIF-8 should not only allow to engineer its bandgap and displace its absorption into the visible-light area, but also to develop new nanomaterials combining both the catalytic and magnetic properties of Cu^{2+} and the high thermal and chemical stability of ZIF-8 crystals. For example, the presence of Cu^{2+} ions in the ZIF-8 structure should enable their use as reusable catalysts for coupling reactions and oxidation-reduction reactions, as recently described for $\text{Cu}(\text{im})_2$,^{27,28} CuBTC^{29} (Basolite™ C300, BTC = 1,3,5-benzene tricarboxylate) and $\text{Fe}(\text{BTC})$.³⁰ The association of Cu^{2+} ions with imidazole or its derivatives as ligands/linkers to construct MOFs^{27,28,31-46} or coordination polymers^{47,48} is well-established. The doping in copper of ZIF-67 ($\text{Co}(\text{im})_2$) and the photocatalytic properties of the $\text{Cu}/\text{ZIF-67}$ crystals under visible light irradiation have recently been reported.⁴⁹ Very recently, Li *et al.* reported also the successful incorporation of six-coordinated nickel(+2) clusters into ZIF-8 crystals cavities.^{50,51} The materials prepared found applications in alcohol sensing or carbon dioxide capture and separation after pyrolysis. So far, Cu^{2+} -doping into $\text{Zn}(\text{im})_2$ (ZIF-1) has only been described one time,⁵² and Cu^{2+} -doping into ZIF-8 has never been explored.

In this work, we report the successful preparation of Cu-doped ZIF-8 crystals and the application of these substitutionally doped particles as efficient heterogeneous catalysts for copper-catalyzed Huisgen 1,3-dipolar cycloadditions and for Friedländer and Combes condensations. These catalytic activities were gained without alteration of the stability of ZIF-8 crystals and with only a slight decrease of the specific area and pore size at high dopant percentage (8.7% Cu relative to Zn). The $\text{Cu}/\text{ZIF-8}$ crystals could be separated from the reaction mixture by simple centrifugation and could be reused up to ten times without a significant alteration in catalytic activity.

Scheme 3.2.1. Schematic representation of the synthesis of Cu-doped ZIF-8 crystals.

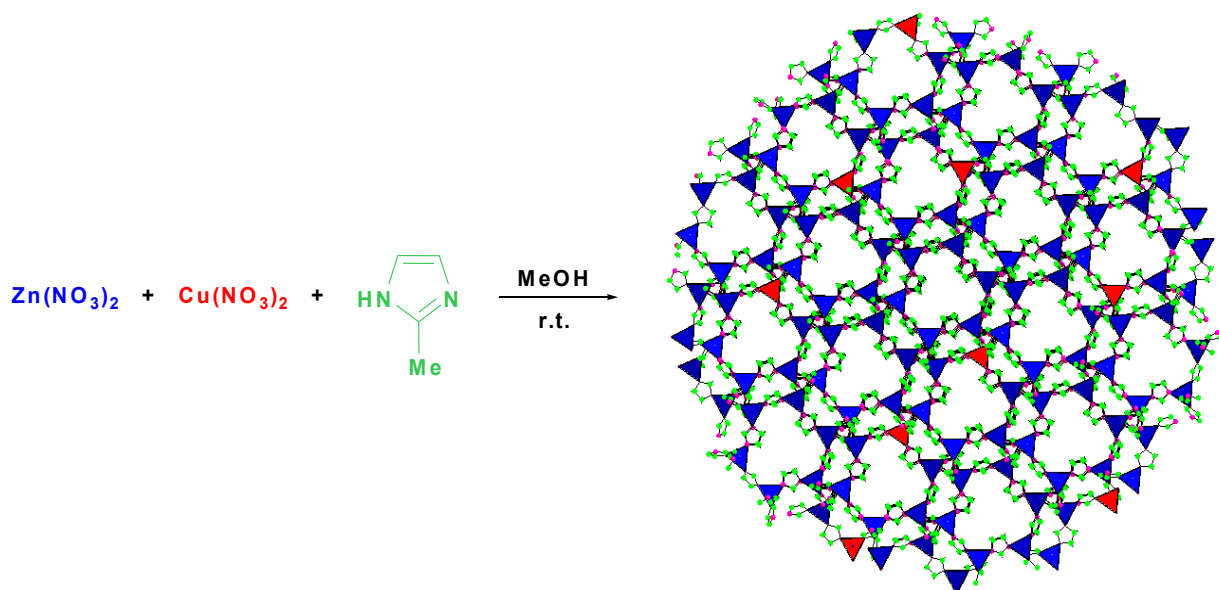


Fig. 3.2.2. Photographs showing the color change of Cu/ZIF-8 crystals upon increasing the doping percentage in copper. (a) ZIF-8 as reference, (b), (c), (d) and (e) are ZIF-8 crystals doped with 0.6, 2.1, 3.9 and 8.7% Cu, respectively.

3.2.3 Results

3.2.3.1 Cu-doped ZIF-8 crystals synthesis. The synthesis of Cu/ZIF-8 crystals was performed under solvothermal conditions by mixing $\text{Zn}(\text{NO}_3)_2$, $\text{Cu}(\text{NO}_3)_2$ and Hmim in ethanol at room temperature for 1 h (Scheme 2.3.1).^{19,55} Molar percentages of 1, 5, 10 and 25% of $\text{Cu}(\text{NO}_3)_2$ to $\text{Zn}(\text{NO}_3)_2$ were used in these experiments. The crystals prepared will be noted $\text{Cu}_{0.6\%}/\text{ZIF-8}$, $\text{Cu}_{2.1\%}/\text{ZIF-8}$, $\text{Cu}_{3.9\%}/\text{ZIF-8}$, and $\text{Cu}_{8.7\%}/\text{ZIF-8}$ thereafter. The incorporation of Cu^{2+} ions in the crystal lattice weakly slows down the kinetics of ZIF-8 particles precipitation (*vide infra*). It is also worth to mention that a complete collapse of ZIF-8 structure was observed at higher doping percentage (50%). The crystals obtained after reaction were recovered by centrifugation, washed and dried before characterization. A significant observation is that the color intensity of the samples and the strength of their main absorption bands (*vide infra*) correlate qualitatively with their Cu^{2+} content. As shown in Fig. 2.3.2, upon increasing the doping percentage in Cu^{2+} from 0.6 to 8.7%, the color changed from white to brown beige.

3.2.3.2 Cu-doped ZIF-8 nanocrystals characterization. When preparing pure ZIF-8 crystals from $\text{Zn}(\text{NO}_3)_2$, the solution became cloudy within 2 min after the addition of Hmim and a dense precipitate was obtained after 1 h of reaction. With the increase of the copper content in the reaction medium, the precipitate became less dense, thus indicating that the number of nuclei generated by the complex formation decreased. This was confirmed by TEM and SEM experiments (Fig. 3.2.3, 3.2.4 and 3.2.5).

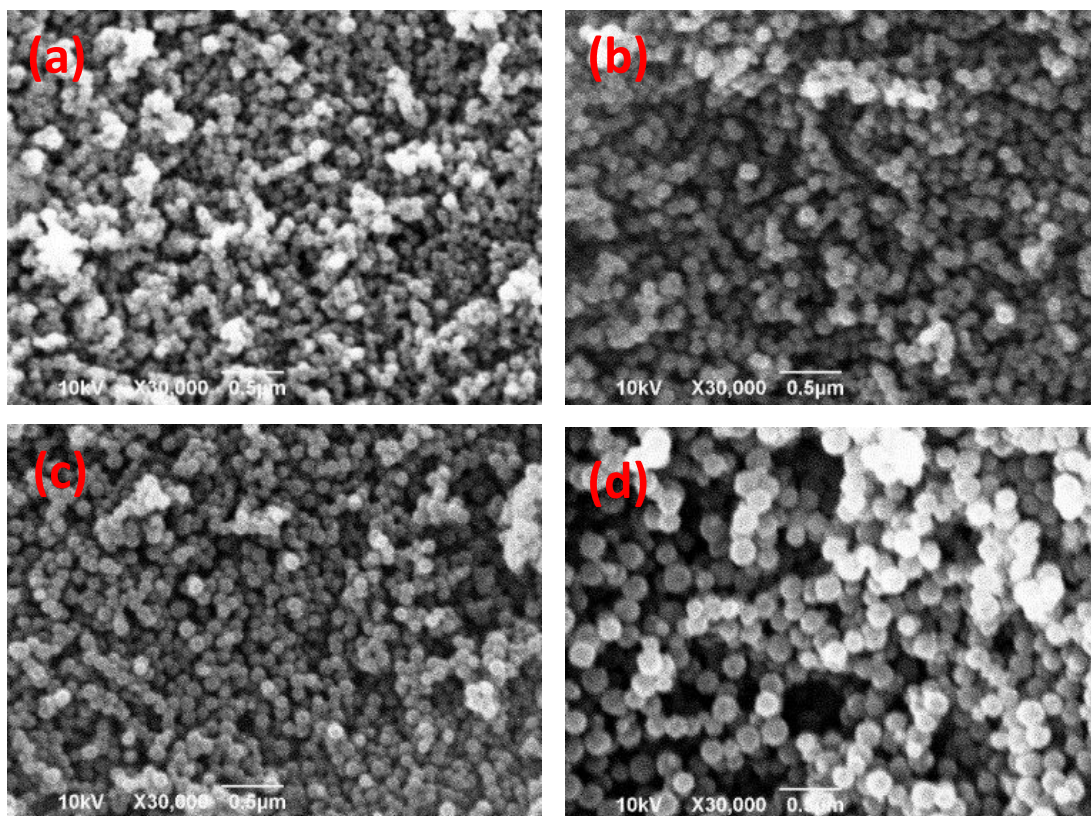


Fig. 3.2.3 SEM images of ZIF-8 crystals doped with (a) 0.6, (b) 2.1, (c) 3.9 and (d) 8.7% Cu^{2+} , respectively.

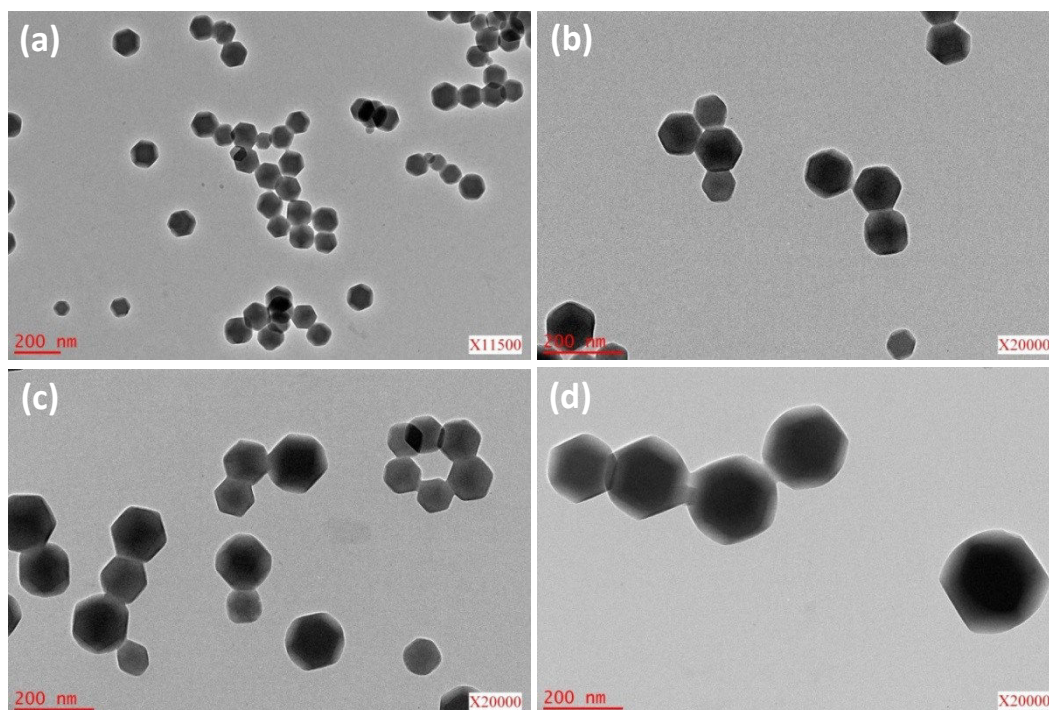


Fig. 3.2.4 TEM images of ZIF-8 crystals doped with (a) 0.6, (b) 2.1, (c) 3.9 and (d) 8.7% Cu^{2+} , respectively.

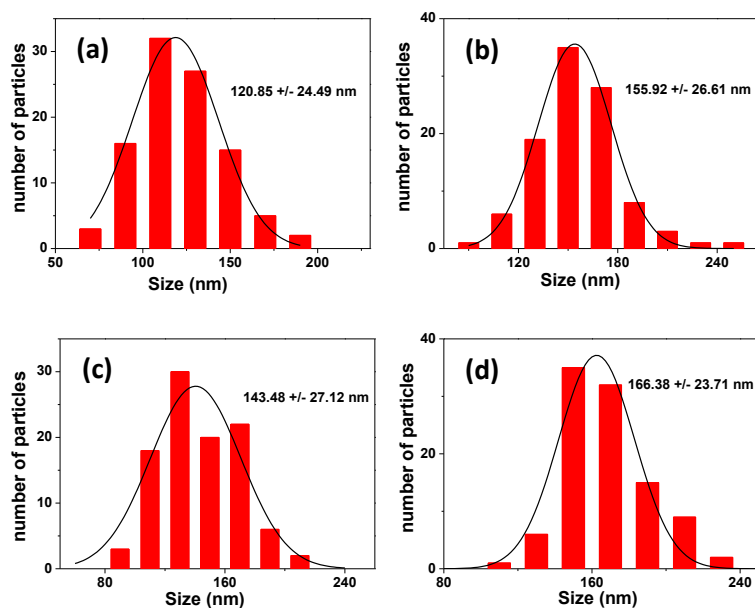


Fig. 3.2.5 Size distributions determined by SEM for ZIF-8 crystals doped with (a) 0.6, (b) 2.1, (c) 3.9, and (d) 8.7% Cu²⁺, respectively.

With increasing the Cu²⁺ doping percentage in the nanocrystals, the average diameters were found to increase from ca. 120 to 170 nm. This confirms that less nuclei were formed upon addition of Hmim and that Cu-doped ZIF-8 crystals initially formed grow through further addition of single monomeric mim⁻ and solvated Zn²⁺ and Cu²⁺ species until the framework is formed. Regardless of the doping percentage, TEM and SEM images showed rather small and monodispersed nanoparticles with a well-defined truncated rhombic dodecahedron structure, which is the typical ZIF-8 morphology. Inductively coupled plasma-optical emission spectrometry (ICP-OES) was used to determine the final copper content of Cu/ZIF-8 crystals for further characterization and catalytic experiments. ICP-OES reveals that the Cu/Zn ratios for all samples are lower than Cu/Zn ratios used for the synthesis, irrespective for the dopant percentage (the Cu²⁺ doping percentage in the crystals are 0.6, 2.1, 3.9, to 8.7% for reactions conducted with 1, 5, 10, and 25% Cu²⁺, respectively).

Powder X-ray diffraction (XRD) patterns of ZIF-8 and Cu/ZIF-8 crystals are shown in Fig. 3.2.6. For all the samples, the Cu/ZIF-8 crystals show a body-centered cubic crystal lattice group $I\bar{4}3m$ with a cell parameter a varying between 17.015 et 17.025 Å, which is in good accordance with the results reported for ZIF-8 in the literature.^{14,56} A slight decrease of the full-width at half-maximum of the (011) peak intensity was also observed when increasing the Cu doping percentage, which is consistent with the crystals size increase observed by TEM and SEM. Ni-substituted ZIF-8 crystals prepared via mechanochemical synthesis exhibited extra peaks in XRD patterns that were assigned to the clusters formed between Ni(+2) ions and Hmim that are trapped in ZIF-8 cavities.^{50,51} These extra peaks were not observed in our solution phase synthesis, thus indicating that Cu²⁺ ions are probably substitutionally doped in ZIF-8 crystals.

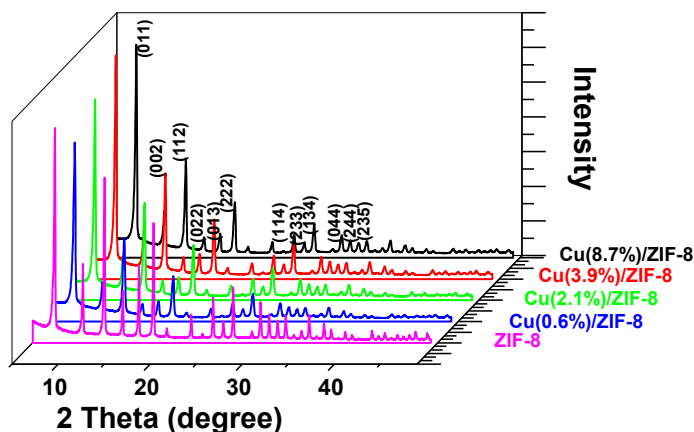


Fig. 3.2.6 XRD patterns of Cu/ZIF-8 crystals prepared with different doping percentages in Cu^{2+} .

Results depicted in Fig. 3.2.6 demonstrate that the presence of Cu^{2+} in the reaction medium during the growth of ZIF-8 crystals did not cause any structure alteration and that ZIF-8 materials still retained crystalline integrity after being doped with Cu^{2+} . It is likely that the doping with Cu^{2+} does not distort the lattice structure of ZIF-8 crystals since the ionic size of Cu^{2+} (0.71 Å) is only slightly smaller than that of Zn^{2+} (0.74 Å) in tetrahedral coordination. Finally, it is worth to mention that Cu^{2+} ions have been demonstrated to damage the crystallinity of ZIF-8 once added to these nanocrystals in aqueous solution due to interactions between Cu^{2+} ions and the mim^- linkers.⁵⁷ Such alterations were not observed under our experimental conditions. The presence of Cu^{2+} in the samples was further confirmed by UV-visible spectroscopy (Fig. 3.2.7). From the diffuse reflectance spectra and the corresponding absorption spectra of pure ZIF-8 and Cu-doped ZIF-8 crystals (Fig. 3.2.7a and 3.2.7b), it can be seen that doping shifts the adsorption edge of ZIF-8 crystals from the UV to the visible region. The absorption spectra of Cu-doped ZIF-8 crystals exhibit a first well-defined band located at ca. 490 nm and a second broad one starting at 600 nm and going to the infrared with a shoulder at ca. 850 nm. These bands can both be attributed to d-d transitions of Cu^{2+} ions and confirm the heterobimetallic nature of the ZIF materials produced.

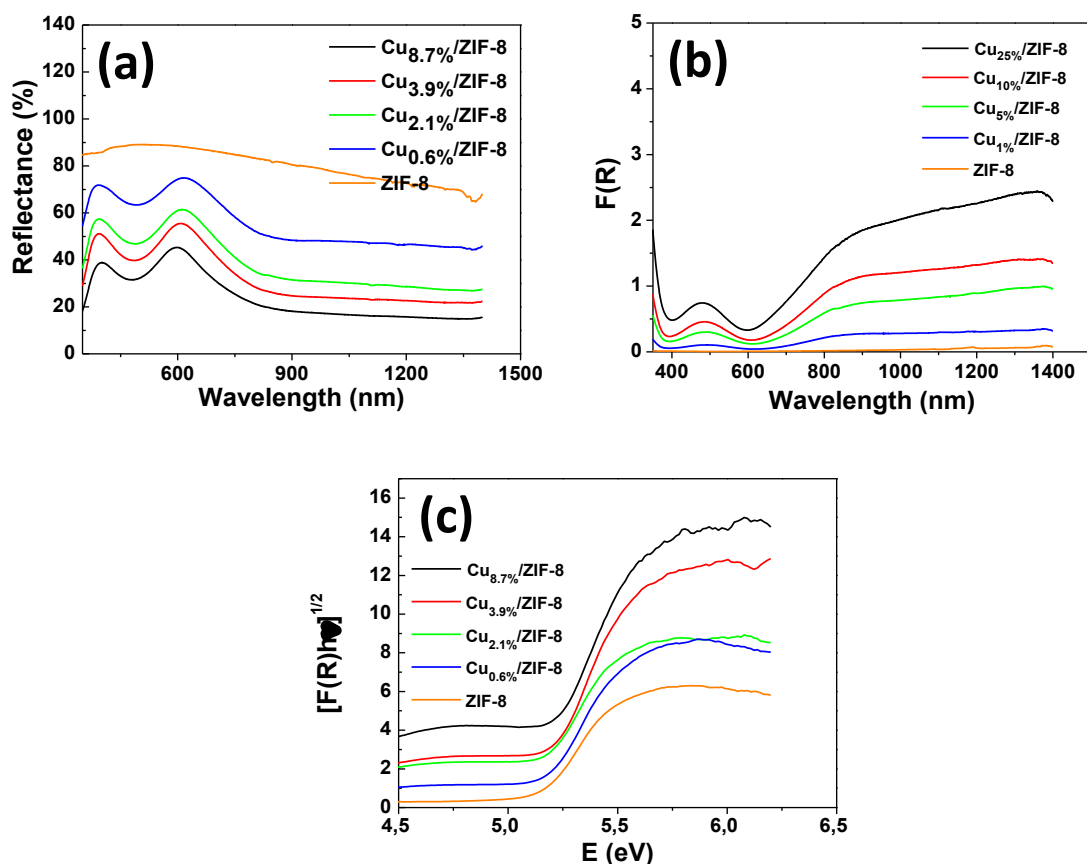


Fig. 3.2.7 (a) Diffuse reflectance and (b) absorption spectra of ZIF-8 and Cu-doped ZIF-8 crystals, and (c) $[F(R)hv]^{1/2}$ vs $h\nu$ curves for ZIF-8 and Cu/ZIF-8 crystals.

The slight differences observed in the absorption spectra compared to Cu(+2)/imidazolate complexes described in the literature may originate from different coordination geometries around Cu(+2) ions.^{58,59} Additionally, reflectance and absorption spectra of all Cu/ZIF-8 crystals exhibit the same bands, demonstrating that the structures of these materials are the same regardless of the doping percentage. ZIF-8 is a wide band gap material with a band gap energy equal to 4.9 eV.²⁶ The band gap energies of the Cu/ZIF-8 samples have been determined from the absorbance $[F(R)]$ spectra using the Kubelka-Munk formalism and Tauc plot. For indirect band gap semiconductors, the energy band gap can be estimated from the tangent line in the plot of the square root of Kubelka-Munk functions $F(R)$ against photon energy, as shown in Fig. 3.2.7c. The tangent lines, which are extrapolated to $(F(R))^{1/2} = 0$, indicate that the band gaps of Cu_{0.6%}/ZIF-8, Cu_{2.1%}/ZIF-8, Cu_{3.9%}/ZIF-8, and Cu_{8.7%}/ZIF-8 are 5.09, 5.07, 5.04, and 4.92 eV, respectively, while the band gap of undoped ZIF-8 is equal to 5.10 eV. These results are in agreement with the emergence of strong absorption bands within ZIF-8 after Cu²⁺ doping. The results are also in line with the stronger absorption intensity observed with increasing Cu²⁺ doping as shown in Fig. 3.2.7b.

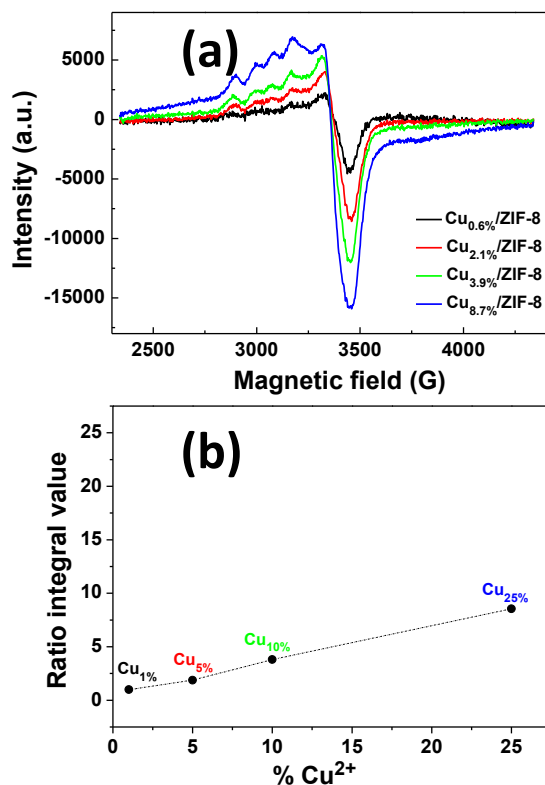


Fig. 3.2.8 (a) ESR spectra for the different Cu/ZIF-8 samples and (b) double integration of the ESR spectrum vs. Cu doping.

The ESR spectra of the Cu/ZIF-8 crystals are shown in Fig. 3.2.8a. The spectra exhibit one intense signal in the high field and four well-resolved peaks in the low field region, which corroborate the presence of Cu(+2) in the materials. Interestingly, the double integration of the ESR spectra increases linearly with the Cu doping (Fig. 3.2.8b). The Cu/Zn ratios estimated by ESR (1.0, 1.87, 3.81 and 8.54% Cu²⁺ for Cu_{0.6%}/ZIF-8, Cu_{2.1%}/ZIF-8, Cu_{3.9%}/ZIF-8, and Cu_{8.7%}/ZIF-8 crystals, respectively) are in good agreement with values determined by ICP-OES (*vide supra*).

3.2.3.3 Porosity and stability of Cu/ZIF-8 crystals. Permanent porosities of Cu/ZIF-8 materials were demonstrated by N₂ adsorption at 77K (Fig. 3.2.9). Type I isotherms were obtained for the four Cu/ZIF crystals with BET surface areas of 1541, 1736, 1639, and 1205 m².g⁻¹ for 0.6, 2.1, 3.9 and 8.7% Cu doping, respectively, indicating microporous structure (Table 3.2.1).

Table 3.2.1. Comparison of BET, pore volume, and pore size for ZIF-8 and Cu-doped ZIF-8 crystals.

Material	BET (m^2g^{-1})	Pore volume (cm^3g^{-1})	Pore size (nm)
ZIF-8	1700 ± 30	0.662	1.2922
Cu _{0.6%} /ZIF-8	1541 ± 40	0.518	1.2214
Cu _{2.1%} /ZIF-8	1736 ± 59	0.601	1.2179
Cu _{3.9%} /ZIF-8	1639 ± 56	0.571	1.2169
Cu _{8.7%} /ZIF-8	1205 ± 47	0.440	1.2190

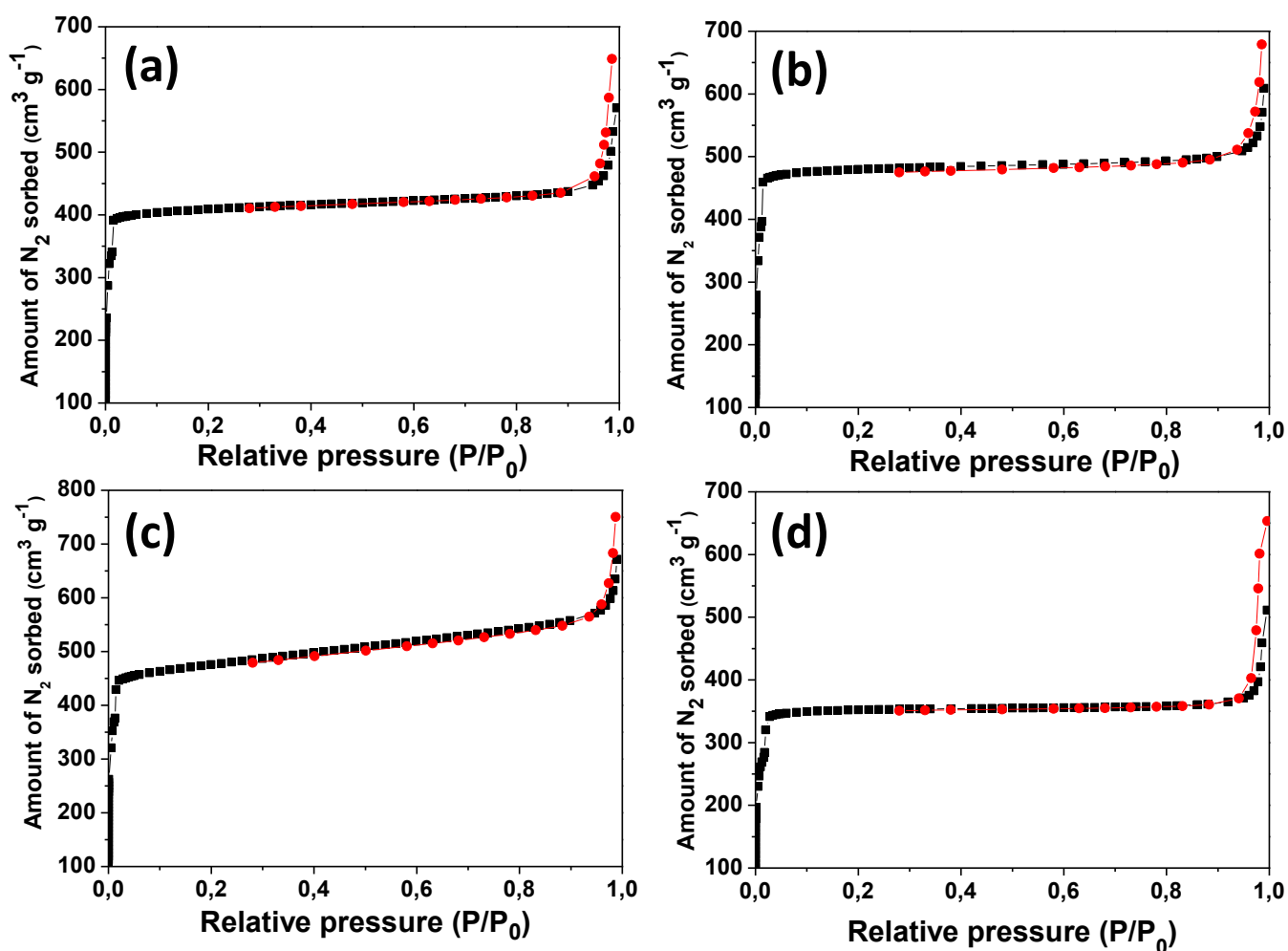


Fig. 3.2.9 N₂ adsorption/desorption curves at 77K for Cu/ZIF materials doped with (a) 0.6% Cu, (b) 2.1% Cu, (c) 3.9% Cu, and (d) 8.7% Cu, giving surface areas of 1541, 1736, 1639, and 1205 m^2g^{-1} , respectively. Black and red data correspond to the adsorption and desorption branches, respectively.

This structure was further confirmed by the increase in the volume adsorbed at low relative pressures ($P/P_0 < 0.08$). The adsorption-desorption hysteresis loop of N_2 near $P/P_0 = 1$, which originates from interparticle mesopores, is consistent with the interparticle voids and further confirms the dual micro- and mesoporosity of Cu/ZIF crystals.⁶⁰ Until 10% of doping in Cu^{2+} , the crystals properties were only slightly affected by the Cu^{2+} substitution. Surface areas and micropore volumes correspond well with those of pure ZIF-8 ($S_{BET} = 1700 \text{ m}^2\text{g}^{-1}$ and $V_{\text{micro}} = 0.63 \text{ cm}^3\text{g}^{-1}$) (Table 3.2.1).^{14,19} The BET surface areas and pore volumes of nanocrystals prepared with 8.7% Cu doping were found to be lower than those measured with weaker doping percentage in Cu. Finally, pore size distribution (calculated by the Horvath-Kawazoe method, Saito-Foley adaptation for cylindrical pore geometry) are centered around 1.2 nm and perfectly agree with that from the ZIF-8 structural model. The thermogravimetric analyses coupled to mass spectrometry (TGA/MS) of ZIF-8 and Cu/ZIF-8 samples only differ slightly (Fig. 3.2.10). From 20 to 200°C, the TGA curves exhibited only a very weak weight loss of less than 0.5%, corresponding to the removal of guest molecules (methanol or Hmim and/or CO_2 from the cavities as indicated by MS analyses). A long plateau was then observed after the formation of the guest-free Cu/Zn(mim)₂ crystals until 350°C, indicating good thermal stability of the three-dimensional network for all samples, which is comparable to the literature.^{14,19}

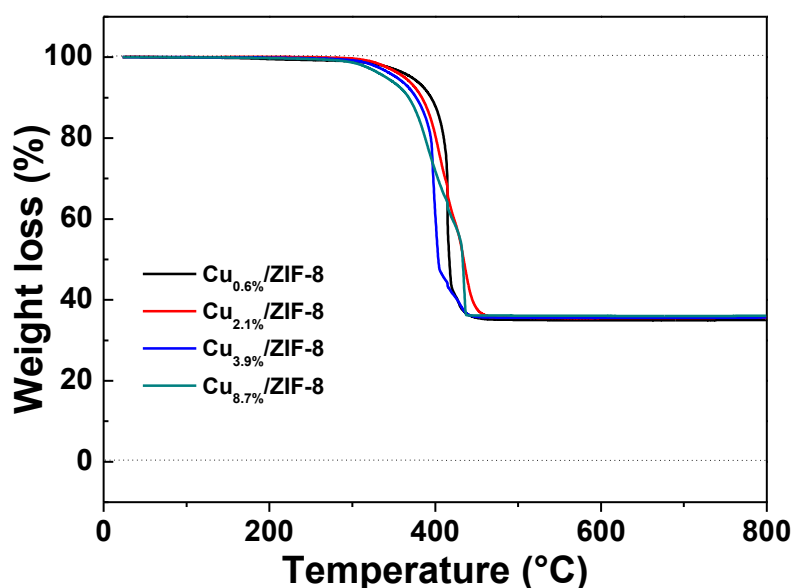


Fig. 3.2.10 TGA traces of ZIF-8 and Cu-doped ZIF-8 crystals.

All curves exhibit one step which can be assigned to the decomposition of the mim^- linker above 350°C (onset of the exothermic decomposition). The sharp weight loss of ca. 63-64% observed upon increasing the temperature from 400 to 500°C is in good agreement with the theoretical weight loss of 64%. The residue is wurtzite Cu-doped ZnO as proven by XRD measurements. It is also worth to mention that Cu/ZIF-8 crystals from this work exhibit higher thermal stability than Cu-based MOFs like Cu(BDC) used for catalytic applications, which already decompose at 200°C.²⁷

Finally, the chemical stability of Cu/ZIF-8 crystals was evaluated by dispersing the samples in boiling water, 1M NaOH, toluene or methanol, conditions that reflect extreme operational parameters of

typical industrial chemical process. Powder XRD patterns recorded for each sample after one week heating indicate that the topology of the ZIF-8 framework is preserved in 1M NaOH, toluene or methanol. Only the sample heated in water at neutral pH gradually decomposed into ZnO (see Fig. 3.2.11).

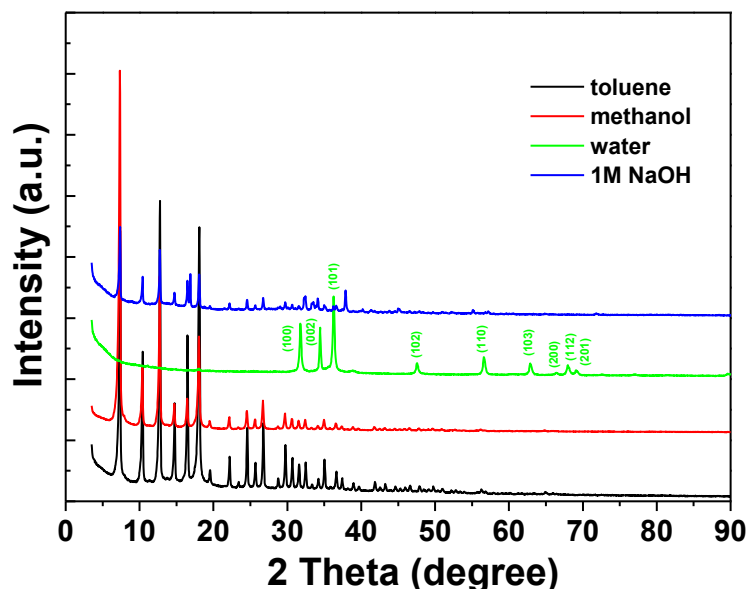
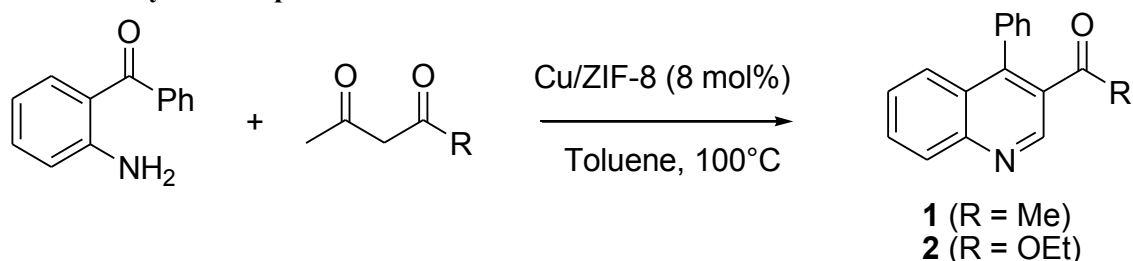


Fig. 3.2.11 XRD patterns of Cu/ZIF-8 crystals after one week heating in refluxing toluene, methanol, water, and 1M NaOH.

3.2.3.5 Cu/ZIF-8 particles as catalysts for Friedländer and Combes condensations. The catalytic activity of Cu/ZIF-8 crystals was first evaluated in the copper-catalyzed synthesis of quinoline derivatives, heterocycles of high interest due to their broad range of pharmaceutical and biological activities.⁶¹⁻⁶⁴ We carried out the condensation of 2-aminobenzophenone with acetylacetone or ethyl acetoacetate in the presence of Cu/ZIF-8 crystals (Scheme 3.2.2).

Scheme 3.2.2 Cu/ZIF-8 catalyzed Friedländer reactions between 2-aminobenzophenone and active methylene compounds.



The reactions were conducted using a 2-aminobenzophenone/active methylene compound molar ratio of 1/1.5 and in toluene at 100°C. Poor conversion of 2-aminobenzophenone (less than 10%) was observed with the Cu_{0.6%}/ZIF-8 material but the reaction proceeded efficiently in 8 h with Cu_{2.1%}/ZIF-8 crystals yielding compounds **1** and **2** in quantitative yields. In addition, although the final yields of **1** and **2** when operating with catalysts containing a higher copper percentage (3.9 or 8.7%) were almost

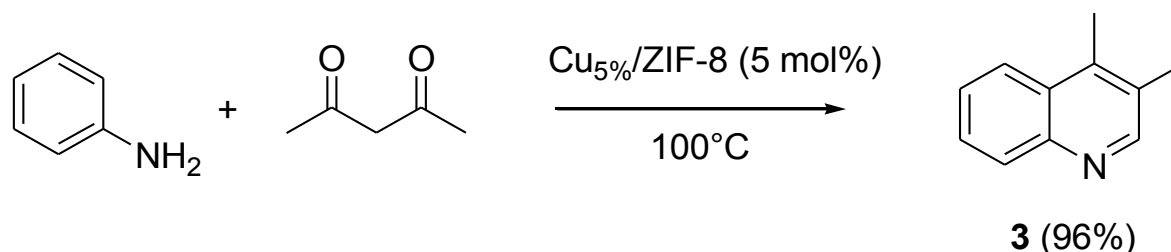
the same, the reaction times were reduced to ca. 5 h. It is also worth to mention that products **1** and **2** of the Friedländer condensation were not obtained in control experiments carried out either without catalyst or with ZIF-8 crystals. Cu^{2+} ions, acting as Lewis acids in the Friedländer reaction, are randomly located in the Cu/ZIF-8 crystals. Poor results obtained with the $\text{Cu}_{0.6\%}/\text{ZIF-8}$ material seem to indicate that the reaction proceeds on the external surface of the catalyst and that Cu^{2+} ions located in the pores are probably not accessible to reactants. With the increase of Cu^{2+} doping, more of these ions should be present at the surface of the Cu/ZIF-8 catalyst and its activity increased. To confirm the key role of Cu^{2+} species in the Friedländer reaction, we carried out the condensation of 2-aminobenzophenone with ethyl acetoacetate in the presence of 100 equivalents of pyridine relative to the Cu/ZIF-8 catalyst. In the presence of the pyridine catalyst poison, the quinoline **2** was not detected, thus indicating that pyridine strongly bounds and completely blocks catalytically active Cu^{2+} sites. Finally, to demonstrate that the Cu/ZIF-8 is a real heterogeneous catalyst and that catalytically active Cu^{2+} ions are not leaked in the medium during the course of the reaction, a centrifugation was carried out after 15 min of reaction and the catalyst separated. No further conversion of starting materials was observed upon further heating the supernatant at 100°C , thus confirming that the condensation is mediated by a heterogeneous catalyst.

We also investigated different catalyst loadings in the course of the reaction leading to quinoline **2** and found that 8 mol% $\text{Cu}_{2.1\%}/\text{ZIF-8}$ afforded the best results. Decreasing the amount of $\text{Cu}_{2.1\%}/\text{ZIF-8}$ led to lower yields of **1** and **2**, therefore the optimum catalyst amount was kept at 8 mol%.

We next studied the Combes condensation using Cu/ZIF-8 as catalyst of aniline with acetylacetone leading to 2,4-dimethylquinoline **3** (Scheme 3.2.3). Since both starting materials are liquid, the reaction was carried out under solvent-free conditions using an excess of acetylacetone (5 equiv.). Quinoline **3** was isolated in 96% yield after column chromatography using the $\text{Cu}_{2.1\%}/\text{ZIF-8}$ catalyst for 5 h at 100°C . As previously observed during the Friedländer condensations, product **3** was not detected in the absence of catalyst or with ZIF-8.

Finally, we checked the reusability of Cu/ZIF-8 as heterogeneous catalyst in Friedländer and Combes reactions yielding products **2** and **3**, respectively. After the reaction, the catalyst was recovered by centrifugation, washed with ethanol, dried at 70°C and used for another consecutive run without further treatment. In both cases, the catalyst exhibited no decrease in activity after five runs. As shown in Fig. 3.2.12, the shape and the crystallinity of the particles after the five cycles remained unchanged, thus showing its stability and recyclability. A strong decrease in catalytic activity was only observed after the 10th run (44%).

Scheme 3.2.3. Cu/ZIF-8-catalyzed Combes reaction between aniline and acetylacetone.



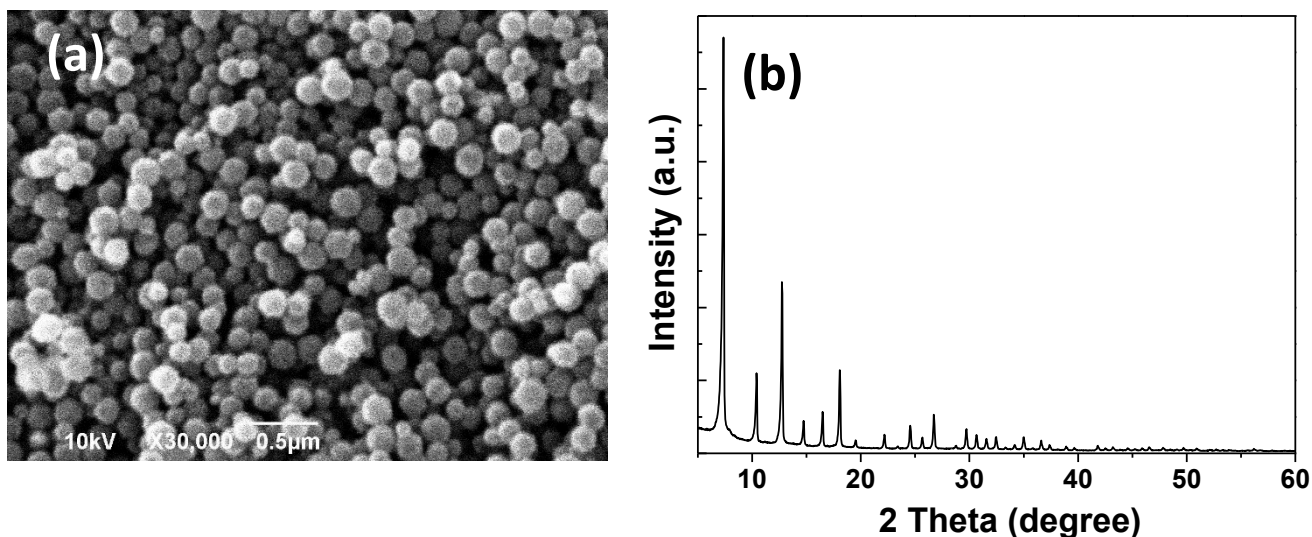
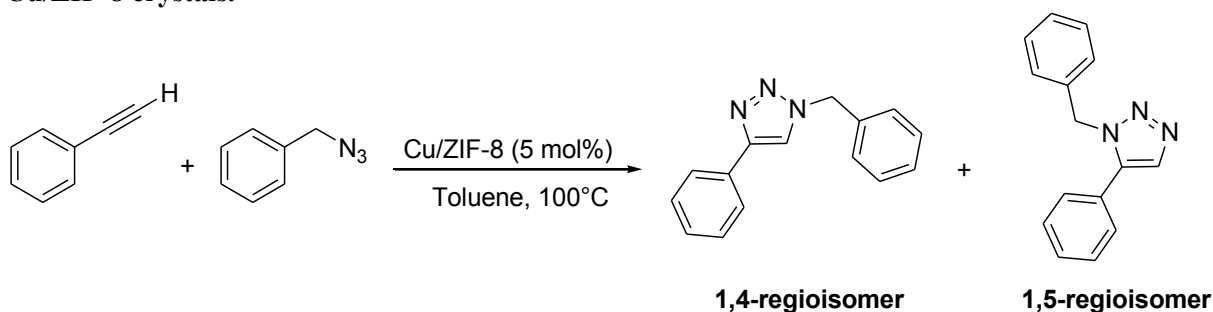


Fig. 3.2.12 (a) SEM image and (b) XRD pattern of ZIF-8 after five reuses in the Combes condensation.

Table 3.2.2 Influence of the Cu-doping on the regioselectivity of cycloadditions catalysed by Cu/ZIF-8 crystals.



Catalyst	1,4-regioisomer ^a	1,5-regioisomer ^a	Yield ^b (%)
Cu _{0.6%} /ZIF-8	45	55	79
Cu _{2.1%} /ZIF-8	50	50	98
Cu _{3.9%} /ZIF-8	62	38	99
Cu _{8.7%} /ZIF-8	92	8	99

^a Percentages determined by ¹H NMR.

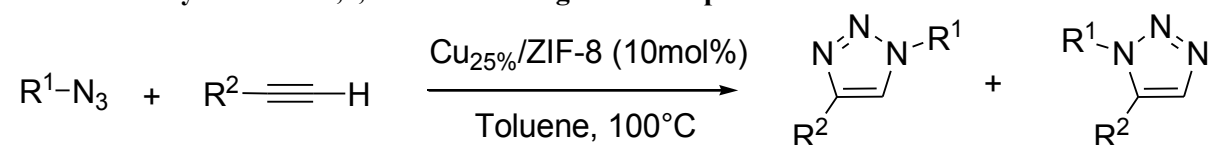
^b Isolated yields after column chromatography.

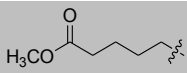
3.2.3.6 Cu/ZIF-8 crystals in 1,3-dipolar cycloadditions. Huisgen's dipolar cycloaddition (click reaction) between organic azides and alkynes is the most important synthetic route to 1,2,3-triazoles.⁶⁵ The discovery that copper(+1) efficiently catalyses this cycloaddition providing triazoles under mild

conditions and the 1,4-isomer with high regioselectivity was a welcome advance.^{66,67} In recent years, click reactions have found many applications in chemistry, biology and materials science.⁶⁸⁻⁷⁰ Cu(+2) in the absence of reducing agent like ascorbate can also catalyse the cycloaddition of azides and alkynes but this reaction generally suffers from drawbacks like high catalyst loading and low yield compared to Cu(+1)-catalyzed reactions.⁷¹⁻⁷⁵ In these screens, a mixture of benzylazide and phenylacetylene (1:1.2 equiv, respectively) was heated in toluene at 100°C for 3 h in the presence of 5 mol% of the Cu/ZIF catalyst. The resulting mixture was next analyzed by ¹H NMR. As shown in Table 3.2.2, we were pleased to find out that Cu/ZIF-8 crystals catalyse the formation of 1,2,3-triazoles with catalytic activity and regioselectivity being dependent on the Cu dopant percentage. With the Cu_{8.7%}/ZIF-8 catalyst, the consumption of benzylazide was complete and the 1,4-isomer was obtained with a high regioselectivity (92/8). Under similar experimental conditions, undoped ZIF-8 crystals were completely ineffective in catalysing the cycloaddition and no trace of triazole was detected even after 24 h heating in toluene at 100°C.

We next evaluated the scope of this new Cu/ZIF-8 catalyzed process. All reactions were performed with 5 mol% of Cu_{8.7%}/ZIF-8 in toluene at 100°C. As can be seen in Table 3.2.3, various combinations of organic azides and alkynes were efficiently converted into the corresponding disubstituted triazoles without any additive. Not only benzylic but also aliphatic azides gave excellent yields. Aliphatic alkynes worked also well as reaction partners of organic azides. The regioselectivity was good, varying from 78/22 to 95/5. After reaction, the Cu_{25%}/ZIF-8 particles were separated through centrifugation and used in click reactions between phenylacetylene and octylazide without loss of catalytic activity during five cycles.

Table 3.2.3. Synthesis of 1,2,3-triazoles using Cu/ZIF-8 particles.



R ¹	R ²	1,4/1,5	Yield ^a (%)
Bn	Ph	92/8	99
Octyl	Ph	79/21	90
Octyl	SiMe ₃	95/5	84
	Ph	78/22	97

^a Isolated yields after column chromatography.

3.2.4 Conclusions

In summary, we have demonstrated that ZIF-8 crystals could be easily doped with Cu²⁺ ions (between 0.6 and 8.7%) without alteration of ZIF-8 thermostability (up to 350°C in air) and crystallinity. An increase of ZIF-8 particles from ca. 120 to 170 nm was observed when increasing the dopant percentage from 0.6 to 8.7%. Until 3.9% doping in copper, the permanent porosities of Cu/ZIF-8

particles were not altered but decreased slightly from ca. 1600 to 1200 m².g⁻¹ when 8.7% Cu²⁺ relative to Zn²⁺ was used. Importantly, Cu/ZIF-8 particles were proven to be efficient and reusable catalysts for the [3+2] cycloaddition of organic azides with alkynes and for Friedländer and Combes condensations. The Cu_{2.1%}/ZIF-8 crystals showed high catalytic activity in the synthesis of quinolines using 2-aminobenzophenone as starting material. 1,4-Disubstituted triazoles were obtained with excellent yields and good regioselectivity using the Cu_{8.7%}/ZIF-8 material. These results combined with the high stability and the ease of regeneration of ZIF-8 particles may serve as a starting point to develop new nanomaterials based on metal organic frameworks with high adsorbent properties and enhanced catalytic properties.

2.3.6 References

- (1) Sco J. S., Whang D., Lee H., Jun S. I., Oh, J., Leon Y. J., Kim K., *Nature*, **2000**, 404, 982-986
- (2) Hayshi H., Cote A. P., Furukawa H., O’Keeffe M. O., Yaghi O. M., *Nat. Mater.*, **2007**, 6, 501-506
- (3) Thallapally P. K., Tian J., Kishan M. R., Fernandez C. A., Dalgarno S. J., Mc Grail P. B., Warren J. E., Atwood J. L., *J. Am. Chem. Soc.*, **2008**, 130, 16842-16843
- (4) Britt D., Tranchemontagne D., Yaghi O. M., *Proc. Natl. Acad. Sci. U.S.A.*, **2008**, 105, 11623-11627
- (5) Britt D., Furukawa H., Wang B., Glover G., Yaghi O. M., *Proc. Natl. Acad. Sci. U.S.A.*, **2009**, 106, 20637-20640
- (6) Li J.-R., Kuppler R. J., Zhou H.-C., *Chem. Soc. Rev.*, **2009**, 38, 1477-1504
- (7) Xiang Z. H., Cao D. P., Lan J. H., Wang W. C., Broom D. P., *Energy Environ. Sci.*, **2010**, 3, 1469-1487
- (8) Benmansour S., Atmani C., Setifi S., Triki S., Marchivie M., Gomez-Garcia C. J., *Coord. Chem. Rev.*, **2010**, 254, 1468-1478
- (9) Morris R., Wheatley P., *Angew. Chem. Int. Ed.*, **2008**, 47, 4966-4981
- (10) Farha O. K., Yazaydin A. O., Eryazici I., Malliakas C. D., Hauser B. G., Kanatzidis M. G., Nguyen S. T., Snurr R. Q., Hupp J. T., *Nat. Chem.*, **2010**, 2, 944-948
- (11) Chen B., Liang C., Yang J., Contreras D. S., Clancy Y. L., Lobkovsky E. B., Yaghi O. M., Dai S. A. A., *Angew. Chem. Int. Ed.*, **2006**, 45, 1390-1393
- (12) Lee J., Farha O. K., Roberts J., Scheidt K. A., Nguyen S. T., Hupp J. T., *Chem. Soc. Rev.*, **2009**, 38, 1450-1459.
- (13) Horcajada P., Chalati T., Serre C., Gillet B., Sebrie C., Baati T., Eubank J. F., Heurtaux D., Clayette P., Kreuz C., Chang J.-S., Hwang Y. K., Marsaud V., Bories P.-N., Cynober L., Gil S., Férey G., Couvreur P., Gref R., *Nat. Mater.*, **2010**, 9, 172-178
- (14) Park K. S., Ni Z., Côté A. P., Choi J. Y., Huang R. D., Uribe-Romo F. J., Chae H. K., O’Keeffe M., Yaghi O. M., *Proc. Natl. Acad. Sci. U.S.A.*, **2006**, 103, 10186-10191
- (15) Huang X. C., Lin Y. Y., Zhang J. P., Chen X. M., *Angew. Chem. Int. Ed.*, **2006**, 45, 1557-1559
- (16) Wang B., Côté A. P., Furukawa H., O’Keeffe M., Yaghi O. M., *Nature*, **2008**, 453, 207-211
- (17) Banerjee R., Phan A., Wang B., Knobler C., Furukawa H., O’Keeffe M., Yaghi O. M., *Science*, **2008**, 319, 939-943
- (18) Wu H., Zhou W., Yildirim T., *J. Am. Chem. Soc.*, **2007**, 129, 5314-5315
- (19) Schejn A., Balan L., Falk V., Aranda L., Medjahdi G., Schneider R., *CrystEngComm*, **2014**, 16, 4493-4500
- (20) Jiang H.-L., Liu B., Akita T., Haruta M., Sakurai H., Xu Q., *J. Am. Chem. Soc.*, **2009**, 131, 11302-11303

- (21) Esken D., Noei H., Wang Y., Wiktor C., Turner S., Van Tendeloo G., Fischer R. A., *J. Mater. Chem.*, **2011**, 21, 5907-5915
- (22) Esken D., Turner S., Wiktor C., Kalidindi S. B., Van Tendeloo G., Fischer R. A., *J. Am. Chem. Soc.*, **2011**, 133, 16370-16373
- (23) Lu G., Li S., Farha O. K., Hauser B. G., Qi X., Wang Y., Wang X., Han S., Liu X., DuChene J. S., Zhang H., Zhang Q., Chen X., Ma J., Loo S. C. J., Wei W. D., Yang Y., Hupp J. T., Huo F., *Nat. Chem.*, **2012**, 4, 310-316
- (24) Li Z., Zeng H. C., *Chem. Mater.*, **2013**, 25, 1761-1768
- (25) Chen L., Peng Y., Wang H., Gu Z., Duan C., *Chem. Commun.*, **2014**, 50, 8651-8654
- (26) Wang F., Liu Z.-S., Yang H., Tan Y.-X., Zhang J., *Angew. Chem. Int. Ed.*, **2011**, 50, 450-453
- (27) Luz I., Llabrés i Xamena F. X., Corma A., *J. Catal.*, **2010**, 276, 134-140
- (28) Luz I., Llabrés i Xamena F. X., Corma A., *J. Catal.* **2012**, 285, 285-291
- (29) Wu Y., Qiu L.-G., Wang W., Li Z.-Q., Xu T., Wu Z.-Y., Jiang X., *Transition Met. Chem.*, **2009**, 34, 263-268.
- (30) Dhakshinamoorthy A., Alvaro M., Garcia H., *J. Catal.*, **2009**, 267, 1-4
- (31) Masciocchi N., Bruni S., Cariati E., Cariati F., Galli S., Sironi A., *Inorg. Chem.*, **2001**, 40, 5897-5905
- (32) Fan J., Gan L., Kawaguchi H., Sun W.-Y., Yu K.-B., Tang W.-X., *Chem. Eur. J.*, **2003**, 9, 3965-3973
- (33) Fan J., Sun W.-Y., Okamura T.-a., Tang W.-X., Ueyama N., *Inorg. Chem.*, **2003**, 42, 3168-3175
- (34) Zhao W., Fan J., Okamura T.-a., Sun W.-Y., Ueyama N., *New J. Chem.*, **2004**, 28, 1142-1150
- (35) Ma L.-F., Meng Q.-L., Wang L.-Y., Liang F.-P., *Inorg. Chim. Acta*, **2010**, 363, 4127-4133
- (36) Pang H.-j., Ma H.-y., Peng J., Zhang C.-j., Zhang P.-p., Su Z.-m., *CrystEngComm*, **2011**, 13, 7079-7085
- (37) Zhu Y., Wang W.-y., Guo M.-w., Li G., Lu H.-j., *Inorg. Chem. Commun.*, **2011**, 14, 1432-1435
- (38) Xu J., Yao X.-Q., Huang L.-F., Li Y.-Z., Zheng H.-G., *CrystEngComm* **2011**, 13, 857-865.
- (39) Fu H., Li Y., Lu Y., Chen W., Wu Q., Meng J., Wang X., Zhang Z., Wang E., *Cryst. Growth Des.*, **2011**, 11, 458-465
- (40) Chen S.-S., Chen M., Takamizawa S., Chen M.-S., Su Z., Sun W.-Y., *Chem. Commun.*, **2011**, 47, 752-754
- (41) Béziau A., Baudron S.A., Pogozev D., Fluck A., Hosseini M.W., *Chem. Commun.*, **2012**, 48, 10313-10315
- (42) Wen L., Zhao J., Lv K., Wu Y., Deng K., Leng X., Li D., *Cryst. Growth Des.*, **2012**, 12, 1603-1612
- (43) Lin H.-Y., Mu B., Wang X.-L., Tian A.-X., *J. Organomet. Chem.* **2012**, 702, 36-44
- (44) Zhou D.-D., He C.-T., Liao P.-Q., Xue W., Zhang W.-X., Zhou H.-L., Zhang J.-P., Chen X.-M., *Chem. Commun.*, **2013**, 49, 11728-11730
- (45) Vlad A., Zaltariov M.-F., Shova S., Novitchi G., Dragoa C.-D., Train C., Cazacu M., *CrystEngComm*, **2013**, 15, 5368-5375
- (46) Li Z.-H., Xu L.-P., Wang L., Zhang S.-T., Zhao B.-T., *Inorg. Chem. Commun.* **2013**, 27, 119-121
- (47) Chawla S. K., Arora M., Nättinen K., Rissanen K., Yakhmi J.V., *Polyhedron*, **2004**, 23, 3007-3019
- (48) Song J.-F., Chen Y., Li Z.-G., Zhou R.-S., Xu X.-Y., Xu J.-Q., *J. Mol. Struct.*, **2007**, 842, 125-131
- (49) Yang H., He X.-W., Wang F., Kang Y., Zhang J., *J. Mater. Chem.*, **2012**, 22, 21849-21851

- (50) Li R., Ren X., Ma H., Feng X., Lin Z., Lin Z., Li X., Hu C., Wang B., *J. Mater. Chem. A*, **2014**, 2, 5724-5727
- (51) Li R., Ren X., Feng X., Li X., Hu C., Wang B., *Chem. Commun.*, **2014**, 50, 6894-6897
- (52) Schubert D. M., Natan D. T., Knobler C. B., *Inorg. Chim. Acta*, **2009**, 362, 4832-4836
- (53) O'Neil E. J., DiVittorio K. M., Smith B. D., *Org. Lett.* **2007**, 9, 199-202
- (54) Versace D. L., Lalevée J., Fouassier J.-P., Guillaneuf Y., Bertin D., Gigmes D., *Macromol. Rapid Comm.*, **2010**, 31, 1383-1388
- (55) Vanna S. R., Jasinski J. B., Carreon M. A., *J. Am. Chem. Soc.*, **2010**, 132, 18030-18033
- (56) Cravillon J., Munzer S., Lohmeier S. J., Fedhoff A., Huber K., Wiebcke M., *Chem. Mater.* **2009**, 21, 1410-1412
- (57) Zhang L., Hu Y.H., *J. Phys. Chem. C*, **2011**, 115, 7967-7971
- (58) Li D., Li S., Yang D., Yu J., Huang J., Li Y., Tang W., *Inorg. Chem.*, **2003**, 42, 6071-6080
- (59) Fang Y.-C., Lin H.-C., Hsu I.-J., Lin T.-S., Mou C.-Y., *J. Phys. Chem. C*, **2011**, 115, 20639-20652
- (60) Sing K. S. W., Everett D. H., Haul R. A. W., Moscou L., Pierotti R. A., Rouquérol J., Siemieniowska T., *Pure Appl. Chem.*, **1985**, 57, 603-619
- (61) Barbero M., Bazzi S., Cadamuro S., Dughera S., *Tetrahedron Lett.*, **2010**, 51, 2342-2344
- (62) Mierde H. V., Voort P. V. D., Verpoort F., *Tetrahedron Lett.*, **2008**, 49, 6893-6895
- (63) O'Donnell F., Smyth T. J. P., Rama-Chandran V. N., Smyth W. F., *J. Antimicrob. Agents*, **2010**, 35, 30-38
- (64) Busatti A., Crawford D. E., Earle M. J., Gilea M. A., Gilmore B. F., Gorman S. P., Lavery G., Lowry A. F., McLaughlin M., Seddon K. R., *Green Chem.*, **2010**, 12, 420-425
- (65) Huisgen R., In 1,3-Dipolar Cycloaddition Chemistry; Padwa, A.; Ed.; Wiley: New York, **1984**.
- (66) Rostovtsev V.V., Green L.G., Fokin V.V., Sharpless K.B., *Angew. Chem. Int. Ed.*, **2002**, 41, 2596-2599
- (67) Tornøe C. W., Christensen C., Meldal M., *J. Org. Chem.*, **2002**, 67, 3057-3064
- (68) Tron G. C., Pirali T., Billington R.A., Canonico P.L., Sorba G., Genazzani A.A., *Med. Res. Rev.*, **2008**, 28, 278-208
- (69) Moses J.E., Moorhouse A.D., *Chem. Soc. Rev.*, **2007**, 36, 1249-1262
- (70) Thirumurugan P., Matosiuk D., Jozuwiak K., *Chem. Rev.*, **2013**, 113, 4905-4979
- (71) Ye M.-C., Zhou J., Huang Z.-Z., Tang Y., *Chem. Commun.*, **2003**, 2554-2555
- (72) Gladysz J. A., *Chem. Rev.*, **2002**, 102, 3215-3216
- (73) Bell A. T., *Science*, **2003**, 299, 1688-1691
- (74) Schlögl R., Hamid S.B.A., *Angew. Chem. Int. Ed.* **2004**, 43, 1628-1637
- (75) Kim J.Y., Park J.C., Kang H., Song H., Park K.H., *Chem. Commun.* **2010**, 46, 439-441

3.3 Fe₃O₄@ZIF-8: Magnetically recoverable catalysts by loading Fe₃O₄ nanoparticles inside a zinc imidazolate framework

Schejn A., Mazet T., Falk V., Balan L., Aranda L., Medjahdi G., Schneider R., Dalton Trans., 2015, 44, 10136-10140



Fig. 3.3.1 Graphical abstract.

3.3.1 Abstract

A simple methodology for encapsulating ca. 10 nm-sized superparamagnetic Fe₃O₄ nanoparticles in zeolitic imidazolate frameworks (ZIF-8) crystals was developed. The corresponding Fe₃O₄@ZIF-8 heterostructured material exhibits bifunctional properties with both high magnetization (Fe₃O₄) and high thermal stability, large specific surface, and catalytic properties (ZIF-8). The Fe₃O₄@ZIF-8 catalyst exhibits fair separation ability and reusability, which can be repeatedly applied for Knoevenagel condensations and Huisgen cycloadditions for at least ten successive cycles.

3.3.2 Introduction

Among metal organic frameworks (MOFs), zeolitic imidazolate frameworks (ZIFs) are microporous crystalline materials with high thermal and chemical stability which have attracted particular attention for gas storage and gas separation.¹⁻⁴ In ZIF-8 crystals, the network consists of Zn^{2+} atoms arranged as of $[\text{ZnN}_4]$ tetrahedrons with the N atoms of 2-methylimidazolate (mim^-) linkers.⁵⁻⁸ ZIF-8 has a sodalite zeolite-type topology with cages of 11.6 Å and pores of 3.4 Å in diameter. The efficiency of ZIF-8 has been demonstrated in gas separation, gas storage, but also for heterogeneous catalytic transformations (Knoevenagel condensations, cycloadditions, oxidations, trans-esterification, and Friedel-Crafts alkylations).^{8,9}

Nevertheless, one major problem with the reuse of ZIF-8 heterogeneous catalysts remains their separation from the reaction products. Because of the ease of magnetic separation from the reaction mixture, this strategy is more effective than nanofiltration through a membrane or centrifugation in that it allows the catalyst to be recovered.¹⁰ Superparamagnetic particles are intrinsically nonmagnetic but can be readily magnetized in the presence of an external magnetic field. This property enables trouble-free separation of the particles from the reaction medium by simply applying an external magnet, thus eliminating filtration or centrifugation operations. Additionally, magnetic particles exhibit high chemical stability and can be considered as inert in most chemical transformations. Finally, magnetic separation of nanoparticles is economical and promising for industrial applications.¹¹⁻¹³

In recent years, a couple of approaches have been developed for the encapsulation of small-sized functional nanoparticles like metal particles (Au, Ag, Pt, Pd, Ni)¹⁴⁻²⁸ or quantum dots (CdSe, ZnO, GaN)²⁹⁻³³ into MOFs to build hybrid materials for catalytic or optical applications.³⁴ Fe_3O_4 nanoparticles capped with the $[(\eta^5\text{-semiquinone})\text{Mn}(\text{CO})_3]$ ligand or with polyacrylic acid have successfully been incorporated in organometallic coordination polymers involving Mn^{2+} , Cd^{2+} or In^{3+} .^{35,36} The MIL-100 MOF (Fe^{3+} associated to 1,3,5-benzenetricarboxylate) has recently been grown onto large Fe_3O_4 or $\text{Fe}_3\text{O}_4/\text{Au}$ particles (200-600 nm) to develop reusable catalysts for Claisen-Schmidt condensations and for the reduction of 4-nitrophenol.^{37,38} A similar approach was also used to deposit small-sized ZIF-8 crystals (70-140 nm) at the outer-surface of Fe_3O_4 crystals (380-600 nm) to prepare core/shell $\text{Fe}_3\text{O}_4/\text{ZIF-8}$ particles without alteration of the properties of both materials.^{39,40} The magnetic properties of these core/shell particles were successfully used for the deposition of catalytically active ZIF-8 material in microreactors or for the development of reusable sorbent particles.

Herein, we report for the first time a simple strategy to spread ca. 10 nm-sized Fe_3O_4 nanoparticles into the cavities and/or channels of ZIF-8 crystals. The porous crystalline $\text{Fe}_3\text{O}_4@\text{ZIF-8}$ particles exhibit high catalytic activity in Knoevenagel condensations and present the advantage of being magnetically recoverable at the end of reactions and reuseable for up to ten cycles with no visible deterioration of their catalytic activity. The method was successfully extended to Cu^{2+} -doped ZIF-8 and allowed the preparation of recyclable catalysts for Huisgen 1,3-dipolar cycloadditions.

3.3.3 Results

The preparation procedure of $\text{Fe}_3\text{O}_4@\text{ZIF-8}$ particles is schematically illustrated in Fig. 3.3.2.

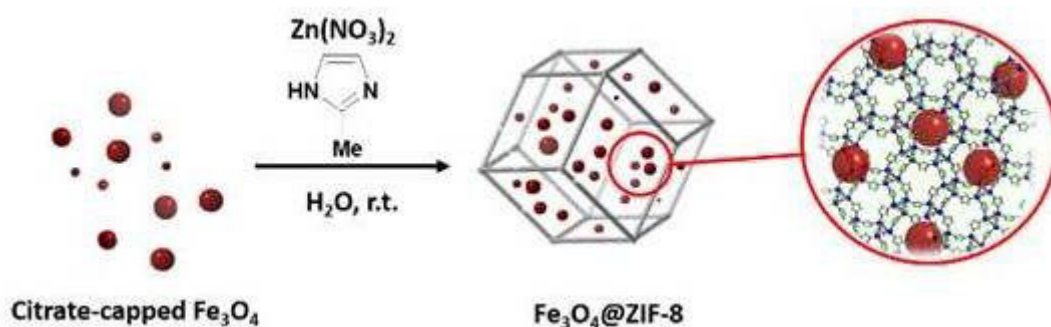


Fig. 3.3.2 Schematic illustration of $\text{Fe}_3\text{O}_4@\text{ZIF-8}$ particles synthesis.

In order to fill up the ZIF-8 framework with Fe_3O_4 particles, water-dispersible Fe_3O_4 particles capped with citrate ligands were used.⁴¹ The three carboxylate groups of citrate are meant to coordinate the Zn^{2+} ions and once these ions react with Hmim, the ZIF-8 structure will develop around the Fe_3O_4 particles. In a typical synthetic procedure, citrate-capped Fe_3O_4 nanoparticles and Hmim were dispersed in water and the mixture stirred for 5 min under inert atmosphere. Next, an aqueous solution of $\text{Zn}(\text{NO}_3)_2$ (molar ratio $\text{Hmim}/\text{Zn}(\text{NO}_3)_2 = 70/1$) was added and the resulting mixture was stirred at room temperature for 10 min. $\text{Fe}_3\text{O}_4@\text{ZIF-8}$ crystals were separated by using an external magnetic field and purified by washing with water and ethanol. The structure and morphology of $\text{Fe}_3\text{O}_4@\text{ZIF-8}$ particles were characterized by powder X-ray diffraction (PXRD), scanning electron microscopy (SEM), transmission electron microscopy (TEM), and N_2 adsorption at 77K.

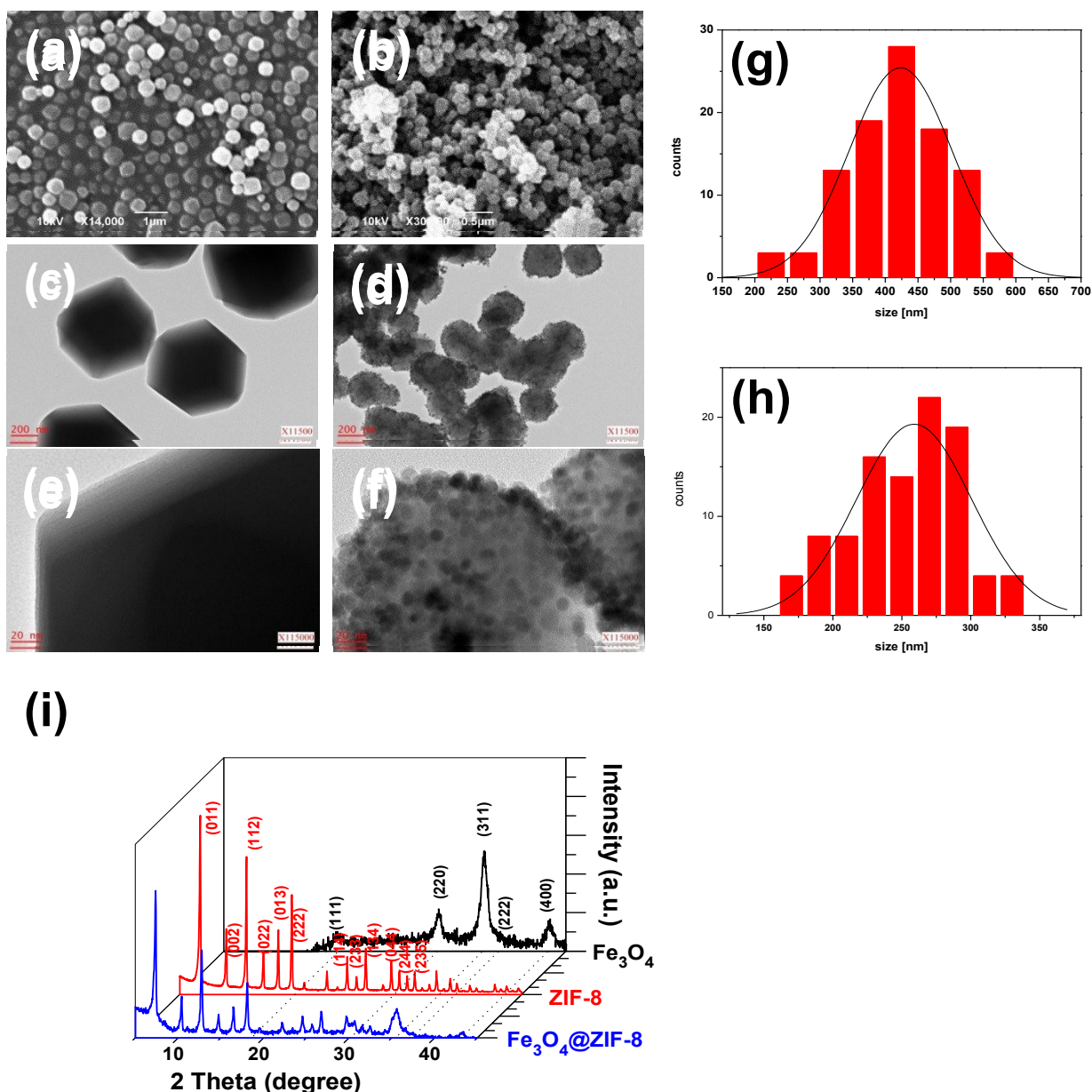


Fig. 3.3.3 SEM images of (a) ZIF-8 and (b) Fe₃O₄@ZIF-8 particles. TEM pictures of (c) and (e) ZIF-8, (d) and (f) Fe₃O₄@ZIF-8 particles. Size distribution of (g) the ZIF-8 and (h) Fe₃O₄@ZIF-8 crystals. (i) Powder XRD patterns of Fe₃O₄, ZIF-8, and Fe₃O₄@ZIF-8 crystals.

As shown by TEM and SEM experiments, ZIF-8 crystals exhibit the well-defined and thermodynamically favorable truncated rhombic dodecahedral shape and have an average diameter of ca. 430 nm (Fig. 3.3.3 a,c,e). Once Fe₃O₄ nanoparticles incorporated into the ZIF-8 framework, the morphology of ZIF-8 crystals is not markedly altered but the particle size decreases to ca. 250 nm (Fig. 3.3.3 b-h), indicating that Fe₃O₄ nanoparticles act as size-controlling agents for ZIF-8 crystals. It is also worth mentioning that there is no apparent change in the diameter of Fe₃O₄ particles in Fe₃O₄@ZIF-8 compared to the native citrate-capped Fe₃O₄ particles (9.6 ± 1.9 nm) (Fig. 3.3.4).

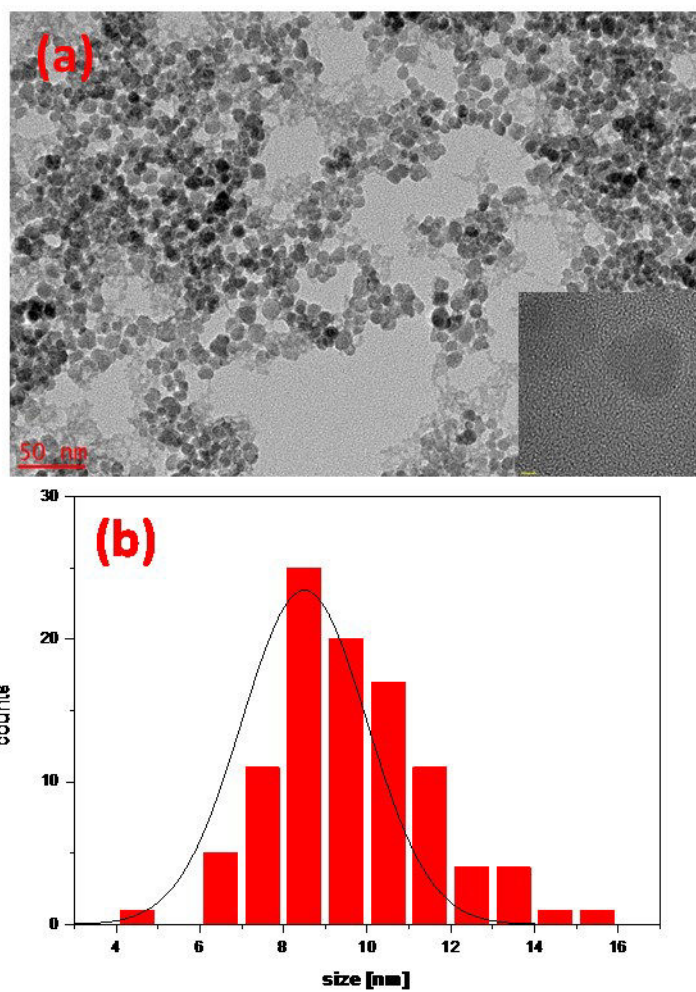


Fig. 3.3.4 (a) TEM image of citrate-capped Fe_3O_4 nanoparticles (the inset shows a HR-TEM image of the crystals) and (b) the corresponding size distribution.

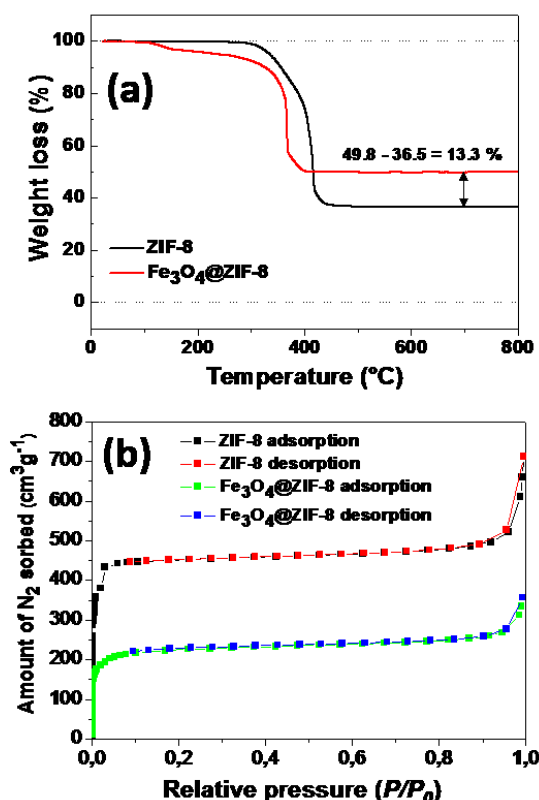


Fig. 3.3.5 (a) TGA traces of ZIF-8 and $\text{Fe}_3\text{O}_4@\text{ZIF-8}$ crystals. **(b)** N_2 adsorption/desorption curves at 77K for ZIF-8 and $\text{Fe}_3\text{O}_4@\text{ZIF-8}$ particles giving surface areas of 1856 and 871 $\text{m}^2 \text{g}^{-1}$, respectively. Black (green) and red (blue) data correspond to the adsorption and desorption branches, respectively.

The encapsulation of Fe_3O_4 in ZIF-8 was further demonstrated by powder X-ray diffraction (PXRD) analysis (Fig. 3.3.3g). $\text{Fe}_3\text{O}_4@\text{ZIF-8}$ particles exhibit a similar XRD pattern compared to ZIF-8 indicating that the sodalite structure of ZIF-8 crystals remained unaffected after loading the Fe_3O_4 particles.^{5,8} Except three peaks at $2\theta = 48.75$, 50.37 , and 57.22° , which correspond to the (220), (311), and (400) crystal facets of magnetite (JCPDS No 19-0629), no additional peaks were detected indicating the high purity of the final $\text{Fe}_3\text{O}_4@\text{ZIF-8}$ particles.

Thermogravimetric analysis (TGA) conducted under air indicate that $\text{Fe}_3\text{O}_4@\text{ZIF-8}$ particles have a slightly lower stability than ZIF-8 crystals (Fig. 3.3.5a). For ZIF-8, the sharp weight loss step of 63–64% was observed at ca. 400°C , corresponding to the decomposition of the mim^- linker and to the formation of ZnO crystals.⁸ The relatively lower decomposition temperature of $\text{Fe}_3\text{O}_4@\text{ZIF-8}$ (350°C) compared to pure ZIF-8 might be attributed to the gradual decomposition of the citrate ligand capping Fe_3O_4 nanoparticles into aconitate and citraconate between 150 and 350°C . Finally, when comparing the weight loss of ZIF-8 and $\text{Fe}_3\text{O}_4@\text{ZIF-8}$ particles, the loading of Fe_3O_4 into ZIF-8 host was estimated to be 13.3%.

Textural parameters such as surface area, pore volume and pore size of $\text{Fe}_3\text{O}_4@\text{ZIF-8}$ particles were obtained from N_2 adsorption-desorption measurements at 77K. As shown in Fig. 3.3.5b, both ZIF-8 and $\text{Fe}_3\text{O}_4@\text{ZIF-8}$ particles display the Type I isotherms, with a steep increase for the N_2 uptake at low relative pressure, which reveals the microporosity for both types of particles. The specific surface areas, determined using the Brunauer-Emmett-Teller (BET) method, were found to be 871 ± 3 and $1856 \pm 46 \text{ m}^2/\text{g}$ for $\text{Fe}_3\text{O}_4@\text{ZIF-8}$ and ZIF-8 particles, respectively. The pore volume was also found

to decrease from 0.71 cm³/g for ZIF-8 to 0.35 cm³/g for Fe₃O₄@ZIF-8. The high decrease in surface area and pore volume after loading Fe₃O₄ nanoparticles into ZIF-8 are not surprising since Fe₃O₄ particles are nonporous. These results also indicate that the cavities of ZIF-8 framework are blocked by the highly dispersed Fe₃O₄ nanoparticles which seem to be mainly located at the surface of ZIF-8 crystals as indicated by TEM images (Fig. 3.3.3 d,f).

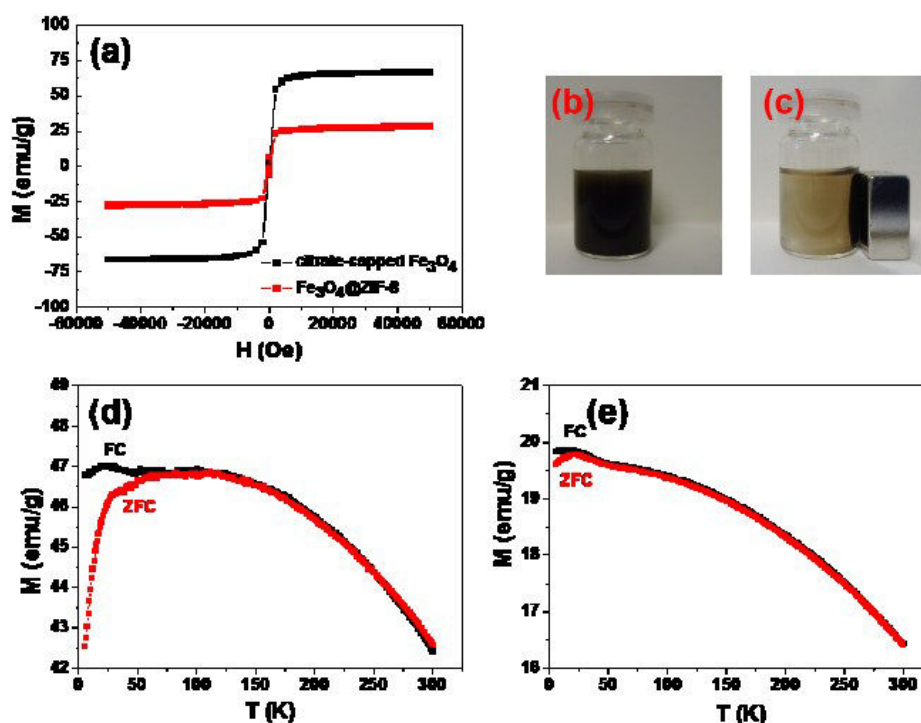
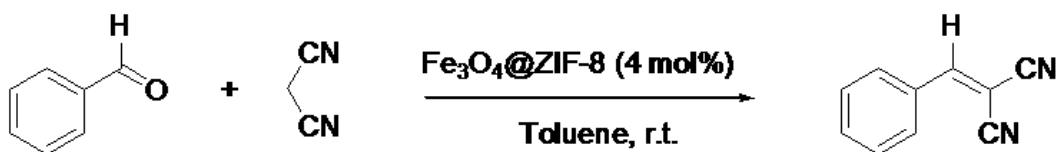


Fig. 3.3.6 (a) Magnetization at 300 K as a function of applied field. Optical images of Fe₃O₄@ZIF-8 particles dispersions (b) before and (c) after applying an external magnetic field. (d,e) Temperature dependent magnetization for citrate-capped Fe₃O₄ and Fe₃O₄@ZIF-8 particles, respectively.

The temperature dependence of the magnetization recorded in FC and ZFC conditions ($H = 1000$ Oe) exhibits characteristic features of superparamagnetism for both Fe₃O₄ and Fe₃O₄@ZIF-8 crystals (Fig. 3.3.6): (i) the ZFC curves go to a rounded maximum at the blocking temperature $T_B \sim 55$ K and ~ 25 K for Fe₃O₄ and Fe₃O₄@ZIF-8, respectively and (ii) the room-temperature hysteresis loop points to negligible coercivity and remanence. The lower blocking temperature of Fe₃O₄@ZIF-8 compared to citrate-capped Fe₃O₄ particles originates from reduced dipolar interactions between magnetic particles encapsulated in ZIF-8 pores.^{42,43} The significantly broader peak observed for Fe₃O₄ implies a distribution of blocking temperature. Since the particle size does not significantly differ for the two materials, the distribution of T_B in Fe₃O₄ is likely due to variation in interparticle interactions across the sample.

To compare the catalytic properties of Fe₃O₄@ZIF-8 with those of pure ZIF-8 crystals, we first evaluated their catalytic activity in a Knoevenagel condensation using benzaldehyde and malononitrile as substrates and toluene as solvent (Scheme 3.3.1).⁸



Scheme 3.3.1 $\text{Fe}_3\text{O}_4@\text{ZIF-8}$ -catalyzed Knoevenagel reaction between benzaldehyde and malononitrile.

Preliminary experiments showed that the reaction proceeded efficiently at room temperature using 6 equiv. malononitrile relative to benzaldehyde and only 4 mol.% of $\text{Fe}_3\text{O}_4@\text{ZIF-8}$ catalyst, yielding 2-(benzylidene)malononitrile in 94% yield after 3 h of reaction. Under similar experimental conditions, ZIF-8 yielded 2-(benzylidene)malononitrile in 98% yield.

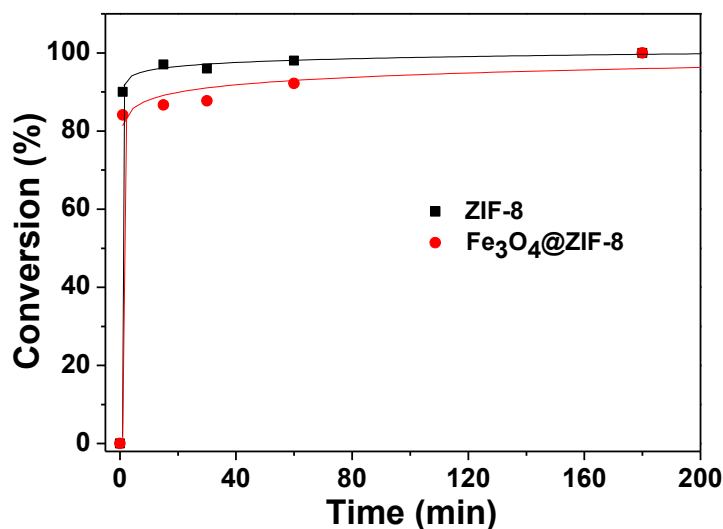


Fig. 3.3.7 Time-dependent conversion plots for the Knoevenagel reaction between 4-bromobenzaldehyde and malononitrile catalyzed by ZIF-8 crystals and $\text{Fe}_3\text{O}_4@\text{ZIF-8}$ crystals (reactions were conducted in toluene at room temperature).

Fig. 3.3.7 shows the conversion of benzaldehyde when reacting with malononitrile in the presence of ZIF-8 or $\text{Fe}_3\text{O}_4@\text{ZIF-8}$ crystals as a function of time. As seen, the condensations proceeded very quickly at room temperature with both catalysts and the reaction is only slightly slowed down using $\text{Fe}_3\text{O}_4@\text{ZIF-8}$ crystals. These results demonstrate that the iron oxide nanoparticles incorporated in ZIF-8 framework do not alter the activity of ZIF-8 and that the reaction probably proceeds on the external surface of the catalyst. We also conducted a control experiment in which Fe_3O_4 nanoparticles were supported on the surface of ZIF-8 crystals by soaking Fe_3O_4 particles in an aqueous dispersion of ZIF-8. When benzaldehyde was reacted with malononitrile in the presence of this catalyst, the product of the Knoevenagel condensation was obtained with a yield of 73% after 3 h reaction at room temperature. We believe that the decrease in reactivity in this case may be due to the higher occupation of ZIF-8 catalytically active surface sites. Finally, catalytic cycles were run to investigate the stability of the catalytic activity and recycling. After each run, $\text{Fe}_3\text{O}_4@\text{ZIF-8}$ particles were separated using a magnet, washed twice with toluene and methanol, dried in air at 60°C , and reused. As shown in Fig. 3.3.8, the catalyst could be recycled at least ten times without any loss of activity for

the Knoevenagel condensation between benzaldehyde and malononitrile.

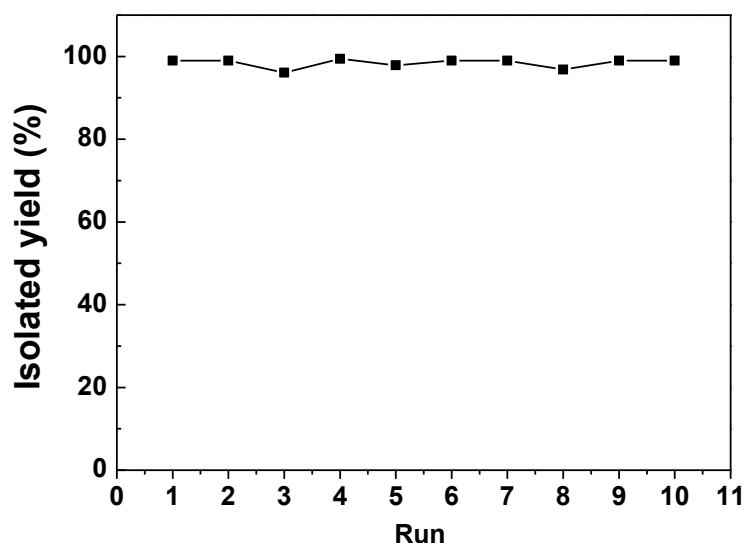
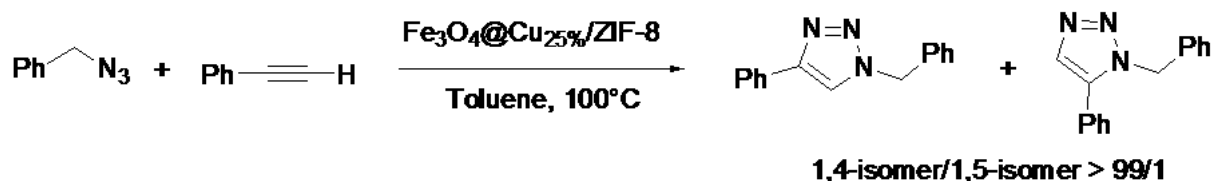


Fig. 3.3.8 Recycling performance of Fe₃O₄@ZIF-8 particles in the Knoevenagel condensation between malononitrile and benzaldehyde.

The loading of magnetite nanoparticles into ZIFs was successfully extended to Cu²⁺-doped ZIF-8 materials developed recently.⁴⁴ Citrate-capped Fe₃O₄ were successfully immobilized in the Cu_{25%}/ZIF-8 framework and the Fe₃O₄@Cu_{25%}/ZIF-8 used for cycloaddition between benzylazide and phenylacetylene (Scheme 3.3.2).

Scheme 3.3.2 Synthesis of 1,2,3-triazoles using Fe₃O₄-loaded Cu²⁺-doped ZIF-8 particles.



The triazoles were obtained in 98% isolated yield using a phenylacetylene/benzylazide molar ratio of 1.2 and conducting the reaction for 3 h in toluene at 100°C. Noteworthy is the improvement of regioselectivity of the cycloaddition with Fe₃O₄-loaded Cu_{25%}/ZIF-8 as compared to Cu_{25%}/ZIF-8 catalyst (1,4/1,5 > 99/1 for Fe₃O₄@Cu_{25%}/ZIF-8 while 1,4/1,5 = 92/8 for Cu_{25%}/ZIF-8). The Fe₃O₄@Cu_{25%}/ZIF-8 catalyst could be successfully recycled three times without any loss in activity (Fig. 3.3.9).

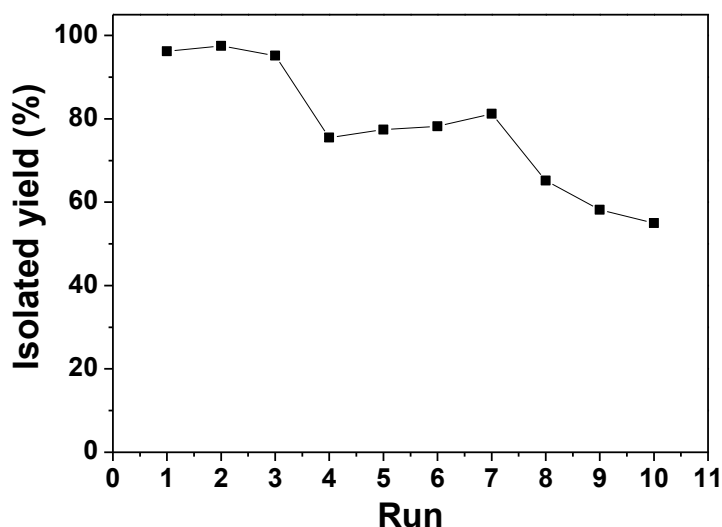


Fig. 3.3.9 Recycling performance of $\text{Fe}_3\text{O}_4@\text{Cu}_{25\%}/\text{ZIF-8}$ particles in the Huisgen cycloaddition between benzylazide and phenylacetylene.

The catalyst activity started to drop in run 4 providing triazoles in ca. 75% yield. A gradual decrease in activity was further observed and triazoles were isolated with ca. 55% yield after the 10th cycle of cycloaddition.

Blank experiments conducted in the presence of citrate-capped Fe_3O_4 nanoparticles showed no detectable amounts of Knoevenagel or cycloaddition products and confirmed that both reactions were catalyzed by ZIF-8 materials associated to Fe_3O_4 . We also examined the leaching behaviour of $\text{Fe}_3\text{O}_4@\text{ZIF-8}$ particles in Knoevenagel and Huisgen reactions. The Fe and Zn contents were determined in the crude reaction products using Inductively Coupled Plasma-Optical Emission Spectrometry (ICP-OES). Low levels for Fe leaching (207 and 39 $\mu\text{g/L}$ in Huisgen and Knoevenagel products, respectively) and Zn leaching (234 and 107 $\mu\text{g/L}$ in Huisgen and Knoevenagel products, respectively) were obtained. These results show that ZIF-8 crystals provide enough binding sites on the surface of Fe_3O_4 particles to minimize deterioration and leaching and thus to facilitate efficient catalyst recycling. Finally, the XRD patterns of $\text{Fe}_3\text{O}_4@\text{ZIF-8}$ and $\text{Fe}_3\text{O}_4@\text{Cu}_{25\%}/\text{ZIF-8}$ catalysts exhibit no significant changes in their crystallinity after five recyclings (Fig. 3.3.10) which further confirms their high stability.

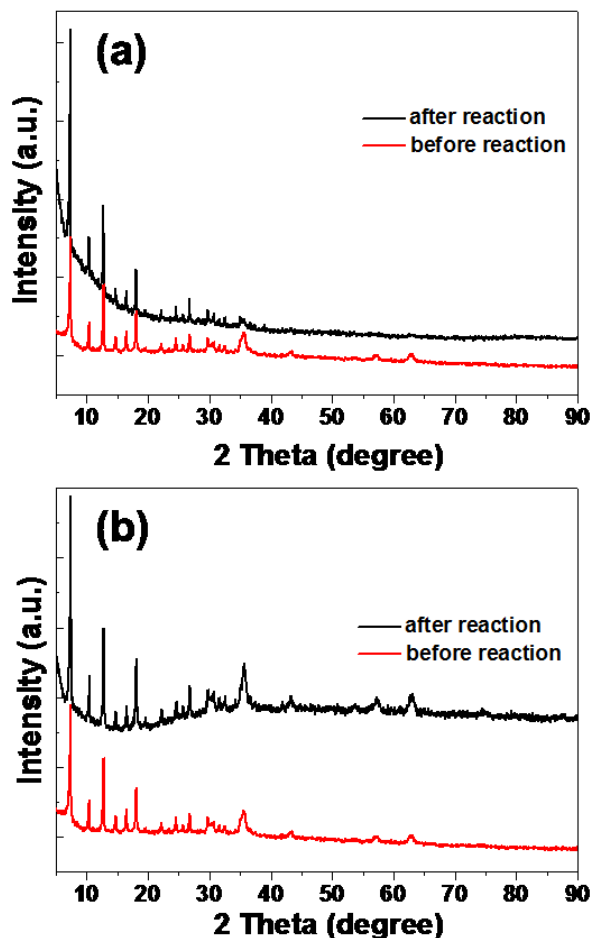


Fig. 3.3.10 XRD patterns of (a) Fe₃O₄@ZIF-8 and (b) Fe₃O₄@Cu_{25%}/ZIF-8 catalysts before and after five recyclings.

3.3.4 Conclusions

To sum up, we have developed an aqueous-based route for incorporating ca 10 nm-sized Fe₃O₄ nanoparticles inside ZIF-8 crystals and used Fe₃O₄@ZIF-8 particles as a heterogeneous catalyst for Knoevenagel condensations between benzaldehyde and malononitrile. The Fe₃O₄@ZIF-8 catalyst is easily recoverable by magnetic separation and can be reused more than ten times without any loss in the catalytic activity. Using the same approach, Fe₃O₄ particles were also loaded into Cu²⁺-doped ZIF-8 crystals and the particles obtained were successfully used for Cu²⁺-catalyzed Huisgen cycloadditions. Results obtained in this study open an avenue to the fabrication of highly efficient and easily recoverable MOFs based nanocatalysts.

3.3.5 References

- (1) Morris R., Wheatley P., *Angew. Chem. Int. Ed.*, **2008**, 47, 4966-4981
- (2) Farha O.K., Yazaydin A.O., Eryazici I., Malliakas C.D., Hauser B.G., Kanatzidis M.G., Nguyen S.T., Snurr R.Q., Hupp J.T., *Nat. Chem.*, **2010**, 2, 944-948
- (3) Li J.-R., Kuppler R. J., Zhou H.-C., *Chem. Soc. Rev.*, **2009**, 38, 1477-1504
- (4) Chen B., Liang C., Yang J., Contreras D.S., Clancy Y.L., Lobkovsky E.B., Yaghi O.M., Dai S.A., *Angew. Chem. Int. Ed.*, **2006**, 45, 1390-1393
- (5) Park K.S., Ni Z., Côté A.P., Choi J.Y., Huang R.D., Uribe-Romo F.J., Chae H.K., O’Keeffe M., Yaghi O.M., *Proc. Natl. Acad. Sci. U.S.A.*, **2006**, 103, 10186-10191
- (6) Wang B., Côté A.P., Furukawa H., O’Keeffe M., Yaghi O.M., *Nature*, **2008**, 453, 207-211
- (7) Banerjee R., Phan A., Wang B., Knobler C., Furukawa H., O’Keeffe M., Yaghi O.M., *Science*, **2008**, 319, 939-943
- (8) Schejn A., Balan L., Falk V., Aranda L., Medjahdi G., Schneider R., *CrystEngComm*, **2014**, 16, 4493-4500
- (9) Lee J., Farha O.K., Roberts J., Scheidt K.A., Nguyen S.T., Hupp J.T., *Chem. Soc. Rev.*, **2009**, 38, 1450-1459
- (10) Guin D., Baruwati B., Manorama S.V., *Org. Lett.*, **2007**, 9, 1419-1421
- (11) Sun S., Zeng H., *J. Am. Chem. Soc.*, **2002**, 124, 8204
- (12) Latham A.H., Williams M.E., *Acc. Chem. Res.*, **2008**, 41, 411-420
- (13) Laurent S., Forge D., Port M., Roch A., Robic C., Vander Elst L., Muller R.N., *Chem. Res.*, **2008**, 108, 2064-2110
- (14) Schröder F., Esken D., Cokoja M., van den Berg M.W.E., Lebedev O.I., Van Tendeloo G., Walaszek B., Buntkowsky G., Limbach H.-H., Chaudret B., Fischer R.A., *J. Am. Chem. Soc.*, **2008**, 130, 6119-6130
- (15) Houk R.J.T., Jacobs B.W., Gabaly F.E., Chang N.N., Talin A.A., Graham D.D., House S.D., Robertson I.M., Allendorf M.D., *Nano Lett.*, **2009**, 9, 3413-3418.
- (16) Jiang H.-L., Liu B., Akita T., Haruta M., Sakurai H., Xu Q., *J. Am. Chem. Soc.*, **2009**, 131, 11302-11303
- (17) Liu H., Liu Y., Li Y., Tang Z., Jiang H., *J. Phys. Chem. C*, **2010**, 114, 13362-13369
- (18) Meilikhov M., Yusenko K., Esken D., Turner S., Van Tendeloo G., Fischer R.A., *Eur. J. Inorg. Chem.*, **2010**, 3701-3714
- (19) Isimjan T.T., Kazemian H., Rohani S., Ray A.K., *J. Mater. Chem.*, **2010**, 20, 10241-10245
- (20) Jiang H.-L., Xu Q., *Chem. Commun.*, **2011**, 47, 3351-3370
- (21) Sugikawa K., Furukawa Y., Sada K., *Chem. Mater.*, **2011**, 23, 3132-3134
- (22) Wang C., deKrafft K.E., Lin W., *J. Am. Chem. Soc.*, **2012**, 134, 7211-7214
- (23) Lu G., Li S., Guo Z., Farha O.K., Hauser B.G., Qi X., Wang Y., Wang X., Han S., Liu X., DuChene J.S., Zhang H., Zhang Q., Chen X., Ma J., Loo S.C.J., Wei W.D., Yang Y., Hupp J.T., Huo F., *Nat. Chem.*, **2012**, 4, 310-316
- (24) Pan Y., Ma D., Liu H., Wu H., He D., Li Y., *J. Mater. Chem.*, **2012**, 22, 10834-10839
- (25) Li Z., Zeng H.C., *Chem. Mater.*, **2013**, 25, 1761-1768
- (26) Ke F., Zhu J., Qiu L.-G., Jiang X., *Chem. Commun.*, **2013**, 49, 1267-1269
- (27) Wang P., Zhao J., Li X., Yang Y., Yang Q., Li C., *Chem. Commun.*, **2013**, 49, 3330-3332
- (28) Chen L., Peng Y., Wang H., Gu Z., Duan C., *Chem. Commun.*, **2014**, 50, 8651-8654

- (29) Esken D., Turner S., Wiktor C., Kalidindi S.B., Van Tendeloo G., Fischer R.A., *J. Am. Chem. Soc.*, **2011**, 133, 16370-16373
- (30) Esken D., Noei H., Wang Y., Wiktor C., Turner S., Van Tendeloo G., Fischer R.A., *J. Mater. Chem.*, **2011**, 21, 5907-5915
- (31) Buso D., Jasieniak J., Lay M.D.H., Schiavuta P., Scopese P., Laid J., Amenitsch H., Hill A.J., Falcaro P., *Small*, **2012**, 8, 80-88
- (32) Biswal B.P., Shinde D.B., Pillai V.K., Banerjee R., *Nanoscale*, **2013**, 5, 10556-10561
- (33) Wakaoka T., Hirai K., Murayama K., Takano Y., Takagi H., Furukawa S., Kitagawa S., *J. Mater. Chem. C*, **2014**, 2, 7173-7175
- (34) Zhu Q.-L., Xu Q., *Chem. Soc. Rev.*, **2014**, 43, 5468-5512
- (35) Kim S.B., Cai C., Sun S., Sweigart D.A., *Angew. Chem. Int. Ed.*, **2009**, 48, 2907-2910
- (36) Kim Y., Choi Y.S., Lee H.J., Yoon H., Kim Y.K., Oh M., *Chem. Comm.*, **2014**, 50, 7617-7620
- (37) Ke F., Qiu L.-G., Zhu J., *Nanoscale*, **2014**, 6, 1596-1601
- (38) Ke F., Wang L., Zhu J., *Nanoscale*, **2015**, 7, 1201-1208
- (39) Zhang T., Zhang X., Yan X., Kong L., Zhang G., Liu H., Qiu J., Yeung K.L., *Chem. Engineer. J.*, **2013**, 228, 398-404.
- (40) Zheng J., Cheng C., Fang W.-J., Chen C., Yan R.-W., Huai H.-X., Wang C.-C., *CrystEngComm*, **2014**, 16, 3960-3964
- (41) Ahmed S.R., Dong J., Yui M., Kato T., Lee J., Park E.Y., *J. Nanobiotechnol.*, **2013**, 11, 28 (9 pages)
- (42) Fonseca F.C., Goya G.F., Jardim R.F., Mucillo R., Carreno N.V.L., Longo E., Leite E.R., *Phys. Rev. B*, **2002**, 66, 104406
- (43) Morup S., Bodker F., Hendriksen P.V., Linderoth S., *Phys. Rev. B*, **1995**, 52, 287
- (44) Schejrn A., Aboulaich A., Balan L., Falk V., Lalevée J., Medjahdi G., Aranda L., Mozet K., Schneider R., *Catal. Sci. Technol.*, **2015**, 5, 1829-1839

Chapter 4: ZIF-8 material for carbon dioxide conversion into cyclic carbonates

In this chapter we would like to:

- (1) demonstrate the conversion of carbon dioxide into cyclic carbonates using ZIF-8 as heterogeneous catalyst in different forms: powder, compressed as pellets and functionalized with Fe_3O_4 particles,
- (2) investigate recyclability and resistance of these ZIF-8 samples towards the cycloaddition reactions,
- (3) answer the question if ZIF-8 modification and shaping could influence on the final results and which form of the catalyst could be considered for scale-up industrial application.

4.1 Synthesis of ZIF-8 crystals and application to carbon dioxide conversion

4.1.1 Abstract

In the current contribution, we report on the utilization of ZIF-8 heterogeneous catalysts in carbon dioxide conversion into various carbonates. The approach involved the synthesis and characterization steps, functionalization and shaping the material to produce the most convenient form of the catalyst that can be applied on an industrial scale. ZIF-8 particles were modified with iron oxide magnetic particles in order to facilitate the catalyst recovery after the reaction. Also we tried to compress the ZIF-8 material and we evaluated the morphology, porous and crystalline properties after processing. We tested the three catalysts in the CO₂ conversion. The results obtained in this study showed that the ZIF-8 particles can be easily functionalized and shaped without significant loss in the activity of the material.

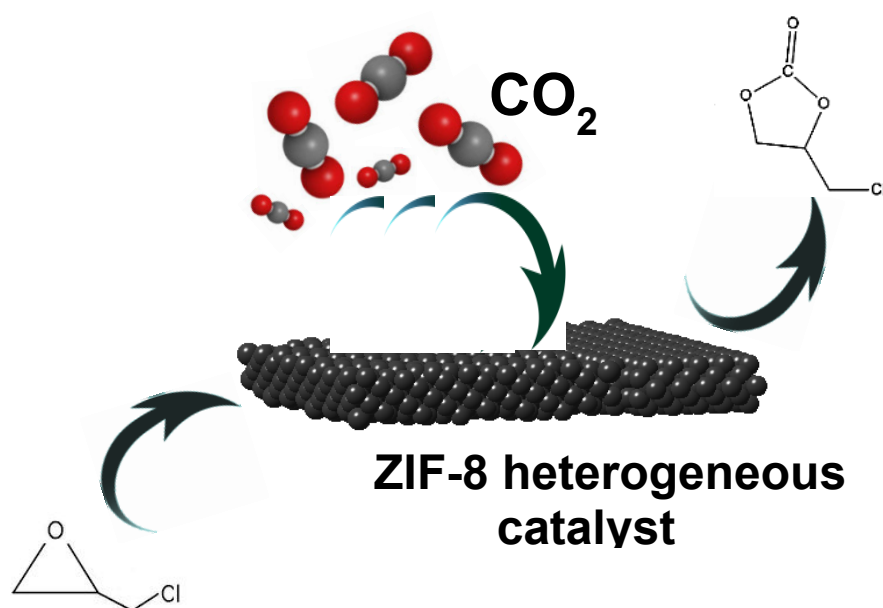


Fig. 4.1.1 Graphical abstract.

4.1.2 Introduction

Carbon dioxide is one of the most abundant gases produced by industrial sources and is suspected to be responsible for global warming. The combustion of fossil fuels produces huge quantities of CO₂ that were estimated as 30 gigatons per year. Since the industrial revolution, the amount of CO₂ in the air increased from 280 to 385 ppm and is still increasing by 1-2 ppm each year.¹ In this context there is a big demand for technologies that can reduce the carbon dioxide level in the atmosphere. Naturally CO₂ is used in the formation of limestone (CaCO₃) or dolomite (MgCO₃) from CaO and MgO respectively. In the industry, carbon dioxide is directly used in the horticulture, refrigeration, welding, beverages or fire extinguishers. Moreover it can be used in chemical transformations. Many researches are therefore devoted to the capture and the conversion of CO₂.² CO₂ is considered to be an attractive molecular C1 synthon in catalytic processes like the synthesis of cyclic carbonates from epoxides and CO₂.³ However, this reaction has several drawbacks like modest epoxide conversion, formation of polymeric by-products and/or diols, long reaction times, and tedious separations of the desired carbonate.⁴ This transformation must be optimized by the development of proper heterogeneous catalysts, which will not only accelerate the conversion but also improve the selectivity.

Metal organic frameworks (MOFs) are promising materials for CO₂ capture and storage. MOFs are metal ions or metal clusters bond together with organic linkers (terephthalates, imidazolates, carboxylates...) to form porous networks. Moreover, the specific surface and pore size of these materials can be easily modulated and be adapted for the desired application (storage, separation, or catalysis). Among MOFs, the zeolitic imidazolate frameworks (ZIFs) have recently gained considerable attention in the area of catalysis and gas storage. In these materials, metal atoms such as Zn²⁺ are linked through N atoms by the ditopic 2-methylimidazolate ligand to form neutral frameworks.⁵ ZIF-8 has a sodalite zeolite-type topology with cages of 11.6 Å and pores of 3.4 Å in diameter.⁶ ZIF-8 crystals are characterized by high thermal stability (550 °C in N₂), large surface area (BET: 1630 m²/g) and high resistance to solvents. Moreover, ZIF-8 crystals have proven to be efficient materials for hydrogen or carbon dioxide storage, but also for catalytic transformations like Knoevenagel condensations, cycloadditions, oxidations, trans-esterification, and Friedel-Crafts alkylation.⁷ ZIF-8 can be employed as heterogeneous catalyst for CO₂ conversion to cyclic carbonates, due to the presence of Zn Lewis acid sites and high carbon dioxide adsorption capacity.⁸

In this work, ZIF-8 crystals were prepared by a mild solvothermal method and characterized by transmission electron microscopy, scanning electron microscopy, X-ray diffraction, thermogravimetry, and BET measurements. Under optimized reaction conditions (time, pressure, temperature, catalyst loading) to limit the by-products formation, ZIF-8 crystals were found to efficiently catalyze the conversion of epichlorohydrin, styrene oxide and glycidol into the corresponding cyclic carbonates.

4.1.3 Results and discussion


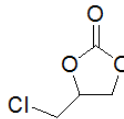

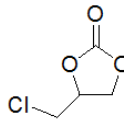

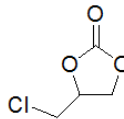

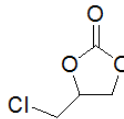

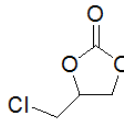

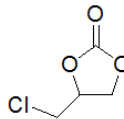
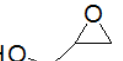
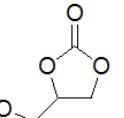
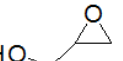
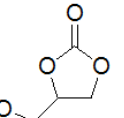
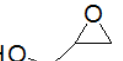
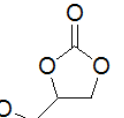
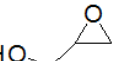
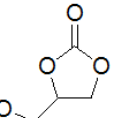
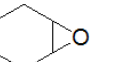
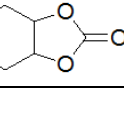
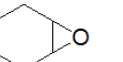
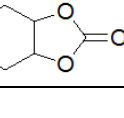
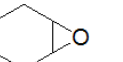
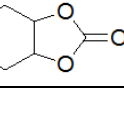
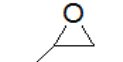
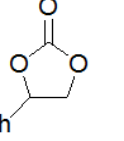
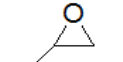
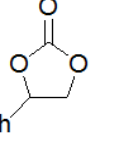
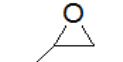
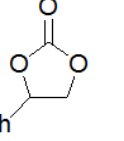
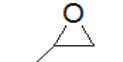
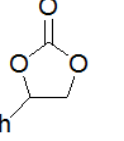
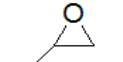
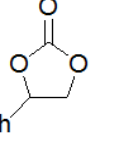
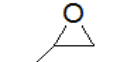
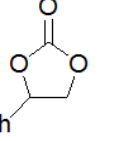
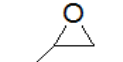
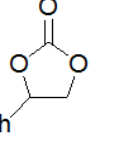
4.1.3.1 Carbon dioxide conversion

Carbon dioxide has reactive sites localized on the carbon atom (an electrophilic Lewis acid centre) and two oxygen atoms (weak nucleophilic Lewis base centres). A central challenge is to overcome its kinetic and thermodynamic stability. To valorise the compound for the conversion into useful chemicals it's necessary to activate the molecule with appropriate catalyst.⁹ The catalyst provides low-energy specific interactions with substrates. Briefly the reaction of cyclic carbonates formation

consists of three stages: opening the ring of epoxide, insertion of carbon dioxide inside the molecule and closing the ring to form the final carbonate. ZIF-8 material is a nice candidate to undertake these actions because its polar structure consists of zinc atoms acting as Lewis acidic sites and 2-methylimidazole linkers that are Lewis basic sites. Electron rich metal centres bond with electrophilic carbon from CO₂ and thus help for efficient epoxide/CO₂ coupling.¹⁰

Inspired with the results previously obtained by Carreon *et al.* with epichlorohydrin and styrene oxide,¹¹ we decided to further explore the area of cyclic carbonates formation. The performance of ZIF-8 catalyst was tested using epichlorohydrin, glycidol, styrene oxide and cyclohexene oxide. The optimal conditions for the reaction were investigated by differing the temperature, carbon dioxide pressure and the reaction time. The results are summarized in the table 4.1.1.

Table 4.1.1 Results obtained with CO₂ conversion into carbonates.

Entry	catalyst	substrat	product	T (°C)	P (bar)	Time (h)	Yield (%)
1	ZIF-8			70	9	15	99
2	ZIF-8			70	9	7	40
3 ^a	Fe ₃ O ₄ /ZIF-8			70	9	15	100
3 ^b	Fe ₃ O ₄ /ZIF-8			70	9	15	88.4
3 ^c	Fe ₃ O ₄ /ZIF-8			70	9	15	88.2
4	ZIF-8 comp			70	9	15	91.13
5	ZIF-8			70	9	6	86.13
6	ZIF-8 comp			70	9	6	85.4
7	ZIF-8			80	9	5	92.4
8	ZIF-8			80	9	4	85.8
9	ZIF-8			70	10	15	42
10	ZIF-8			70	9	15	6.12
11	ZIF-8			100	10	24	14.8
12	ZIF-8			100	12	24	49
13 ^d	ZIF-8			100	12	24	80.2
14 ^e	ZIF-8			100	10	19	97.7
15 ^f	ZIF-8			100	10	15	83.5
16 ^g	ZIF-8			100	10	10	26.5
17 ^h	ZIF-8			100	10	19	68.2
18 ⁱ	ZIF-8			100	10	19	35.8

^{a, b, c} executive runs of the conversion

^d double mass of the catalyst

^{e, f, g} reaction with chlorobenzene

^h reaction with DMF

ⁱ reaction with dioxane

Typically, the synthesis of cyclic carbonates requires the carbon dioxide pressure of about 50-100 atm and the reaction temperature in the range of 70-150°C depending on the starting substrate. Most of the reactions were carried out under solvent-free conditions. For epichlorohydrin conversion into 3-chloropropene carbonate, the reaction was performed at 70°C and 9 bar of carbon dioxide pressure. We slightly increase the pressure of carbon dioxide inside the reaction vessel without increasing the

temperature to improve the carbonate formation. The reaction time necessary to convert 40 % of epichlorohydrin was 7 h, when total conversion was achieved after 15h using ZIF-8 as catalyst with 100% selectivity for chloropropene carbonate. It is worth to note that when increasing the temperature, the reaction is more favorable for diols, dimers and polymers, because the formation of these compounds requires much higher activation energy than in the case of monomeric cyclic carbonate.¹² To facilitate recovery of the catalyst we functionalize ZIF-8 material with Fe₃O₄ magnetic nanoparticles (entry 3a, 3b, 3c). The magnetic separation is being known as much faster and efficient than standard centrifuge-based method. By applying an external neodymium magnet, we were able to separate the catalyst from the reaction mixture and purify the catalyst within much shorter time. Moreover, the magnetic functionalization didn't alter the conversion level. The obtain yield for cyclic carbonate was 100 %. The second and third run of the carbon dioxide conversion we obtained lower yield of 88.4 % and 88.2 %. These lower conversions were probably due to the fact that ZIF-8 pores were blocked by the adsorbed product or collapsed after the first cycle of manipulation, thus the surface area diminished and finally the efficiency of the catalyst slowed down. Then, we explored epichlorohydrin conversion with compressed ZIF-8 and the yield attained 91.13 %. This result could be as well considered from the point of lower surface area of the catalyst caused by the compression.

For the reaction conducted using glycidol, we got the best reaction conditions at 80 °C with 9 bar CO₂ over 5h. The reaction was much faster than with epichlorohydrin. The yield for glycerol carbonate was 92.4 %. We tried to improve the results by increasing the reaction time and decreasing the temperature but this lead to the formation of by products in much bigger quantity. Then, we tested compressed ZIF-8 catalyst in this reaction and we successfully were able to convert 85.4 % of glycidol into glycerol carbonate.

When cyclohexene oxide was used as a substrate, the yields were dramatically lower when compared to the other epoxides. The best value of the yield - 42% was obtained at 70 °C after 15h using 10 bar of CO₂ pressure. This behaviour is described by the low reactivity of electron-rich molecule and bigger steric hindrance of cyclohexene oxide.¹³

Styrene oxide was then used as aromatic derivative of cyclic epoxide and reacted with CO₂ under optimized and non-solvent conditions. The best results were obtained at 100 °C and 12 bar CO₂. We observed that the reaction required twice more catalyst and longer reaction time. After 24 h, the yield was 80.2 % for styrene carbonate. Then decreasing the pressure at 11 bar and 10 bar we had 34.8 % and 10 % of the conversion respectively. For this substrate, we also tested different solvents and the most prominent results were achieved with chlorobenzene. We obtained 97.7 % of the yield for expected cyclic carbonate under following conditions: 10 bar, 100 °C and the reaction time 19h. The reaction progress was then evaluated by decreasing the reaction time. After 10h and 15h, the conversions were 26.5 and 83.5 % , respectively. Moreover, we determined the efficiency of this coupling in DMF and dioxane where we found 68.2 % and 35.8 % of styrene carbonate under the same reaction conditions, respectively. For the reaction in toluene, anisole and dichloromethane we didn't detect any traces of the expected product.

ZIF-8 powders after the reaction and the process of extensive washing and drying were characterized to take an insight into purity and stability of the framework after the reaction (figure 4.1.2 and 4.1.3). SEM images showed that rhombic dodecahedron structure was maintained and no changes of the crystal size or products of framework degradation were detected. However, N₂-sorption isotherms indicated the surface area decreased probably due to the pore collapse or blockage of the product inside the cavities. We also detected two new peaks with weak intensities on XRD pattern (11.02 and 18.97 2 theta degree) that appeared probably with the fact of product adsorption.

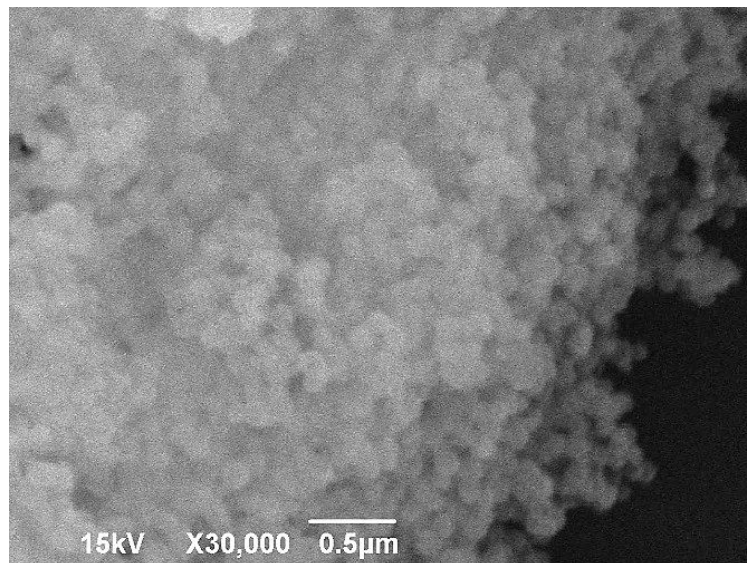


Fig. 4.1.2 SEM micrograph of the ZIF-8 powder after reaction.

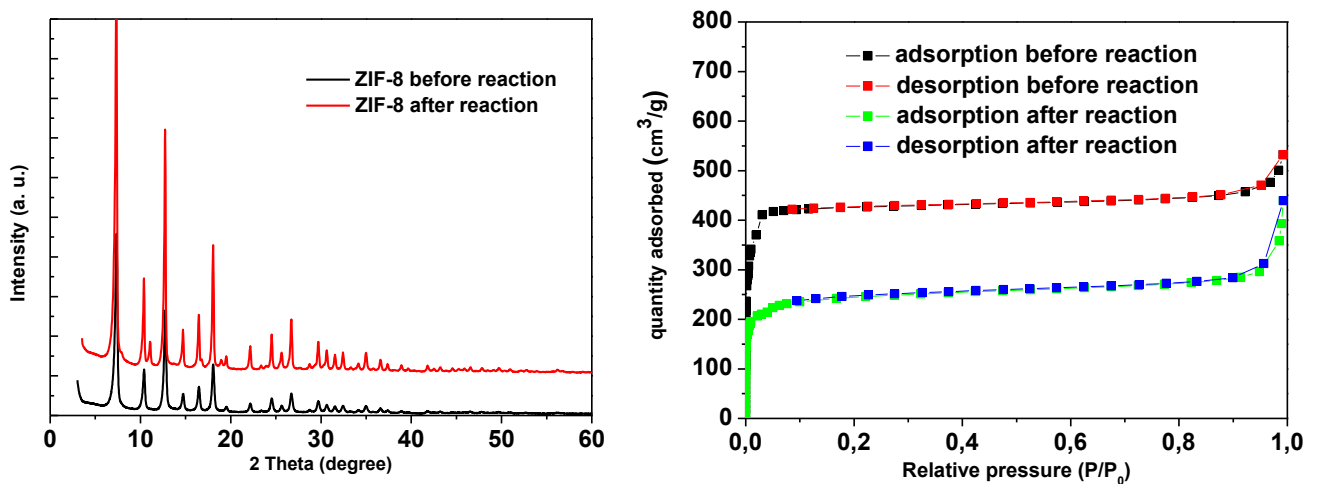


Fig. 4.1.3 XRD and N₂-sorption isotherms of the ZIF-8 material (powder) before and after CO₂ conversion. (BET surface areas and pore volume: before reaction $1713.24 \pm 45 \text{ m}^2/\text{g}$, $0.635 \text{ cm}^3/\text{g}$ and $941 \pm 6 \text{ m}^2/\text{g}$, $0.36 \text{ cm}^3/\text{g}$ respectively).

4.1.3.2 Catalyst shaping

4.1.3.2.1 Characterization of the tablets

Use of the powders in the industry may require processing steps to produce more resistant forms which are more convenient for high-scale application. The most common processes for powder shaping are pelletization or compression. In our study we used direct compression method to obtain

ZIF-8 tablets that were further investigated in carbon dioxide conversion. We tested various compression forces 1, 2, 3.5 and 5 kN. Tablets thickness is between 1.71 and 2.93 mm. The native powder of ZIF-8 and prepared tablets were then analyzed with techniques, such as scanning electron microscopy, X-ray diffraction and N₂ physisorption.

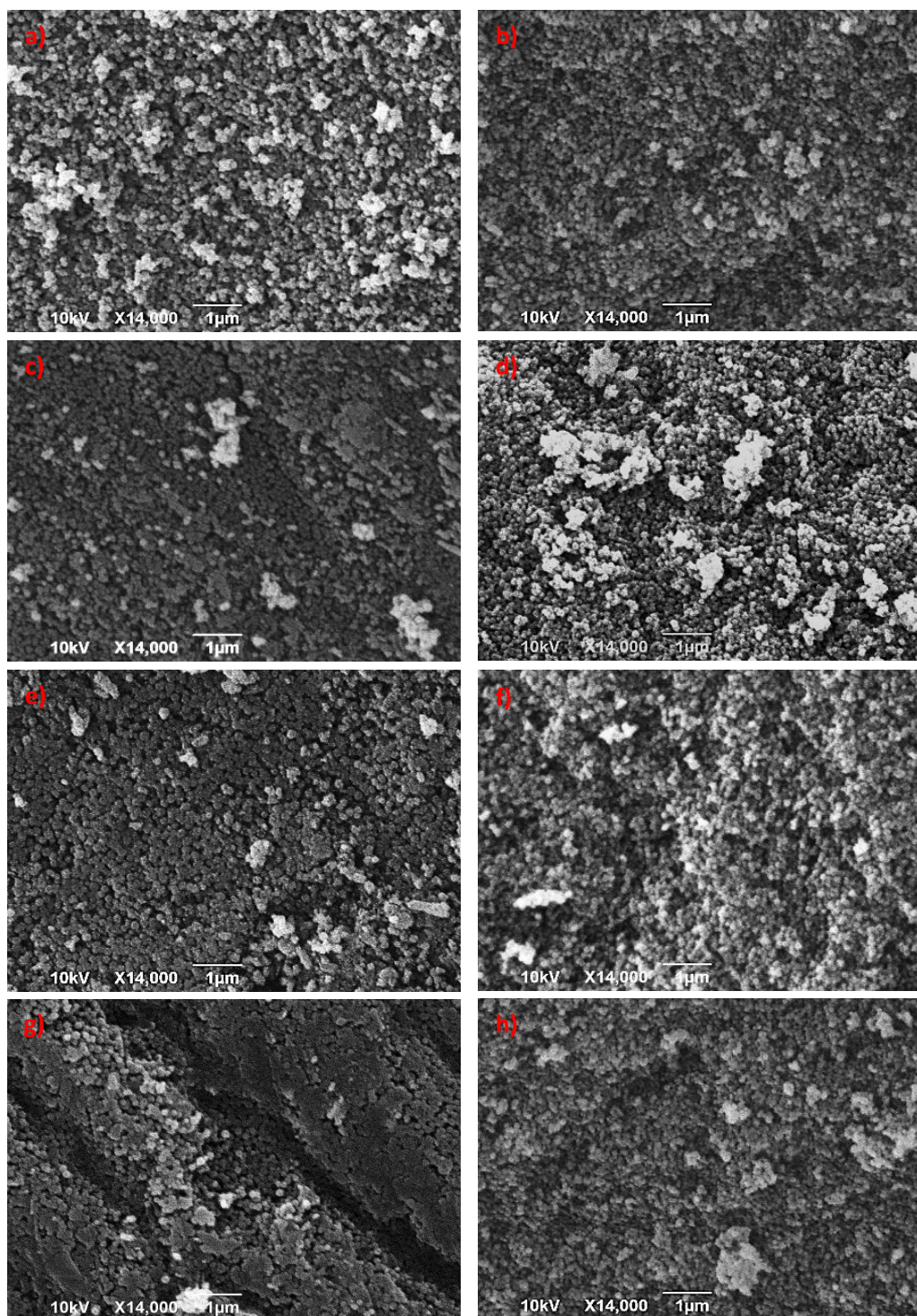


Fig. 4.1.4 SEM images of the surface (left) and the interior (right) of ZIF-8 tablets compressed at 1 kN (a, b), 2 kN (c, d), 3.5 kN (e, f) and 5 kN (g, h).

The pictures of scanning electron microscopy analysis (figure 4.1.4) show the microstructural properties of the ZIF-8 powder after being compressed. No visible modifications of the crystal morphology or fraction of the particles were observed up to 3.5 kN. However, when we used 5 kN compression force the particles at the external surface of the tablet were flattened and some amorphous phases appeared. This was not detected for the ZIF-8 dodecahedrons present in the internal part of the pastille.

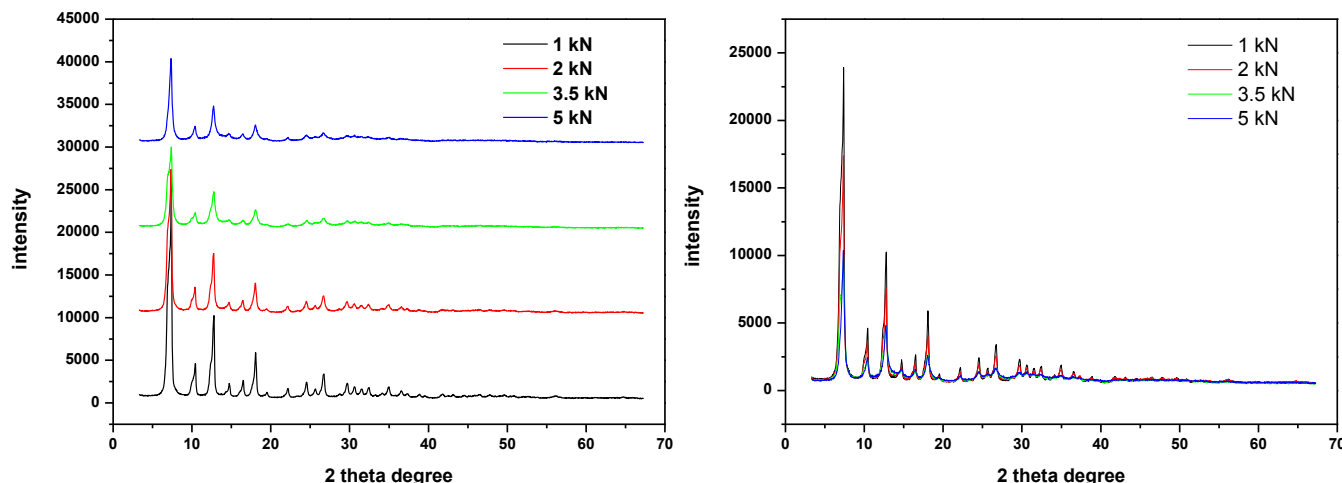


Fig. 4.1.5 XRD spectra of the ZIF-8 sample before and after compression with 1, 2, 3.5 and 5 kN.

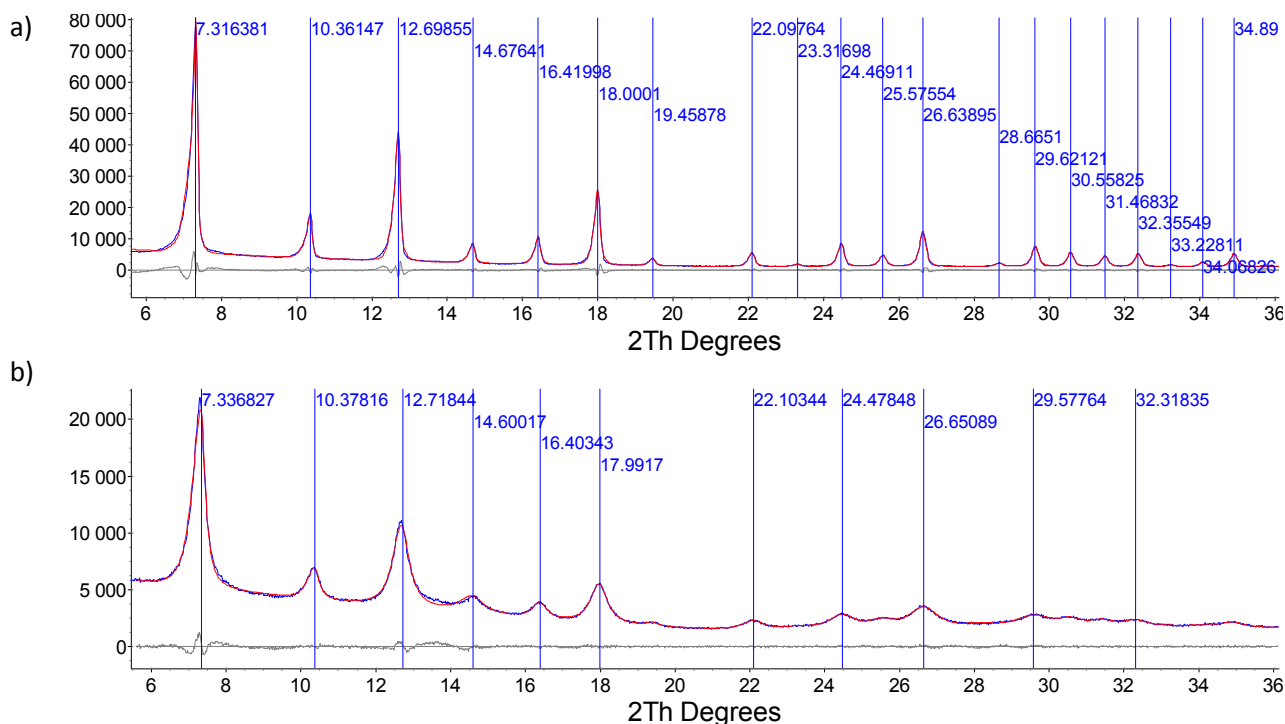


Fig. 4.1.6 XRD peaks analysis of the ZIF-8 before (a) and after compression with 5 kN (b).

We also recorded the compression behavior of ZIF-8 by XRD. The results are depicted at the figure 4.1.5 and 4.1.6. For each measurement we used the same conditions for analyses. The X-ray diffractions are observed to broaden with increasing pressure and some peaks with the smallest intensity disappeared. What is interesting, the peaks are also shifted of 0.02 and 0.06° from the powder ZIF-8 reference sample. This phenomenon can be explained in the decrease of the lattice parameters due to the residual stress or defects originating from the applied forces.¹⁴ The pressure causes the compression of the lattice planes perpendicular to the loading direction. In general, the residual stress results in peak broadening (micro residual stress) and peak shift (macro residual stress):

$$\sigma = \sigma^I + \sigma^{II} + \sigma^{III} \quad [1]^{15}$$

σ – stress

σ^I – macro residual stress; involves many grains in the sample

σ^{II} – micro residual stress; range of a single grain (anisotropy or different phases)

σ^{III} – micro residual stress; within a grain (crystal imperfections)

We also analyzed the tablets with N₂ physisorption and the specific surface area for each sample was calculated by Brunauer-Emmett-Teller equation. The N₂ isotherms revealed the gradual loss of the surface area with increasing compression force (figure 4.1.7).

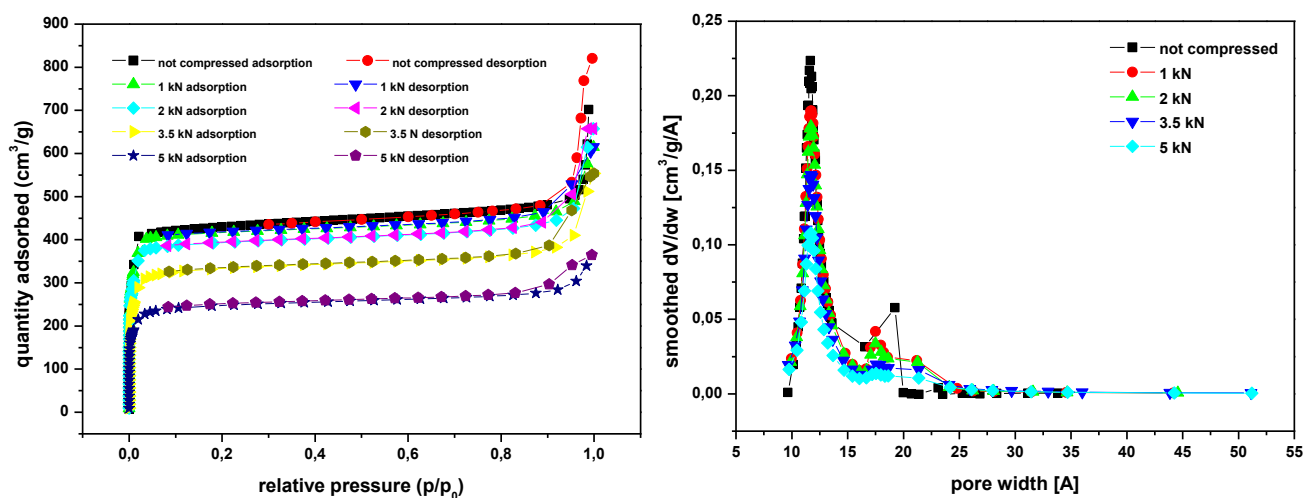


Fig. 4.1.7 BET isotherms and microporous HK distribution for the ZIF-8 in powder and compressed with different forces.

Table 4.1.2 Summary of porous properties of the ZIF-8 samples.

ZIF-8 sample	BET surface area (m ² /g)	Pore volume (cm ³ /g)	Pore size (Å)
Powder	1713 ± 45	0.635	12.65
compressed 1 kN	1758 ± 14	0.645	12.9
compressed 2 kN	1666 ± 12	0.608	12.86
compressed 3.5 kN	1361 ± 7	0.519	12.76
compressed 5 kN	1000 ± 4	0.386	12.69

The analysis of pores shows that the pore volume diminished when the compression forces increased. We also observed the relative disappearance of the peak at 17.5 Å compared to the one at 11.8 Å (table 4.1.2). This was also observed by Rotaru *et al.* 2005¹⁶ for Fe₂O₃-Cr₂O₃ catalyst. With increase of the tableting pressure the percent of smaller pores increase, finally becoming majority.

4.1.3.2.2 Application of the compact form of ZIF-8 in catalytic reactions

ZIF-8 material has been investigated in many types of catalytic reactions, such as transesterification, Friedel-Crafts, Friedländer or Knoevenagel.¹⁷ In this study and for the first time, ZIF-8 in the form of tablet was used for the evaluation of catalytic properties. We chose the material compressed at 5 kN for the catalytic tests in the carbon dioxide conversion into carbonates. Prior to the experiments, the stability of ZIF-8 tablets was investigated under different reaction conditions. The tablet was placed in a Parr reactor vessel under pressure ranging from 7 to 12 bar of CO₂ and the temperature of 100°C for 24 h. No changes in the morphology of the tablets were detected after reaction. Next, we tried the tablet in the presence of chlorobenzene (solvent used in the reaction with styrene oxide) under a pressure of 12 bar and at 100 °C for 19 h. The tablet resisted during the operating conditions (only a slight change in the color was observed). However, during the carbon dioxide catalytic experiments, when the cyclic oxides were present in the reaction environment, the tablet lost the shape and crashed into smaller pieces. To solve the problem of weak mechanical strength, we suggest the compression of ZIF-8 material with 5% of commonly used pharmaceutical binders, like Avicel or CMC sodium salt. The tablets prepared with this method were more resistant and kept the integrity during the reaction. Also the addition of the two binders didn't influence on the obtained yield for the product (92% and 90.7% respectively; compared with compressed ZIF-8). Moreover we evaluated the uniaxial mechanical strength of the tablets compressed with CMC-Na and Avicel. The obtained values were indicated as 1.1 and 0.77 MPa respectively. Taking into account these findings, compressed ZIF-8 gives the future perspective for industrial wide application.

4.3.4 Conclusions

Continuous accumulation of carbon dioxide in the atmosphere and its chemical transformation into useful chemicals has recently gained a lot of attention. The synthesis of carbonates is one of the proposed options. Cyclic organic carbonates are found to be valuable intermediate compounds for chemical synthesis of carbamates, esters, glycol ether, polycarbonates, biopolymers and pharmaceuticals.¹⁸ Moreover, they are regarded as solvents, additive modified diluents, cross-linking agents, plasticizers and surfactants because of their high polarity, high flash and boiling temperatures, low toxicity, and biodegradability.¹⁹ In our work, we conducted the synthesis of four different cyclic carbonates by using cyclic oxides, C1 synthon carbon dioxide and ZIF-8 catalysts. ZIF-8 metal organic framework was used as a powder, compressed and functionalized with magnetic nanoparticles.

The results described above indicate the best catalytic conditions necessary to have the highest yield and selectivity for expected carbonates products using ZIF-8. We also propose the protocols for the ZIF-8 functionalization and the conditions for the tableting of the ZIF-8 catalyst. The present study is a perspective for the possibility to scale-up the utilization of ZIF-8 material at the industrial scale.

4.3.5 References

- (1) Doney S. C., Fabry V. J., Feely R. A., Kleypas J. A., *Annu. Rev. Mat. Sci.* **2009**, 1, 169-192
- (2) Kim et al., *Applied Catalysis A* 2013, 453, 175-180
- (3) Li H., Niu Y., *Asian J. Chem.*, **2011**, 23, 3344-3346
- (4) Rokicki G., Rakoczy P., Parzuchowski P., Sobiecki M., *Green Chem.*, **2005**, 7, 529-539
- (5) Cho H.-Y., Kim J., Kim S.-N., Ahn W.-S., *Microporous and Mesoporous Materials* **2013**, 169, 180-184
- (6) Park K.; S., Ni Z., Côté A. P., Choi J. Y., Huang R., Uribe-Romo F. J., Chae H. K., O’Keeffe M., Yaghi O. M., *Proc. Natl. Acad. Sci. U.S.A.* **2006**, 103, 10186-10191
- (7) Cychosz K. A., Matzger A. J., *Langmuir* **2010**, 26, 17198-17202
- (8) Miralda C. M., Macias E. E., Zhu M., Ratnasamy P., Carreon M. A., *ACS Catal.*, **2012**, 2, 180-183
- (9) Liu Q., Wu L., Jackstell R., Beller M., *Nature Communications*, **2015**, 6, 5933, 1-15
- (10) Martin C., Fiorani G., Kleij A. W., *ACS Catal.*, **2015**, 5, 1353-1370
- (11) (a) Miralda C. M., Macias E. M., Zhu M., Ratnasamy P., Carreon M. A., *ACS Catal.*, **2012**, 2, 180-183; (b) Carreon M. A., *Indian Journal of Chemistry*, **2012**, 51A, 1306-1314; (c) Zhu M., Srinivas D., Bhogeswararao S., Ratnasamy P., Carreon M. A., *Catalysis Communications*, **2013**, 32, 36-40
- (12) Wu G.-P., Wei S.-H., Ren W.-M., Lu X.-B., Xu T.-Q., Darensbourg D. J., *J. Am. Chem. Soc.*, **2011**, 133, 15191-15199
- (13) Peng J., Yang H.-J., Song N., Guo C.-Y., *Journal of CO₂ Utilization*, **2015**, 9, 16-22
- (14) Gan W. M., Randau C., Hofmann M., Brokmeier H. G., Mueller M., Schreyer A., *Journal of Physics: Conference Series*, **2012**, 340, 012100, 1-5
- (15) (a) *X-ray Diffraction Residual Stress Measurement. An Introduction*, **2011**, PROTO; (b) Fitzpatrick M. E., Fry A. T., Holdway P., Kandil F. A., Shackleton J., Suominen L., *Determination of Residual Stresses by X-ray Diffraction from A National Measurement Good practice Guide No. 52*, **2005**, National Physical Laboratory, Teddington Middlesex, UK
- (16) Rotaru P., Blejoiu S. I., Stanciu M., Stoenescu G., Matcescu M., Voiculescu V., *Microporous and Mesoporous Materials*, **2005**, 83, 159-164
- (17) (a) Chizallet C., Lazare S., Bazer-Bachi D., Bonnier F., Lecocq V., Soyer E., Quoineaud A.-A., Bats N., *J. Am. Chem. Soc.*, 2010, 132, 12365-12377; (b) Nguyen L. T. L., Le K. K. A., Phan N. T. S., *Chin. J. Catal.*, **2012**, 33, 688-696; (c) Tran U. P. N., Le K. K. A., Phan N. T. S., *ACS Catal.*, **2011**, 1, 120-127; (d) Schejn A., Balan L., Falk V., Aranda L., Medjahdi G., Schneider R., *Cryst. Eng. Comm.*, **2014**, 16, 4493-4500
- (18) (a) Byrne C. M., Allen S. D., Lobkovsky E. B., Coates G. W., *J. Am. Chem. Soc.*, **2004**, 126, 11404-11405; (b) Zhang Y. J., Yang J. H., Kim S. H., Krische M. J., *J. Am. Chem. Soc.*, **2010**, 132, 4562-4563; (c) Zhang H., Liu H.-B., Yue J.-M., *Chem. Rev.*, **2014**, 114, 883-898; Khan A., Yang L., Xu J., Jin L. Y., Zhang Y. J., *Angew. Chem., Int. Ed.*, **2014**, 53, 11257-11260.
- (19) Clements J. H., *Ind. Eng. Chem. Res.*, **2003**, 42, 663-674

Chapter 5: Cytotoxicity of ZIF-8 doped and undoped samples

In this chapter we would like to present our investigation of cytotoxicity on ZIF-8 doped and undoped samples. We decided to test ZIF-8, Cu/ZIF-8 and Fe/ZIF-8 samples using *in vitro* models of human skin cells IHK keratinocytes and alveolar lung cells A549. The results originated from this part will be presented in the first paper. The second part is indicating some aspects and conclusions on the particles digestion. For this study, we used *in vitro* digestion model that gives the information on the particles stability in different physiological pH conditions. We simulated what will happen with ZIF-8 samples when mixed with different fluids of the gastrointestinal tract: saliva, stomach and intestine.

ZIF-8, as many other products in a powder state form dust, can be found as aerosols and can contaminate the air and thus be inhaled by the human body. The A549 cell line has characteristic features of Type II cells of pulmonary epithelium and is being considered as an ideal model for toxicological studies. This pulmonary epithelium component is responsible for the production of the surfactant (stored in organelles called lamellar bodies), xenobiotics metabolism by cytochromes CYP1A1 and CYP2B6. Type II cells are also progenitor of Type I pulmonary cells that cover ~96% of lung surface.⁵ In this context, the A549 model cell line, under the influence of nanoparticles, can provide useful information on implications and severe damages that could happen during aspiring the airborne ZIF-8.

The second cell line, immortalized human keratinocytes can serve to study the pathogenesis and toxicity of nanoparticles through dermal contact. Keratinocytes are the outermost layer of the skin (epidermis) that forms a barrier protecting against the environment. Thus keratinocytes can be a perfect model to investigate the impact of different xenobiotics, bacteria, viruses, drugs, etc. However, keratinocytes have a finite lifespan in culture that limits their proliferative capacity and laboratory or clinical utilization.⁶ In our study, we used immortalized human keratinocytes IHK where the growth was arrested by telomerase reverse transcriptase (TERT). Normal somatic cell has a limited number of divisions that is signed by telomeres present at the edges of chromosomes. These telomeres protect DNA against damages. When the telomeres are too short, the cell can no longer divide and either becomes inactive, senescent or dies. TERT maintains the telomeres caps throughout the multiple cell division and development, thus makes the cell immortalized and long-life to be useful model to make toxicological evaluation.⁷

We also tested *in vitro* digestion of Cu-, Fe- and undoped ZIF-8 materials. Orally ingested nanoparticles could have negative health impact when pass through gastrointestinal barrier, reach organs and tissues by circulatory blood system. However, the particles have to resist different physiological acid-base conditions during the digestion process. This situation rarely happens (especially when the particles meet stomach fluids with pH 1-2). Consequently, the final effect of the material is summarized with totally or partially digested particles (products of degradation).⁸ The digested particles can have different properties compared to their parental versions and that gives difficulties in assessing the health risk.⁹

We would like to show the very first results on this subject.

5.1 Impact of ZIF-8 samples on viability and reactive oxygen species production in A549 alveolar lung cells and IHK keratinocytes cell cultures.

5.1.1 Abstract

Recently, ZIF-8 metal-organic framework was shown to play an important role towards many research fields, thus leading the future possibility for a big expansion within the environment, risks of exposure, influence on human health and well-being. However, the toxicity of this material is not fully described yet and still many questions arise from its safety. In this paper, we investigated the cytotoxic character of pure, Cu- and Fe-doped ZIF-8 crystals with immortalized human keratinocytes (IHK) and pulmonary alveolar A549 cells. The results indicate that the keratinocytes are more sensitive when getting in contact with ZIF-8 samples. We also determined reactive oxygen species production (ROS) induced by these materials for both cell lines as one of the possible mechanism responsible for loss in cell viability. We hope that the present work will put some basic knowledge about the toxicity of ZIF-8 material in aspects of the potential exposure.

5.1.2 Introduction

Nanomaterials science has grown markedly with the promise of wide and beneficial applicability towards various fields as electronics, optics, engineering and healthcare. The spread of different nanostructures into the environment could cause risks and dangerous effects on nature and human life. Human faces the nanoparticles during synthesis (laboratory level), manufacture (industry level), utilization (consumer products, like cosmetics, medicines, devices, etc.) and disposal within the environment.¹ An exposure to nanoparticles provokes deep considerations on urgent development of rapid, simple and efficient tests to assess their biological influence. The skin and the lungs are directly exposed and contacted with nanomaterials. Due to their size, the nanoproducts can be distributed in a whole respiratory tract and reach pulmonary alveoli. Some particles can also diffuse and penetrate within the dermal barrier, especially through hair follicles and damages.² It was shown for multi-walled carbon nanotubes (MWCNTs) that were easily internalized by human epidermal keratinocytes in cell culture experiments.³ Consequently, the studies on penetration and toxicity evaluation should be strictly carried out for all types of the nanomaterials.

Metal organic frameworks (MOFs) represent a class of porous hybrid nanomaterials, formed by self-assembly of inorganic and organic part into infinite network. Metal ions or clusters linked with polydentate ligands form a complex structure with large surface area and accessible pores.^{4,5} These beneficial properties, together with high thermal and chemical stability, possibility to functionalize the structure make them potentially useful for drug delivery, hydrogen storage, catalysis, separations, nonlinear optics or chemical sensors.^{6,7,8} However, due to the high expansion and numerous publications on the application area of MOFs, there is still not enough information on their safety.

This study examined cytotoxicity of a member of MOFs zeolitic imidazolate frameworks subfamily - ZIF-8 undoped and doped with copper and iron. We evaluated the toxicity of these materials over human alveolar epithelial A549 cells and immortalized human keratinocytes IHK. The culture cells were mixed with different concentrations of nanoparticles ranging from 1 to 100 µg/mL and the viability after 24 h incubation was determined with MTS assay. Finally, we determined ROS production using flow cytometry system (FACS).

5.1.3 Results

5.1.3.1 ZIF-8 samples synthesis and characterization

The synthesis of Cu/ZIF-8 and Fe/ZIF-8 crystals was performed under solvothermal conditions by mixing $\text{Zn}(\text{NO}_3)_2$, $\text{Cu}(\text{NO}_3)_2$ or $\text{Fe}(\text{AcO})_2$ and Hmim in methanol at room temperature for 1 h.⁹ Molar percentages of 1, 5, 10% of $\text{Fe}(\text{AcO})_2$ and 1, 5, 10, 25% of $\text{Cu}(\text{NO}_3)_2$ to $\text{Zn}(\text{NO}_3)_2$ were used in these experiments. The crystals prepared will be noted $\text{Fe}_{1\%}/\text{ZIF-8}$, $\text{Fe}_{5\%}/\text{ZIF-8}$, $\text{Fe}_{10\%}/\text{ZIF-8}$, $\text{Cu}_{1\%}/\text{ZIF-8}$, $\text{Cu}_{5\%}/\text{ZIF-8}$, $\text{Cu}_{10\%}/\text{ZIF-8}$, and $\text{Cu}_{25\%}/\text{ZIF-8}$ thereafter. The Cu/ZIF-8, Fe/ZIF-8 and ZIF-8 samples characterization included the determination of the particle size and morphology using electron microscopy techniques (scanning and transmission), crystallinity by X-ray diffraction, specific surface area by BET and thermal stability by thermogravimetry.

The scanning and transmission electron microscopy images reveal that the ZIF-8 samples doped with copper and iron display the same morphology as original ZIF-8 (figure 5.1.1). We observed only pure phase of the material. The size of the crystals differs markedly for the samples synthesized with iron acetate (figure 5.1.2). This may originate from the utilization of the different salts than nitrate in this case, the phenomenon we previously reported for ZIF-8 crystals synthesized with various Zn^{2+} salts.¹⁰ The crystals are bigger when the contribution of the iron to the inorganic part is higher.

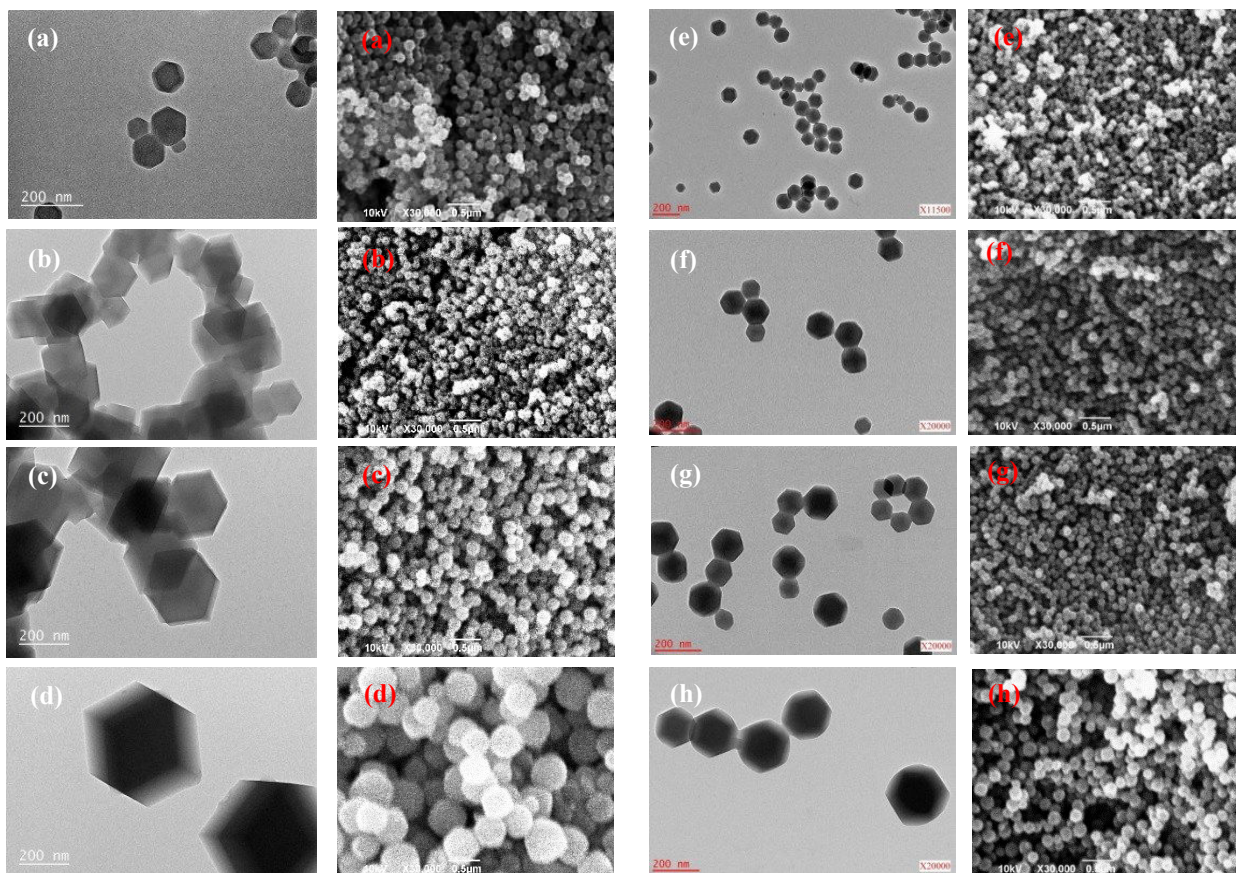


Fig. 5.1.1 Transmission and scanning electron microscopy images for ZIF-8 (a), $\text{Fe}_{1\%}/\text{ZIF-8}$ (b), $\text{Fe}_{5\%}/\text{ZIF-8}$ (c), $\text{Fe}_{10\%}/\text{ZIF-8}$ (d), $\text{Cu}_{1\%}/\text{ZIF-8}$ (e), $\text{Cu}_{5\%}/\text{ZIF-8}$ (f), $\text{Cu}_{10\%}/\text{ZIF-8}$ (g), $\text{Cu}_{25\%}/\text{ZIF-8}$ (h).

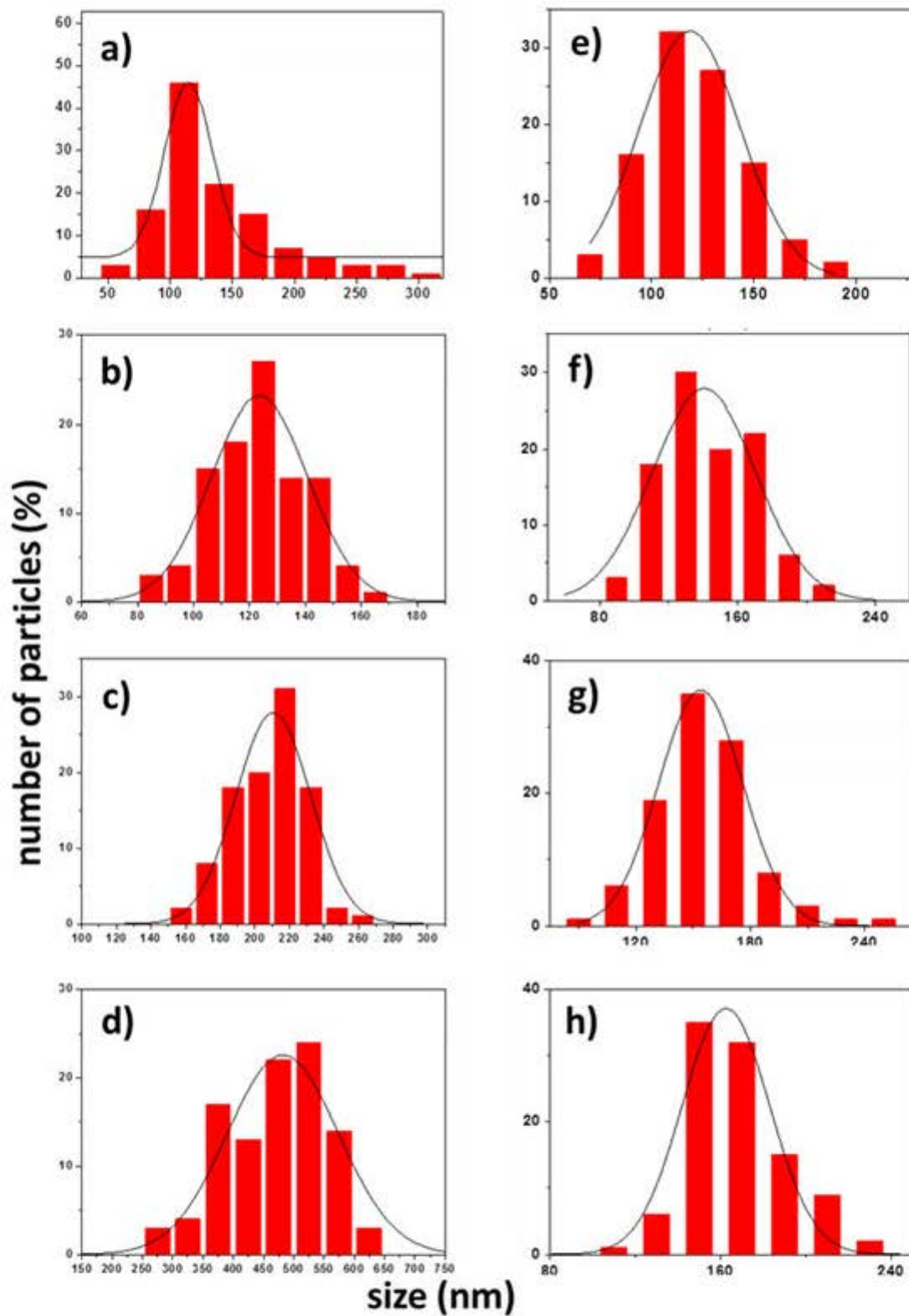


Fig. 5.1.2 Size distributions of the samples: ZIF-8 (a), Fe_{1%}/ZIF-8 (b), Fe_{5%}/ZIF-8 (c), Fe_{10%}/ZIF-8 (d), Cu_{1%}/ZIF-8 (e), Cu_{5%}/ZIF-8 (f), Cu_{10%}/ZIF-8 (g), Cu_{25%}/ZIF-8 (h).

Table 5.1.1 ZIF-8 size evaluated from SEM and porosity determined by nitrogen sorption study.

Sample	crystal size (nm)	BET surface area (m²/g)	pore volume (cm³/g)	pore width (nm)
ZIF-8	141 ± 48	1700 ± 30	0.662	1.2922
Cu_{1%}/ZIF-8	121 ± 25	1541 ± 40	0.518	1.2214
Cu_{5%}/ZIF-8	143 ± 27	1736 ± 59	0.601	1.2179
Cu_{10%}/ZIF-8	156 ± 27	1639 ± 56	0.571	1.2169
Cu_{25%}/ZIF-8	166 ± 24	1205 ± 47	0.440	1.2190
Fe_{1%}/ZIF-8	124 ± 35	1774 ± 32	0.693	1.2955
Fe_{5%}/ZIF-8	211 ± 43	1805 ± 30	0.691	1.2929
Fe_{10%}/ZIF-8	482 ± 184	1516 ± 25	0.597	1.2920

The BET surface area and porosity measurements were performed via nitrogen sorption experiment (table 5.1.1 and figure 5.1.3). The distribution of micropores was calculated by the Saito-Foley method. The obtained isotherms have a typical I-type behavior indicating microporosity and mesoporosity of these samples. The specific surface area markedly decreased for the samples with the highest doping level: Cu_{25%}/ZIF-8 and Fe_{10%}/ZIF-8. Until 10% of doping in Cu²⁺ and 5% of Fe²⁺, the crystals properties were only slightly affected by the substitution.

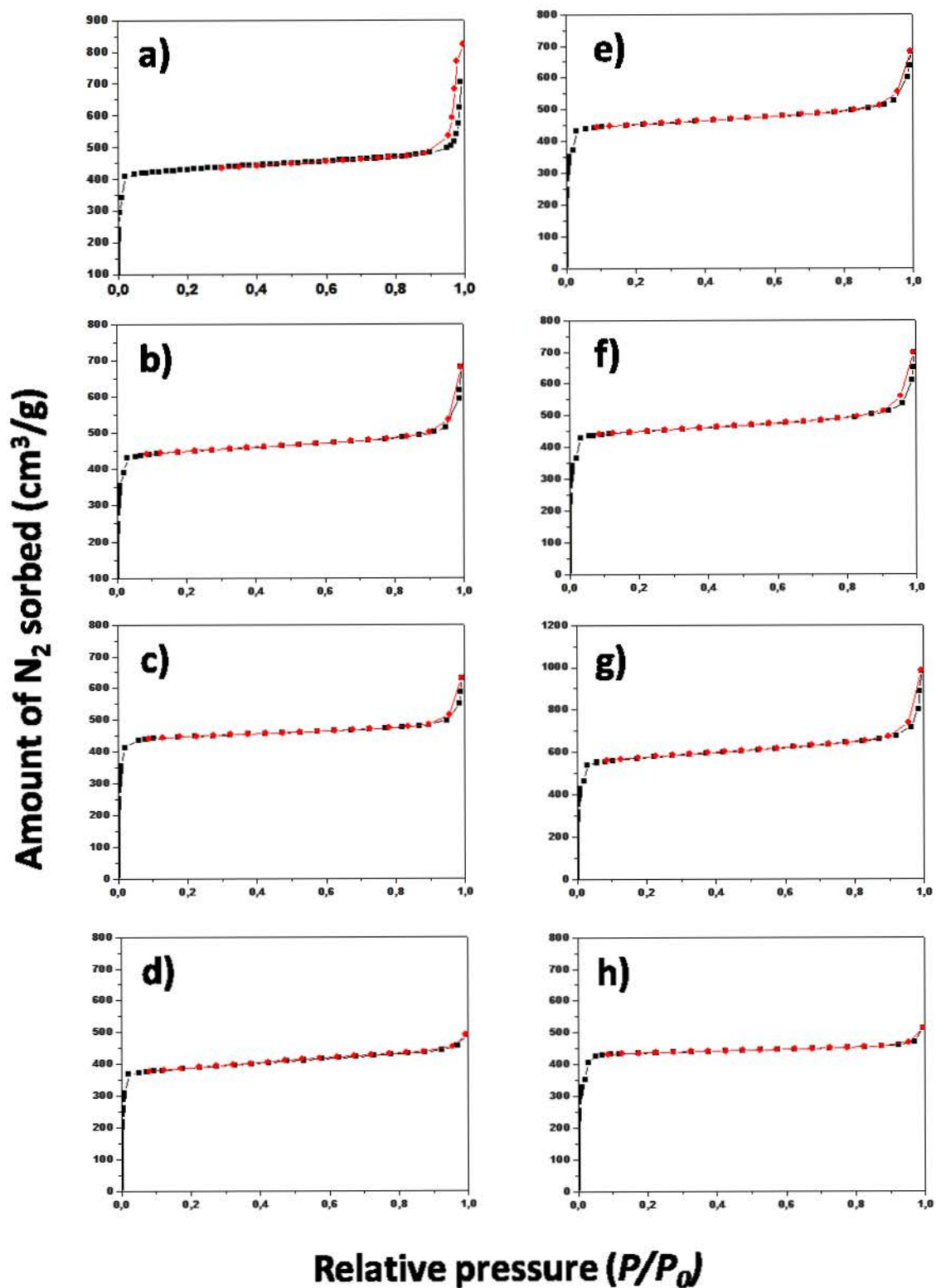


Fig. 5.1.3 N_2 sorption isotherms of: ZIF-8 (a), $Fe_{1\%}/ZIF-8$ (b), $Fe_{5\%}/ZIF-8$ (c), $Fe_{10\%}/ZIF-8$ (d), $Cu_{1\%}/ZIF-8$ (e), $Cu_{5\%}/ZIF-8$ (f), $Cu_{10\%}/ZIF-8$ (g), $Cu_{25\%}/ZIF-8$ (h).

The XRD patterns of the samples are also in agreement with the pure ZIF-8 material (figure 5.1.4).

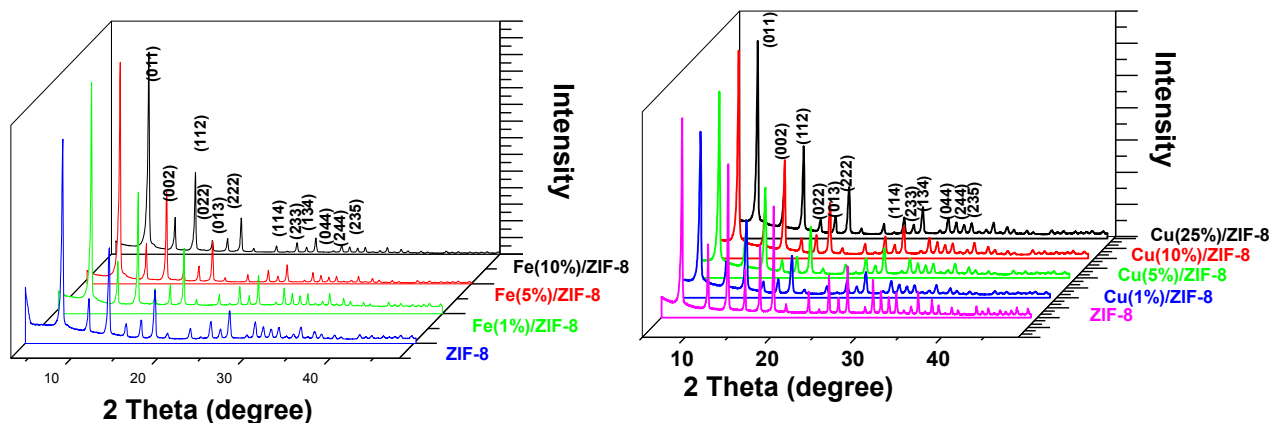


Fig. 5.1.4 XRD patterns for ZIF-8 samples with indexed characteristic peaks of the material.

No impurities or crystal disorders were detected. For all the samples, the ZIF-8 crystals show a body-centered cubic crystal lattice group $I\bar{4}3m$. The indexed peaks for each material were in correlation with the standard ZIF-8 pattern. The thermal stability of these materials was observed by TG profiles (figure 5.1.5). The TGA curves of ZIF-8 and Cu-doped ZIF-8 showed a similar trend in range 20 to 250°C, exhibited only a very weak weight loss of less than 0.5%, corresponding to the removal of guest molecules (methanol or Hmim) and/or CO₂ from the cavities as indicated by MS analyses. However, for the Fe-doped structures, the weight loss of 5-10% was detected at lower temperatures. A long plateau was then observed after the formation of the guest-free phase Zn(mim)₂ until 350°C, indicating the good thermal stability of the three-dimensional network. The sharp weight loss upon increasing the temperature from 400 to 500°C was found for all materials. The weight loss was evaluated as 64% for ZIF-8 and Cu/ZIF-8, and 60% for Fe/ZIF-8. The difference originated from the final product composition after calcination. The XRD analysis showed ZnO phase from ZIF-8, Cu-doped ZnO from Cu/ZIF-8 and Fe_xO_n/ZnO hybrid from Fe/ZIF-8.

We also confirmed the presence of homogenous phases of ZIF-8 for all the samples by Raman spectroscopy analysis. In the Raman spectra (figure 5.1.5), we only observed standard peaks for ZIF-8 material. Raman peaks for ZIF-8 and doped ZIF-8 materials correspond to:

- at 168 and 273 cm⁻¹ - stretching Zn-N,
- 686 cm⁻¹ – imidazole ring puckering,
- 755 cm⁻¹ - C=N out of plane bend and bending N-H,
- 833, 950, 1021 cm⁻¹ – C-H out of plane bend,
- 1146, 1187 cm⁻¹ – stretching C-N,
- 1311 cm⁻¹ – ring expansion + N-H wag,
- 1384 cm⁻¹ – bending CH₃,
- 1455 cm⁻¹ – C-H wag,
- 1499 cm⁻¹ – C-N, N-H wag,
- 1508 cm⁻¹ – stretching C-C.

No additional peaks were observed after Cu- or Fe-doping of ZIF-8

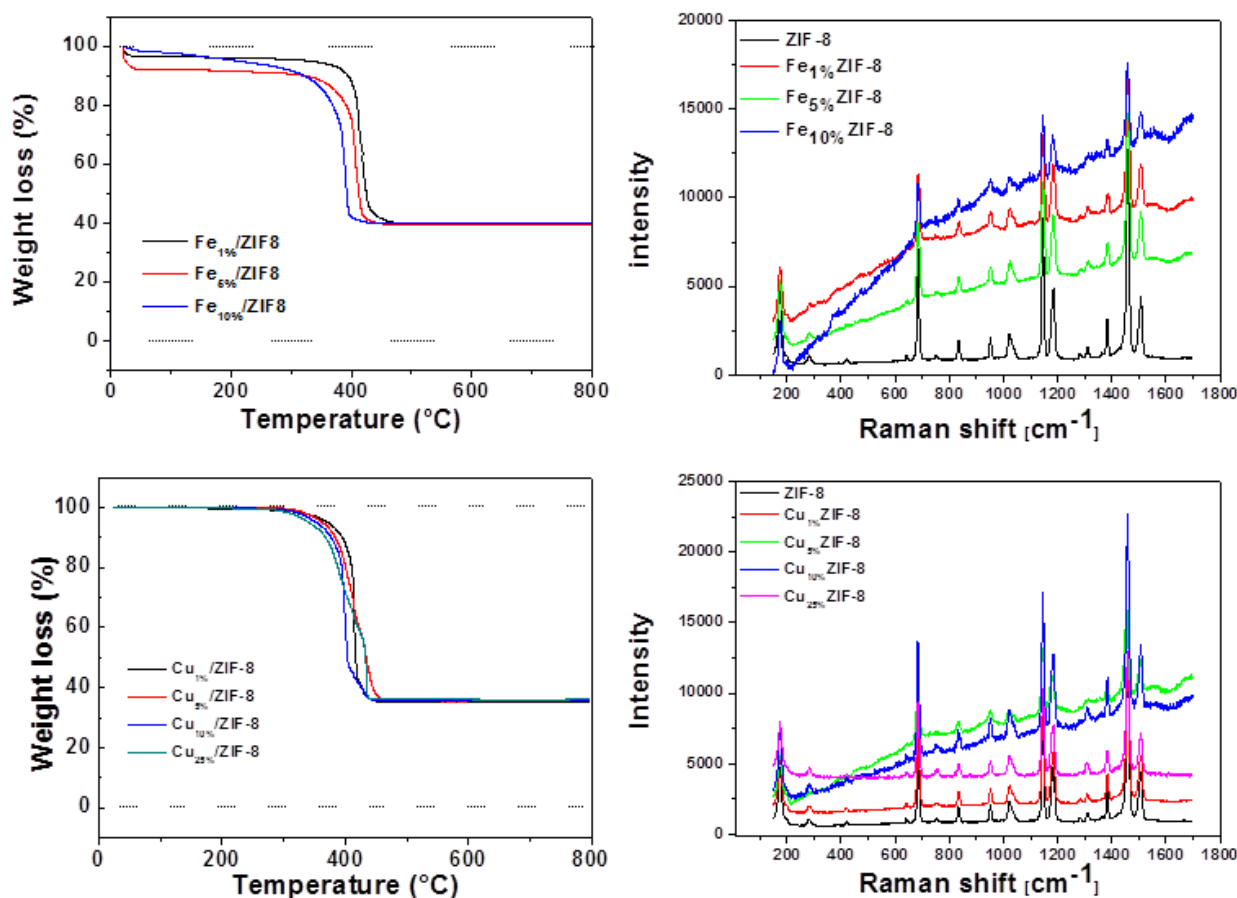


Fig. 5.1.5 TG diagrams and Raman spectra for the ZIF-8 samples doped with iron and copper.

5.1.3.2 Cytotoxicity studies

Concerning the metal-organic framework chemistry, many factors can influence on the resulting cytotoxicity.¹¹ The effect is attributed to the materials characteristics, building blocks, arrangement of the subunits but as well to the behavior and the stability of these structures in the cell culture media. Herein, the A549 and IHK cells were exposed to Cu/ZIF-8, Fe/ZIF-8 and the reference, undoped ZIF-8 at the concentrations 1, 10, 25, 50, 100 $\mu\text{g}/\text{mL}$ for 24 h. The MTS assay evaluated the viability of the cells after 24 h incubation. The results presented on the graphs (figure 5.1.6) show a concentration-dependent toxicity profiles for all tested samples. In general, the keratinocytes were more sensible for the treatment with ZIF-8 particles than A549 cells. The viability was markedly affected with 25 $\mu\text{g}/\text{mL}$ and 100 $\mu\text{g}/\text{mL}$ nanoparticles doses for IHK and A549 respectively. It is worth to mention that the ZIF-8 samples are highly hydrophobic and the stock solutions in water had the tendency to aggregate over time. Before each test, the dispersions were sonicated for 15 min to maintain good homogeneity. However for the experiment with IHK cells the two samples – Cu_{5%}/ZIF-8 and Fe_{5%}/ZIF-8 we deposited on the microtiter plates only after manual shaking to see the influence of these aggregates on the final viability of the cells. As it is shown on figure 4.2.6 – the viability is much

higher compared with the pre-sonicated samples. For these two examples, the IC_{50} was 100 $\mu\text{g/mL}$ and for the sonicated samples 25 $\mu\text{g/mL}$. We indicated that the sample preparation before the test should be highly considered to avoid false response and masked effects.

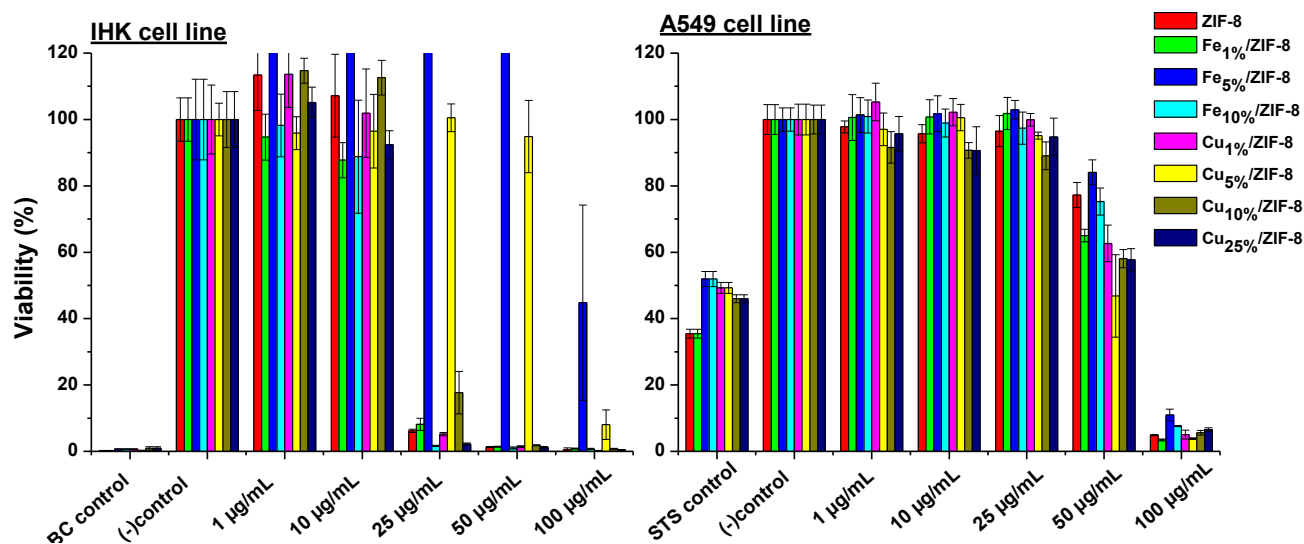


Fig. 5.1.6 MTS assay results. Relative cell viability (%) of IHK and A549 treated for 24 h/37 °C with ZIF-8 samples.

According to the toxicity of ZIF-8, there are only few reports. The work of Ruyra *et al.* 2015 suggests that the material is highly cytotoxic for zebrafish embryo (*Danio rerio*) causing severe multiple morphological and physiological defects.¹² In this study, they mentioned the degradation of about $19.1 \pm 0.8\%$ ZIF-8 ($1916.2 \pm 75.4 \mu\text{M}$) in the culture containing 10% fetal bovine serum after incubation 24 h at 37 °C. The gradual degradation products of ZIF-8 in the phosphate-containing media (pH 7.4) and in the endosomal environment (pH ~6.5 - 4.5 and enzymes) were determined as Zn^{2+} ions and methyl-imidazole ($\text{pK}_a \sim 7.0$ and 14.5) in the work of Tamames-Tabar *et al.* 2014.¹¹ ZIF-8 crystals cytotoxicity was tested on human cervical cancer cell line (HeLa) and mouse macrophage cell line J774. IC_{50} for HeLa cells was $\sim 100 \mu\text{g/mL}$ and for J774 $25 \mu\text{g/mL}$. The authors also evaluated the possible mechanism of ZIF-8 toxicity that was deduced as Zn^{2+} competition with Fe^{2+} and Ca^{2+} through ion channels and/or due to the DNA damage in the cells. Moreover, they showed on a series of MOFs that Fe-based MOFs are less toxic than Zn- or Zr-containing frameworks. For Zn-containing materials, like ZnO nanoparticles studied in A549 culture, it was proved that Zn^{2+} release interfered with zinc homeostasis and thus implying in mitochondrial dysfunction, increase in the cellular reactive oxygen species level and loss of cell integrity.^{13,14}

On the other hand, Vasconcelos *et al.* 2012 reported on the non-toxic of a 109 μM concentration of ZIF-8 towards three cell lines: mucoepidermoid carcinoma of lung (NCI-H292), colorectal adenocarcinoma (HT-29) and promyelocytic leukemia (HL-60).¹⁵ ZIF-8 was used as a controlled-release drug delivery system of doxorubicin to the cancer cells. Some works suggested that the importance of toxicity assessments for such MOF-drug carriers has to be highlighted in terms of advanced biomedical applications. For example, IRMOF-3, a Zn-based aminobenzene dicarboxylate

network, released large amounts of metal ions over 6 days at 37°C and thus showed a dose-dependent differentiation impair of PC12 (rat pheochromocytoma) neural cells.¹⁶

5.1.3.3 Reactive oxygen species production

To determine the eventual oxidative stress caused by ZIF-8 particles, we examined ROS induction using the DCF-DA (2',7'-dichlorofluorescein diacetate) assay. DCF-DA diffuses easily inside the cells where it is hydrolyzed by specific esterases. These enzymes convert DCF-DA into the stable fluorescent product DCF in the presence of oxidative species. The oxidized DCF has green fluorescence and quantitatively indicates the amount of ROS. The intensity of highly fluorescent DCF is proportional to ROS produced by the sample and is therefore readily detectable by flow cytometry. In our work, we tested this mechanism on the two cell lines: A549 and IHK using 67.7 and 15 µg/mL concentrations of the particles, respectively. We also traced the behavior of the cells before and after each step of the analysis by optical microscopy. Some of the representative pictures are shown at the figures 5.1.7 and 5.1.8. As previously mentioned, the concentration of the ZIFs samples were adapted not to cause complete cell death (15 µg/mL for IHK and 67.7 µg/mL for A549). The images demonstrate some of the cells are floating, round-shaped, detached from the surface of the well, which is typical for cells altered by the ZIF-8 crystals. However, some of the cells resisted and remained well-attached.

The crude data acquired using flow cytometry are shown at the figure 5.1.9 and 5.1.10. We applied the collection of large enough sample size (10000 events) to ensure a precision for labeled population of interest. Each result for the samples treated with ZIF-8 particles was compared with SIN-1 control to visualize the difference between them. All the samples were measured in triplicate. The gating scheme used for the analyses is included and shown at the figures.

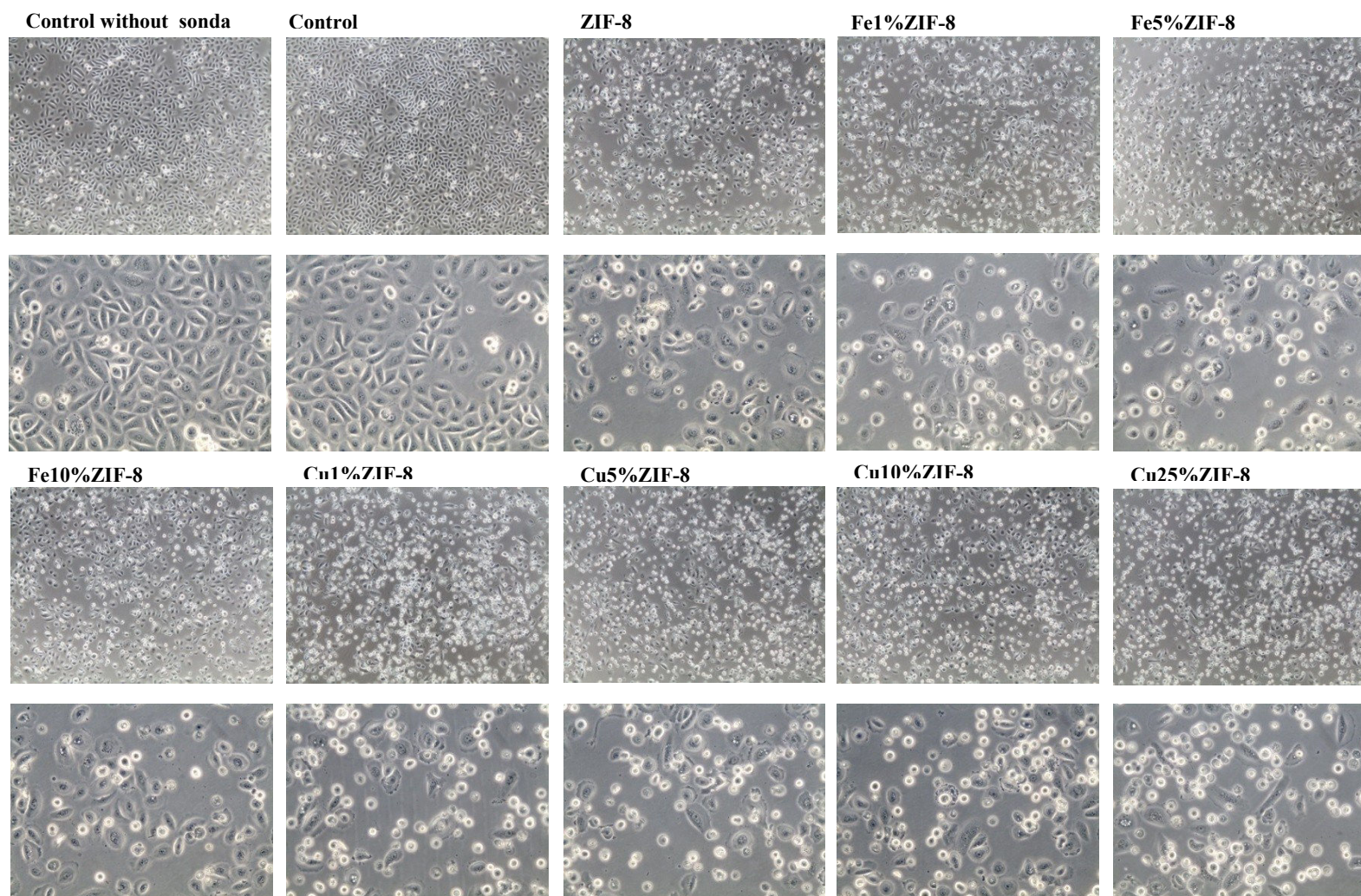


Fig. 5.1.7 Optical microscopy images of IHK cells incubated for 24h with ZIF-8 nanoparticles (concentration 15 $\mu\text{g/mL}$). Control samples were conducted in the parallel. Images were obtained at $\times 63$ and $\times 100$ magnifications.

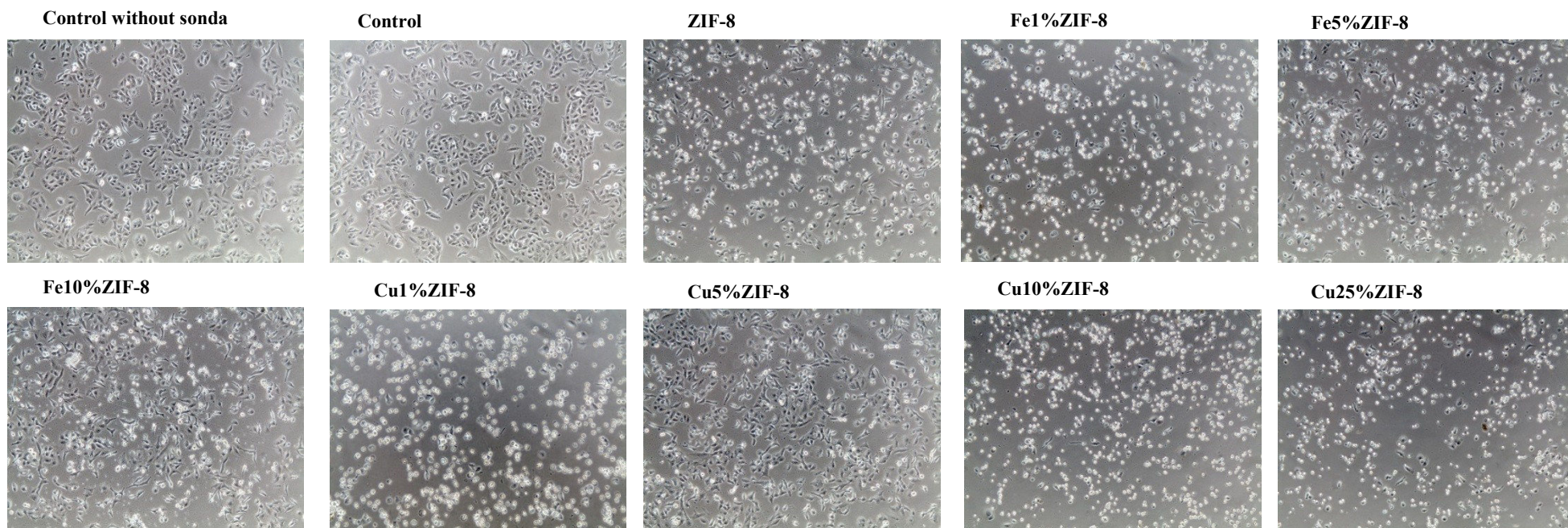


Fig. 5.1.8 Optical microscopy images of A549 cell line after 24 h incubation with ZIF-8 samples (concentration 67.7 $\mu\text{g/mL}$) and control probes. Images were obtained at $\times 63$ magnification.

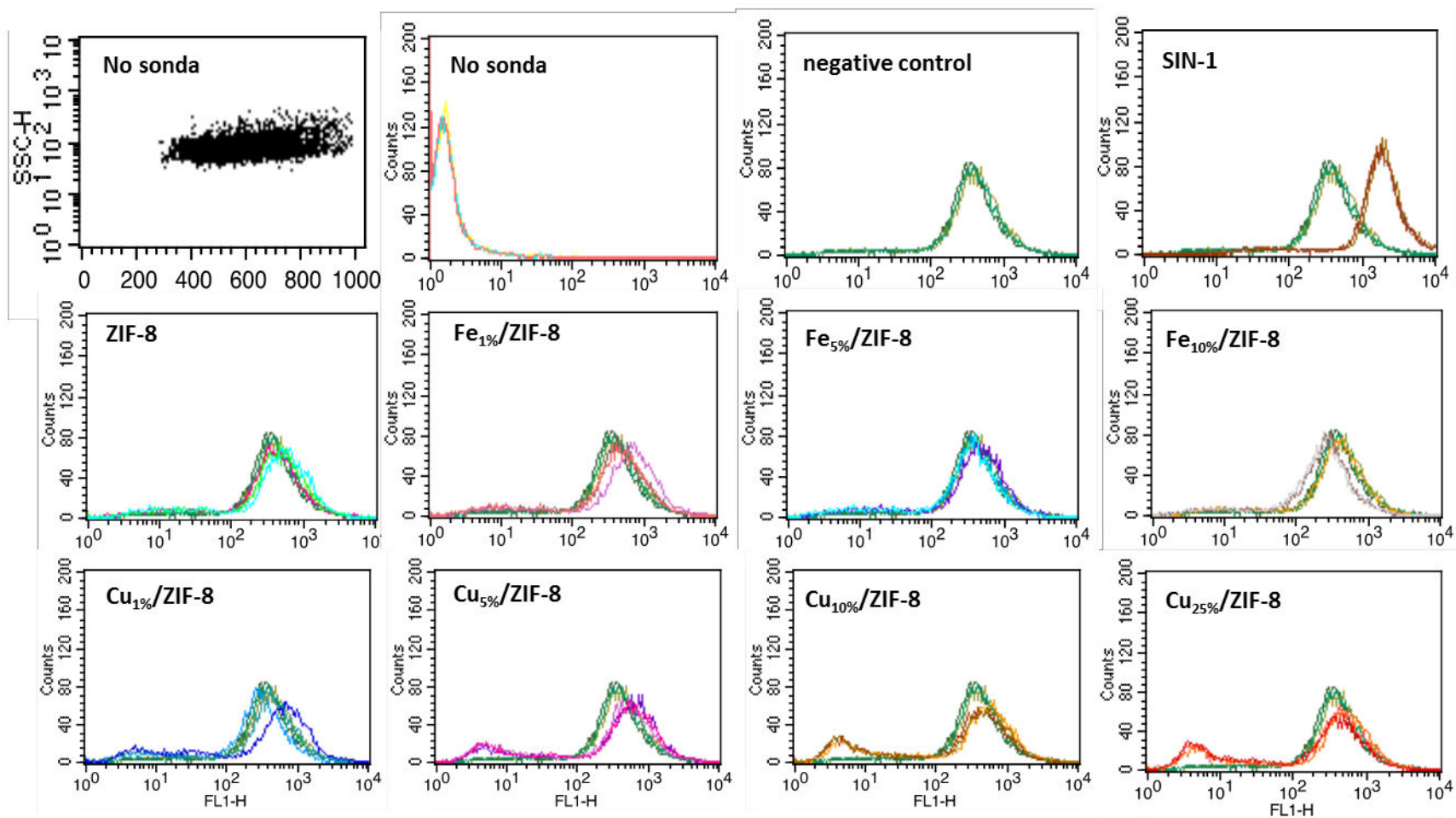


Fig. 5.1.9 Results of flow cytometry analysis for the IHK cells incubated with ZIF-8 particles.

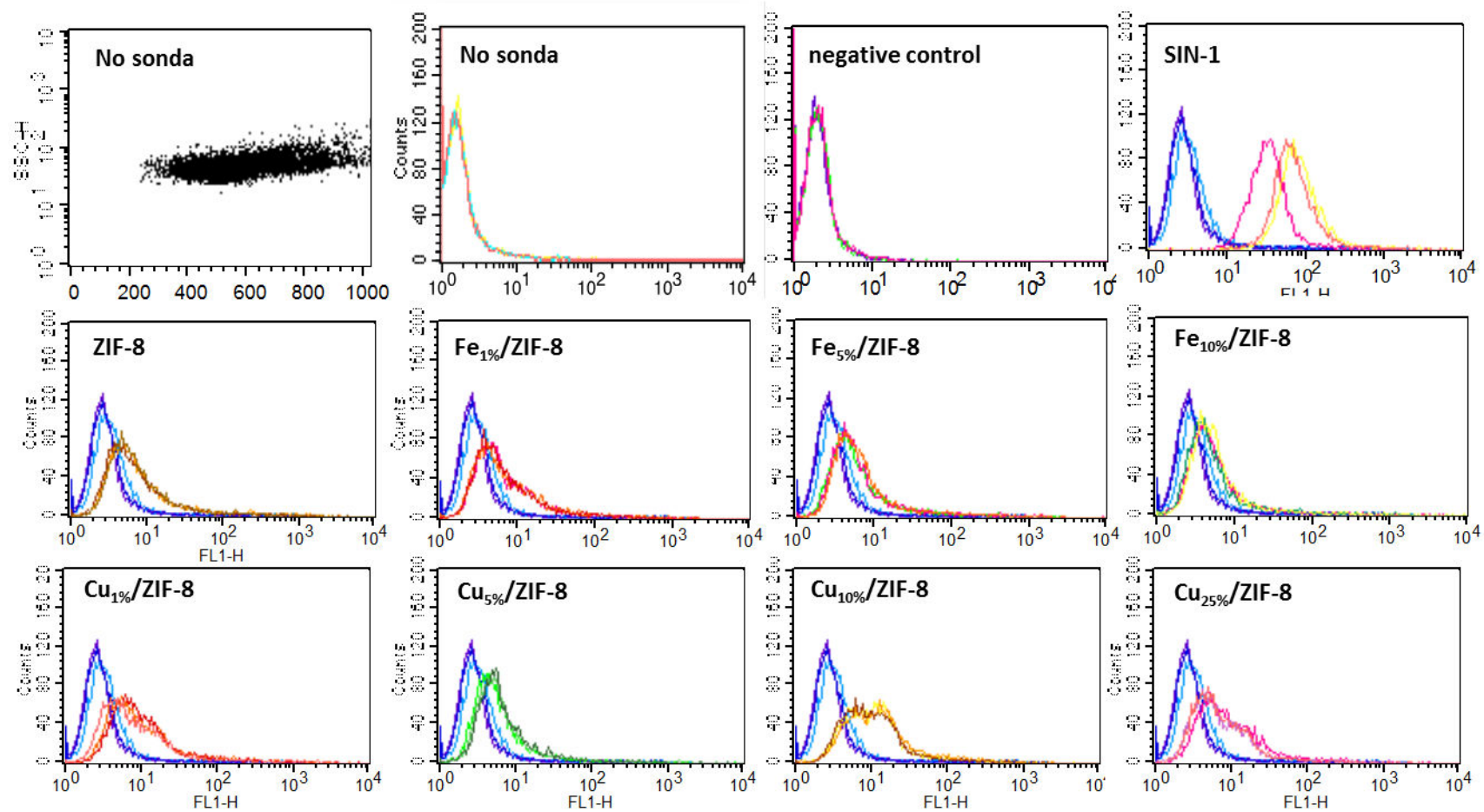


Fig. 5.1.10 Results of flow cytometry analysis for the A549 cells incubated with ZIF-8 particles.

The results show that there is a slight difference between ZIF-8 and the other samples, especially with the highest doping level. The summary of FACS is shown at the figure 5.1.11. The materials Cu_{25%}/ZIF-8 and Fe_{10%}/ZIF-8 present lower ROS production when compared to undoped ZIF-8. The estimated ROS levels indicate that it can be one of the possible mechanisms of cytotoxicity that contribute to the total effect.

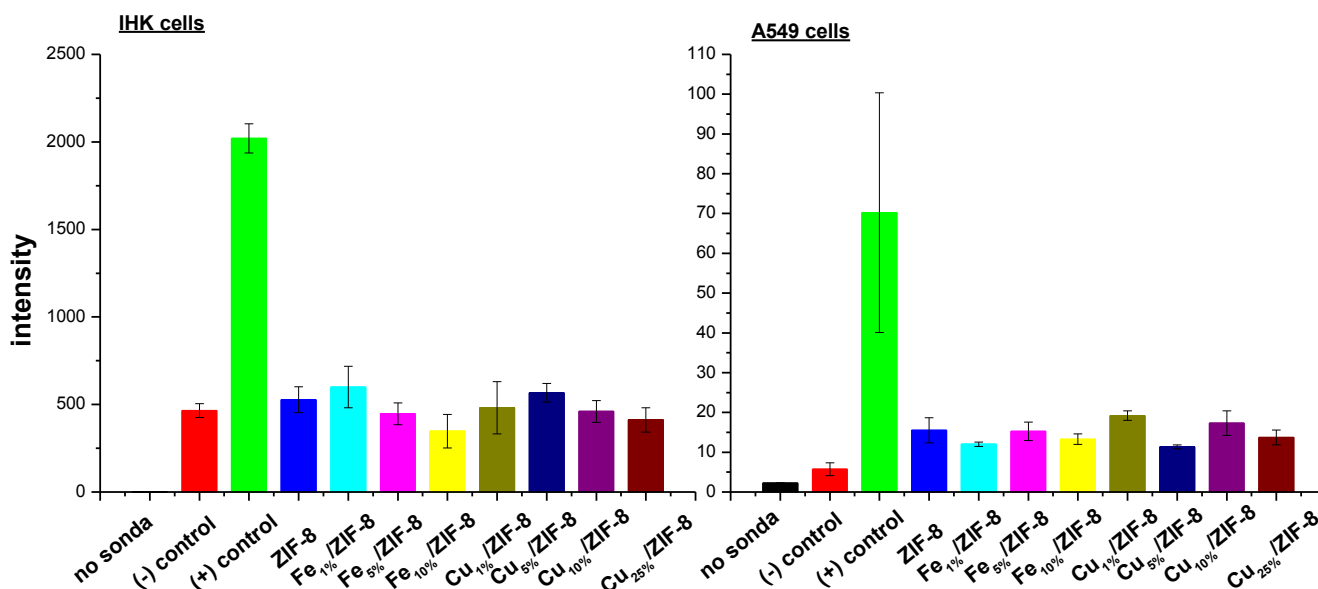


Fig. 5.1.11 FACS assay results. Intensity of the fluorescence for the DCF analysed for IHK and A549 treated for 24 h/37 °C with ZIF-8 samples.

5.1.4 Conclusions

ZIF-8 is one of the most prominent examples in the rapidly expanding field of metal-organic frameworks. Many investigations showed that ZIF-8 can be applied in the fields such as catalysis, gas storage, separation, drug delivery, molecular sensing, encapsulation and medical applications.¹⁷ The most relevant health risks can originate from exposure to these materials via skin contact or/and inhalation. Thus, in this work, A549 lung cells and IHK keratinocytes were used as an *in vitro* models to determine the possible induced cytotoxicity. Our data demonstrate that the ZIF-8 samples, pure or doped either with copper or iron, produce cytotoxic effects in a dose-dependent manner. We observed higher influence on IHK keratinocytes than on lung cells A549. This study suggests the necessity of the precautions against potential direct exposition to these nanoparticles, especially via dermal way. We also showed that reactive oxygen species generation by the particles is not the only one mechanism contributed to the cytotoxicity. The detected ROS levels were relatively low compared to the untreated control cells. We hope to further investigate the mechanisms responsible for these effects and supplement the general information on ZIF-8 toxicity given by this article.

5.1.5 References

- (1) Kansara K., Patel P., Shah D., Shukla R. K., Singh S., Kumar A., Dhawan A., *Environ. Mol. Mutagenesis*, **2015**, 56, 204-217
- (2) Baroli B., *J. Pharmaceutical Sci.*, **2010**, 99, 21-50
- (3) Monteiro-Riviere N. A., Nemanich R. J., Inman A. O., Wang Y. Y., Riviere J. E., *Toxicol. Lett.*, **2005**, 155, 377-384
- (4) Liu J., Chen L., Cui H., Zhang J., Zhang L., Su C.-J., *Chem. Soc. Rev.*, **2014**, 43, 6011-6061
- (5) Valvekens P., Vermoortele F., De Vos D., *Catal. Sci. Technol.*, **2013**, 3, 1435-1445
- (6) Ahmad N., Younus H. A., Chughtai A. H., Verpoort F., *Chem. Soc. Rev.*, **2015**, 44, 9-25
- (7) Sun J., Yu G., Huo Q., Kan Q., Guan J., *RSC Adv.*, **2014**, 4, 38048-38054
- (8) Cuhna S., Yahia M. B., Hall S., Miller S. R., Chevreau H., Elkaïm E., Maurin G., Horcajada P., Serre C., *Chem. Mater.*, **2013**, 25, 2767-2776
- (9) Schejn A., Aboulaich A., Balan L., Falk V., Lalevée J., Medjahdi G., Aranda L., Mozet K., Schneider R., *Catal. Sci. Technol.*, **2015**, 5, 1829-1839
- (10) Schejn A., Balan L., Falk V., Aranda L., Medjahdi G., Schneider R., *Cryst. Eng. Comm.*, **2014**, 16, 4493-4500
- (11) Tamames-Tabar C., Cunha D., Imbuluzqueta E., Ragon F., Serre C., Blanco-Prieto M. J., Horcajada P., *J. Mater. Chem. B*, **2014**, 2, 262-271
- (12) Ruyra Á., Yazdi A., Espin J., Carné-Sánchez A., Roher N., Lorenzo J., Imaz I., MasPOCH D., *Chem. Eur. J.*, **2015**, 21, 2508-2518
- (13) Kim Y. H., Fazlollahi F., Kennedy I. M., Yacobi N. R., Hamm-Alvarez S. F., Borok Z., Kim K.-J., Crandall E. D., *Am. J. Respir. Crit. Care Med.*, **2010**, 182, 1398-1409
- (14) Kao Y. Y., Chen Y. C., Cheng T. J., Chiung Y. M., Lin P. S., *Toxicol. Sci.*, **2012**, 125, 462-472
- (15) Vasconcelos I. B., da Silva T. G., Militão G. C. G., Soares T. A., Rodrigues N. A., Rodrigues M. O., da Costa Jr N. B., Freire R. O., Junior S. A., *RSC Adv.*, **2012**, 2, 9437-9442
- (16) Ren F., Yang B., Cai J., Jiang Y., Xu J., Wang S., *J. Hazardous Mater.*, **2014**, 271, 283-291
- (17) (a) Yang X.-Q., Yang C.-X., Yan X.-P., *J. Chromatography A*, **2013**, 1304, 28-31; (b) Jiang J.-Q., Yang C.-X., Yan X.-P., *ACS Appl. Mater. Interfaces*, **2013**, 5, 9837-9842; (c) Chang N., Gu Z.-Y., Yan X.-P., *J. Am. Chem. Soc.*, **2010**, 132, 13645-13647; (d) Pan Y., Wang B., Lai Z., *Journal of Membrane Science*, **2012**, 421-422, 292-298; (e) Liedana N., Galve A., Rubio C., Tellez C., Coronas J., *ACS Appl. Mater. Interfaces*, **2012**, 4, 5016-5021

5.2 In vitro digestion model of ZIF-8 particles

5.2.1 Abstract

The study presented was designed to evaluate human *in vitro* tests on the gastrointestinal resistance of ZIF-8 samples: pure, doped with 10% of iron(II) or 10% of copper(II). The ZIFs samples were characterized before and after incubation with the digestive fluids. The results of *in vitro* studies indicated that the gastric environment is the compartment where particles transformations or formation of aggregates take place. Moreover, we conducted stability tests of the particles in methanol, water and PBS buffers of pH 4.8 and 8.0. According to the parental ZIF-8 properties, all the samples were hydrophobic and remained unchanged in methanol dispersion after 3 days of incubation. However, we observed that the Fe_{10%}ZIF-8 particles are very sensible in various aqueous media, even in pure water after 1 h of the incubation. ZIF-8 and Cu-doped ZIF-8 materials remained relatively stable in the different mild and strong acid-base conditions.

5.2.2 Introduction

Prosperous use of different types of nanomaterials leads to wide consideration on their potential impact on humans and the nature. Released nanostructures could originate from the manufacturing processes of their synthesis or from consumer goods (food, water, cosmetics, drugs or drug delivery systems).¹ Nanoparticles could potentially enter the human's body mostly by inhalation, ingestion or dermal contact.² The ultrafine size of nanomaterials is advantage for the large scale deposition in the organism because the rate of the crossing through physiological barriers is much improved.³ However, to understand the fate of the nanoparticles, we should also consider dynamic exchanges with biomolecules and the influence of different acid-base conditions. Thus, the status of the material can vary during *in vivo* exposure. We could observe the processes such as particle wrapping, surface free energy releases, phase transformations, restructuring, degradation, dissolution and/or agglomeration.⁴ The stability of nanoparticles depends strictly on the environmental pH value.⁵ Within biological system, in gastrointestinal tract, the pH varies from 5.5-6 in the mouth, 1-2 in the stomach and 11 in the intestine. *Ex situ* techniques of the analysis cannot accurately describe these phenomena. *In vitro* approaches and models for analyzing could much better interpret what exactly happens to the nanoparticles in the body.

Zeolitic imidazolate framework-8 (ZIF-8), an interesting example of metal organic framework, has recently gained wide attention. ZIF-8 is constructed with zinc atoms tetrahedrally coordinated with 2-methylimidazole linkers forming infinite, three-dimensional (3D) network with sodalite topology.⁶ The main advantage is that ZIF-8 is more flexible in structure modification and functionalization. The surface and structure properties could be properly design to fit with a specific application.⁷ Moreover, the material is commonly known as thermally and chemically stable, comparable to zeolites.⁸ The chemical stability was proven in refluxing benzene, methanol, water up to 7 days and in aqueous sodium hydroxide till 24 h.⁹ Some studies suggest gradual hydrolysis of the pH-sensitive ZIF-8 particles in acidic environment (pH 5.5) led to prolonged release of encapsulated anticancer drug doxorubicin.¹⁰ As far, there is no information about the behavior of these particles in physiological juices of gastrointestinal tract.

The objective of this study was to determine if the ingested ZIF-8 samples remain unchanged in the digestive fluids and what exactly happen with the framework when contacted with complex physiological juices and harsh pH environment of gastrointestinal tract. We used an *in vitro* model to mimic the human digestion under fed conditions. We also conducted stability experiments using standard PBS buffers with adapted pH of 4.8 and 8.0, water and methanol. The materials tested in this evaluation were ZIF-8, Fe_{10%}/ZIF-8 and Cu_{10%}/ZIF-8. We would like to present our observations and final conclusions on this subject.

5.2.3 Results

ZIF-8, Fe_{10%}/ZIF-8 and Cu_{10%}/ZIF-8 nanoparticles were investigated with the aim to see their behavior in a simulated environment of human mouth, stomach and intestine. Representative SEM images of the materials (figure 5.2.1) before incubation in the digestive fluids showed individual rhombic dodecahedron structures. Corresponding size distributions indicate the size of ca. 141 nm, 482 nm and 156 nm for ZIF-8, Fe_{10%}/ZIF-8 and Cu_{10%}/ZIF-8, respectively. At the first stage of the digestion, upon exposure to saliva for 15 min (pH 6.8), the particles were morphologically unchanged. Afterwards, the significant alterations were observed in a simulated stomach juice for all the samples. During the incubation conducted for 5 min, 15 min and 2 h with ZIF-8, we observed that the material had mostly the tendency to agglomerate into big clusters. The EDX analysis showed higher concentration of Cl in the analyzed remnants. Thus, we assumed that ZIF-8 was partially hydrolyzed into its constituent parts – Hmim and Zn ions that reacted with Cl⁻ ions of the stomach juice forming ZnCl₂. A similar behavior was observed for Cu_{10%}/ZIF-8, but the process of aggregation was delayed with the time. After 5 min of being exposed to the gastric juice, the particles resist as individuals. Then, after 15 min, the nanoparticles of Cu_{10%}/ZIF-8 fused together into bigger clusters. Interestingly, Fe_{10%}/ZIF-8 behaved differently from the other two samples deposited in an acidic environment (pH 1.3) of gastric juice. By contrast, after 5 min we could clearly see the rhombic dodecahedrons with big holes at the surface of the crystals indicating the digestion progress. Then, after 15 min and 2 h, we detected the transformed product – the rods. This morphology belongs to the ZnO particles, which was confirmed with EDX analysis. No Cl⁻ ions were present in the remnants. The ZIF-8 and Cu-doped ZIF-8 samples were unchanged in the basic intestinal fluid (pH 8.1). On the other hand, Fe_{10%}/ZIF-8 started to transform that was visible by appearance of single rods within the sample.

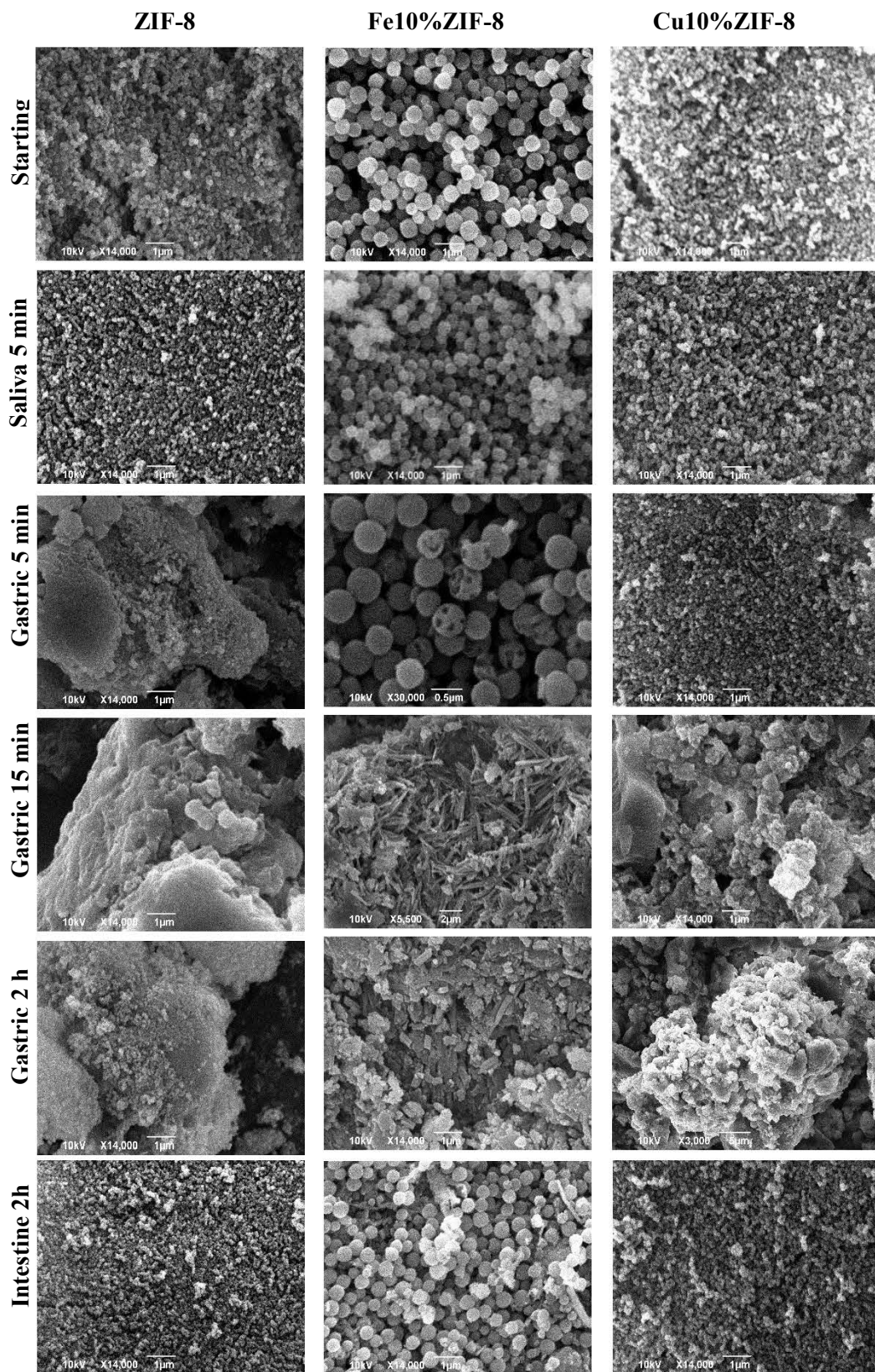


Fig. 5.2.1 SEM images of ZIF-8, Fe_{10%}/ZIF-8 and Cu_{10%}/ZIF-8 represent the morphologies of the particles after incubation in digestive juices.

Table 5.2.1 DLS hydrodynamic diameter and zeta potential results.

sample	SEM [nm]	DLS [nm]		Zeta potencial [eV]
		In methanol	In water	
ZIF-8	141.7±48.9	239.3±38.6	553.5±60.0	-2.96
Fe _{1%} ZIF-8	123.6±34.7	273.5±48.3	785.9±89.8	2.28
Fe _{5%} ZIF-8	210.7±43.4	290.9±36.2	625.7±61.2	3.65
Fe _{10%} ZIF-8	452.2±153.7	457.4±54.9	502.3±61.3	5.4
Cu _{1%} ZIF-8	120.9±24.5	246.8±46.0	360.9±58.3	2.43
Cu _{5%} ZIF-8	143.5±27.1	183.8±37.2	454.1±65.9	2.26
Cu _{10%} ZIF-8	155.9±26.6	251.4±45.2	463.5±62.6	2.05
Cu _{25%} ZIF-8	166.4±23.7	255.2±31.0	443.5±72.7	3.15

We also evaluated the hydrodynamic diameter of the nanocrystals by using a centrifugal liquid sedimentation technique. The measurements were undertaken with CPS disc centrifuge operating at 24000 rpm. The resulted diagrams of hydrodynamic diameters for all the samples were displayed as weight-related and number-related sizes in a logarithmic scale. The relative weight versus hydrodynamic diameter graphs showed the agglomeration state profile of the hydrophobic ZIF-8 samples. Standard DLS measurements indicated that the particle size, for each of the analyzed sample, vary between the methanol and water media (table 5.2.1). In water, we observed two times higher values of the size than in methanol. The digestive fluids are more charged and some of the components (proteins, ions) can attached to the surface of the ZIF-8 particles. This could cause much bigger interference between the particles compared with simple aqueous media and these phenomena are illustrated with the profiles recorded by CLS (figure 5.2.2). The relative number correlation of the size for ZIF-8 incubated in saliva indicated the individual particles with the diameter of 200 nm that is in accordance with the results investigated by SEM. For the ZIF-8 sample placed for 5 min, 15 min and 2 h in a gastric juice, we detected the clusters of 500-600 nm. The similar trends were observed for the Cu_{10%}/ZIF-8 with little difference in the amount of the aggregates detected after 2 h of the incubation in a gastric fluid. Broad hydrodynamic diameter distribution of Fe_{10%}/ZIF-8 particles was determined after dispersion in saliva for 5 min with the three main maxima at 180 nm, 355 nm and 650 nm that is in agreement with the polydispersity evaluated also by standard SEM size distributions. During the digestion process in gastric juice, the relative intensity of the peak located around 200 nm diminished in favor of the last peak shifted at 740 nm that could be contributed to the formation of the bigger rods. The CLS diagrams of the samples incubated in the intestine juice showed the presence of very fine particles and the aggregates contributed in a very small quantity (less than 6%) to the total amount of the analyzed particles.

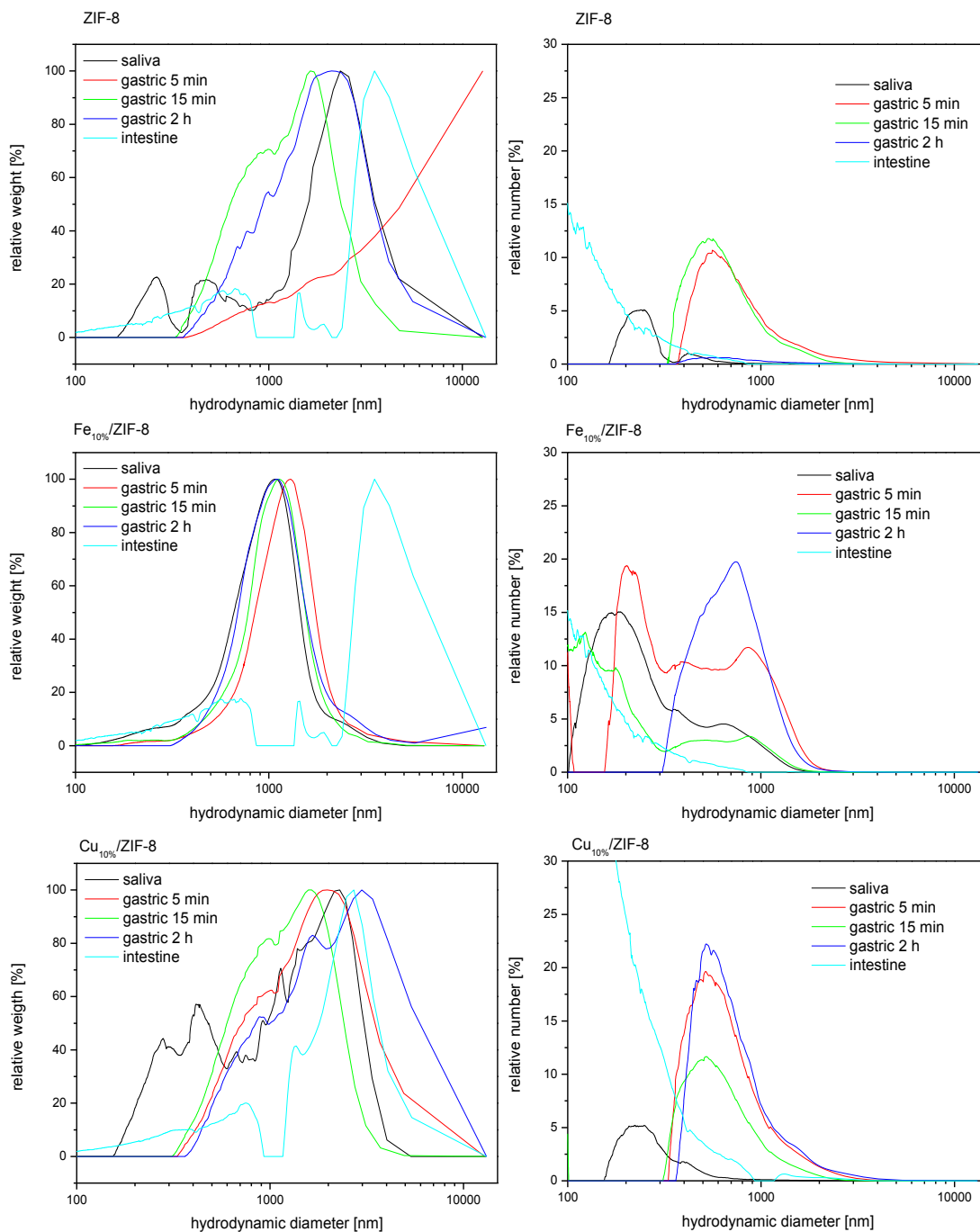


Fig. 5.2.2 Hydrodynamic diameter measurements by CLS for ZIF-8, Fe_{10%}/ZIF-8 and Cu_{10%}/ZIF-8 shown as relative weight and relative number.

In parallel, we decided to conduct stability tests of the particles in various media, including PBS buffers pH 4.8 and 8.0, water and methanol (figure 5.2.3). The same doses of the particles were dispersed in the media and incubated for 3 days in methanol and pure water and for 2 h in PBS buffers. We noticed that simple media such as pure water or PBS buffers didn't interact with the particles of ZIF-8 and Cu-doped ZIF-8 in terms of the crystal aggregation. We observed slow dissolution of the material in PBS buffer pH 4.8. The mass of the materials recovered after the tests diminished of about 10%. However for Fe_{10%}/ZIF-8, we detected the similar transformation into rods

like in tests of more complex gastric fluids. Either using pure water or PBS (wide range from 4.8 to 8.0 – figure 5.2.4), the particles clearly tend to change in the morphology. Although single rhombic dodecahedrons were still present in the remnants, most of the material was composed of rods and destroyed native structures.

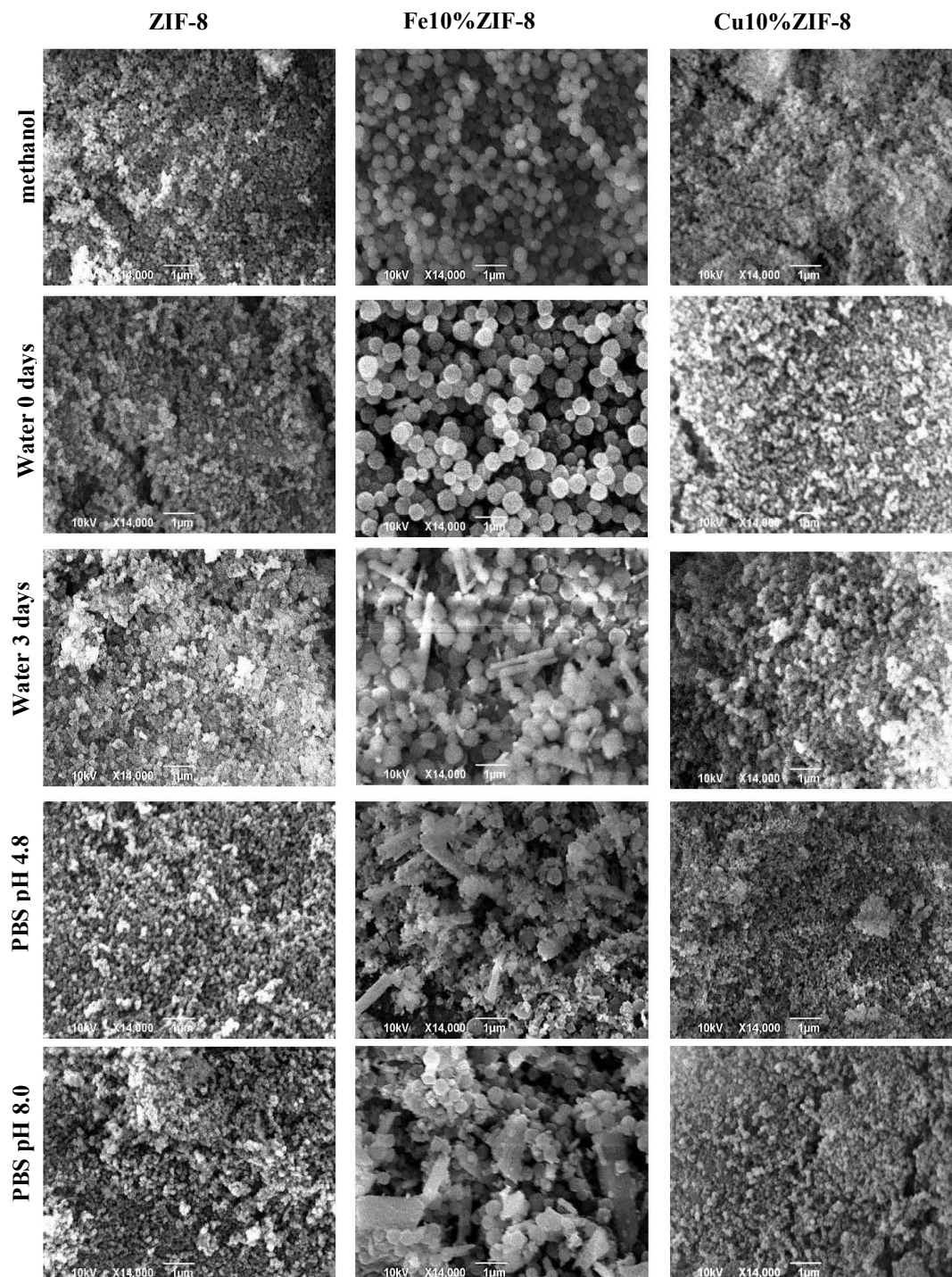
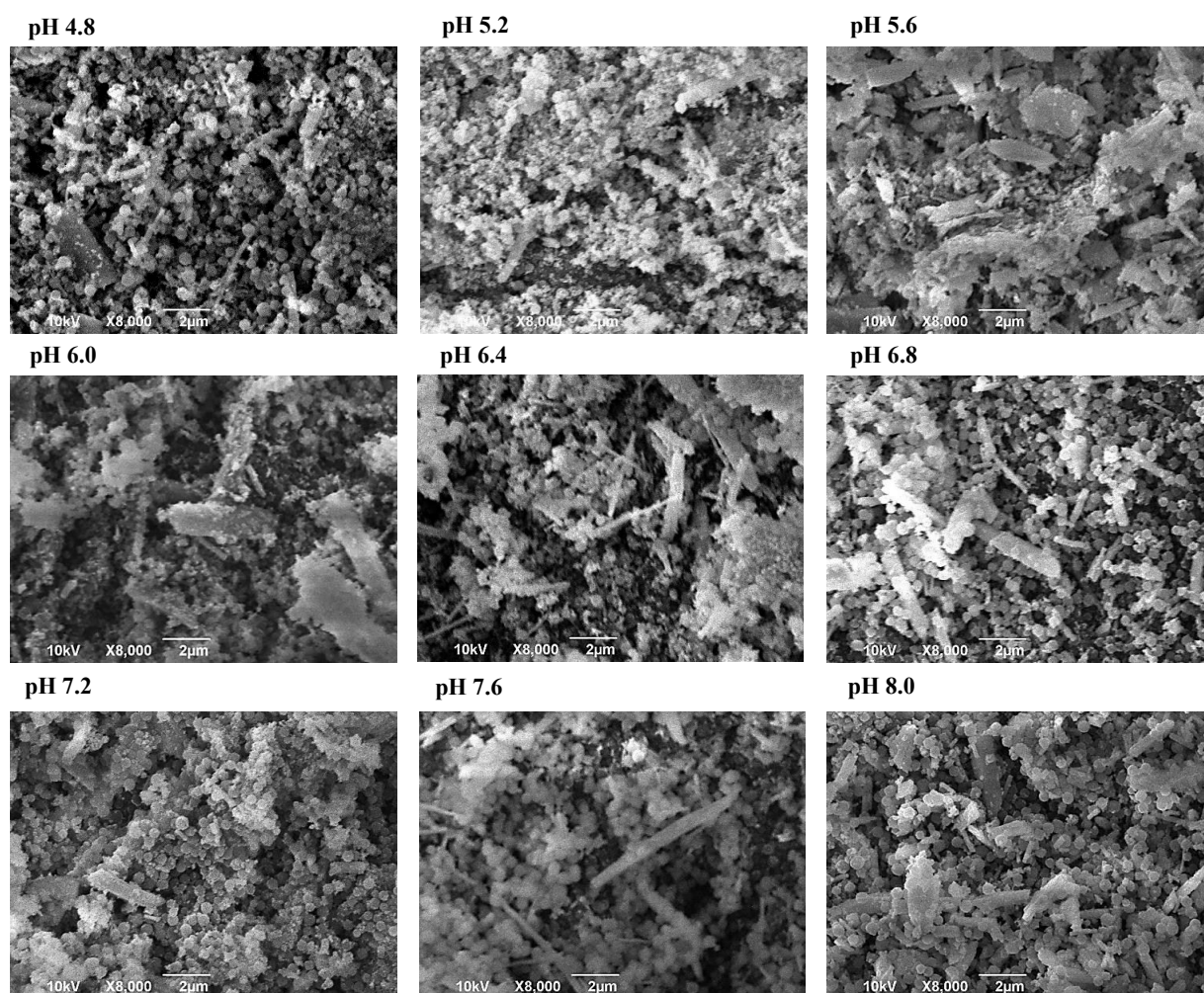


Fig. 5.2.3 SEM images of the ZIF-8, Fe₁₀%/ZIF-8 and Cu₁₀%/ZIF-8 samples after dispersion in methanol and aqueous media.



	pH 4.8	pH 5.2	pH 5.6	pH 6.0	pH 6.4	pH 6.8	pH 7.2	pH 7.6	pH 8.0
C [%]	38	38	31.4	12.2	33.2	28.9	18.5	27.4	29.1
N [%]	8.6	5.3	5.7	7.4	9.6	15.1	14.7	21.4	16
O [%]	24.4	25.2	22.9	26.3	25.6	22.1	21.2	17.1	20.9
Fe [%]	7.5	5	12.3	6.3	7.2	8.7	7.2	6.2	8.1
Zn [%]	21.5	26.5	27.7	47.8	23.9	25.2	38.4	27.9	25.9

Fig. 5.2.4 SEM images of Fe_{10%}/ZIF-8 incubated during 2h in PBS buffers of various pH and corresponding EDX analysis.

We also incubated Fe-doped ZIF-8 with lower percentages of iron incorporated in the network in pure water for 3 days (figure 5.2.5). The samples with 1% and 5% of iron produced only the population of thin ZnO particles of the sizes much smaller than parental ZIF-8. In case of Fe_{10%}/ZIF-8 material, we observed both small particles and big rods of ZnO. We assumed that the iron could act here like a catalyst and provoke different kinetics of the crystal growth after destruction of rhombic dodecahedrons of FeZIF-8.

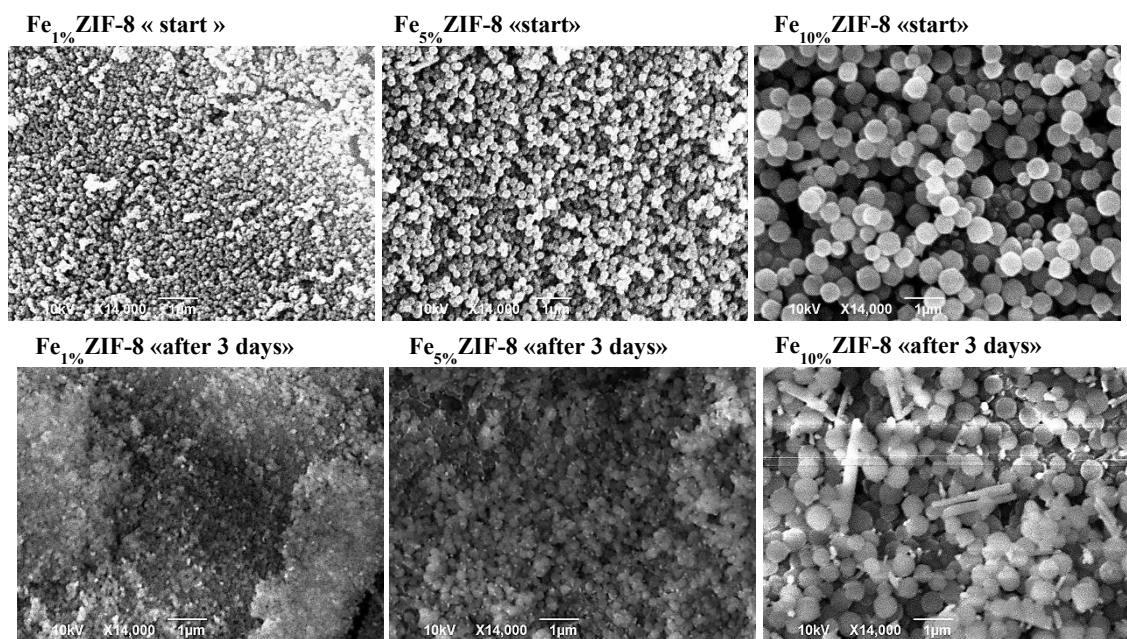
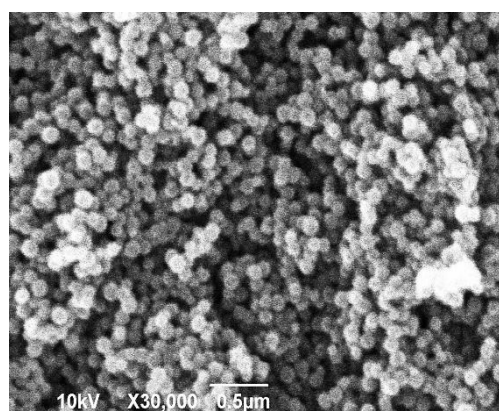
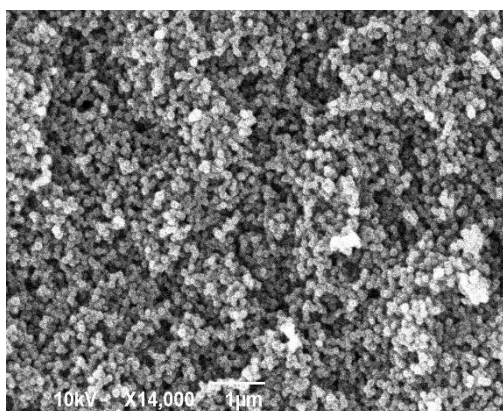


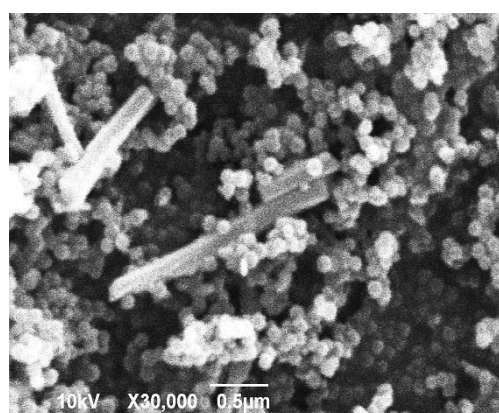
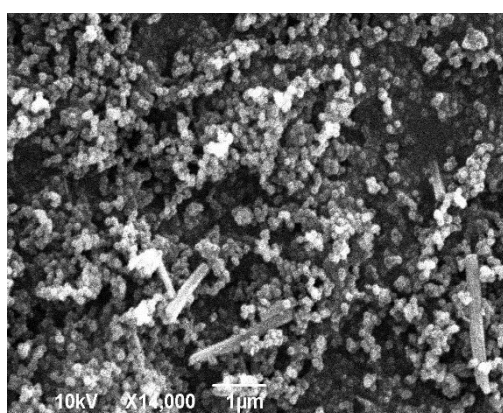
Fig. 5.2.5 SEM images of the Fe-doped ZIF-8 materials before and after incubation for 3 days in pure water.

Motivated with these results, we conducted another experiment that based on soaking of undoped ZIF-8 crystals in an aqueous solution of iron acetate for the same incubation time (72 h). We observed morphological changes of the materials with 5% and 10% of iron acetate. The results of scanning electron microscopy are depicted on the figure 5.2.6. The particles behaved similar as in previous experiments forming rod-shaped structures.

ZIF-8 + 1% Fe-acetate



ZIF-8 + 5% Fe-acetate



ZIF-8 + 10% Fe-acetate

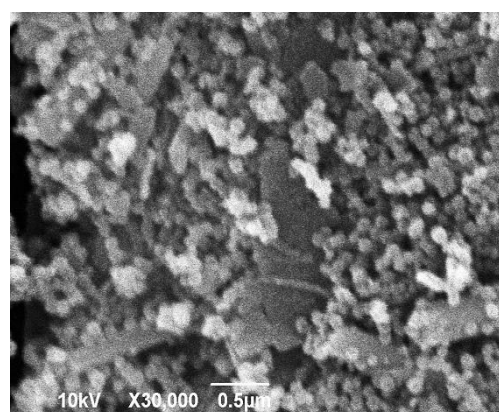
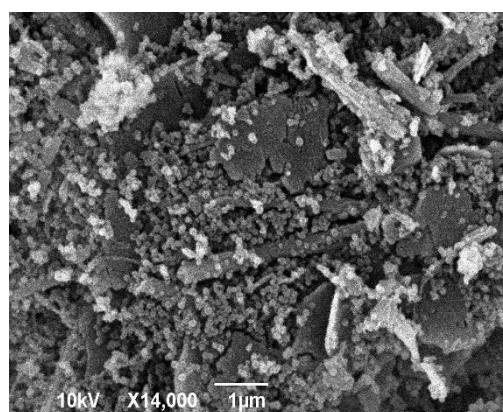


Fig. 5.2.6 ZIF-8 particles treated with 1, 5 and 10 % of Fe-acetate (molar %) for 72h.

The information on ZIF-8 stability was supplemented with an additional experiment in hydrochloric acid buffer pH 1.3. As presented on the XRD pattern (figure 5.2.7), the particles gradually lost their crystallinity. We assumed that ZIF-8 dissolved on their constituents and free zinc ions reacted with chloride anions from the buffer. That evolution resulted in $ZnCl_2$ formation and was further confirmed with EDX analysis (figure 5.2.8).

Time [min]	Mass [%]
5	27.5
15	33.9
30	45
45	34.4
60	46.3
90	55.4

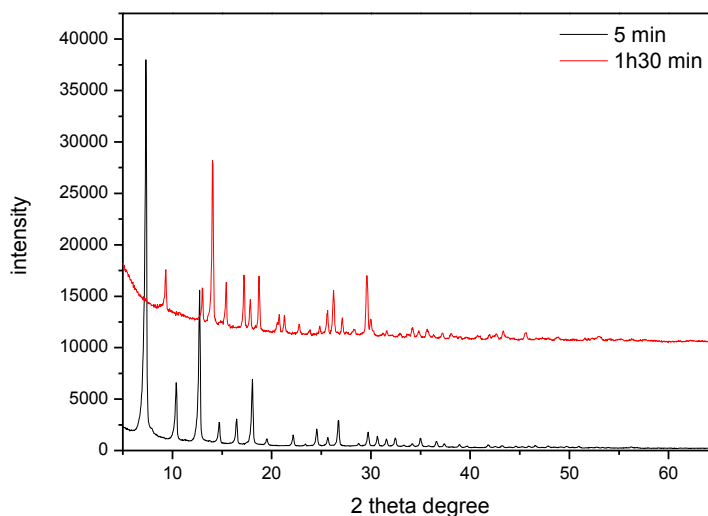


Fig. 5.2.7 Table showing the change in the mass of the sample incubated in HCl buffer pH 1.3 and XRD characterization of the particles after 5 min and 1h30 min.

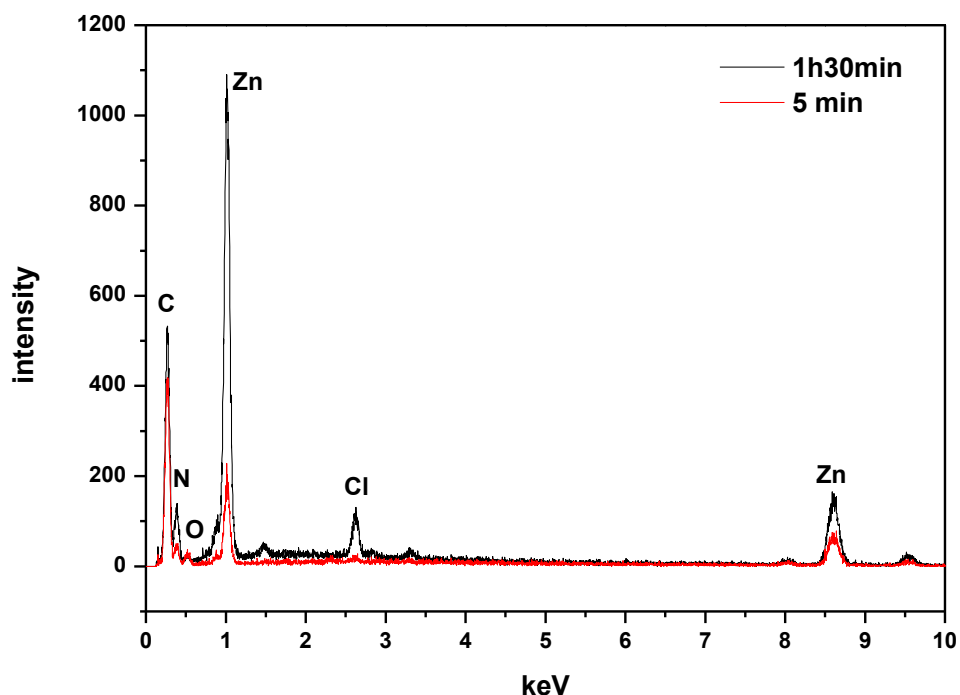


Fig. 5.2.8 EDX spectrum of the ZIF-8 sample incubated in HCl buffer pH 1.3.

5.2.4 Conclusions

Results of the ZIFs stability in different pH environments evaluated in this study suggest that the materials may aggregate, chemically modify or hydrolyze. These processes hardly depend on composition of the ZIF-8 crystals. Copper-doped ZIF-8 behaved similar to the parental pure ZIF-8 in

the digestive fluids, in simple aqueous media and methanol. *In vitro* digestion under fed conditions test showed that the particles were more sensitive to low pH gastric juice and became aggregated and partially dissolved. In the resulting clusters, we detected chloride ions that belonged to zinc chloride formed during the incubation. These phenomena were not observed for the particles incubated either in water or PBS buffers. Furthermore, Fe_{10%}/ZIF-8 behaved differently than the other samples. In this case, we observed transformations of the rhombic dodecahedrons into ZnO rods when placed in aqueous complex gastric fluid or even in the water and simple PBS buffers. Thus, we assumed the iron-doped ZIF-8 as the least stable from the all three investigated samples. Moreover, the current study demonstrates that the complexity of the digestive fluids could markedly influence the aggregation profile that we analyzed with CLS method. We also note that these very first results on the fate of ingested ZIF-8 particles pronounce the necessity for further work on the human exposure assessment using more advanced models.

5.2.5 References

- (1) Vega-Villa K. R., Takemoto J. K., Yáñez J. A., Remsberg C. M., Forrest M. L., Davies N. M., *Adv. Drug Delivery Rev.*, **2008**, 60, 929-938
- (2) Yang Y., Westerhoff P., Book series: *Nanomaterial. Advances in Experimental Medicine and Biology*. **2014**, 811, 1-17, Springer Netherlands
- (3) Kumar P., Robins A., Vardoulakis S., Britter R., *Atmospheric Environment*, **2010**, 44, 5035-5052
- (4) Wang B., He X., Zhang Z., Zhao Y., Feng W., *Acc. Chem. Res.*, **2013**, 46, 761-769
- (5) Sajid M., Ilyas M., Basheer C., Tariq M., Daud M., Baig N., Shehzad F., *Environ. Sci. Pollut. Res.*, **2015**, 22, 4122-4143
- (6) Moh P. Y., Cubillas P., Anderson M. W., Attfield M. P., *J. Am. Chem. Soc.*, **2011**, 133, 13304-13307
- (7) Pan Y., Lin Y., Zeng G., Zhao L., Lai Z., *Chem. Commun.*, **2011**, 47, 2071-2073
- (8) Wang H., Zhao L., Xu W., Wang S., Ding Q., Lu X., Guo W., *Theor. Chem. Acc.*, **2015**, 134:31, 1-9
- (9) Park K. S., Ni Z., Côté A. P., Choi J. Y., Huang R., Uribe-Romo F. J., Chae H. K., O’Keeffe M., Yaghi O. M., *PNAS*, **2006**, 103, 10186-10191
- (10) Ren H., Zhang L., An J., Wang T., Li L., Si X., He L., Wu X., Wang C., Su Z., *Chem. Commun.*, **2014**, 50, 1000-1002

Chapter 6: Conclusions and perspectives

Metal organic frameworks have gained considerable attention as heterogeneous catalytic systems. According to their complex structure formed by metal centers coordinated with polydentate linkers, MOFs expose abundance of Lewis acid-base sites that are crucial for the material's activity and selectivity towards specific reactions. Moreover, these materials have many other attractive properties, including large surface area, low density and high porosity.

Discovered in 2006, the ZIF-8 material has well-documented performances in many types of catalytic reactions. Composed of zinc-ions and 2-methylimidazole ligands, the ZIF-8 framework has been explored towards Knoevenagel, Friedel-Crafts alkylation, transesterification, oxidation, and cycloaddition reactions. The potential of ZIF-8 lies in the structure flexibility, ease tunability and possibility of functionalization. This enabled the preparation of the most desirable form of the catalyst. This work has been discussed and concluded in Chapter 2. Some of the new findings described in the manuscript contributed highly to the statements which have been already presented in the literature, and open new perspectives for rational design of the ZIF-8 and control of the crystal properties.

The main objectives of this study were the preparation of ZIF-8 materials and ZIF-8 heterostructures with properties adapted to the desired application, and then shaping of the catalyst to obtain the best form of material for industrial scale-up.

The first goal was achieved by testing different protocols for ZIF-8 synthesis. We tried various reaction conditions, like molar ratio of the two precursors, different zinc salts, time, temperature and solvents. We firstly examined the best reaction environment for the synthesis of ZIF-8 with commonly used zinc nitrate precursor and then applied exactly the same settings for the experiments with other various Zn-salts. The crystal sizes and size distributions changed with the precursor, thus influencing the activity of these materials. Small ZIF-8 nanocrystals with diameters varying between ca. 50 and 200 nm were obtained with reactive zinc salts like $\text{Zn}(\text{acac})_2$, $\text{Zn}(\text{NO}_3)_2$, ZnSO_4 or $\text{Zn}(\text{ClO}_4)_2$. The use of ZnCl_2 , $\text{Zn}(\text{OAc})_2$ or ZnI_2 afforded crystals with sizes varying between ca. 350 and 650 nm. Finally, the low reactive ZnBr_2 was found to generate microsized crystals. The catalytic activity of ZIF-8 with three diverse dimensions (synthesized with zinc bromide: biggest, acetate: medium, nitrate: smallest) was examined in Knoevenagel condensation. The results showed increased activity for small crystals compared with bigger ones.

Moreover, we exploited the ZIF-8 material in the substitutional incorporation of copper into the ZIF-8 lattice and functionalization of the frameworks with magnetic nanoparticles. We synthesized Cu-doped ZIF-8 crystals to further address the hybrid frameworks for Cu-mediated catalytic reactions, like Friedländer, Combes, and Huisgen 1,3-dipolar cycloaddition. We showed the increased percentage of copper within ZIF-8 allows improvement the yield of the expected products and selectivity. Cu/ZIF-8 particles were proven to be efficient and reusable catalysts. The $\text{Cu}_{2.1\%}$ /ZIF-8 crystals showed high catalytic activity in the synthesis of quinolines using 2-aminobenzophenone as starting material. 1,4-Disubstituted triazoles were obtained with excellent yields and good regioselectivity using the $\text{Cu}_{8.7\%}$ /ZIF-8 material. These results combined with the high stability and the ease of regeneration of ZIF-8 particles may serve as a starting point to develop new nanomaterials based on metal organic frameworks with high adsorbent properties and enhanced catalytic properties.

The magnetic $\text{Fe}_3\text{O}_4@\text{ZIF-8}$ and $\text{Fe}_3\text{O}_4@\text{Cu}_{2.5\%}/\text{ZIF-8}$ nanocomposites were synthesized and successfully applied to the rapid separation of the catalyst from the reaction mixture. The materials properties, including high resistance and stability in the experimental conditions, were advantageous in the recovery and reutilization of the material up to 10 times in Knoevenagel and Huisgen's cycloaddition. Moreover, the catalytic activity was not altered by this functionalization.

Then, we considered the ZIF-8 as a heterogeneous catalyst in the conversion of carbon dioxide into cyclic carbonates. The subject of too high carbon dioxide concentration in the atmosphere is a major worldwide environmental problem. The techniques that could markedly contribute to the reduction of CO_2 were evaluated in the direction of the storage and sequestration or direct reutilization. Carbon dioxide can act as a C1-synthon for some chemical transformations thus leading new products, chemicals, solvents. In this context, we used ZIF-8 particles as catalyst for the reaction of CO_2 with cyclic oxides to synthesize cyclic carbonates. We tested powder ZIF-8, $\text{Fe}_3\text{O}_4@\text{ZIF-8}$ hybrid and compressed ZIF-8. We tried these three counterparts to study the influence of ZIF-8 shaping and functionalization on the activity and reusability in Parr reactor experiments. We found that ZIF-8 powder could be successfully applied just for one run of the manipulation, while iron oxide@ZIF-8 showed the recovery up to three times. The obtained yields for the desired products (carbonate monomers) were high for all the catalysts. However, the ZIF-8 pellets were poorly resistant in the experimental conditions. After the reaction, the compressed tablets were disintegrated and crumbled. Thus we worked on the mechanical strength improvement of the ZIF-8 tablets. We used common pharmaceutical binders: 5% of Avicel and CMC-Na. The new pellets were resistant and could be reused for several times. We ought to address these shaped forms of ZIF-8 as a perspective for an industrial application.

In the last set of experiments, we evaluated the toxicity of ZIF-8 materials. We analysed pure, copper-doped and iron-doped ZIF-8 particles. As test cell-lines, we chose alveolar A549 lung cells and keratinocytes IHK of human skin according to the potential first exposure toxic influence. We also investigated *in vitro* digestion under fed condition of these materials. Our results show that keratinocytes are more sensitive when they get in contact with ZIF-8 particles than alveolar lung cells. The cytotoxicity was observed with the concentrations 25 $\mu\text{g}/\text{mL}$ for IHK and 100 $\mu\text{g}/\text{mL}$ for A549. We indicated that big aggregates observed for $\text{Cu}_{5\%}\text{ZIF-8}$ and $\text{Fe}_{5\%}\text{ZIF-8}$ resulted in lower toxicity. The second step of the toxicity test consisted of the *in vitro* digestion model under fed conditions that imitate the real ingestion of the particles. We followed the particles morphological and compositional changes when placed in saliva, stomach and intestinal fluids. Moreover, we prepared a screening of ZIF-8 behaviour in different pH-media to take an insight into the stability of the particles. We observed that iron-doped ZIF-8 was the most sensitive towards digestive environment, wide range of buffers and pure water. The aggregation profile graphs concluded also that the particles in relation to their hydrophobic character have a tendency to make bigger clusters in aqueous media to maximally decrease the surface contact. These very first findings on the toxicity of ZIF-8 we would like to devote to the potential exposure security that has to be considered in the context of wider application of these materials.

In the perspective to our work, we would like to propose several directions that are interesting for further development:

- 1) Functionalization of ZIF-8 crystals with luminescent quantum dots for sensing and bioimaging applications.

Host-guest hybrid structures based on metal organic frameworks are considered as very interesting as carriers of different species. We conducted some preliminary experiments on ZIF-8 functionalization by incorporating highly luminescent semiconductor crystals. We analyzed various types of water-dispersed quantum dots for this purpose: $\text{CuInS}_2/\text{ZnS}@MPA$, $\text{CdZnTe}@MPA$ and $\text{CdSe}/\text{ZnS}@DHLA$. We used two protocols: “ship-around bottle” and “bottle-around-ship”. In the first one, QDs were used as seeds for ZIF-8 growth ($\text{CuInS}_2/\text{ZnS}@MPA$, $\text{CdSe}/\text{ZnS}@DHLA$). In the second one, ZIF-8 crystals were used as support for QDs growth ($\text{CdZnTe}@MPA$). In this case, we observed that the quantum dots growth was limited within the size of the ZIF-8 pores. The very first results on the characterization are presented in figure 6.1.

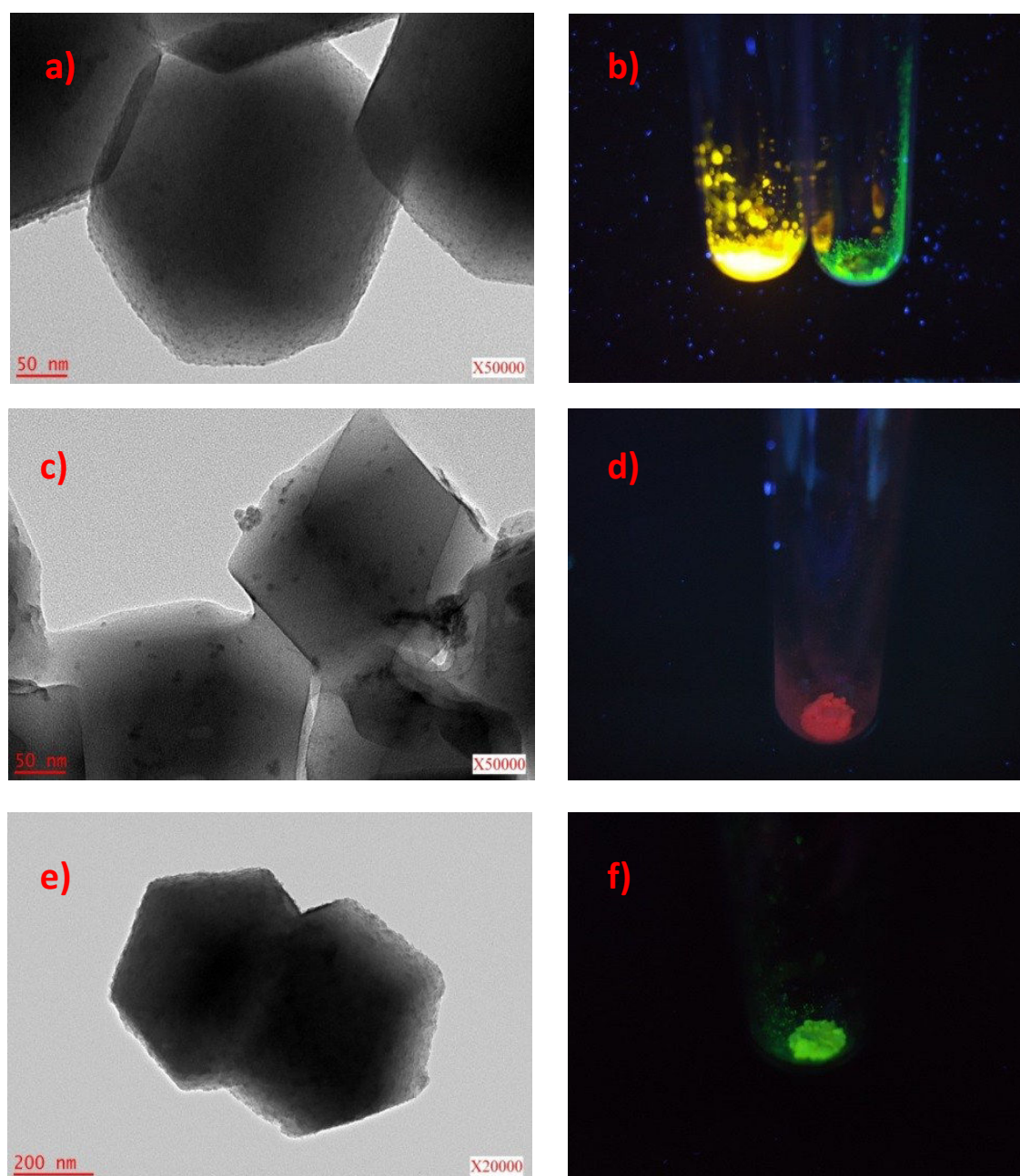


Fig. 6.1 TEM images (a, c, e) and photos of the materials under UV irradiation (b, d, f) of $\text{CdZnTe}@MPA$, $\text{CuInS}_2/\text{ZnS}@MPA$ and $\text{CdSe}/\text{ZnS}@DHLA$ respectively.

The crystal structure of the ZIF-8 rhombic dodecahedrons was not affected after introducing the guest nanoparticles. Our results of solid state spectroscopy show that the optical properties of QDs were maintained through the two types of processing (figure 6.2).

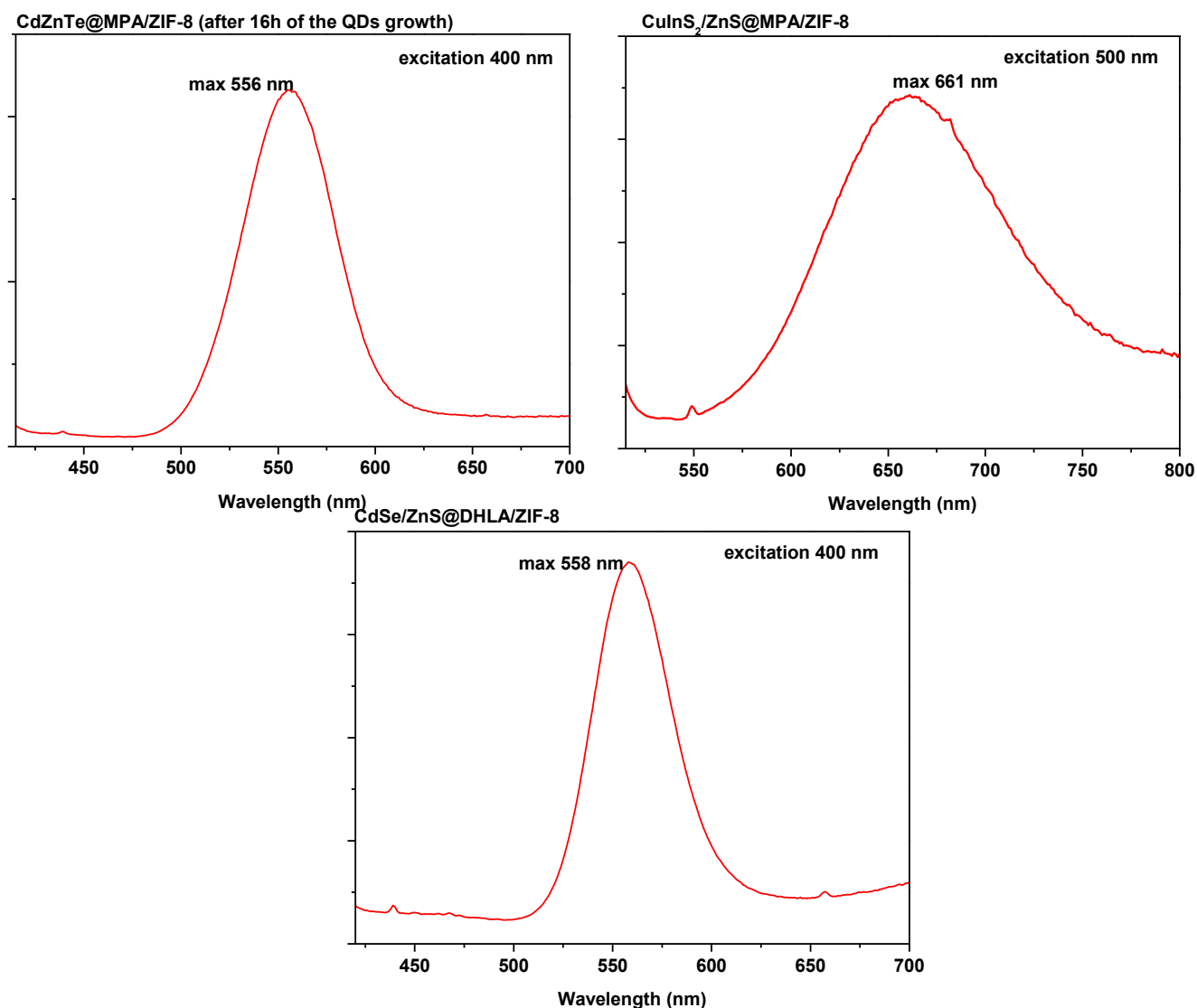


Fig. 6.2 Solid state spectroscopy analyses of the hybrid structure.

However we still have not enough information on the quantity of QDs introduced in the network. There is necessity to evaluate the exact mechanism of hybrids formation, for example with scanning probe microscopy. We would also like to determine the fluorescence lifetime of quantum dots incorporated in the ZIF-8 dodecahedrons.

Due to their tunable pore surfaces, the new luminescent ZIF-8 crystals engineered should have great potential for the sensing of ions or small molecules or for (photo)catalytic applications. We would like to further explored these application possibilities.

- 2) The work on ZIF-8 cytotoxicity presented in this dissertation is at the preliminary stage and involves utilization of cell cultures models. These results could be extended by more advanced testing. To complete the work the following future experiments are recommended:
- *in vivo* monitoring on an animal lung model to predict the ability of particles to penetrate the epithelial barrier and disrupt epithelial monolayer function,
 - tests of aerosol delivery via a mechanical ventilator (breath-actuated nebulization) to see the deposition of ZIF-8 particles in the respiratory tract,
 - *in vivo* percutaneous absorption and skin penetration modelling,
 - *in vivo* digestion tests on animals and organ accumulation of decomposition products.
- The aforementioned points could act as a background to expect ZIF-8 as a host for encapsulation of various guest species for prolonged release studies.
- 3) ZIF-8 as a drug delivery system (figure 6.3) – our investigations on the ZIF-8 stability in various media forced us to consider the employment of the particles as carriers of molecules like peptides or drugs. We would like to propose several candidates for the encapsulation inside ZIF-8 pores, then testing of prolonged release for pharmaceutical and medical purposes. According to the ZIF-8 properties the best choices are compounds of acidic character, like aspirin, methotrexate, furosemide, phenylbutazone, indomethacin or weakly acidic sulfonamides.

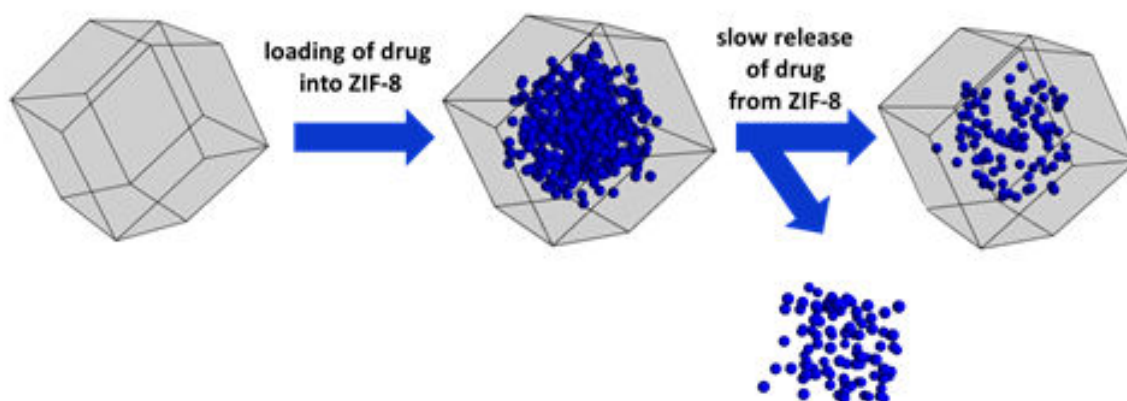


Fig. 6.3 ZIF-8 as carrier of drug molecules.

Moreover, in terms of pharmaceutical processing of the hybrid material, it is also possible to directly compress the material without any additives and use the tablet as a final form of delivery system.

List of figures

Fig. 1.1 Scheme of metal-organic framework's assembly: MOF-5 from Ranocchiari M., van Bokhoven J. A., <i>Phys. Chem. Chem. Phys.</i> , 2011, 13, 6388–6396	12
Fig. 1.2 Different strategies for MOF's functionalization: (a) non-modified, (b) metal-exchanged, (c) ligand-exchanged, (d) active species-encapsulated networks.	16
Fig. 1.3 Example of structural dislocations within the framework (simplified picture).....	17
Fig. 1.4 Different post-synthetic strategies for MOF's functionalization. [from Cohen, 2010].....	18
Fig. 1.5 Optical microscopic images of the Zn-PMOF-2 single crystal after exchange with Cu. ³⁰	19
Fig. 1.6 Transmetalation of Co-containing SBU for Ni-ions conducted on $M_6(1,3,5\text{-benzenetribenzoate})_4(4,4'\text{-dipyridyl})_3$ framework. ³¹	19
Fig. 1.7 Scheme of the techniques for the formation of nanoparticles supported on MOFs. The MOF framework can be decorated outside with NPs (A), interpenetrated with NPs (B), enclose the NPs within pores (C). [from Rösler <i>et al.</i> 2015].....	20
Fig. 1.8 MOFs functional composites.	21
Fig. 1.9 Steam stability map for the MOFs discussed by Willis <i>et al.</i> ³⁰	25
Fig. 1.10 Scheme presenting possible emission phenomena in MOFs. (ref. Chem. Soc. Rev., 2009, 38, 1330-1352 – from the website of C. A. Bauer)	26
Fig. 1.11 Example of a fluorescent metal-organic framework: evolution of luminescence in BioMOF-1 upon excitation 340 nm. (ref. Yu J., Cui Y., Xu H., Yang Y., Wang Z., Chen B., Qian G., Nature Communication, 2013, 4:2719, 1-7)	27
Fig. 1.12 Scheme of metal-organic frameworks activity in gas separation (Chem.Soc.Rev., 2014, 43, 5419).....	30
Fig. 1.13 Different strategies to entrap the therapeutic agents inside the framework: (2a) covalent and (2b) by non-covalent attachment. (reprinted from Della Rocca J., Liu D., Lin W., <i>Accounts of Chemical Research</i> , 2011, 44, 957-968)	32
Fig. 1.14 Zeolite ZK5 (Si tetrahedra – green, O – red).	33
Fig. 1.15 Examples of ZIFs classified from the topology. Indications: ZnN_4 polyhedra in blue, CoN_4 polyhedra in pink, C in black, N in green, O in red, Cl in pink, yellow ball – empty void within the single unit cage (copied from Phan A., Doonan C. J., Uribe-Romo F. J., Knobler C. B., O'Keeffe M., Yaghi O. M., <i>Acc. Chem., Res.</i> , 2010, 43, 58-67)	34
Fig. 1.16 Scheme of the ZIF-8 structure and Zn-(2-methylim)-Zn and Si-O-Si linkages in tetrahedral ZIF-8 and zeolite network respectively (green ball in the ZIF-8 presents an empty void).	36
Fig. 1.17 Evolution of the geometrical particle shapes over time determined for ZIF-8.	41
Fig. 1.18 Carbon dioxide conversion into useful chemicals. (reprinted from [])	45
Fig. 1.19 Elastic characteristics of the material. [reprinted from Ortiz <i>et al.</i> 2012].....	48
Fig. 1.20 <i>In situ</i> compression experiment on ZIF-8 crystal. Images present: the ZIF-8 single crystal before the test (a), during the increased compression force (b), (c), (d) [reprinted from] and simulation of the linkers arrangement with voids analysis of ZIF-8 material upon pressure. [reprinted from Moggach <i>et al.</i> 2009].....	50
Fig. 1.21 Kinetic properties of nanoparticle in the body (ADME model). [reprinted from Hagens <i>et al.</i> 2007].....	52
Fig. 1.22 The factors that can affect particles dissolution and the particles fate when exposed to the cell culture environment.....	52
Fig. 1.23 Illustration of the signals produced by electron beam-specimen interactions.....	53

Fig. 1.24 Scheme of scanning electron microscope [from Skilbred A. W. B., Fjeld H., University of Oslo, Mena3100 presentation]	54
Fig. 1.25 Examples of Ni-embedded MesMOF-1 [ref. Park <i>et al.</i> , 2010] (a) and Pd/Ni@MIL-101 [ref. Hermannsdörfer <i>et al.</i> , 2012](b).....	56
Fig. 1.26 Illustration of Bravais lattices (<i>P</i> – primitive, <i>I</i> – body-centered, <i>F</i> – face-centered, <i>C</i> – base-centered). [Ref. van Holde K. E., Johnson W. C., Ho P. S., X-Ray Diffraction (chapter 6) from Principles of Physical Biochemistry, Prentice-Hall, 1998, 242-311].....	58
Fig. 1.27 Simulation of nitrogen loading in IRMOF-16. [ref. Walton <i>et al.</i> , 2007].....	59
Fig. 1.28 Illustration of the adsorption isotherms and description for the different types.	60
Fig. 1.29 Scheme of TGA instrument.	62
Fig. 1.30 Optical design of the integrating sphere (Perkin Elmer instrumentation).....	64
Fig. 1.31 Hysteresis loops for diamagnetic (a), paramagnetic (b), superparamagnetic (c), uniaxial, single domain (d), magnetocrystalline, single domain (e), “pseudo-single domain”(f) materials. [Tauxe L. <i>et al.</i> , 2014]	65
Fig. 1.32 Magnetization as a function of temperature for ferromagnetic material. (ref. McElfresh M., 1994).....	66
Fig. 1.33 SQUID superconducting loop (two Josephson junctions/insulating barriers responsible for the loop is no longer quantized) – two yellow blocks — sandwiched between the two superconductors (red and blue).	67
Fig. 1.34 Reduction of MTS reagent into colorful formazan product.....	67
Fig. 1.35 Principal of the fluorescence-activated cell sorting and an example on STEM cell sorting.	68
Fig. 2.1 Experimental setup of the Parr reactor: mixing system (1), pressure controller (2), temperature sonda (3), CO ₂ inlet (4), reaction vessel (5), inox reactor (6), temperature controller (7), CO ₂ bottle (8).	79
Fig. 3.1.1 Graphical abstract.	84
Fig. 3.1.2 XRD patterns of ZIF-8 nanocrystals prepared with different zinc precursors.	87
Fig. 3.1.3 SEM and TEM images of ZIF-8 crystals obtained after 1 h reaction using a Hmim/Zn ratio of 8/1 and starting from (a) Zn(Acac) ₂ , (b) Zn(NO ₃) ₂ , (c) ZnSO ₄ , (d) Zn(ClO ₄) ₂ , (e) Zn(OAc) ₂ , (f) ZnCl ₂ , (g) ZnI ₂ , and (h) ZnBr ₂	88
Fig. 3.1.4 Size distributions of ZIF-8 crystals obtained from SEM images described in Fig. 3.1.3.	89
Fig. 3.1.5 Illustration of the crystal morphology evolution with time: (a) cube, (b) cube with truncated edges, (c) rhombic dodecahedron with truncated corners, and (d) rhombic dodecahedron.	90
Fig. 3.1.6 TGA curves of ZIF-8 nanocrystals prepared from Zn(NO ₃) ₂ (black line), Zn(OAc) ₂ (red line), and ZnBr ₂ (blue line) and XRD patterns of ZnO crystals obtained upon TGA experiments on ZIF-8 nanocrystals. (a) ZIF-8 prepared from zinc nitrate, (b) ZIF-8 prepared from zinc bromide, and (c) ZIF-8 prepared from zinc acetate.	90
Fig. 3.1.7 Nitrogen sorption isotherms measured at 77K on the powder ZIF-8 crystals obtained from (a) Zn(NO ₃) ₂ , (b) Zn(OAc) ₂ , and (c) ZnBr ₂ . Black and red data correspond to the adsorption and desorption branches, respectively.....	91
Fig. 3.1.8 Catalytic activities of ZIF-8 crystals prepared from different zinc sources in the Knoevenagel reaction.	91
Fig. 3.2.1 Graphical abstract.	94
Fig. 3.2.2. Photographs showing the color change of Cu/ZIF-8 crystals upon increasing the doping percentage in copper. (a) ZIF-8 as reference, (b), (c), (d) and (e) are ZIF-8 crystals doped with 0.6, 2.1, 3.9 and 8.7% Cu, respectively.	96
Fig. 3.2.3 SEM images of ZIF-8 crystals doped with (a) 0.6, (b) 2.1, (c) 3.9 and (d) 8.7% Cu ²⁺ , respectively.....	97

Fig. 3.2.4 TEM images of ZIF-8 crystals doped with (a) 0.6, (b) 2.1, (c) 3.9 and (d) 8.7% Cu ²⁺ , respectively.....	97
Fig. 2.3.5 Size distributions determined by SEM for ZIF-8 crystals doped with (a) 0.6, (b) 2.1, (c) 3.9, and (d) 8.7% Cu ²⁺ , respectively.....	98
Fig. 3.2.6 XRD patterns of Cu/ZIF-8 crystals prepared with different doping percentages in Cu ²⁺	99
Fig. 3.2.7 (a) Diffuse reflectance and (b) absorption spectra of ZIF-8 and Cu-doped ZIF-8 crystals, and (c) [F(R)hv] ^{1/2} vs hv curves for ZIF-8 and Cu/ZIF-8 crystals.	100
Fig. 3.2.8 (a) ESR spectra for the different Cu/ZIF-8 samples and (b) double integration of the ESR spectrum vs. Cu doping.....	101
Fig. 3.2.9 N ₂ adsorption/desorption curves at 77K for Cu/ZIF materials doped with (a) 0.6% Cu, (b) 2.1% Cu, (c) 3.9% Cu, and (d) 8.7% Cu, giving surface areas of 1541, 1736, 1639, and 1205 m ² g ⁻¹ , respectively. Black and red data correspond to the adsorption and desorption branches, respectively.	102
Fig. 3.2.10 TGA traces of ZIF-8 and Cu-doped ZIF-8 crystals.....	103
Fig. 3.2.11 XRD patterns of Cu/ZIF-8 crystals after one week heating in refluxing toluene, methanol, water, and 1M NaOH.	104
Fig. 3.2.12 (a) SEM image and (b) XRD pattern of ZIF-8 after five reuses in the Combes condensation.....	106
Fig. 3.3.1 Graphical abstract.	111
Fig. 3.3.2 Schematic illustration of Fe ₃ O ₄ @ZIF-8 particles synthesis.....	113
Fig. 3.3.3 SEM images of (a) ZIF-8 and (b) Fe ₃ O ₄ @ZIF-8 particles. TEM pictures of (c) and (e) ZIF-8, (d) and (f) Fe ₃ O ₄ @ZIF-8 particles. Size distribution of (g) the ZIF-8 and (h) Fe ₃ O ₄ /ZIF-8 crystals. (i) Powder XRD patterns of Fe ₃ O ₄ , ZIF-8, and Fe ₃ O ₄ @ZIF-8 crystals.	114
Fig. 3.3.4 (a) TEM image of citrate-capped Fe ₃ O ₄ nanoparticles (the inset shows a HR-TEM image of the crystals) and (b) the corresponding size distribution.	115
Fig. 3.3.5 (a) TGA traces of ZIF-8 and Fe ₃ O ₄ @ZIF-8 crystals. (b) N ₂ adsorption/desorption curves at 77K for ZIF-8 and Fe ₃ O ₄ @ZIF-8 particles giving surface areas of 1856 and 871 m ² g ⁻¹ , respectively. Black (green) and red (blue) data correspond to the adsorption and desorption branches, respectively.	116
Fig. 3.3.6 (a) Magnetization at 300 K as a function of applied field. Optical images of Fe ₃ O ₄ @ZIF-8 particles dispersions (b) before and (c) after applying an external magnetic field. (d,e) Temperature dependent magnetization for citrate-capped Fe ₃ O ₄ and Fe ₃ O ₄ @ZIF-8 particles, respectively.	117
Fig. 3.3.7 Time-dependent conversion plots for the Knoevenagel reaction between 4-bromobenzaldehyde and malononitrile catalyzed by ZIF-8 crystals and Fe ₃ O ₄ @ZIF-8 crystals (reactions were conducted in toluene at room temperature).....	118
Fig. 3.3.8 Recycling performance of Fe ₃ O ₄ @ZIF-8 particles in the Knoevenagel condensation between malononitrile and benzaldehyde.....	119
Fig. 3.3.9 Recycling performance of Fe ₃ O ₄ @Cu _{25%} /ZIF-8 particles in the Huisgen cycloaddition between benzylazide and phenylacetylene.....	120
Fig. 3.3.10 XRD patterns of (a) Fe ₃ O ₄ @ZIF-8 and (b) Fe ₃ O ₄ @Cu _{25%} /ZIF-8 catalysts before and after five recyclings.	121
Fig. 4.1.1 Graphical abstract.	125
Fig. 4.1.2 SEM micrograph of the ZIF-8 powder after reaction.	129
Fig. 4.1.3 XRD and N ₂ -sorption isotherms of the ZIF-8 material (powder) before and after CO ₂ conversion. (BET surface areas and pore volume: before reaction 1713.24 ± 45 m ² /g, 0.635 cm ³ /g and 941 ± 6 m ² /g, 0.36 cm ³ /g respectively).	129

Fig. 4.1.4 SEM images of the surface (left) and the interior (right) of ZIF-8 tablets compressed at 1 kN (a, b), 2 kN (c, d), 3.5 kN (e, f) and 5 kN (g, h).	130
Fig. 4.1.5 XRD spectra of the ZIF-8 sample before and after compression with 1, 2, 3.5 and 5 kN. .	131
Fig. 4.1.6 XRD peaks analysis of the ZIF-8 before (a) and after compression with 5 kN (b).	131
Fig. 4.1.7 BET isotherms and microporous HK distribution for the ZIF-8 in powder and compressed with different forces.	132
Fig. 5.1.1 Transmission and scanning electron microscopy images for ZIF-8 (a), Fe _{1%} /ZIF-8 (b), Fe _{5%} /ZIF-8 (c), Fe _{10%} /ZIF-8 (d), Cu _{1%} /ZIF-8 (e), Cu _{5%} /ZIF-8 (f), Cu _{10%} /ZIF-8 (g), Cu _{25%} /ZIF-8 (h).	137
Fig. 5.1.2 Size distributions of the samples: ZIF-8 (a), Fe _{1%} /ZIF-8 (b), Fe _{5%} /ZIF-8 (c), Fe _{10%} /ZIF-8 (d), Cu _{1%} /ZIF-8 (e), Cu _{5%} /ZIF-8 (f), Cu _{10%} /ZIF-8 (g), Cu _{25%} /ZIF-8 (h).	138
Fig. 5.1.3 N ₂ sorption isotherms of: ZIF-8 (a), Fe _{1%} /ZIF-8 (b), Fe _{5%} /ZIF-8 (c), Fe _{10%} /ZIF-8 (d), Cu _{1%} /ZIF-8 (e), Cu _{5%} /ZIF-8 (f), Cu _{10%} /ZIF-8 (g), Cu _{25%} /ZIF-8 (h).	140
Fig. 5.1.4 XRD patterns for ZIF-8 samples with indexed characteristic peaks of the material.	141
Fig. 5.1.5 TG diagrams and Raman spectra for the ZIF-8 samples doped with iron and copper.	142
Fig. 5.1.6 MTS assay results. Relative cell viability (%) of IHK and A549 treated for 24 h/37 °C with ZIF-8 samples.	143
Fig. 5.1.7 Optical microscopy images of IHK cells incubated for 24h with ZIF-8 nanoparticles (concentration 15 µg/mL). Control samples were conducted in the parallel. Images were obtained at ×63 and ×100 magnifications.	145
Fig. 5.1.8 Optical microscopy images of A549 cell line after 24 h incubation with ZIF-8 samples (concentration 67.7 µg/mL) and control probes. Images were obtained at ×63 magnification.	146
Fig. 5.1.9 Results of flow cytometry analysis for the IHK cells incubated with ZIF-8 particles.	147
Fig. 5.1.10 Results of flow cytometry analysis for the A549 cells incubated with ZIF-8 particles. ...	148
Fig. 5.1.11 FACS assay results. Intensity of the fluorescence for the DCF analysed for IHK and A549 treated for 24 h/37 °C with ZIF-8 samples.	149
Fig. 5.2.1 SEM images of ZIF-8, Fe _{10%} /ZIF-8 and Cu _{10%} /ZIF-8 represent the morphologies of the particles after incubation in digestive juices.	153
Fig. 5.2.2 Hydrodynamic diameter measurements by CLS for ZIF-8, Fe _{10%} /ZIF-8 and Cu _{10%} /ZIF-8 shown as relative weight and relative number.	155
Fig. 5.2.3 SEM images of the ZIF-8, Fe _{10%} /ZIF-8 and Cu _{10%} /ZIF-8 samples after dispersion in methanol and aqueous media.	156
Fig. 5.2.4 SEM images of Fe _{10%} /ZIF-8 incubated during 2h in PBS buffers of various pH and corresponding EDX analysis.	157
Fig. 5.2.5 SEM images of the Fe-doped ZIF-8 materials before and after incubation for 3 days in pure water.	158
Fig. 5.2.6 ZIF-8 particles treated with 1, 5 and 10 % of Fe-acetate (molar %) for 72h.	159
Fig. 5.2.7 Table showing the change in the mass of the sample incubated in HCl buffer pH 1.3 and XRD characterization of the particles after 5 min and 1h30 min.	160
Fig. 5.2.8 EDX spectrum of the ZIF-8 sample incubated in HCl buffer pH 1.3.	160
Fig. 6.1 TEM images (a, c, e) and photos of the materials under UV irradiation (b, d, f) of CdZnTe@MPA, CuInS ₂ /ZnS@MPA and CdSe/ZnS@DHLa respectively.	165
Fig. 6.2 Solid state spectroscopy analyses of the hybrid structure.	166
Fig. 6.3 ZIF-8 as carrier of drug molecules.	167

List of tables

Table 1.1 Typical metal organic frameworks and their composition.	13
Table 1.2 Examples of hybrid guest-MOF systems.	21
Table 1.3 Comparison of surface area and pore volumes of zeolites vs. different MOFs.	23
Table 1.4 Comparison between MOFs and zeolites.(adapted and supplemented from)	25
Table 1.5 Selected examples of metal-organic frameworks in the catalysis.	28
Table 1.6 Functionalization of different MOFs and benefits arising form the hybrid structure.	31
Table 1.7 Summary of ZIF-8 topologies and building units.	35
Table 1.8 Summary of different synthetic protocols and properties of resulting ZIF-8 material.	38
Table 1.9 Examples of host-guest systems based on ZIF-8 material.	42
Table 1.10 Humic acid adsorption for various adsorbents (Lin K.-Y. A., Chang H.-A., <i>Water Air Soil Pollut.</i> , 2015, 226, 1-17).....	44
Table 1.11 Examples of carbon dioxide conversions by using cyclic epoxides and various heterogeneous catalysts.	47
Table 1.12 Definition of crystal systems.	57
Table 1.13 The secondary standards definition.	64
Table 2.1. Preparation of the juices for the fed <i>in vitro</i> digestion model.	81
Table 3.2.1. Comparison of BET, pore volume, and pore size for ZIF-8 and Cu-doped ZIF-8 crystals.	102
Table 3.2.2 Influence of the Cu-doping on the regioselectivity of cycloadditions catalysed by Cu/ZIF-8 crystals.	106
Table 3.2.3. Synthesis of 1,2,3-triazoles using Cu/ZIF-8 particles.	107
Table 4.1.1 Results obtained with CO ₂ conversion into carbonates.	127
Table 4.1.2 Summary of porous properties of the ZIF-8 samples.	133
Table 5.1.1 ZIF-8 size evaluated from SEM and porosity determined by nitrogen sorption study. ...	139
Table 5.2.1 DLS hydrodynamic diameter and zeta potential results.	154

Résumé

Depuis plusieurs années, les MOFs (Metal Organic Frameworks) suscitent une grande attention pour leur potentiel en catalyse hétérogène mais ils sont également étudiés dans les domaines de la séparation, du stockage de gaz, de la libération contrôlée ou comme systèmes de vectorisation de médicaments. Leur structure complexe étant formée par des centres de coordination métalliques unis par des ligandsliens polydentates, les MOFs disposent de nombreux sites acido-basiques de Lewis qui sont cruciaux pour l'activité et la sélectivité des produits lors des réactions catalysées par les ZIFs. Ces matériaux présentent de nombreuses autres propriétés intéressantes, notamment une grande surface spécifique (par exemple: NU-110^E 7140 m²/g), une faible densité, une forte porosité ainsi qu'une excellente stabilité chimique et thermique.

Les MOFs sont des solides hybrides constitués de sous-unités métalliques (par exemple: Cu, In, Co, Zr ou Zn) connectées entre elles par des ligands organiques (par exemple, téréphthalate, imidazolate,...). Ces structures ont fait l'objet de nombreuses publications au cours des dix dernières années. Les particules MOFs sont des structures organométalliques poreuses organisées en réseaux cristallins 1D, 2D ou 3D. Dans la cadre de ce travail, différentes stratégies de design rationnel des ZIFs, de modification et de fonctionnalisation ont été testées afin de mieux comprendre les possibilités de coordination, de création de structures et d'optimiser les conditions opératoires de préparation de ces matériaux.

Depuis sa découverte en 2006, l'utilisation du ZIF-8 (Zeolitic Imidazolate Framework) est bien documentée dans de nombreux types de réactions catalytiques. Composé d'ions zinc(+2) et de ligands 2-méthylimidazole, le ZIF-8 a été employé pour des réactions de Knoevenagel, des alkylations de Friedel-Crafts, des transestérifications, des oxydations ou des cycloadditions. Le fort potentiel du ZIF-8 réside à la fois dans la souplesse de sa structure, ainsi que dans la facilité de sa fonctionnalisation. Ces propriétés permettent la préparation de la forme la plus souhaitable de catalyseur.

Les principaux objectifs de cette étude étaient :

- (1) la préparation de particules de ZIF-8 et d'hétérostructures à base de ZIF-8 avec des propriétés adaptées à l'application souhaitée,
- (2) la compression de ce catalyseur afin d'obtenir la meilleure forme pour l'utilisation industrielle sans altérer les propriétés catalytiques.

Le premier objectif a été atteint en testant différents protocoles pour la synthèse des ZIF-8. Diverses conditions de réaction ont été expérimentées, comme le rapport molaire des deux précurseurs,

différentes sources de sel de zinc, la durée de réaction, la température et le choix des solvants. Nous avons sélectionné les meilleures conditions de réaction pour la synthèse de ZIF-8 avec le nitrate de zinc, couramment utilisé comme précurseur puis nous avons appliqué exactement les mêmes paramètres pour les expériences avec les autres sels de zinc. La taille des cristaux et les distributions granulométriques sont modifiées en fonction du choix du précurseur, ce qui influe ainsi sur l'activité des structures produites. Les plus petits nanocristaux ZIF-8, de diamètre variant entre environ 50 et 200 nm, ont été obtenus avec des sels de zinc réactifs comme $\text{Zn}(\text{acac})_2$, $\text{Zn}(\text{NO}_3)_2$, ZnSO_4 ou $\text{Zn}(\text{ClO}_4)_2$. L'utilisation de ZnCl_2 , $\text{Zn}(\text{OAc})_2$ ou ZnI_2 a conduit à des cristaux avec des tailles plus importantes, variant entre entre 350 et 650 nm. Enfin, la faible réactivité de ZnBr_2 conduit à la génération de cristaux micronisés. L'activité catalytique de chacune de ces catégories de ZIF-8 (synthétisés avec le bromure de zinc pour la plus grande taille, avec l'acétate pour la taille moyenne, avec le nitrate pour la plus petite taille) a été examinée en utilisant la réaction de condensation de Knoevenagel. Les résultats ont montré une activité supérieure des petits cristaux par rapport aux plus grands.

Par la suite, nous avons réalisé une réaction de substitution partielle des ions $\text{Zn}(+2)$ par du cuivre dans le ZIF-8 (dopage) et une fonctionnalisation des cristaux par des nanoparticules magnétiques.

La synthèse des cristaux de ZIF-8 dopés au cuivre a permis d'étendre l'utilisation des structures hybrides pour des réactions catalysées par le cuivre, comme la synthèse de Friedländer, la synthèse de Combes, ou la cycloaddition de Huisgen. Nous avons montré que l'augmentation du pourcentage de cuivre entrant dans la composition du ZIF-8 permet d'améliorer le rendement et la sélectivité pour les produits attendus. Par ailleurs, ces particules $\text{Cu}/\text{ZIF-8}$ se sont révélées être des catalyseurs efficaces et réutilisables. Plus particulièrement, les cristaux $\text{Cu}_{2,1\%}/\text{ZIF-8}$ ont montré une activité catalytique élevée dans la synthèse de quinoléines en utilisant le 2-aminobenzophénone comme produit de départ. Des triazoles 1,4-disubstitués ont aussi été obtenus avec d'excellents rendements et une bonne régiosélectivité en utilisant le $\text{Cu}_{8,7\%}/\text{ZIF-8}$. Ces résultats combinés à la haute stabilité et la facilité de régénération des particules de ZIF-8 peuvent servir de point de départ au développement de nouveaux nanomatériaux basés sur la structure des MOFs ayant des propriétés d'adsorption élevées et des propriétés catalytiques améliorées.

Les nanocomposites magnétiques $\text{Fe}_3\text{O}_4/\text{ZIF-8}$ et $\text{Fe}_3\text{O}_4/\text{Cu}_{25\%}/\text{ZIF-8}$ ont été synthétisés et utilisés avec succès pour la séparation rapide du catalyseur au sein du mélange réactionnel. Les propriétés de ce matériau, notamment sa haute résistance et sa stabilité dans les conditions expérimentales, sont avantageuses pour sa récupération et sa réutilisation, jusqu'à 10 fois dans les réactions de cycloaddition de Knoevenagel et de Huisgen. En outre, l'activité catalytique n'a pas été modifiée par cette fonctionnalisation.

Ensuite, nous avons examiné le ZIF-8 en tant que catalyseur hétérogène dans la conversion du dioxyde de carbone pour la production de carbonates cycliques. En effet, la concentration de dioxyde de carbone trop élevée dans l'atmosphère est un problème environnemental majeur pour lequel différentes solutions techniques pouvant contribuer notablement à sa réduction ont été évaluées, comme par exemple le stockage, la séquestration ou la réutilisation directe. Le dioxyde de carbone peut être considéré comme un synthon C_1 pour certaines transformations chimiques permettant la fabrication de nouveaux produits chimiques ou de solvants. Dans ce contexte, nous avons utilisé des particules de ZIF-8 comme catalyseur dans la réaction entre le CO_2 et des oxydes cycliques pour l'obtention de carbonates cycliques. Nous avons testé les particules de ZIF-8, de $Fe_3O_4@ZIF-8$ hybride et de ZIF-8 sous forme de comprimé. Nous avons testé ces trois types de particules dans un réacteur de Parr en cherchant à mettre en évidence l'influence de la mise en forme et de la fonctionnalisation des particules de ZIF-8 sur l'activité et la capacité de réutilisation. Nous avons constaté que le ZIF-8 en poudre pouvait être utilisé avec succès pour un seul essai, tandis que le catalyseur $Fe_3O_4@ZIF-8$ a pu être réutilisé jusqu'à trois fois. Les rendements obtenus pour les produits désirés (monomères de carbonate) sont élevés pour tous les catalyseurs. Les pastilles ZIF-8 sont cependant peu résistantes dans les conditions expérimentales. Après la réaction, les comprimés avaient perdu leur forme initiale et étaient retrouvés désintégrés et émiettés. Ainsi, nous avons travaillé sur l'amélioration de la résistance mécanique des comprimés ZIF-8.

La mise en forme des cristaux de ZIF-8 étant une étape incontournable de leur industrialisation, nous avons donc approfondi ce point. Pour la réalisation des essais de compression, nous avons utilisé une machine universelle d'essai INSTRON 5549. Nous avons réalisé la compression directe de la poudre de ZIF-8 mais aussi ajouté des liants classiquement utilisés dans l'industrie pharmaceutique (5% d'Avicel ou de CMC-Na) afin d'améliorer la résistance mécanique des pastilles. Les résultats obtenus montrent que les comprimés préparés avec des liants sont beaucoup plus résistants dans les conditions expérimentales choisies et peuvent être réutilisés plusieurs fois. Certains compacts ont également été employés dans le procédé catalytique de conversion de CO_2 . Nous avons démontré que le mélange du ZIF-8 avec les liants n'a pas d'influence sur les résultats de conversion finaux. Le rendement obtenu pour le produit de la réaction catalytique est constant que le compact soit fabriqué avec ou sans liant.

Dans la dernière série d'expériences, nous avons évalué la toxicité des matériaux ZIF-8. Nous avons analysé le ZIF-8, le ZIF-8 dopé au cuivre et le ZIF-8 dopé au fer. Pour réaliser des essais sur des lignées cellulaires, nous avons choisi les cellules pulmonaires (alvéolaires) A549 et les kératinocytes IHK de la peau humaine qui correspondent aux premières expositions potentielles des producteurs et des utilisateurs de ces matériaux. Nous avons également étudié la digestion *in vitro* de ces matériaux.

Nos résultats montrent que les kératinocytes sont plus sensibles aux particules de ZIF-8 que les cellules alvéolaires du poumon. La cytotoxicité a été observée avec des concentrations de 25 µg/mL pour IHK et 100 µg/mL pour A549. Nous avons notamment observé de fortes concentrations en cellules pour le Cu_{5%}/ZIF-8 et le Fe_{5%}/ZIF-8, ce qui semble correspondre à une toxicité inférieure de ces matériaux.

La deuxième étape de l'essai de toxicité a été le modèle *in vitro* de digestion qui imite la « vraie ingestion » des particules. Nous avons observé des changements morphologiques et de compositions des particules lorsqu'elles sont placées dans la salive, dans l'estomac et dans les fluides intestinaux. Ensuite, nous avons préparé une projection du comportement du ZIF-8 dans différents milieux de pH variable afin d'obtenir un aperçu de la stabilité des particules. Nous avons observé que le ZIF-8 dopé par le fer était le plus sensible à l'environnement digestif, dans une large gamme de tampons et dans de l'eau pure. Le profil d'agrégation a également montré que les particules, en fonction de leur caractère hydrophobe, ont tendance à générer de plus grands édifices dans des milieux aqueux pour réduire au maximum le contact avec la surface. Ces premières conclusions sur la toxicité du ZIF-8 que nous avons focalisée sur la sécurité liée à l'exposition potentielle doivent être considérées dans le contexte de l'application plus large de ces matériaux.

Comme perspectives à notre travail, nous aimerions présenter les premiers résultats de fonctionnalisation des cristaux ZIF-8 avec des quantum dots (QDs). Ces structures hybrides « hôte-invité » sont considérées comme très intéressantes et sont susceptibles de trouver de nombreuses applications en photocatalyse ou comme détecteur. Nous avons synthétisé différents types de QDs dispersables dans l'eau: CuInS₂/ZnS@MPA, CdZnTe@MPA et CdSe/ZnS@DHLA. Nous avons utilisé deux méthodes pour la préparation des matériaux QDs@ZIF-8, à savoir "bottle-around-ship" et "ship-in-the-bottle". Dans la première, les QDs ont été utilisés comme germes pour la croissance du matériau ZIF-8 (CuInS₂/ZnS@MPA, CdSe/ZnS@DHLA). Dans la seconde méthode, les cristaux ZIF-8 ont été utilisés comme support pour la croissance des points quantiques (CdZnTe@MPA). Dans ce cas, nous avons observé une croissance limitée des points quantiques au sein des pores ZIF-8. Toutefois, nous ne disposons pas de suffisamment d'informations sur la quantité des QDs introduits dans le réseau du ZIF-8 et il est nécessaire d'évaluer le mécanisme exact de la formation de ces matériaux hybrides, par exemple par microscopie électronique à sonde de balayage ou microscopie électronique en transmission. Nous aimerions également déterminer la durée de vie de fluorescence des points quantiques incorporés dans les particules ZIF-8.

Le travail sur la ZIF-8 cytotoxicité présenté dans cette thèse est au stade préliminaire et implique l'utilisation de modèles de cultures cellulaires. Ces résultats pourraient être étendues à des tests plus avancés. Les futures expériences suivantes sont envisagées:

- le suivi *in vivo* sur un modèle animal de poumon afin de déterminer la capacité des particules à traverser la barrière épithéliale et de la perturber,
- des tests de distribution paraérosol à l'aide d'un ventilateur mécanique (nébulisation actionné par la respiration) pour observer le dépôt des particules ZIF-8 dans les voies respiratoires et leurs conséquences,
- des tests percutanés de modélisation d'absorption et de pénétration dans la peau,
- des essais *in vivo* (sur des modèles animaux) de digestion et d'accumulation des produits de décomposition des ZIFs.

- (1) Li S., Huo F., *Nanoscale*, **2015**, 7482-7501
- (2) Zhang H., Zou R., Zhao Y., *Coord. Chem. Rev.*, **2015**, 292, 74-90
- (3) Park K. S., Ni Z., Côté A. P., Choi J. Y., Huang R., Uribe-Romo F. J., Chae H. K., O'Keeffe M., Yaghi O. M., *PNAS*, **2006**, 103, 10186-10191
- (4) Eddaoudi M., Sava D. F., Eubank J. F., Adil K., Guillerme V., *Chem. Soc. Rev.*, **2015**, 44, 228-249
- (5) Katsenis A. D., Puškarić A., Štruhil V., Mottillo C., Julien P. A., Užarević K., Pham M.-H., Do T.-O., Kimber S. A. J., Lazić P., Magdysyuh O., Dinnebier R. E., Halasz I., Friščić T., *Nat. Commun.*, **2015**, 6:6662
- (6) Lim I. H., Schrader W., Schüth F., *Chem. Mater.*, **2015**, 27-3088-3095
- (7) Moh P. Y., Cubillas P., Anderson M. W., Attfield M. P., *J. Am. Chem. Soc.*, **2011**, 133, 13304-13307
- (8) Pan Y., Lin Y., Zeng G., Zhao L., Lai Z., *Chem. Commun.*, **2011**, 47, 2071-2073
- (9) Chughtai A. H., Ahmad N., Younus H. A., Laypkov A., Verpoort F., *Chem. Soc. Rev.*, **2015**, advanced article
- (10) Zheng H., Xing L., Cao Y., Che S., *Coord. Chem. Rev.*, **2013**, 257, 1933-1944
- (11) Motakef-Kazemi N., Shojaosadati S. A., Morsali A., *Micropor. Mesopor. Mat.*, **2014**, 186, 73-79

Les résultats de cette thèse ont été présentés à des conférences nationales et internationales:

International Symposium of Metal-Mediated Chemistry, Strasbourg FRANCE, 22 Novembre 2013 – la presentation: “Controlling ZIF-8 nano- and microcrystal formation and reactivity through zinc salts variations” (Com4)

The 8th International Conference on Quantum Dots, Pisa ITALY, 11-16 Mai 2014 – le poster: “ZIF-8 crystals as hosts for Quantum Dots” (M106)

1st International Symposium on Energy Challenges and Mechanics, Aberdeen UK, 8-10 Julliet 2014 – la presentation: “Magnetic iron oxide/ZIF-8 nanostructures and their catalytic activity”

J3P (Journées Promotions Procédés Produits) "du Captage aux Procédés de valorisation du CO2", Nancy France, 26 Mars 2015 – le poster: “Synthesis of catalyst for cyclic carbonates production”

Colloque STPMF 2015 (Seminar on Science and Technology of Powders), Nancy FRANCE, 8-10 April 2015 – la presentation: “Synthesis of ZIF-8 crystals and application to carbon dioxide conversion”

Les résultats ont également été publiés dans trois articles:

Schejn A., Balan L., Falk V., Aranda L., Medjahdi G., Schneider R., Controlling ZIF-8 nano- and microcrystal formation and reactivity through zinc salt variations. *CrystEngComm*, 2014, 16, 4493-4500
doi: 10.1039/C3CE42485E

Schejn A., Aboulaich A., Balan L., Falk V., Lalevée J., Medjahdi G., Aranda L., Mozet K., Schneider R., Cu²⁺-doped zeolitic imidazolate frameworks (ZIF-8): Efficient and stable catalysts for cycloadditions and condensation reactions. *Catal. Sci. Technol.*, 2015, 5, 1829-1839
doi: 10.1039/C4CY01505C

Schejn A., Mazet T., Falk V., Balan L., Aranda L., Medjahdi G., Schneider R., Fe₃O₄@ZIF-8: magnetically recoverable catalysts by loading Fe₃O₄ nanoparticles inside a zinc imidazolate framework. *Dalton Trans.*, 2015, 44, 10136-10140
doi: 10.1039/C5DT01191D

Synthèse et activité catalytique du cristaux ZIF-8 et ZIF-8 dopés. Evaluation de leur stabilité et de leur toxicité.

Résumé

Depuis plusieurs années, les MOFs (Metal Organic Frameworks) suscitent une grande attention pour leurs applications potentielles en catalyse hétérogène. Ces matériaux sont également étudiés dans les domaines de la séparation, du stockage de gaz, de la libération contrôlée ou comme systèmes de vectorisation de médicaments. Leur structure complexe étant formée par des centres de coordination métalliques unis par des ligands polydentates, les MOFs disposent de nombreux sites acido-basiques de Lewis ou de Brønsted qui sont cruciaux pour l'activité des matériaux et la sélectivité des produits lors des réactions catalysées par les MOFs. Dans ce travail, nous nous sommes tout particulièrement intéressés à une classe de MOFs appelée « zéolithic imidazolate frameworks » (ZIF-8). Les ZIF-8 présentent de nombreuses propriétés intéressantes, notamment une grande surface spécifique, une faible densité, une forte porosité ainsi qu'une excellente stabilité chimique et thermique.

Dans une première partie, la préparation de matériaux ZIF-8 et d'hétérostructures à base ZIF-8 a été développée afin de conférer à ces matériaux des propriétés adaptées à l'application souhaitée. La mise en forme de ces catalyseurs a également été étudiée afin d'obtenir la forme optimale pour une utilisation industrielle de ces matériaux.

En variant le précurseur d'ions Zn^{2+} utilisé pour la synthèse, nous avons démontré que les propriétés (taille, porosité, ...) de ZIF-8 cristaux pouvaient être contrôlées en fonction de l'application catalytique recherchée. Ces ZIF-8 cristaux ont été utilisés avec succès en tant que catalyseurs hétérogènes dans les réactions de Knoevenagel et Friedländer. Nous avons développé de nouveaux matériaux ZIF-8 dopés par des ions Cu^{2+} . Les particules Cu/ZIF-8 se sont montrés être des catalyseurs efficaces dans la réaction de Combes et la cycloaddition de Huisgen. La recyclabilité du matériau a été évaluée et il a notamment été montré que les particules ZIF-8 pouvaient être réutilisées jusqu'à dix fois sans perte d'activité catalytique. Nous avons également fonctionnalisé les cristaux ZIF-8 avec des particules magnétiques Fe_3O_4 . L'hétérostructure hybride $Fe_3O_4@ZIF-8$ peut facilement être récupérée par séparation magnétique après les expériences de catalyse. Afin d'étendre le champ d'application des catalyseurs ZIF-8, le matériau a également utilisé pour la conversion du dioxyde de carbone en carbonates cycliques en utilisant un réacteur du Parr. Comme la réaction est d'un grand intérêt industriel, le catalyseur a été mis en forme par compression.

Dans la dernière partie de ce mémoire, la toxicité des particules ZIF-8 et ZIF-8 dopé par Cu ou Fe a été évaluée en utilisant des cellules alvéolaires A549 et de la peau IHK comme modèles. La stabilité des particules a été déterminée à l'aide de milieux mimant la digestion des particules *in vivo*. Les résultats obtenus montrent que les particules sont très sensibles aux variations de pH ainsi qu'aux sels présents dans les différents milieux.

Synthesis and catalytic activity of ZIF-8 and doped-ZIF-8 crystals. Stability and cytotoxicity evaluation.

Abstract

Metal organic frameworks (MOFs) have gained considerable attention as heterogeneous catalytic systems and also have been studied in the area of separation, gas storage, controlled release or as drug delivery systems. According to their complex structure formed by metal centers coordinated with polydentate linkers, MOFs expose abundance of Lewis and/or Brønsted acid-base sites that are crucial for the materials catalytic activity and selectivity towards specific reactions. Moreover, these materials have many other attractive properties, including a large surface area, a low density and a high porosity. In this work, we focused on the zeolitic imidazolate framework (ZIF-8) material – a MOF exhibiting high porosity and stability and which can also be used as a template for further functionalization and modification. Firstly, we focused on the preparation of ZIF-8 crystals and ZIF-8 heterostructures with properties adapted to the desired application, and then shaping of the catalyst to obtain the best form of material for industrial scale-up utilization.

By varying Zn^{2+} precursors used for the synthesis, we demonstrated that the properties (size, porosity,...) of ZIF-8 crystals can be controlled and tuned depending on the applications. These ZIF-8 crystals were successfully applied as heterogeneous catalysts in Knoevenagel and Friedländer reactions. Next, we developed protocols for the synthesis of Cu^{2+} -doped ZIF-8 crystals. The use of these crystals could be extended to Cu-mediated reactions, like the Combes condensation and the Huisgen cycloaddition. We evaluated recyclability and we showed that the nanomaterials could be reused up to ten times without any loss of catalytic activity. Moreover, we functionalized ZIF-8 crystals with magnetic Fe_3O_4 nanoparticles. The hybrid $Fe_3O_4@ZIF-8$ heterostructures could be easily recovered by magnetic separation after catalytic experiments. To show multiple benefits originating from the ZIF-8 structure and properties, we also used this material for the conversion of CO_2 into cyclic carbonates using a Parr reactor. As the reaction could be scale-up at the industrial level, we shaped the powder in the form of pellets and use it under the same conditions.

In the last chapter, we evaluated the toxicity and the stability in biological media of ZIF-8, Cu- and Fe-doped ZIF-8 particles using A549 alveolar cells, IHK skin cells as models and *in vitro* ingestion under fed conditions. These models were chosen according to the most probable first contact entering gates for nanoparticles inside human body, skin, lungs and digestive tract. Outcomes from these preliminary studies motivated us to conduct extended stability tests of the particles in different media. We showed that the particles are altered by pH changes and medium complexity.